WALL-MODELS FOR LARGE EDDY SIMULATION BASED ON A GENERIC ADDITIVE-FILTER FORMULATION

A Dissertation
Presented to
The Academic Faculty

by

Martín Sánchez Rocha

In Partial Fulfillment
of the Requirements for the Degree
Doctor of Philosophy in the
School of Aerospace Engineering

Georgia Institute of Technology
May 2009

WALL-MODELS FOR LARGE EDDY SIMULATION BASED ON A GENERIC ADDITIVE-FILTER FORMULATION

Approved by:

Prof. Suresh Menon, Committee Chair
School of Aerospace Engineering
Georgia Institute of Technology

Prof. P.K. Yeung
School of Aerospace Engineering
Georgia Institute of Technology

Prof. Marilyn J. Smith
School of Aerospace Engineering
Georgia Institute of Technology

Prof. Predrag Cvitanović
School of Physics
Georgia Institute of Technology

Prof. Lakshmi N. Sankar
School of Aerospace Engineering
Georgia Institute of Technology

Date Approved: December 12, 2008

To all who have left a mark in my life,

specially,

my Parents, Siblings, and Zazy.

ACKNOWLEDGEMENTS

I would like to express my sincere gratitude and respect to my advisor Professor Suresh Menon, who gave me the freedom to explore my ideas even when they were not directly related to the research objectives that I was originally assigned. I thank him for his continuous and energetic push, which introduced me to the real demanding world of scientific research. Here, I can only hope that my work has reached his high standards. Finally, I want to thank him for being patience with me in my earliest days at Georgia Tech, when my inexperience made me felt incapable to succeed at CCL. Thanks for the second chance to stay in the lab, I learned to never give up no matter how bad things may look!

I would like to express my gratitude to México for supporting my graduate education through the National Council of Science and Technology (CONACYT). This dissertation would have not been possible without the back up of my country.

I would like to thank the academic faculty Prof. Marilyn J. Smith, Prof. Lakshmi N. Sankar, Prof. P.K. Yeung, and Prof. Predrag Cvitanović for taking time from their busy schedule to integrate my dissertation reading committee.

I would like to express my gratitude to all the Georgia Tech community, who not only contribute to my understanding of academic problems, but most importantly, contribute to the enrichment of my life by sharing aspects of their culture and life with me. It was a pleasure working and knowing Hossam, Mehmet, Ion, Chris, Justin, Orcun, Satish, Franklin, Gilles, Matthieu, Kaushik, Miguel, Luchi, Jason, JP, Joey, Nathalie, Vaidya, Nayan, and Feiz. My gratitude goes to Baris, Nuri, Ayse, and all the Turkish community who always were eager to share with me the wonders of Turkey. Arigatou gozaimasu to my awesome "samurai" friend Kenji Miki for sharing

part of japan and his life with me, I had one of the best meals of my life in your parents house, also thanks for never complaining when I started my drumming. My respect to past and present roasters of *Time for Glory*, it was a honor fighting with you in the field! A special mention goes to Diego Donzis and Cristian Escauriaza for the most enlightening discussions that I have ever had in topics so diverse as: physics, religion, pidulles, porongas, fulbo, etc... Here, I am afraid that despite your strong arguments and the overwhelming evidence, views also shared by Matthieu and JP, you could not convince me that México is not in the elite class of world soccer. Finally, my deepest gratitude to all who have influenced every aspect of my life during my days at Tech, it was a real privilege being among so many bright people.

I would like to express my deepest gratitude to my parents Honorio and Lupita for their boundless love and all the sacrifices that they made to provide me the best education possible. I want to think about this dissertation as my way to say *"thanks for your effort"*, I can only hope that I still make you proud, *los quiero mucho y si se pudo!* To my siblings Liliana and Edgar, thanks for always being there when I needed help and advise, and sorry for the burden of bearing a hyperactive never-quiet big brother. Thanks also to llillisito, for sharing with me those long and boring studding days, it was then when I realize how much you could sleep *fojosito!* I would like also to thank the rest of my family, Sánchez and Rocha, who always make me feel welcome and missed. I miss you all.

Finally but not least, I would like to thank you Zazy, without your help I could not have made it. Thanks to you, I have fulfilled my goals and came close to the man that I always dreamed to be. Thanks for loving and understanding me, even when I did not make sense. Although you may disagree, at your side I finally mature, I am able of many things that I never thought possible, thanks for teaching me how to survive, but most importantly, for teaching me how to live. I cannot change my past but, if you want, my present and future could be only yours. *Mollenito siempre*

querrá a zazyta. . . , muchos panditas, abazitos, y bbesitos de telefonito!

TABLE OF CONTENTS

LIST OF TABLES

LIST OF FIGURES

SUMMARY

Based on the philosophy of only resolving the large scales of turbulent motion, Large Eddy Simulation (LES) has demonstrated potential to provide high-fidelity turbulence simulations at low computational cost. However, when the scales that control the turbulence in a particular flow are not *large*, LES has to increase significantly its computational cost to provide accurate predictions. This is the case in wall-bounded flows, where the grid resolution required by LES to resolve the near-wall structures is close to the requirements to resolve the smallest dissipative scales in turbulence. Therefore, to reduce this demanding requirement, it has been proposed to model the near-wall region with Reynolds-Averaged Navier-Stokes (RANS) models, in what is known as hybrid RANS/LES approach.

In this work, the mathematical implications of merging two different turbulence modeling approaches are addressed by deriving the exact hybrid RANS/LES Navier-Stokes equations. These equations are derived by introducing an additive-filter, which linearly combines the RANS and LES operators with a blending function. The equations derived with the additive-filter predict additional hybrid terms, which represent the interactions between RANS and LES formulations. Theoretically, the prediction of the hybrid terms demonstrates that the hybridization of the two approaches cannot be accomplished only by the turbulence model equations, as it is claimed in current hybrid RANS/LES models.

The importance of the exact hybrid RANS/LES equations is demonstrated by conducting numerical calculations on a turbulent flat-plate boundary layer. Results indicate that the hybrid terms help to maintain an equilibrated model transition when

the hybrid formulation switches from RANS to LES. Results also indicate, that when the hybrid terms are not included, the accuracy of the calculations strongly relies on the blending function implemented in the additive-filter. On the other hand, if the exact equations are resolved, results are only weakly affected by the characteristics of the blending function. Unfortunately, for practical applications the hybrid terms cannot be exactly computed. Consequently, a reconstruction procedure is proposed to approximate these terms. Results show, that the model proposed is able to mimic the exact hybrid terms, enhancing the accuracy of current hybrid RANS/LES approaches.

In a second effort, the Two Level Simulation (TLS) approach is proposed as a near-wall model for LES simulations. Here, TLS is first extended to compressible flows by deriving the small-scale equations required by the model. The new compressible TLS formulation, is validated simulating the flow over a flat-plate turbulent boundary layer. Overall, results are found in reasonable agreement with experimental data and LES calculations. Here, issues related with the integration criteria of the TLS small-scale equations are commented. Finally, TLS is implemented in the additive-filter formulation by replacing the RANS operator with the TLS large-scale operator. The new hybrid TLS/LES approach, is evaluated on the turbulent boundary layer case, in general, results are found in good agreement with experimental data and LES calculations. Here, the dependency of hybrid TLS/LES formulation on the blending function is similar to the hybrid RANS/LES approach when the hybrid terms are neglected. However, contrary to the hybrid RANS/LES case, including the hybrid terms in the TLS/LES formulation does not seem to improve the predictions. The low impact of the hybrid terms in the accuracy of the calculations, is explained by the similarity exhibited between the large-scale TLS operator and the LES space filter. Here, both operators represent space filters, therefore, the difference between TLS and LES variables is almost negligible, reducing drastically the importance of the hybrid terms.

CHAPTER I

INTRODUCTION

Due to the fast development of computational technology, science and engineering rely more and more on Computational Fluid Dynamics (CFD) to get insight in the physics of fluids and conduct critical engineering analysis, specially in areas where experiments become extremely expensive, dangerous, or inaccessible [9, 10, 96]. Unfortunately, the presence of turbulence in industrial and scientific applications has limited the reach of CFD as a research and analysis tool.

The modeling of turbulence is not the only aspect that has limited the proliferation of CFD as a research and engineering analysis tool [83]. However, high Reynolds number (Re) flows, invariably require demanding computational resources to account for the effects of turbulence [64]. Therefore, turbulence modeling is still considered the major aspect that has to be addressed to extend the reach of CFD as a analysis and research tool in fluid dynamics [75, 83].

Currently, there exist many approaches to simulate turbulent flows. However, most of them can be loosely characterized into four groups: 1) Direct Numerical Simulation (DNS), 2) Reynolds-Averaged Navier-Stokes equations (RANS), 3) Large Eddy Simulation (LES), and 4) PDF methods. In DNS, all the time and space scales present in the flow are resolved. This approach is extremely accurate, which makes it suitable for fundamental research. However, due to its high cost, which is dictated by the smallest viscous dissipative scales, and the high accuracy of the numerical algorithms required, it can only be used to conduct simulations on simple flow configurations at low to moderate Re numbers [64]. In RANS, only the mean flow variables are resolved, while all the scales of turbulence are modeled. Consequently, its cost

is dictated by the mean characteristic scales of the flow, which allows simulations at high Re numbers. Additionally, the numerical algorithms usually implemented in RANS are of low accuracy-order [106], which can be easily implemented in complex geometries. Unfortunately, the accuracy of RANS predictions strongly relies on the turbulence model implemented, which usually performs poorly when conditions outside its calibration limits are encountered [89, 106]. An additional drawback of RANS is its inherent inability to provide any unsteady flow information. In the LES approach, only the large-scales of the flow responsible for the turbulence generation are resolved. In principle, LES is less sensitive to the subgrid[1] model implemented as long as the turbulent driving forces are correctly resolved. Although, LES does not require numerical schemes as accurate as DNS, LES does requires high accuracy to correctly resolve the large scales of the flow, which posts significant challenges in simulations on complex geometries. Nevertheless, LES is able to provide reliable high fidelity unsteady flow information at costs lower than DNS [36, 41, 61, 69, 71, 72, 75]. In PDF methods a transport equation for the Eulerian PDF of the velocity $f(V; x, t)$ is derived from the Navier-Stokes equations, here the convective terms are found in closed form, however, the closure for the governing equations is obtained using stochastic models since the PDF does not contain information on the turbulence time scales [72].

The decision of conducting RANS, LES, or DNS simulations strongly depends on the issues that need to be addressed in the flow of interest. Therefore, if the interest is in understand how the high-order statistics in turbulence are affected by internal intermittency at high Re numbers, DNS simulations will be pursued to obtain the physical insight regardless of its high cost [43, 64]. On the contrary, if the interest is in obtaining a quick calculation for the mean friction coefficient or heat flux in

[1]The subgrid terms refers to the turbulent scales not resolved confined within the LES grid resolution.

a configuration for which a RANS model can predict accurate results, there is no need to conduct a DNS or LES calculation just because DNS and LES appear to be superior than RANS [36, 41, 75, 83]. Therefore, it is important to keep in perspective the relevance of each turbulence modeling approach and what can be obtained from them. DNS is not just a massive solution of the Navier-Stokes equations without any possible engineering application, nor is RANS an old-fashioned model on the verge of being replaced by more accurate approaches, nor is LES capable of producing calculations with DNS accuracy at a RANS cost.

In particular, for turbulence simulations where the interest is in high fidelity unsteady flow structures and for which DNS cannot be practically applied, LES may be the option of choice. As it was mentioned before, as long as the scales driving the turbulence of the flow are resolved, LES will be able to produce accurate results almost independent of the subgrid model implemented [27, 57, 61, 75, 83]. However, it is important to highlight an important assumption made explicitly/implicitly in LES. The driving turbulent scales that are resolved must be *large*, on the order of the flow geometry, if LES is to be practical [41, 61, 71, 72, 75, 83]. Contrary, if the scales driving the turbulence are not *large* and are instead on the order of viscous dissipative scales (which decrease inversely with the Re number), LES is forced to implement grid resolutions close to DNS requirements [69, 75]. In fact, in this scenario it would be more appropriate to change the name of LES to Small Eddy Simulation, which more closely reflects the simulation methodology.

Unfortunately, for wall-bounded flows the scales that drive the turbulence are not *large*. Quite contrary, at high Re numbers these structures become quite small when normalized with the characteristic scales of the flow, since they scale with the viscous shear stress at the wall imposing tremendous resolutions requirements. Previous analysis estimated that the total number of grid points ($N_x N_y N_z$) required by LES to resolve the near-wall structures is proportional to $N_x N_y N_z \propto Re^{1.8}$ [12]. Whereas, the

total number of grid points required by DNS to resolve the dissipative turbulent-scales is on the order of $N_x N_y N_z \propto Re^{9/4}$ [69, 72]. On the other hand, the total number of grid points required by LES to resolve the large scale structures in a boundary layer, which scale with the boundary layer thickness, is proportional to $N_x N_y N_z \propto Re^{0.4}$ [69]. These estimations demonstrate that the cost of LES simulations, measured in terms of number of grid points, is very close to DNS. Unfortunately, wall-bounded flows occur in engineering application as a rule and not as an exception explaining why LES is not commonly use as an engineering analysis tool.

Although the previous scaling demonstrated the high cost of wall-bounded LES calculations, it is important to mention that the structures that require the highest resolution are confined within (depending on the Re number) 10% or less of the boundary layer thickness, in what is known as the inner layer [69]. Therefore, in principle it would be possible to conduct affordable LES calculations if the inner layer is modeled instead of resolved, which would reduce significantly the cost of the simulations since only the outer layer[2] needs to be resolved with a resolution scaling as $N_x N_y N_z \propto Re^{0.4}$. This approach is known as near-wall, wall-layer, or wall-model for LES. However, it is important to keep in mind that the dependence of LES on the turbulence modeling strategy will increase due to the additional empiricism incurred in modeling the inner layer.

Currently, most of the available wall-models can be classified in the following groups [68, 69, 75]:

- *Equilibrium laws*: In this approach approximate boundary conditions are implemented assuming that the logarithmic law-of-the-wall [98] holds in the mean velocity profile. Here, the local wall shear stress is computed from data at the outer layer, which then is used to feed back information into the outer layer to

[2]This region is defined as $0.1 < y/\delta < 1$, where δ is the boundary layer thickness and y the wall-normal distance.

mimic the wall-normal flux of momentum at the inner layer [16, 79].

- *Use of boundary layer equations*: In this approach, the turbulent boundary layer equations are integrated analytically using an algebraic turbulence model to derive relations for the local stress [103].

- *Zonal approaches*: In this approach a different set of equations or formulations are resolved at the inner and the outer layers, usually RANS equations are selected as the near-wall model. This methodology can be implemented in two ways: 1) using different grids in each formulation domain, known as Two Layer Model; and 2) using the same grid for both formulations, here a discontinuous interface is defined to delimit the domain of each formulation.

- *Hybrid approaches*: In this approach different equations or formulations are implemented to resolve the inner and the outer layer. Usually, RANS equations are implemented. The transition between formulations takes place smoothly in a hybrid region where the solution is composed by both RANS and LES approaches. Here, the same grid is implemented for both formulations.

Although wall-layer models based on boundary layer equations and equilibrium laws have been successfully demonstrated predicting equilibrium flows[3] with no significant extra cost, their underlying assumptions are too restrictive and usually break down when flow separation or strong adverse-pressure gradients are encountered, reducing drastically their range of applications [69]. On the other hand, zonal and hybrid approaches have been found more robust handling flow separation and adverse pressure-gradient flows in arbitrary configurations [68, 85]. Therefore, due to the importance that hybrid and zonal methods have gained [68, 83, 85] the interest of this work is to develop advancements in this approach.

[3]Flows where the Law-of-the-wall holds.

1.1 Background on Hybrid RANS/LES Models

The hybrid[4] RANS/LES methodology is a relatively new concept designed to simulate complex high Re number turbulence flows found in engineering applications. It was motivated by the inability of RANS to predict complex unsteady flows and the prohibitively high cost of LES in high Re wall-bounded flows. In general, the hybrid RANS/LES formulation can be interpreted as a model intended to reduce the high cost of LES simulations. Although the idea of using RANS as a near-wall model can be traced back to the early work of Schumann [79], hybrid RANS/LES models were not seriously considered until Spalart et al. [88] and Speziale [90] explicitly introduced practical hybrid approaches.

In the approach of Spalart et al. [88], the Spalart-Allmaras RANS model [87] is modified to reduce the amount of turbulence viscosity provided in regions of massive flow separation, while in attached flow regions the original RANS model is implemented. This model was named Detached Eddy Simulation (DES) implying that it should be used in flows where massive flow separation controls the unsteady flow dynamics. DES has been successfully applied to a broad range of problems spanning complex engineering applications to canonical flows studies [47, 66, 67, 70, 83, 85, 92, 93, 102]. However, as any other model, DES has advantages and disadvantages which compromise the accuracy of its predictions [66, 84, 92]. A characteristic limitation of DES is its transition from RANS to LES, which is grid controlled. Here, grid refinements made to improve the description of the geometry could dramatically interfere with the model transition, inducing inaccurate predictions. An heuristic correction for this latent source of error have been proposed in a new version of this model [86], which employs a smooth transition function for the model transition.

A different hybrid RANS/LES approach was introduced by Speziale [90]. He

[4]Here the hybrid term also include the zonal approach.

proposed a formulation capable of bridging DNS with RANS modeling with LES in-between. He referred to this model as very-large eddy simulations (VLES). In his approach, the subgrid stress tensor (τ_{ij}^s) is computed by rescaling the RANS Reynolds stress tensor (τ_{ij}^R) as

$$\tau_{ij}^s = \alpha \tau_{ij}^R, \quad \alpha = [1 - \exp(-\beta \Delta/\eta)]^n, \tag{1.1}$$

depending on whether or not the grid is fine enough to resolve the local turbulent scales. Speziale only suggested the form of the rescaling factor (α) as function of the grid resolution (Δ) and the Kolmolgorov length scale (η); the constants β and n, were left unspecified. Other researchers proposed different formulations to implement this approach. Some examples are the limited numerical scales (LNS) model of Batten et al. [5], the partially resolved numerical simulation of Liu et al. [58], the renormalization group model of Delanghe et al. [18], the partially averaged Navier-Stokes model of Girimaji [33], and the model of Befeno and Schiestel [8]. These models in general compare locally, the modeled scales provided by RANS and LES to determine which turbulence modeling closure is to be implemented, their main differences rely on the RANS and LES models implemented, and in the way the modeled scales are compared. It is important to highlight that Speziale's formulation is not restricted to act as a near-wall model for LES, since the transition can occur in any flow region where the grid resolution is fine enough to sustain LES or even DNS simulations.

Recently, other hybrid formulations have appeared in the literature, such as the zonal [13, 14, 29, 34, 35, 69, 77, 97, 100, 111] and the blended [3, 6, 25, 46, 108, 109] approaches. In the zonal approach, RANS modeling is implemented as a near-wall model. The matching plane or interface between the models is specified arbitrarily. Different research groups have proposed zonal approaches by combining specific RANS and LES models, some of them include: Davidson and Peng [15], and Tucker and Davidson [100] they combined the RANS $k-\omega$ and $k-l$ models, respectively, with a one-equation model for the subgrid kinetic energy (k^{sgs}), Hamba [34, 35] used

a mixing-length RANS model with the Smagorinsky LES model [82], Temmerman et al. [97] explore a zonal approach where the RANS $k-\epsilon$ and the $k-l$ were coupled with the Smagorinsky LES model, among many others.

In the blended approach, a hybrid model is constructed by smoothly combining compatible RANS and LES model equations. This formulation is similar to the zonal approach since RANS is used as a near-wall model, however, the transition between models occurs smoothly in a well-defined region, where the turbulence closure is composed by both RANS and LES. Baurle et al. [6] proposed that any trusted RANS and LES models containing equations for the turbulent kinetic energy (k) and subgrid kinetic energy (k^{sgs}) could be smoothly combined to design a single hybrid model equation. They combined a two-equation RANS $k-\omega$ model and a one-equation LES model for k^{sgs} to conduct simulations of cavity flows. Xiao et al. [108, 109] and Fan et al. [25] implemented RANS $k-\zeta$ and RANS-SST $k-\omega$ models with a LES one-equation for k^{sgs} to simulate the flow over a compression ramp. In general, the performance of these models is encouraging. Nevertheless, significant amount of work still has to be conducted to evaluate and quantify the effect of the blending function and the turbulence models used in the simulations even when some of these issues have been already investigated in the past [108, 109]. In principle, there is no reason why only models containing equations for k and k^{sgs} should be used to construct hybrid blended models. The hybrid blended approach should be presented in a general form independent of the kind of RANS and LES models employed.

1.2 Multi Scale Decomposition Approaches

Although the focus of this thesis is in near-wall models for LES, it is important to provide some background in Multi Scale Decomposition (MSD) methods, since the second part of this research effort deals with an alternative method to construct hybrid near-wall models for LES.

The main idea in MSD is to decompose the total flow variables (ϕ) into a resolved (large-scale ϕ^L) and unresolved (small-scale ϕ^S) parts $\phi = \phi^L + \phi^S$. Contrary to other popular multi-scale methods like RANS or LES, where the effect of the unresolved scales is modeled using an eddy viscosity closure, in MSD the effect of the unresolved scales is modeled by explicitly reconstructing the small-scale field and from it the unclosed terms appearing in large-scale equations are exactly computed.

In order to reconstruct the small-scale field, governing equations for these scales have to be derived. The small-scale equations are usually derived by applying the scale decomposition in the Navier-Stokes equations and conducting some simplifications. Some of the current MSD approaches include the dynamic multilevel method of Dubois et al. [22], the additive turbulent decomposition approach by Hylin and McDonough [42], the rapid distortion theory model of Laval et al. [23, 55, 56], the variational multiscale method of Hughes et al. [39, 40], and the Two Level Simulation (TLS) of Kemenov and Menon [48, 49].

The differences between MSD approaches rely in the way the scale separation and the small-scale equations are derived. For instances, the dynamic multilevel method of Dubois et al. [22] implements dynamical systems theory to approximate the attractor of the Navier-Stokes equations to derive the small-scale equations. These equations are further simplified using physical arguments. In the other hand, the model of Laval et al. [23, 55, 56] conducts the scale separation using a space filter. The small-scale equations are obtained by subtracting the filtered operated Navier-Stokes equations from the unfiltered Navier-Stokes equations. The small-scale equations are further simplified by only keeping products between large and small scale variables, while the rest of the terms are modeled using an eddy viscosity model.

Similar to the model of Laval et al., the TLS model of Kemenov and Menon [48, 49] separates the velocity field into large and small scales by postulating a large scale operator. However, this operator is not directly applied in the Navier-Stokes equations

to derive the large scale equations. In TLS, the small-scale equations are derived by applying the scale decomposition directly to the Navier-Stokes equations. By collecting large and small scale terms, a fully-coupled set of large and small scale equations is derived. Furthermore, to reduce the cost of the simulations, the three-dimensional small-scale equations are simplified and resolved over one-dimensional lines embedded in the large-scale grid. This approach has been successfully applied to incompressible isotropic turbulence, temporal mixing layers, and turbulent channel flow. The implicit unsteady nature and the ability to simulate homogeneous and inhomogeneous turbulent flows make TLS an excellent candidate to formulate a near-wall model for LES.

1.3 Current Issues in Hybrid RANS/LES Models

Although impressive results have been obtained with hybrid RANS/LES simulations in complex massive separated flow conditions [85], hybrid simulations of attached turbulent flows, like channel flows and boundary layer have been quite disappointing [15,34,66,70]. This discrepancy in success is explained by the fact that in massive separated flows, the turbulence is driven by the large-scale structures, which are resolved by the LES part of the hybrid model. However, if the near-wall dynamics is the driven mechanism for the turbulence generation, current hybrid models cannot predict accurate results.

Nikitin et al. [66] conducted simulations of high Re channel flow using DES as a near-wall model, results predicted mean velocity profiles with severe deviation from the law-of-the-wall at the logarithmic region. They found that the anomalous predictions were insensitive to changes in grid resolution and location of the RANS/LES model interface, indicating a pathological behavior of the hybrid model. Davidson and Peng [100], and Tucker and Davidson [15] simulated the flow over a plane and

ribbed channel, and over a three-dimensional hill. Their results predicted discontinuities in the flow statistics and in the turbulence variables, independently of the location of models interface. Hamba [34, 35] conducted zonal simulations in channel flows and reported unphysical mismatches in the flow statistics close to the model interface. He demonstrated that even when LES is conducted in the near-wall region and RANS in the core of the channel, the zonal approach still predict unphysical results. He proposed to filter the flow variables at the models interface to correct the flow statistics. Temmerman et al. [97] observed similar issues in their channel zonal simulations and proposed a bounding criterion in the modeled stresses to reduce the discontinuities predicted in the flow statistics at the model interface. Davidson and Dahlström [14] proposed the inclusion of turbulence fluctuations at the interface to reduce the discrepancies observed in previous channel simulations. Their approach improved zonal predictions for channel flows, however, it required a precursor DNS simulation. Davidson and Billson [13] proposed the inclusion of synthesized turbulence at the model's interface. They explored isotropic and anisotropic fluctuations in channel flow simulations with good results. Similar stochastic forcing approaches have been also proposed by Piomelli et al. [70], Keating and Piomelli [47], and Batten et al. [5].

The consistent anomalous predictions obtained with different hybrid models in attached flows, indicate that the hybrid formulation is not able to correctly model the near-wall turbulent dynamics. In fact, it was found that the shift in the logarithmic profile and discontinuities in the statistics, are caused by an imbalance in the turbulent transport generated in the region where the hybrid model switches from RANS to LES [5, 70]. In this region, the hybrid model reduces, either abruptly or gradually, the modeled RANS stresses to LES levels. However, the resolved turbulent stresses are not generated at the same rate at which the modeled stresses are suppressed. This induces a significant decrease in the turbulent momentum transport, which is

refered as artificial turbulence dissipation (ATD), which forces viscous stresses to compensate the transport of momentum leading to the incorrect mean velocity profile and discontinuous statistics [5, 34, 70]. This problem becomes more significant when the transition from RANS to LES occurs abruptly.

The problem induced by the mismatch between the rates at which resolved and modeled stresses are generated and suppressed in the RANS to LES transition (RTLT) zone, is similar to the problem faced in turbulent inflow generation [59]. In the later was found that if synthetic conditions are imposed (mean velocity profile with and without random fluctuations superimposed), the flow requires a significant long transition distance before physical turbulence develops. This is the same situation faced at the RTLT zone, where LES requires a transition either in space or time[5], before resolved turbulence develops from the quasi-steady RANS field.

Attempts to correct the anomalous ATD in hybrid simulations have been proposed with relative degrees of success. Some of these include application of filtering at the models interface to eliminate the discontinuities in the statistics [34, 35], imposing compatibility conditions in the RANS and LES stresses to prevent ATD [97], and implementing unsteady forcing terms to the governing equations, computed either synthetically or from precursor simulations, to trigger the development of resolved turbulence in the RTLT region to control ATD [5, 13, 14, 47, 70]. However, despite the success that these methods have shown, they lack fundamental justification, which limits their systematic improvement. Thus, at best these methods can only be considered heuristic and their improvement is subject to trial and error [35, 70, 97].

[5]Depending on the way the switch from RANS to LES occurs.

1.4 Objectives

Although significant progress has been made in developing and applying hybrid RANS/LES models, in general very few researchers have developed a theoretical formulation for the hybrid RANS/LES approach. In combining RANS with LES, most methods ignore their fundamental differences [36, 70]. Consequently, most reported formulations become engineering methods driven by practical necessity for simulating high Reynolds number flows with available computational resources. This lack of theoretical foundation, has hindered systematic improvements in this promising approach. Indeed, most of the currently employed hybrid approaches, can be seriously questioned from a theoretical standpoint. For instance, the fundamental implication of merging two sets of equations that describe differently the physics of fluids is usually overlooked. Its omission is justified most of the time by the fact that both RANS and LES governing equations look very similar [36]. The theoretical issues are less of a concern to applied engineer, who forced by time and cost constrains, applies and modifies hybrid models to produce better calculations. He may not realize that without a theoretical framework, the options to improve hybrid RANS/LES models reduce to trial and error, a practice that in the long term will induce higher costs and more time to the design process.

There have been, however, some theoretical attempts to develop a general framework for the hybrid approach [31, 37, 53, 75]. In particular, the framework set forth by Germano [31] is the most adequate to address the hybrid RANS/LES formulation from a near-wall model standpoint. He demonstrated that the governing equations derived by applying a hybrid filter (created by smoothly combining the RANS and the LES operators) include new hybrid terms that should not be neglected. His formal derivation (albeit, restricted to incompressible flows) indicates that hybrid formulations cannot rely only on the capability of the turbulence models to switch from RANS to LES. However, the importance of these new hybrid terms was only

speculated, since no calculation implementing these equations was conducted.

The status of the hybrid RANS/LES approach motivates research into the open theoretical issues. The principal goal of this dissertation is to present fundamental and technical advancement in hybrid RANS/LES models with implication as near-wall models. Additionally, due to the potential of TLS to simulate turbulent flows, is the interest of this work to explore its ability to perform as an alternative near-wall model.

In order to achieve the goals of the dissertation, the following objectives are defined:

1. Derive the exact compressible hybrid RANS/LES Navier-Stokes equations. These equations have not been derived before, thus, presenting them is an original contribution.

2. Assess the importance of the derived hybrid RANS/LES governing equations and demonstrate its advantages over standard hybrid RANS/LES methodologies. This includes: identify the issues involved in the merging of RANS with LES and to propose solutions for such problems. These efforts have not been done in the past, therefore, resolving the exact hybrid RANS/LES governing equations is an original contribution with direct impact in turbulence modeling.

3. Develop a new hybrid RANS/LES turbulence model equation from well-established RANS and LES models. The interest of this dissertation is not only in the exact hybrid RANS/LES equations, but also in presenting a new reliable hybrid RANS/LES model equation.

4. Develop improvements to the hybrid RANS/LES methodology based on the theoretical framework developed. This effort is important, since brings new improvements to hybrid RANS/LES models based on the new formulation.

5. In a second effort toward near-wall models for LES, the TLS method is extended to compressible flows by deriving the governing equations for the flow and thermodynamic small-scale variables. It is important to extend TLS to compressible flows, since these equations have not been derived before.

6. Asses the potential of the TLS formulation as an unsteady near-wall model for LES. Currently, TLS have been demonstrated as a full turbulence modeling formulation. However, its potential as a near-wall model has to be demonstrated.

7. Implement the numerical and modeling tools required to conduct the previous objectives:

    - Implement realistic turbulent inflow boundary condition. This is a critical aspect in turbulence simulations. Although, a new approach for realistic turbulence inflow is not developed in this work, it is important to stress that a realistic turbulence inflow generation technique is currently not available in the baseline code. Thus, its implementation is an important contribution.
    - Implement a high order numerical scheme for spatial discretization. Although, a new numerical scheme is not developed in this work, it is important to implement this capability in the baseline code, which lacks enough spatial discretization-accuracy to conduct high fidelity turbulence simulations.

- Implement RANS, LES, and TLS models. The baseline version of the code does not have turbulence modeling capabilities. Therefore, each turbulent modeling approach has to be implemented in the code from scratch. This requires significant effort at the PhD level.

1.5 Dissertation's Outline

The rest of the dissertation is organized as follows.

Chapter II introduces the governing equations of fluid motion. Here, the governing and model equations for RANS and LES are presented.

Chapter III describes the numerical approach developed to conduct the turbulence simulations.

Chapter IV presents the validation of the numerical approach developed, emphasis is given to demonstrate the LES and RANS capabilities.

Chapter V presents the derivation of the generic additive-filter operated compressible Navier-Stokes equations. In particular, the additive filter is constructed by combining the RANS and LES operators. Here the properties of the hybrid filter and its implications in the derivation of the governing equations are discussed. The hybrid equations for incompressible flows and for hybridization conducted in time are also presented and briefly discussed. The importance of the derived governing equations is assessed by conducting numerical calculations of turbulent boundary layer. Finally, a model to approximate the hybrid terms is proposed to improve the accuracy of hybrid RANS/LES models.

Chapter VI presents the derivation of the compressible Two Level Simulation equations. The formulation is assessed by conducting calculations of turbulent boundary layers. Finally, the potential of the method to be used as a near-wall model is demonstrated.

Chapter VII discusses concluding remarks and the proposed future work.

The appendix present the abstract of an accepted publication of part of the material presented in this dissertation.

CHAPTER II

MATHEMATICAL FORMULATION

In this chapter, the mathematical formulation that describes the fluid motion is introduced. The governing equations are presented in their integral and differential form, using tensor notation to allow a compact and clear presentation. Therefore, before developing the mathematical formulation, the tensor definitions used throughout this work have to be defined. However, for a complete exposure on tensor theory see Refs. [78, 80, 94].

Informally, the term *tensor* or *tensor field* is defined as a mathematical object in $\mathbb{R}^m$ with n indexes (order n) and m^n elements, which obeys certain transformation rules [94]. One of the most important rules that a tensor obeys, hence its importance in mathematical physics, is that of being invariant to coordinate transformation [94]. Therefore, expressing the laws of physics with tensors, warrants the invariance of these laws to coordinate transformation as well [78, 80].

In tensor manipulation, it is common to use the Einstein summation convention. This convention states, that when a tensor or group of tensors include repeated indexes a summation is implied $A_{ik}B_{kj} = \sum_{k=1}^{m} A_{ik}B_{kj}$ or $C_{ikk} = \sum_{k=1}^{m} C_{ikk}$, here A and B are 2^{nd} order tensors and C is a 3^{rd} order tensor. For notation purposes, this rule applies only to indexes appearing in italic characters, thus, if repeated indexes appear in greek characters no summation is implied $A_{i\alpha}B_{\alpha j} \neq \sum_{\alpha=1}^{m} A_{i\alpha}B_{\alpha j}$. Under this convention, tensor indexes cannot appear repeated more than twice i.e., $A_{kk}B_{kk}$ or C_{kkk} are not allowed. However, if summation is required over more than two indexes, different characters have to be used $A_{jj}B_{kk} = \sum_{j=1}^{m} A_{jj} \sum_{k=1}^{m} B_{kk}$. On the other hand, it is possible to have many repeated greek indexes, since they do not

intend summation.

A common tensor that will be used extensively in this work, is the Kronecker delta of order two. This tensor is a function defined as:

$$\delta_{ij} = \begin{cases} 1 & \text{if } i = j \\ 0 & \text{if } i \neq j \end{cases} \tag{2.1}$$

in $\mathbb{R}^m$. The contraction (summation over its indexes) of the Kronecker delta is equal to its dimensionality $\delta_{kk} = m$.

The spacetime on which the equations of fluid motion are described in this work, is an Euclidean continuous space defined in $XT = (x_1, x_2, x_3, x_4) \in \mathbb{R}^4$. Here XT includes the three spatial coordinates, referred indistinctly as (x, y, z) or (x_1, x_2, x_3), and time $x_4 = t$. The velocity, $\frac{\partial x_i}{\partial t} = u_i$, is indistinctly referred as (u_1, u_2, u_3) or (u, v, w). Finally, for pure notation purposes, when a tensor of order one is expressed as x_i, i.e. using "i" for its index, it is implied "x_i for $i = 1, 2, 3, \ldots, m$" and not just a single component.

2.1 The Governing Equations of Fluid Motion

The fundamental laws required to fully describe the fluid motion are, the conservation of mass, momentum, and energy. If these laws are expressed over an arbitrary control volume within a continuous media [80, 101], it can be shown that the integral version of the governing equations take the following form [4]:

$$\frac{\partial}{\partial t}\iiint_\Omega \rho dV + \iint_\Sigma \rho u_j n_j ds = \iiint_\Omega Q_\rho dV \tag{2.2}$$

$$\frac{\partial}{\partial t}\iiint_\Omega \rho u_i dV + \iint_\Sigma \rho u_i u_j n_j ds = \iint_\Sigma (-p\delta_{ij} + \tau_{ij}) n_j ds + \iiint_\Omega \rho F_i dV \tag{2.3}$$

$$\begin{aligned} \frac{\partial}{\partial t}\iiint_\Omega \rho E dV + \iint_\Sigma \rho E u_j n_j ds = &- \iint_\Sigma q_j n_j ds \\ &+ \iint_\Sigma u_i(-p\delta_{ij} + \tau_{ij}) n_j ds + \iiint_\Omega \rho Q_E dV \end{aligned} \tag{2.4}$$

here, ρ is the fluid density, p is pressure, $E = e + 1/2 u_i u_i$ is the total energy per unit of mass, e is the internal energy per unit of mass, τ_{ij} is the viscous shear stress, q_i is the heat flux, Q_ρ is the mass source, F_i is an external force field, Q_E is the total energy source, Ω is the arbitrary control volume, Σ is the volume boundary surface, and n_j is a normalized vector normal to the surface Σ. These equations state, that the changes in the conserved variables depend on the changes within the control volume, the net fluxes through the volume boundary, and the effect of external sources.

Since, these equations integrate to zero for an arbitrary domain, the only way that this is possible is by the integrand being zero. Thus, by applying the divergence theorem on Eqs. (2.2)-(2.4), the differential form of the conservation laws can be easily derived [4]:

$$\frac{\partial \rho}{\partial t} + \frac{\partial}{\partial x_j}(\rho u_j) = 0 \tag{2.5}$$

$$\frac{\partial \rho u_i}{\partial t} + \frac{\partial}{\partial x_j}(\rho u_i u_j) = \frac{\partial}{\partial x_j}\big(- p\delta_{ij} + \tau_{ij}\big) \tag{2.6}$$

$$\frac{\partial \rho E}{\partial t} + \frac{\partial}{\partial x_j}\big(\rho u_j E\big) = \frac{\partial}{\partial x_j}\bigg(- q_j + (-p\delta_{ij} + \tau_{ij})u_i\bigg) \tag{2.7}$$

These equations, are known as the Navier-Stokes (Navier-Stokes) equations and for convenience, the external sources are omitted from the differential form. The Navier-Stokes equations require additional relations to obtain p, τ_{ij}, q_i as function of ρ, u_i, and E. However, these relations are not universal, instead, they are determined by the fluid properties and the assumptions underlying the fluid modeling approach [101]. Here, it is assumed that the working fluid is a continuous, diatomic, ideal, and calorically perfect gas. Therefore, from kinetic theory it is possible to derive exact relations for p, τ_{ij}, and q_i [101]:

$$p = \rho R T \tag{2.8}$$

$$e = C_v T \tag{2.9}$$

$$\tau_{ij} = 2\mu\big(S_{ij} - \frac{1}{3}S_{kk}\delta_{ij}\big), \quad S_{ij} = \frac{1}{2}\Big(\frac{\partial u_i}{\partial x_j} + \frac{\partial u_j}{\partial x_i}\Big). \tag{2.10}$$

$$q_i = -\kappa\frac{\partial T}{\partial x_i} \tag{2.11}$$

here, T is temperature, R is the gas constant, C_v is the specific heat at constant volume, μ is the molecular viscosity, and κ is the thermal conductivity. Kinetic theory also provides relations for the molecular diffusion coefficients [101]. However, for the functional relation between molecular viscosity and temperature, the experimental Sutherland's formula is implemented [104]:

$$\mu = \mu_0\frac{T_0 + C}{T + C}\Big(\frac{T}{T_0}\Big)^{3/2}. \tag{2.12}$$

Here, C is a constant that depend on the fluid analyzed. Finally, the thermal conductivity is obtained from the molecular viscosity

$$\kappa = C_p\frac{\mu}{Pr} \tag{2.13}$$

where, C_p is the specific heat at constant pressure and Pr is the fluid Prandtl number.

Equations (2.2)-(2.13), in either the integral or differential form, is the minimum set of equations required to completely describe the evolution of fluid motion. However, it is convenient to define additional nondimensional parameters to characterize the fluid flow regimes. Although, these parameters are not explicitly required by the Navier-Stokes equations, they are convenient, since different fluid flow regimes require different theoretical/numerical approaches for their analysis. Depending on the characteristics of the flow problem, different nondimensional parameters can be defined [104]. In particular, for the problem analyzed on this dissertation, only two nondimensional parameters are required:

- Mach number:

$$Ma = \frac{U}{a} = \frac{U}{\sqrt{\gamma RT}} \tag{2.14}$$

and

- Reynolds number:

$$Re = \frac{\rho U L}{\mu} \tag{2.15}$$

Here, a is the speed of sound, γ is the ratio of specific heats $\gamma = C_p/C_v$, and U and L represent the characteristic velocity and length scales of the problem, respectively. The Mach number (Ma) characterizes the effect of compressibility on the fluid flow. In general, the physics of fluid flow can be loosely described as incompressible and compressible [4, 81, 104], nonetheless, different physical phenomenon can be further observed in the compressible regime [1, 81, 101]. The Reynolds number (Re) characterizes the effects of molecular transport processes in the fluid flow. Loosely, two principal flow regimes can be defined laminar [104] and turbulent [98]. Here, it is important to mention, that the turbulent regime is the most commonly observed in nature and engineering application.

2.2 Turbulence Modeling

As mentioned before, Eqs. (2.2)-(2.4) and (2.5)-(2.7) include all the physics required to describe the fluid flow problem. Nevertheless, the extreme complexity of the Navier-Stokes equations precludes the derivation of analytical solutions, but in exceptional simplified cases. Therefore, in general it is required to apply numerical algorithms to obtain solutions for arbitrary flow problems. In addition to the complexity of the governing equations, obtaining a solution becomes more demanding if the flow is in the turbulent regime. Presenting a clear and unambiguous definition of turbulence still poses significant challenges. Therefore, a turbulence description is presented rather than a formal definition. Turbulence is a flow property, independently of the fluid, with the following characteristics [72, 98]:

- *Irregularity*: The flow variables evolve in a random form. However, the more appropriate way to define this characteristic is by stating that the Navier-Stokes equations present a chaotic behavior in the turbulent regime. This implies that

the evolution of the equations is sensitive to small perturbation in initial and boundary conditions. Therefore, the exact reproduction of a turbulent flow (realization) is subject to an exact match of all initial and boundary conditions of the flow, which cannot be satisfied in reality. This sensitivity, chaotic behavior, is only triggered at high Reynolds number, explaining why the evolution of laminar flows is completely deterministic and can always be exactly reproduced.

- *Diffusivity*: the transfer of mass, momentum, and energy is significantly enhanced by turbulence.

- *Large Reynolds Number*: As mentioned before, at large Re the Navier-Stokes equations present a chaotic behavior which induce a stochastic behavior in the fluid flow.

- *Three-dimensionality*: Turbulence is characterized by the presence of vorticity fluctuations. These effects are present even when the mean flow is two-dimensional. In fact, vortex stretching, which only occurs in three-dimensions, is an important process responsible for the generation of turbulent kinetic energy.

- *Dissipative*: Turbulence is a dissipative process, where the turbulent kinetic energy generated in the fluid flow, is converted into internal energy by viscous effects. Therefore, it is required to maintain a constant supply of energy to sustain a turbulent flow, otherwise the turbulence will always decay.

- *Multi-Scale*: Turbulence presents a wide range of scales, characterizing the different aspects of turbulence dynamics.

- *Continuous*: Turbulence is a regime of fluid flow governed by the Navier-Stokes equations. Therefore, regardless of how small the scales of turbulence can be, they will always be bigger than molecular scales, satisfying the conditions of

continuous media embodied in the derivation of the Navier-Stokes equations [80, 101].

From the previous description the *multi-scale*, *three-dimensionality*, and *dissipative* properties are what post the highest challenge in turbulence simulation. Turbulence theory [98] states that the range of length and time scales present in a turbulent flow is proportional to $\eta/l \sim Re^{-3/4}$ and $\tau u/l \sim Re^{-1/2}$, respectively. Here, η and τ represent the Kolmolgorov length and time viscous microscales, respectively, and u and l represent the inertial large velocity and length scales of the flow, respectively. Since turbulence is a dissipative phenomenon, its prediction requires to resolve all the scales present in the flow. Additionally, the simulations have to be conducted in three-dimensions.

Estimations for the total number of grid points (N) and total number of time steps (M) required to resolve all the scales present in a turbulent flow [72], predict scalings of $N^3 \sim Re_\lambda^{9/2}$ and $M \sim Re_\lambda^{3/2}$ based on a Re characteristic of the turbulence Re_λ. From these estimations, is clear that the high number of grid points and number of time iterations, required in high Re turbulent flows simulations, restrict the calculation of every turbulent scale in the flow (DNS).

2.2.1 Reynolds Averaged Navier-Stokes Equations

Since resolving all the scales of turbulence is unrealistic at high Re, other approaches have to be explored to model these flows. The RANS approach is the first systematic methodology proposed to model the physics of turbulence. In this approach the flow variables, represented as ϕ, are decomposed into a mean $\overline{\phi}$ and unsteady fluctuation ϕ' as follows:

$$\phi = \overline{\phi} + \phi' \tag{2.16}$$

or in an alternative decomposition which is commonly used in compressible flows, known as Favre or density-weighted decomposition:

$$\phi = \tilde{\phi} + \phi'' \tag{2.17}$$

$$\tilde{\phi} = \frac{\overline{\rho\phi}}{\overline{\rho}} \tag{2.18}$$

although other definitions can also be used [106], here, the RANS operator is defined as a statistical ensemble average

$$\overline{\phi}(X,t) = \lim_{N\to\infty} \frac{1}{N} \sum_{k=1}^{N} \phi^{(k)}(X,t) \tag{2.19}$$

where, $\phi^{(k)}$ is a single flow realization/experiment and N represents the number of realization/experiments conducted for ϕ. In order to warrant that the statistics converge, it is assumed that the RANS operator satisfies the ergodic hypothesis. Additionally, the following rules of averaging, know as Reynolds rules of averaging, are also satisfied [65, 75]:

$$\overline{\phi + \psi} = \overline{\phi} + \overline{\psi}, \tag{2.20a}$$

$$\overline{\alpha} = \alpha, \tag{2.20b}$$

$$\overline{\alpha\phi} = \alpha\overline{\phi}, \tag{2.20c}$$

$$\overline{\phi\overline{\psi}} = \overline{\phi}\,\overline{\psi}, \tag{2.20d}$$

$$\overline{\overline{\phi}} = \overline{\phi}, \qquad \tilde{\tilde{\phi}} = \tilde{\phi}, \tag{2.20e}$$

$$\overline{\phi'} = 0, \qquad \overline{\phi''} \neq 0, \tag{2.20f}$$

$$\overline{\rho\phi'} \neq 0, \qquad \overline{\rho\phi''} = 0. \tag{2.20g}$$

Here ψ and α are a dummy variable and a constant, respectively. If the RANS operator, Eqs. (2.19) and (2.18), is applied in the Navier-Stokes equations, it can be shown [105] that the RANS governing equations take the following form:

$$\frac{\partial\overline{\rho}}{\partial t} + \frac{\partial}{\partial x_j}(\overline{\rho}\tilde{u}_j) = 0 \tag{2.21}$$

$$\frac{\partial \dot{\overline{\rho}}\dot{\widetilde{u}}_i}{\partial t} + \frac{\partial}{\partial x_j}(\dot{\overline{\rho}}\dot{\widetilde{u}}_i\dot{\widetilde{u}}_j) = \frac{\partial}{\partial x_j}(-\dot{\overline{p}}\delta_{ij} + \dot{\overline{\tau}}_{ij} - \dot{\overline{\tau}}(u_i, u_j)) \tag{2.22}$$

$$\begin{aligned}\frac{\partial \dot{\overline{\rho}}\dot{\widetilde{E}}}{\partial t} + \frac{\partial}{\partial x_j}\big(\dot{\overline{\rho}}\dot{\widetilde{E}}\dot{\widetilde{u}}_j\big) = \frac{\partial}{\partial x_j}\Bigg(&- \dot{\overline{p}}\dot{\widetilde{u}}_j + \dot{\overline{\kappa}}\frac{\partial \dot{\widetilde{T}}}{\partial x_j} + \dot{\overline{\tau}}_{ij}\dot{\widetilde{u}}_i - \dot{\overline{\tau}}(E, u_j) \\ &- \dot{\overline{\chi}}(u_j, p) + \dot{\overline{\chi}}\Big(\frac{\partial T}{\partial x_j}, \kappa\Big) + \dot{\overline{\zeta}}(\tau_{ij}, u_i)\Bigg)\end{aligned} \tag{2.23}$$

where,

$$\dot{\overline{\tau}}(a, b) = \dot{\overline{\rho}}(\dot{\widetilde{ab}} - \dot{\widetilde{a}}\dot{\widetilde{b}}), \quad \dot{\overline{\chi}}(a, b) = \dot{\overline{ab}} - \dot{\widetilde{a}}\dot{\overline{b}}, \quad \dot{\overline{\zeta}}(a, b) = \dot{\overline{ab}} - \dot{\widetilde{a}}\dot{\widetilde{b}} \tag{2.24}$$

here, τ, χ, and ζ are the generalized second-order central-moments [30], extended to compressible flows, and a and b are dummy variables. Equations (2.21)-(2.23) evolves the RANS-averaged variables without resolving the unsteady turbulent scales. This eliminates the demanding space and time resolution requirements of DNS. However, the effect of the turbulence Eq. (2.24) has to be still considered. Unfortunately, there is no exact theoretical relation for these terms, which are known as unclose terms. Therefore, they have to be invariably modeled.

It is common practice to compute the unclose terms, Eqs. (2.22)-(2.23), using models based on the Boussinesq and gradient diffusion approximations [106]:

$$\dot{\overline{\tau}}(u_k, u_k) = 2\dot{\overline{\rho}}k \tag{2.25}$$

$$\dot{\overline{\tau}}(u_i, u_j) = -2\dot{\overline{\rho}}\nu_t(\dot{\widetilde{S}}_{ij} - \frac{1}{3}\dot{\widetilde{S}}_{kk}\delta_{ij}) + \frac{2}{3}\dot{\overline{\rho}}k\delta_{ij} \tag{2.26}$$

$$\begin{aligned}\dot{\overline{\chi}}\Big(\frac{\partial T}{\partial x_j}, \kappa\Big) + \dot{\overline{\zeta}}(\tau_{ij}, u_i) - \dot{\overline{\tau}}(E, u_j) - \dot{\overline{\chi}}(u_j, p) =& \frac{\dot{\overline{\rho}}C_p\nu_t}{\mathrm{Pr}_T}\frac{\partial \dot{\widetilde{T}}}{\partial x_j} \\ &+ \dot{\overline{\rho}}(\dot{\overline{\nu}} + \nu_t\sigma^*)\frac{\partial k}{\partial x_j} - \dot{\overline{\tau}}(u_i, u_j)\dot{\widetilde{u}}_i.\end{aligned} \tag{2.27}$$

where, k is the turbulent kinetic energy, ν_t is the turbulent viscosity, and Pr_T and σ^* are model coefficients [105]. However, there exist other more advanced closure

strategies, like the nonelinear-closure approach and the stress-transport models [105]. Nevertheless, due to their complexity and inherent extra cost, they are not widely implemented.

The Boussinesq assumption provides a simple functional form to compute the unclosed terms. However, it does not provide explicit expressions for k and ν_t. Therefore, in order to completely close Eqs. (2.25)-(2.27), model equations for k and ν_t have to be provided. In the literature a vast diversity of turbulence models can be found spanning algebraic relation to n-equations models. However, it has to be born in mind, that every RANS model is calibrated using specific benchmark cases. Therefore, is unrealistic to expect, that a single RANS model can be successfully applied in every turbulent flow problem. Consequently, selecting a RANS model is completely determined by the problem to solves.

2.2.1.1 RANS-SST Model

For the cases simulated in this work, the two-equation $k-\omega$ RANS-SST model [63] is selected to close Eqs. (2.25)-(2.27), due to its success predicting external flows on adverse and favorable pressure-gradient conditions [41, 63]. Additionally, this model has the advantage of not presenting singularities at the wall, which is a common problem present in other RANS models [63, 105, 106]. Here, the RANS-SST model is reproduced from its orgininal reference [63]:

$$\frac{\partial \dot{\overline{\rho}} k}{\partial t} + \frac{\partial}{\partial x_j}\left(\dot{\overline{\rho}}\dot{\widetilde{u}}_j k\right) = \frac{\partial}{\partial x_j}\left(\dot{\overline{\rho}}(\dot{\overline{\nu}} + \sigma_k \nu_t)\frac{\partial k}{\partial x_j}\right) - \dot{\overline{\tau}}(u_i, u_j)\frac{\partial \dot{\widetilde{u}}_i}{\partial x_j} - \beta^* \dot{\overline{\rho}} k\omega. \tag{2.28}$$

$$\begin{aligned}\frac{\partial}{\partial t}(\dot{\overline{\rho}}\omega) + \frac{\partial}{\partial x_j}(\dot{\overline{\rho}}\dot{\widetilde{u}}_j\omega) = \frac{\partial}{\partial x_j}\left(\dot{\overline{\rho}}(\dot{\overline{\nu}} + \sigma_\omega \nu_t)\frac{\partial \omega}{\partial x_j}\right) - \frac{\gamma}{\nu_t}\dot{\overline{\tau}}(u_i, u_j)\frac{\partial \dot{\widetilde{u}}_i}{\partial x_j} - \beta \dot{\overline{\rho}}\omega^2 \\ + 2(1 - F_1)\dot{\overline{\rho}}\sigma_{\omega 2}\frac{1}{\omega}\frac{\partial k}{\partial x_j}\frac{\partial \omega}{\partial x_j}\end{aligned} \tag{2.29}$$

$$F_1 = \tanh(\chi^4), \quad \chi = \min\left(\max\left(\frac{\sqrt{k}}{0.09\omega y}; \frac{500\dot{\overline{\nu}}}{y^2\omega}\right); \frac{4\dot{\overline{\rho}}\sigma_{\omega 2}k}{CDy^2}\right) \tag{2.30a}$$

$$CD = \max\left(2\dot{\overline{\rho}}\sigma_{\omega 2}\frac{1}{\omega}\frac{\partial k}{\partial x_j}\frac{\partial \omega}{\partial x_j}; 10^{-20}\right) \tag{2.30b}$$

$$\nu_t = \frac{a_1 k}{\max(a_1\omega; \Omega F_2)} \tag{2.31}$$

and

$$F_2 = \tanh(\eta^2), \quad \eta = \max\left(2\frac{\sqrt{k}}{0.09\omega y}; \frac{500\dot{\overline{\nu}}}{y^2\omega}\right). \tag{2.32}$$

Equation (2.28) is the transport equation for the turbulent kinetic energy, and (2.29) is the equation for the specific energy dissipation rate. Here Ω, F_1, and y are the vorticity magnitude, a blending function, and the wall-normal distance, respectively. The constants for the RANS-SST model, here represented as ψ, are computed from two set of constants ψ_1 and ψ_2 as $\psi = F_1\psi_1 + (1 - F_1)\psi_2$. Here, the values of these two sets are: $\psi_1\{\ \sigma_{k1} = 0.85,\ \sigma_{\omega 1} = 0.5,\ \beta_1 = 0.075,\ a_1 = 0.31,\ \beta^* = 0.09,\ \kappa = 0.41,\ \gamma_1 = \beta_1/\beta^* - \sigma_{\omega 1}\kappa^2/\sqrt{\beta^*}\ \}$ and $\psi_2\{\ \sigma_{k2} = 1.0,\ \sigma_{\omega 2} = 0.856,\ \beta_2 = 0.0828,\ \beta^* = 0.09,\ \kappa = 0.41,\ \gamma_2 = \beta_2/\beta^* - \sigma_{\omega 2}\kappa^2/\sqrt{\beta^*}\ \}$.

2.2.2 Large Eddy Simulation

The accuracy of RANS simulations is subject to the ability of the turbulence model implemented, to account for the effects of the turbulence. However, if instead of completely modeling the turbulence in the flow, the modeling is restricted to just a fraction of it, the numerical calculations relay less in the model implemented [75]. Phenomenologically, LES resolves the turbulent large scale structures of the flow, whereas the small viscous dissipative process are modeled. In spectral grounds, LES resolves the low wave-number energy of the turbulent kinetic energy spectrum, while, the energy at high wave-numbers is modeled. Dimensional analysis in turbulence theory,

predicts an equilibrium region in the energy spectrum known as *inertial range* [98]. In this region, the energy is cascaded down from the energetic low wave-numbers to the dissipative high wave-numbers. It is argued, that the turbulent scales lose their directional information, once the energy transfer reaches the inertial range. Therefore, at the inertial range, the turbulence can be assumed as locally isotropic and universal [52], conditions more suitable for its modeling. Thus, only the turbulent scales beyond the inertial range are modeled in LES, making the calculations less sensitive to the model implemented.

In LES the scale separation is conducted by mean of a space filter, which is operated in the unsteady variable, such that a scale separation is achieved:

$$\phi = \overline{\overline{\phi}}^{\cdot\cdot} + \phi^{\cdot\cdot\prime} \tag{2.33}$$

$$\phi = \widetilde{\widetilde{\phi}}^{\cdot\cdot} + \phi^{\cdot\cdot\prime\prime} \tag{2.34}$$

where the LES space filter is defined as:

$$\overline{\overline{\phi}}^{\cdot\cdot}(X,t) = \int_{-\infty}^{+\infty} G(X-r,\Delta)\phi(r,t)dr \tag{2.35}$$

$$\widetilde{\widetilde{\phi}}^{\cdot\cdot}(X,t) = \frac{\overline{\overline{\rho\phi}}^{\cdot\cdot}}{\overline{\overline{\rho}}^{\cdot\cdot}} \tag{2.36}$$

However, unlike the RANS operator which is general, the LES operator requires an additional kernel function (G) and filter width (Δ) that need to be defined, constraining the generality of the LES operator. In the literature, different LES filters have been proposed spanning explicit and implicit (grid) filters [75]. Nevertheless, their mathematical properties differ and general properties cannot be easily stated. Here, it is only mention that for most LES filters [30, 75] not all the Reynolds rules of

averaging apply. The properties that are most commonly followed by LES filters are:

$$\overline{\overline{\phi+\psi}} = \overline{\overline{\phi}} + \overline{\overline{\psi}}, \tag{2.37a}$$

$$\overline{\overline{\alpha}} = \alpha, \tag{2.37b}$$

$$\overline{\overline{\alpha\phi}} = \alpha\overline{\overline{\phi}}, \tag{2.37c}$$

$$\overline{\overline{\phi\psi}} \neq \overline{\overline{\phi}}\,\overline{\overline{\psi}}, \tag{2.37d}$$

$$\overline{\overline{\overline{\phi}}} \neq \overline{\overline{\phi}}, \qquad \widetilde{\widetilde{\phi}} \neq \widetilde{\phi}, \tag{2.37e}$$

$$\overline{\overline{\phi'}} \neq 0, \qquad \overline{\overline{\phi''}} \neq 0, \tag{2.37f}$$

$$\overline{\overline{\rho\phi'}} \neq 0, \qquad \overline{\overline{\rho\phi''}} \neq 0 \tag{2.37g}$$

where ϕ' and ϕ'' represent the subgrid fluctuation and the subgrid density-weighted fluctuation, respectively. In this study, a generic low-pass LES filter is considered, with the only restrictions that it commutes with differentiation and with the statistical operator

$$\overline{\overline{\frac{\partial\phi}{\partial x_i}}} = \frac{\partial\overline{\overline{\phi}}}{\partial x_i} \tag{2.38}$$

$$\dot{\overline{\overline{\phi}}} = \dot{\overline{\phi}} = \dot{\overline{\phi}}. \tag{2.39}$$

Having defined the LES operator, the LES governing equations are derived by applying Eqs. (2.35) and (2.36) into the Navier-Stokes equations:

$$\frac{\partial\overline{\overline{\rho}}}{\partial t} + \frac{\partial}{\partial x_j}(\overline{\overline{\rho}}\,\widetilde{\widetilde{u}}_j) = 0 \tag{2.40}$$

$$\frac{\partial\overline{\overline{\rho}}\,\widetilde{\widetilde{u}}_i}{\partial t} + \frac{\partial}{\partial x_j}(\overline{\overline{\rho}}\,\widetilde{\widetilde{u}}_i\widetilde{\widetilde{u}}_j) = \frac{\partial}{\partial x_j}(-\overline{\overline{p}}\delta_{ij} + \widetilde{\widetilde{\tau}}_{ij} - \overline{\overline{\tau}}(u_i,u_j)) \tag{2.41}$$

$$\begin{aligned}\frac{\partial\overline{\overline{\rho}}\,\widetilde{\widetilde{E}}}{\partial t} + \frac{\partial}{\partial x_j}\big(\overline{\overline{\rho}}\,\widetilde{\widetilde{E}}\widetilde{\widetilde{u}}_j\big) = \frac{\partial}{\partial x_j}\Bigg(&-\overline{\overline{p}}\widetilde{\widetilde{u}}_j + \overline{\overline{\kappa}}\frac{\partial\widetilde{\widetilde{T}}}{\partial x_j} + \widetilde{\widetilde{\tau}}_{ij}\widetilde{\widetilde{u}}_i - \overline{\overline{\tau}}(E,u_j) \\ &- \overline{\overline{\chi}}(u_j,p) + \overline{\overline{\chi}}\Big(\frac{\partial T}{\partial x_j},\kappa\Big) + \overline{\overline{\zeta}}(\tau_{ij},u_i)\Bigg)\end{aligned} \tag{2.42}$$

where,

$$\overset{\cdot\cdot}{\overline{\tau}}(a,b) = \overset{\cdot\cdot}{\overline{\rho}}(\overset{\cdot\cdot}{\widetilde{ab}} - \overset{\cdot\cdot}{\widetilde{a}}\overset{\cdot\cdot}{\widetilde{b}}), \quad \overset{\cdot\cdot}{\overline{\chi}}(a,b) = \overset{\cdot\cdot}{\overline{ab}} - \overset{\cdot\cdot}{\widetilde{a}}\overset{\cdot\cdot}{\overline{b}}, \quad \overset{\cdot\cdot}{\overline{\zeta}}(a,b) = \overset{\cdot\cdot}{\overline{ab}} - \overset{\cdot\cdot}{\widetilde{a}}\overset{\cdot\cdot}{\widetilde{b}} \tag{2.43}$$

here, τ, χ, and ζ are the generalized second-order central-moments [30], extended to compressible flows, and a and b are dummy variables. Similarly to RANS, the LES equations predict additional unclose terms that need to be modeled. However, contrary to RANS, the effect of the LES closure on the accuracy of the simulations is expected to be less significant. Therefore, gradient diffusion and Boussinesq equations can be used to model the LES unclose central-moments:

$$\overset{\cdot\cdot}{\overline{\tau}}(u_k,u_k) = 2\overset{\cdot\cdot}{\overline{\rho}}k^{sgs} \tag{2.44}$$

$$\overset{\cdot\cdot}{\overline{\tau}}(u_i,u_j) = -2\overset{\cdot\cdot}{\overline{\rho}}\nu_{sgs}(\overset{\cdot\cdot}{\widetilde{S}}_{ij} - \frac{1}{3}\overset{\cdot\cdot}{\widetilde{S}}_{kk}\delta_{ij}) + \frac{2}{3}\overset{\cdot\cdot}{\overline{\rho}}k^{sgs}\delta_{ij} \tag{2.45}$$

$$\begin{aligned}\overset{\cdot\cdot}{\overline{\chi}}\Big(\frac{\partial T}{\partial x_j},\kappa\Big) + \overset{\cdot\cdot}{\overline{\zeta}}(\tau_{ij},u_i) - \overset{\cdot\cdot}{\overline{\tau}}(E,u_j) - \overset{\cdot\cdot}{\overline{\chi}}(u_j,p) =& \frac{\overset{\cdot\cdot}{\overline{\rho}}C_p\nu_{sgs}}{\mathrm{Pr}_t}\frac{\partial\overset{\cdot\cdot}{\widetilde{T}}}{\partial x_j} + \overset{\cdot\cdot}{\overline{\rho}}\frac{\nu_{sgs}}{Pr_t}\frac{\partial\overset{\cdot\cdot}{\widetilde{E}}}{\partial x_j} \\ &+ \frac{\nu_{sgs}}{Pr_t}\frac{\partial\overset{\cdot\cdot}{\overline{p}}}{\partial x_j} - \overset{\cdot\cdot}{\overline{\tau}}(u_i,u_j)\overset{\cdot\cdot}{\widetilde{u}}_i.\end{aligned} \tag{2.46}$$

However, there exist other explicit approaches to reconstruct the unclose subgrid terms that do not rely on gradient diffusion and Boussinesq equations, being TLS one example [75].

2.2.2.1 Localized Dynamic K-Equation Model

In order to close Eqs. (2.44)-(2.46), the subgrid viscosity ν^{sgs} and subgrid kinetic energy k^{sgs} are modeled using the Localized Dynamic K-equation Model (LDKM), due to its success predicting complex and fundamental turbulent flows [51, 62]:

$$\frac{\partial\overset{\cdot\cdot}{\overline{\rho}}k^{sgs}}{\partial t} + \frac{\partial}{\partial x_j}\Big(\overset{\cdot\cdot}{\overline{\rho}}\overset{\cdot\cdot}{\widetilde{u}}_j k^{sgs}\Big) = \frac{\partial}{\partial x_j}\left(\overset{\cdot\cdot}{\overline{\rho}}(\overset{\cdot\cdot}{\overline{\nu}}/Pr + \nu_{sgs})\frac{\partial k^{sgs}}{\partial x_j}\right) - \overset{\cdot\cdot}{\overline{\tau}}(u_i,u_j)\frac{\partial\overset{\cdot\cdot}{\widetilde{u}}_i}{\partial x_j} - C_\varepsilon\overset{\cdot\cdot}{\overline{\rho}}\frac{{k^{sgs}}^{3/2}}{\Delta}. \tag{2.47}$$

$$\nu_{sgs} = C_\nu\Delta\sqrt{k^{sgs}} \tag{2.48}$$

Here, C_ν and C_ϵ are LES coefficients that are obtained dynamically as a part of the solution using a scale similarity approach. Further details on the dynamic evaluation can be found in the original references [51, 62].

CHAPTER III

NUMERICAL FORMULATION

To conduct high fidelity turbulent simulations of complex flows in arbitrary geometries, the governing equations have to be integrated with the highest consistency and accuracy possible, in both space and time. Therefore, the finite volume approach is selected over the traditional finite-difference approach, since the conservation laws are exactly satisfied at the discretized level. In addition, the finite volume approach can be used in arbitrary geometries without requiring any coordinate-transformation in its formulation [95].

Achieving high accuracy for space discretization is not always simple to obtain. Contrary to time integration, the space accuracy is not only determined by the scheme implemented, but also by the flow to be simulated. For instance, DNS requires high-accuracy spectral methods to resolve all the range of scales encountered in turbulent flows [11,74]. However, spectral methods can only be applied in simple problems with periodic boundary conditions.

On the other hand, RANS simulations are only concerned with low-wave number scales in complex flows. Therefore, the space-accuracy, usually not higher than 2^{nd} order, is usually relaxed to calculate flows in complex domains and to reduce the cost of the numerical scheme. Additionally, it is a common practice to include numerical-dissipation to enhance the stability of the numerical scheme, specially when coarse grids are implemented.

In LES, defining the proper space-accuracy is more complicated than in the previous cases. LES faces the disjunctive of resolving high-wave number turbulent scales on complex geometries with complex boundary conditions. Therefore, the type of

scheme used and its accuracy is problem dependent, without even mentioning that applying high-order schemes in complex geometries is not always easy. Finally, the built in numerical dissipation of some schemes can smear out the resolved turbulence.

In this study, it is considered that orders of accuracy above 2^{nd} order are good enough for LES. For a complete discussion on the effect of numerical scheme on LES refer to the study of Ghosal [32].

3.1 Finite Volume Approach

In order to developt the finite volume formulation, the governing equations have to be presented in their integral conservative form Eqs. (2.2)-(2.4)

$$\frac{\partial}{\partial t}\iiint_{\Omega} Q dV + \iint_{\Sigma} F_j(Q) n_j ds = 0 \tag{3.1}$$

Here, Eq. (3.1) represents any of the conservation equations, Q represents the conserved quantity, F_j is the flux vector which includes all the transport terms involved, Ω is the, arbitrary, domain for the volume integral, and Σ is the boundary of Ω, see (Figure 3.1). However, before attempting to apply any integration numerical scheme to Eq. (3.1), it can be significantly simplified by recalling the integral version of the differential mean-value theorem. This theorem states that for a continuous function $f : [a, b] \to \mathbb{R}$, there is some $c \in [a, b]$ such that

$$f(c) = \frac{1}{b-a}\int_a^b f(x)dx. \tag{3.2}$$

This theorem warrant the existence of a point c in the integration domain at which the function to be integrated, takes exactly the mean value of the integral. Therefore, the integral can be replaced by the mean value of the function times the domain of integration. This theorem is readily extended to surface and volume integrals by stating that for a continuous function $g : [a, b] \times [c, d] \to \mathbb{R}$, there is some $\alpha \in [a, b]$ and $\beta \in [c, d]$ such that

$$g(\alpha, \beta) = \frac{1}{(b-a)(d-c)}\int_c^d \int_a^b g(x, y)dxdy \tag{3.3}$$

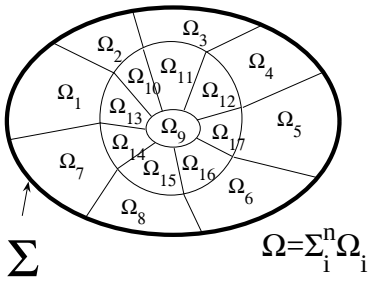

Figure 3.1: Arbitrary domain composed by arbitrary subdomains.

and for $h : [a, b] \times [c, d] \times [e, f] \rightarrow \mathbb{R}$, there is some $\alpha \in [a, b]$, $\beta \in [c, d]$ and $\gamma \in [e, f]$ such that

$$h(\alpha, \beta, \gamma) = \frac{1}{(b-a)(d-c)(f-e)} \int_e^f \int_c^d \int_a^b h(x, y, z) dx dy dz. \tag{3.4}$$

Therefore, by substituting Eqs. (3.3) and (3.4) in (3.1) an alternative form for the integral conservation equation is obtained

$$\frac{\partial \widehat{Q}\Omega}{\partial t} + F_j(\breve{Q})\Sigma_j = 0 \tag{3.5}$$

Where, $\widehat{Q}$ represents the volumetric average $\widehat{Q} = \frac{1}{\Omega} \iiint_\Omega Q dV$ and $\breve{Q}$ represents the surface average $\breve{Q} = \frac{1}{\Sigma} \iint_\Sigma Q ds$. Here it is important to point out that, Eq. (3.5) provides the advantage of bypassing the requirement of explicitly conducting a numerical integration for Q. By using Eq. (3.5) the mean variable $\widehat{Q}$ is resolved instead of the continuous Q. Although Eq. (3.5) is an exact relation independent of Ω, it is recommended to discretize the domain to be simulated into small sub-volumes Ω_i, (see Figure 3.1), in order to better represent Q with $\widehat{Q}$, since

$$\lim_{\Omega_i \rightarrow 0} \widehat{Q} \rightarrow Q. \tag{3.6}$$

A second aspect to mention about Eq. (3.5) is the incompatibility between variables used to compute the fluxes. Here, the time integration evolves the volume-averaged variables $\widehat{Q}$, while the fluxes are computed using surface-averaged quantities

$\breve{Q}$. Therefore, it is necessary to apply a special spatial discretization/reconstruction scheme to compute the fluxes at the boundaries, using the volume-averaged variables up to n^{th} order of accuracy i.e., $F(\breve{Q}) = F(\widehat{Q}) + \vartheta(\widehat{Q}^n)$.

Thus far, it has not been necessary to introduce any numerical discretization scheme for the unsteady term or the fluxes. This, illustrates the generality of the finite volume formulation, which only apply Eq. (3.5) into a set of small volumes which add up the domain of integration, Figure 3.1.

3.2 Time and Space Integration

Having established the most convenient form of the governing equations (3.5), the particular schemes used to discretize the unsteady term and the fluxes are discussed. In order to clearly introduce the schemes, the governing equations for a differential volume V_i and its differential boundaries S_j, in each spatial direction, are presented (see Figure 3.2).

$$\frac{\partial \widehat{Q}}{\partial t} V_i + F(\breve{Q})_j S_j = 0 \tag{3.7}$$

where

$$F(\breve{Q})_j = \mathcal{C}(\breve{Q})_j - \mathcal{D}(\breve{Q})_j. \tag{3.8}$$

Here, Q represents the conserved variables $Q = \{\rho, \rho u_i, \rho E\}$, $\mathcal{C}(\breve{Q})_j$ represents the convective fluxes and $\mathcal{D}(\breve{Q})_j$ represents the diffusion fluxes. Additionally, it is assumed that the finite volumes are non-deforming in time $\frac{\partial V_i}{\partial t} = 0$. The definition of the residual as fluxes $F(\breve{Q})_j$, allows to treat the system of partial differential equations as a time dependent ordinary differential equation or time marching problem. In this work, a low-storage explicit Runge-Kutta (RK) scheme is selected for time discretization due to its high accuracy. This scheme, when applied to Eq. (3.7), takes the following

form:

$$\widehat{Q}^0 = \widehat{Q}^n, \tag{3.9a}$$

$$\widehat{Q}^k = \widehat{Q}^0 - \alpha_k \Delta t F(\widehat{Q}^{k-1})_j S_j / V_i, \tag{3.9b}$$

$$\widehat{Q}^{n+1} = \widehat{Q}^m. \tag{3.9c}$$

here, Δt is the physical time step used to advance in time the solution. The main parameters of the generic RK scheme Eq.(3.9) are, the number of stages n and the coefficient for each stage α_k. Here, the accuracy of the RK scheme is determined by the number of stages, n, whereas α_k determine the stability of the scheme. The accuracy is equal to the number of stages when $1 \leq n \leq 4$ and potentially less than n when $n \geq 5$ [44, 54]. In the present work, instead of conducting an optimization study to come up with an appropriate set of α_k for a particular n, which is above the scope of this work. The five-stage scheme developed by A. Jameson is selected. This scheme is known by its high convergence rates and high accuracy [44].

$$\widehat{Q}^0 = \widehat{Q}^n, \tag{3.10a}$$

$$\widehat{Q}^k = \widehat{Q}^0 - \alpha_k \Delta t \big[\mathcal{C}(\widehat{Q}^{k-1}) \tag{3.10b}$$

$$+ \gamma_k (\mathcal{D}_V(\widehat{Q}^{k-1}) + \mathcal{D}_T(\widehat{Q}^{k-1})) \tag{3.10c}$$

$$+ \beta_k \mathcal{D}_N(\widehat{Q}^{k-1}) + (1 - \beta_k) \mathcal{D}_N(\widehat{Q}^{k-2}) \big], \tag{3.10d}$$

$$\widehat{Q}^{n+1} = \widehat{Q}^m. \tag{3.10e}$$

Here, $\mathcal{D}_V(Q)$ and $\mathcal{D}_T(Q)$ represent the viscous and turbulence fluxes, respectively. Jameson's original five-stage scheme (Eq. (3.10)) includes an additional artificial numerical dissipation term, $\mathcal{D}_N(Q)$, intended to stabilize the second-order central scheme used to compute the convective terms. Additionally, to further increase the stability of the scheme and to reduce the cost of the scheme, a second set of coefficients is introduced (β_k and γ_k), to evaluate the diffusion fluxes only at every other stage.

The stage coefficients used in this scheme are the following [44]:

$$\begin{aligned} n &= 5, \\ \{\alpha_k\} &= \{1/4, 1/6, 3/8, 1/2, 1\}, \\ \{\gamma_k\} &= \{1, 0, 1, 0, 1\}, \\ \{\beta_k\} &= \{1, 0, 0.56, 0, 0.44\}, \end{aligned} \tag{3.11}$$

3.2.1 Dual Time Stepping

Another important add-on to the original Jameson's scheme [44] is its capability to advance by a time step higher than the allowed by the numerical stability criteria. This enhancement is known as dual-time stepping (DTS) and it is possible by casting the unsteady time-accurate problem as a steady state problem in an artificial time scale

$$\frac{\partial \widehat{Q} V_i}{\partial \tau} = \frac{\partial \widehat{Q} V_i}{\partial t} + F(\breve{Q})_j S_j = 0 \tag{3.12}$$

here, τ is the artificial time variable. This modification indicates that when Eq. (3.12) reaches a steady state, $\frac{\partial \widehat{Q}}{\partial \tau} = 0$, a converged time accurate solution is obtained. Consequently, Eq. (3.12) can be integrated using common acceleration techniques implemented in steady state problems. Here, the physical-unsteady term $\frac{\partial \widehat{Q}}{\partial t}$ represent just a source for the equations in the unphysical time variable.

In the present work, the simulations conducted do not implement the DTS capability. Thus, a complete discussion on this approach together with the acceleration techniques is out of the scope of this work. However, the interested reader can refer to Jameson's original paper [44] or to a comprehensive exposure of the DTS approach by Radespiel et al. [73].

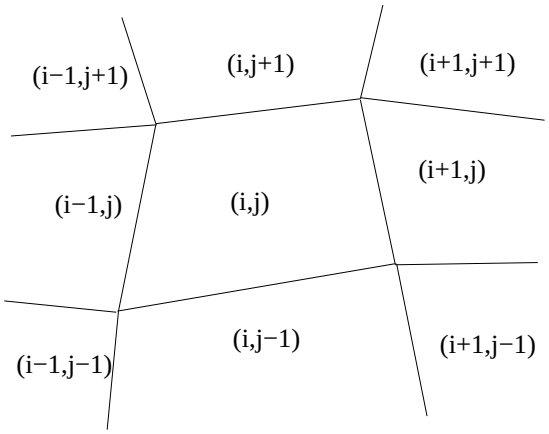

Figure 3.2: Arbitrary finite volume cells.

3.3 Flux Reconstruction

Figure 3.2 presents a 2-D finite volume cell and its neighboring cells in an structure grid set up. The convention is to use integer numbers in the index to identify variables at the center of the volume, $Q_{i,j}$, and fractional indexes to denote variables at the boundaries of the volume cells, $Q_{i+1/2,j}$. Here, for convenience, the convective fluxes are written in a generic form QV. Thus, $\widehat{Q}_{i,j}\widehat{V}_{i,j}$ represents the nonlinear term evaluated at the cell-center, whereas, $\breve{Q}_{i+/1/2,j}\breve{V}_{i+1/2,j}$ represents the nonlinear flux evaluated at the right boundary of the cell in Figure 3.2. The reconstruction of the convective nonlinear fluxes $\mathcal{C}(\breve{Q})_j$ in Eq. 3.7 is conducted with second-order and fourth-order central schemes. For the second-order central scheme, the convective fluxes are evaluated at the cell-boundary as an average from the values computed at the cell centers [95]:

$$\mathcal{C}(\breve{Q})_{i+1/2} = \frac{1}{2}\Big(\widehat{Q}_i\widehat{V}_i + \widehat{Q}_{i+1}\widehat{V}_{i+1}\Big) + \vartheta(x_i^2). \tag{3.13}$$

For higher accuracy, a fourth-order central scheme in divergence-form [24] is selected:

$$\begin{aligned}\mathcal{C}(\breve{Q})_{i+1/2} = \frac{1}{12}\Big(&- \widehat{Q}_{i+2}\widehat{V}_{i+2} + 7\widehat{Q}_{i+1}\widehat{V}_{i+1} + 7\widehat{Q}_i\widehat{V}_i - \widehat{Q}_{i-1}\widehat{V}_{i-1}\Big) \\ &+\frac{1}{3}\Big(\frac{1}{2}\big(\widehat{Q}_{i+1}\widehat{V}_{i+1} + \widehat{Q}_i\widehat{V}_i\big) - \frac{1}{4}\big(\widehat{Q}_{i+1} + \widehat{Q}_i\big)\big(\widehat{V}_{i+1} + \widehat{V}_i\big)\Big) \\ &+\vartheta(x_i^4).\end{aligned} \tag{3.14}$$

In this work, all the simulations are conducted using the fourth order accurate scheme unless the contrary is explicitly stated.

3.3.1 Numerical Stabilization

For turbulence simulations, it is desired to implement schemes that include low built-in numerical dissipation to better represent the high wave-number turbulent scales. Therefore, central schemes are attractive since they do not exhibit any numerical dissipation [24,95]. However, the absence of numerical-dissipation, although beneficial for turbulence simulations, is not recommended in grounds of numerical stability. Since the buildup of numerical disturbances, usually originated at high wave-numbers, cannot be controlled, thus, leading to the failure of the scheme. Therefore, to use central schemes, it is necessary to include an additional stabilization approach able to control the numerical instabilities, without interfering with the resolved physical turbulent scales.

One of the most common approaches to stabilize central schemes is to include artificial numerical dissipation [24, 44, 54]. However, this approach apply the stabilizing damping force over all the spectrum of scales, therefore it cannot distinguish fluctuations created by numerical instability from those created by turbulence. Consequently, this approach is not suited for turbulence simulations, despite its reliability as a stabilizing scheme.

In this work, numerical stability is ensured by applying a high-order explicit filter as proposed by Gaitonde and Visbal [28]. Their original filtering scheme relies on a Padé-type filter, which is an implicit filter that requires the solution of a tridiagonal

Table 3.1: Coefficients for central filter formula.

Order	a_0	a_1	a_2	a_3	a_4	a_5
2	$\frac{1}{2}+\alpha_f$	$\frac{1}{2}+\alpha_f$	0	0	0	0
4	$\frac{5}{8}+\frac{3\alpha_f}{4}$	$\frac{1}{2}+\alpha_f$	$-\frac{1}{8}+\frac{\alpha_f}{4}$	0	0	0
6	$\frac{11}{16}+\frac{5\alpha_f}{8}$	$\frac{15}{32}+\frac{17\alpha_f}{16}$	$-\frac{3}{16}+\frac{3\alpha_f}{8}$	$\frac{1}{32}-\frac{\alpha_f}{16}$	0	0
8	$\frac{93+70\alpha_f}{128}$	$\frac{7+18\alpha_f}{16}$	$\frac{-7+14\alpha_f}{32}$	$\frac{1}{16}-\frac{\alpha_f}{8}$	$-\frac{1}{128}+\frac{\alpha_f}{64}$	0
10	$\frac{193+126\alpha_f}{256}$	$\frac{105+302\alpha_f}{256}$	$\frac{15(-1+2\alpha_f)}{64}$	$\frac{45(1-2\alpha_f)}{512}$	$\frac{5(-1+2\alpha_f)}{256}$	$\frac{1-2\alpha_f}{512}$

system of equation, derived from spectral consideration. Therefore, the stabilization approach does not rely on the Navier-Stokes equations as in the numerical-dissipation approach [24,44,45,54]. In general, a central nth order Padé-type filter can be written in the following form:

$$\alpha_f\overline{\phi}_{i-1}+\overline{\phi}_i+\alpha_f\overline{\phi}_{i+1}=\sum_{k=0}^{N}\frac{a_k}{2}(\phi_{i+k}+\phi_{i-k}) \tag{3.15}$$

Here, ϕ represents the non-filtered variable, $\overline{\phi}$ represents the filtered variable, α_f is a free parameter, a_k are coefficient derived in terms of α_f with Taylor and Fourier-series analysis to provide an $n=2N^{th}$ order of accuracy, using a $2N+1$ point-stencil. On uniform meshes, this filtering scheme is nondispersive, does not amplify any wave, preserves constant functions, and completely eliminates the odd-even mode [28].

Unfortunately, high-order filters require large stencils, which makes their implementation difficult at the N points next to the physical boundaries. Here, instead of progressively reducing the order of the central filter as the physical boundaries is approached (LOC approach), one-sided filter formulas are implemented to conserve the accuracy of the filtering scheme as introduced by Gaitonde and Visbal [28].

$$\alpha_f\overline{\phi}_{i-1}+\overline{\phi}_i+\alpha_f\overline{\phi}_{i+1}=\sum_{k=1}^{2N+1}a_{k,i}\phi_k,\quad i\in\{2,\ldots,N\} \tag{3.16}$$

$$\begin{aligned}\alpha_f\overline{\phi}_{i-1}+\overline{\phi}_i+\alpha_f\overline{\phi}_{i+1}=&\sum_{k=0}^{2N}a_{IL-k,i}\phi_{IL-k},\\ &i\in\{IL-N-1,\ldots,IL-1\}\end{aligned} \tag{3.17}$$

here, IL represent the last point in the physical domain. Using Eqs. (3.16) and (3.17) at the boundaries have demonstrated being more robust than the LOC approach, which on coarse grids become the dominant parameter affecting the global accuracy of the solution [28]. Therefore, in this work one-sided filters are applied to treat wall-boundary conditions.

In this work a 10^{th} order filter is implemented to achieve the highest accuracy at interior points and at wall-boundaries. However, to reduce the complexity of the filter implementation at the processor boundaries, the LOC approach is used. Therefore, the order of the filter is reduced progressively from 10^{th} to 6^{th} as the processor boundaries are reached. Here, only three cells are required to exchange among processors to apply the filter.

In order to reduce more the cost of the filter evaluation, the arbitrary coefficient α_f is set to zero in Eqs. (3.15)-(3.17), to recover an explicit scheme, thus, avoiding the inversion of a tridiagonal matrix. The coefficients required in Eq. (3.15) are reproduced on Table 3.1. However, for Eqs. (3.16) and (3.17) refer to the original reference [28].

CHAPTER IV

CODE VALIDATION

In this chapter, the validation of the numerical algorithm developed is conducted. However, instead of validating the code with multiple test cases, the validation focuses on attached external flow. Therefore, the studies presented only consider LES and RANS simulations on turbulent boundary layer over a flat-pate.

4.1 Cases Simulated, Grids Implemented, Boundary and Initial Conditions

LES calculations are conducted for a turbulent boundary layer at two Reynolds numbers based on the momentum thickness $Re_\theta = 1400$ and $Re_\theta = 3330$, the experimental data is obtained from DeGraaff and Eaton [17] and Aubertine and Eaton [2], respectively. For these simulations it is decided to change the Re by modifying the space dimension such that the same free stream conditions are used in both cases. For the RANS validation, the laminar to turbulence transition in a flat-plate boundary layer is simulated, here the mean velocity profile at $Re_\theta = 1400$ is compared against experimental data and LES calculations. Additionally, the friction coefficient is compared against well-known laminar and turbulent equations.

Boundary conditions are applied explicitly for the flow and the turbulence variables. At the wall, no-slip and adiabatic conditions are imposed. At the free stream boundary, the variables are computed from the one-dimensional Riemann invariants [38]. In the spanwise direction, periodic boundary conditions are implemented, and at the outflow, a zero gradient condition is enforced. For the LES simulation, realistic turbulence is provided at the inflow boundary by using the rescaling method of Lund et al. [59]. For the RANS simulation, a uniform profile is imposed.

Table 4.1: Summary of grids implemented in validation studies

Grid	Number of grid points $n_x \times n_y \times n_z$	Grid resolution Δx^+	Δy^+_{min}	Δy^+_{max}	Δz^+
LES $Re_\theta = 1400$	$201 \times 91 \times 121$	30	0.5	63	10
LES $Re_\theta = 3330$	$361 \times 91 \times 221$	36	0.5	190	12
RANS† $Re_x = 0 - 10^8$	$201 \times 61 \times 1$	$3 - 90000$	0.5	20000	–

† Resolution computed for a $Re_x = 10^8$

Based on previous LES [59] and DNS [26] studies the domain extend and resolution is selected for LES calculations: $L_x = 10\delta$ (streamwise), $L_y^{Re_\theta=1400} = 3\delta$ and $L_y^{Re_\theta=3330} = 3.5\delta$ (wall-normal), and $L_z = 2\delta$. Here, δ is the boundary layer thickness. For both Re cases (1400 and 3330) the same resolution given in wall-units is implemented (see Table 4.1).

For LES, the initial conditions chosen for the $Re_\theta = 1400$ case, consist of random noise superimposed on the law-of-the-wall profile. This artificial flow field is evolved using periodic boundary conditions in the streamwise direction to promote transition to turbulence. Once realistic turbulence develops, the flow field is rescaled and then used as initial condition for LES, it is at this point when the rescaling approach of Lund et al. [59] is used to provide turbulent inflow conditions. The initial conditions for $Re_\theta = 3330$ are obtained by rescaling the realistic LES field at $Re_\theta = 1400$. Furthermore, The initial transients are washed away by integrating the governing equations during a non-dimensional period of $t_{\text{trans}} u_\tau^2/\nu_{\text{wall}} \sim 1000$ [59]. Here, $u_\tau = \sqrt{\tau_{wall}/\rho_{wall}}$ is the friction velocity, τ_{wall} is the shear stress at the wall, ρ_{wall} is the density at the wall, and ν_{wall} is the kinematic viscosity evaluated at the wall. Finally, after the flow reached a stationary state, flow statistics are collected during a non-dimensional period of $t_{\text{aver}} u_\tau^2/\nu_{\text{wall}} \sim 1800$ [59]. For the RANS simulation uniform conditions are used to initialize the simulation.

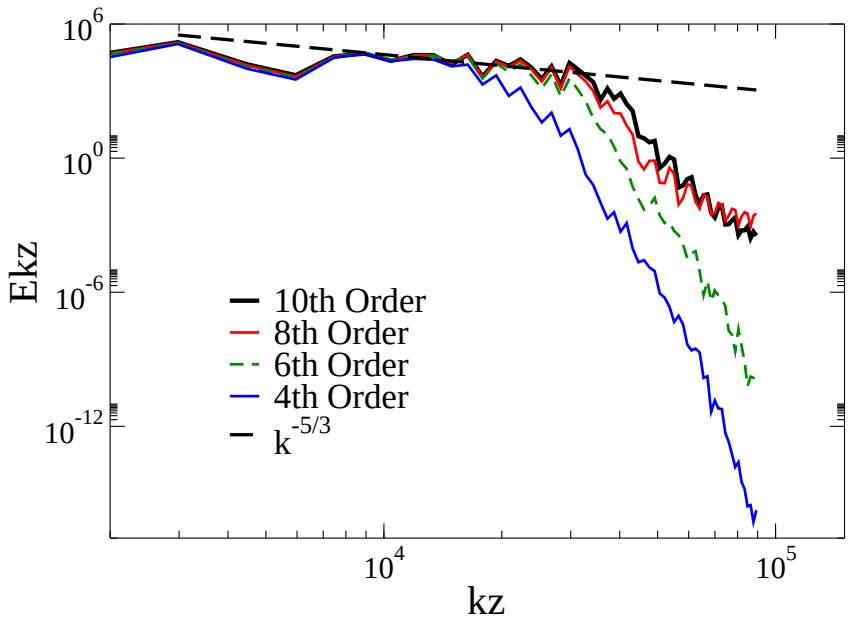

Figure 4.1: Effect of the accuracy-order of the explicit filter Eqs. (3.15)-(3.17) in the turbulent kinetic energy spectrum, the application-frequency is the same for all cases.

4.2 Numerical Scheme Assessment

The validation of the numerical-algorithm is conducted by simulating the turbulent flow over a flat-plate boundary layer at $Re_\theta = 1400$, here based on a priori tests the best configuration of parameters for the numerical scheme are found. For LES the 4^{th} order spatial scheme Eq. (3.14) in combination with the 10^{th} order explicit filter Eqs. (3.15)-(3.17) yield the best results. The explicit filter is applied at the end of the five-stage R-K integration scheme on the conserved variables.

Mathematically speaking, the explicit filter scheme can be applied at the end of each time integration to stabilize the central schemes. However, for turbulent flow simulations the continuous application of such filter has a negative impact on the resolved turbulence. Since the explicit-filter cannot exactly reproduce a sharp-spectral filter, its continuous application dissipates the resolved small turbulent-scales. Therefore, it is important to find an application-frequency that stabilize the central scheme without interfering with the resolve turbulent-scales.

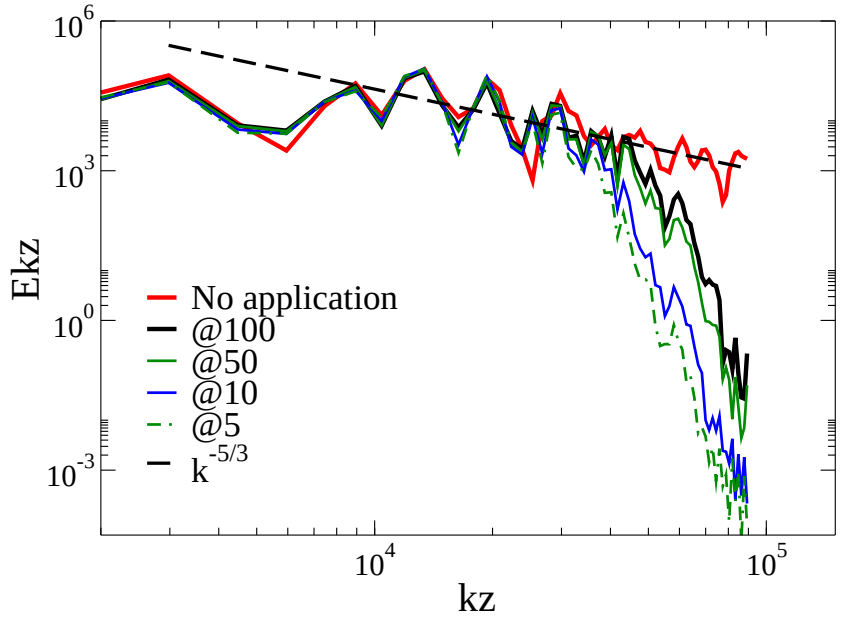

Figure 4.2: Effect of the explicit filter application-frequency in the turbulent kinetic energy spectrum, 10^{th} order filter.

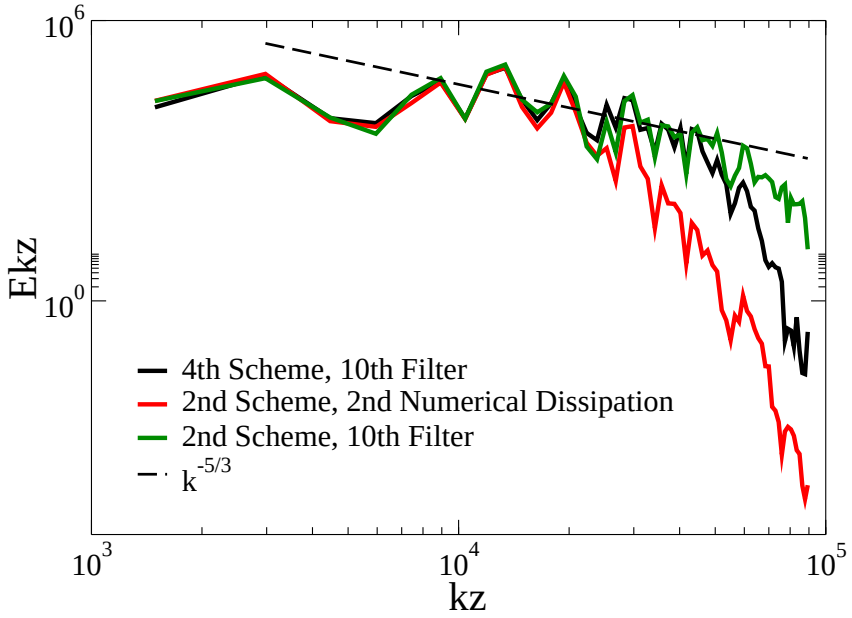

Figure 4.3: Effect of the spatial discretization scheme, central-order scheme and stabilization method, on the resolved energy spectrum.

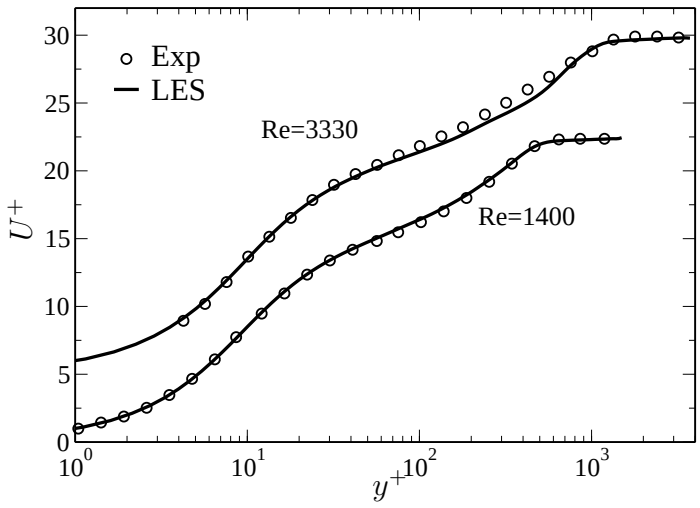

Figure 4.4: Mean Streamwise velocity profile normalized with wall-units, LES simulations for $Re_\theta = 1400$ and $Re_\theta = 3330$ (results shifted 5 wall-units for clear presentation).

Unfortunately, due to the complexity of the two constraints that must be satisfied (numerical stabilization and turbulence preserving), there is no general way to a priori estimate the application-frequency. In the original reference, Gaitonde and Visbal [28] comment that the way in which the filter is applied and the application-frequency can vary, furthermore, they also comment that the filtering scheme has to be assessed through practical applications. Additionally, all the validation cases conducted by the authors are in laminar flows, leaving unconsidered the effect of the filter in turbulence simulations. Therefore, to investigate the effect of the filter accuracy-order and application-frequency, it is decided to conduct a priori tests in the turbulent boundary layer problem.

For the turbulent boundary layer calculations, conducted with the grid summarized in Table 4.1, the a priori tests indicate that the best combination of parameters are the 4^{th} order scheme Eq. (3.14) and 10^{th} order filter with an application-frequency of 100 (i.e. the explicit filter is evaluated every 100 iterations). Therefore, this setup serves as the benchmark case.

Figure 4.1 presents the effect of the filter accuracy-order in the resolved energy

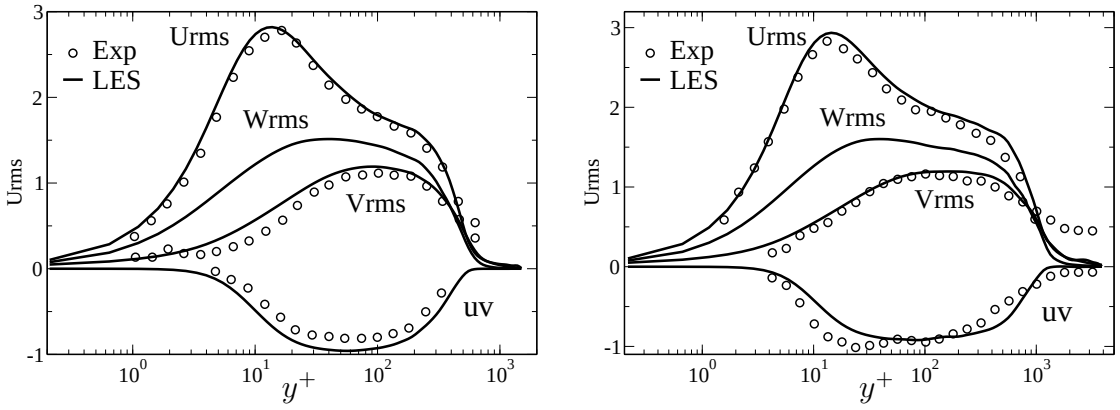

Figure 4.5: Total Second-order Statistics, normalized with wall-units, LES simulations for: (a) $Re_\theta = 1400$ and (b) $Re_\theta = 3330$.

spectrum, which is computed over the homogeneous spanwise direction. Here, the application-frequency is kept constant for all cases. As expected, results indicate that the accuracy of the explicit filter has a dramatic effect on the resolved spectrum. Here, the 4^{th} and 6^{th} order filters significantly dissipate the energy at high wave-numbers, reducing dramatically (specially the 4^{th} order) the extent of the suggested inertial range predicted with the benchmark configuration. On the other hand, results indicate that the 8^{th} order filter does not significantly interfere with the resolved turbulent scales. Although, the 8^{th} order is almost as good as the 10^{th} order, it was decided to use the 10^{th} order filter in order to use the LOC approach at the processor boundaries. Here the reduction goes from $10^{th} - 6^{th}$ order, however, only the last point is computed with the 6^{th} order, allowing the maximum accuracy possible.

Figure 4.2 evaluates the effect of the application-frequency on the resolved energy spectrum using the 10^{th} order filter. Results indicate that as the application-frequency is reduced, $f \rightarrow 1$, the filtering operation interferes with the resolved turbulence, dissipating the energy at high wave-numbers. However, if the application-frequency is increased, $50 < f < 100$, the interference with the resolve turbulence is reduced significantly. Nevertheless, if the application-frequency is further increased, the numerical

simulation starts to develop an unphysical buildup of energy at high wave-numbers, which eventually leads to the failure of the scheme. Therefore, a compromise has to be made, find an application-frequency that does not interfere with the resolve turbulence and prevent buildup of energy induced by numerical instabilities. Here, the application-frequency of 100 is found to provide the required stabilization to the central-scheme, the solution is stable without any energy build up, without significantly interfering with the resolved turbulence. Additionally, the sporadic application of the filtering operator brings in a beneficial reduction in the cost of the simulation, by not applying the filter operator at every time iteration.

Having selected the filter accuracy-order and application-frequency, the combined spatial discretization scheme, central-scheme and filtering stabilization, is evaluated next. Figure 4.3 present the effects of the order of the discretization scheme, results indicate that by using the low 2^{nd} order-central scheme Eq. (3.13), the explicit filter struggles stabilizing the scheme since the numerical errors are more prominent with Eq. (3.13). This is indicated by the more significant build up of energy at high wave-numbers when compared with the more accurate 4^{th} order central-scheme Eq. (3.14). For comparison purposes, results obtained using the 2^{nd} order scheme with the artificial numerical-disipation [44], for stabilization, are also included. Results demonstrate the over dissipative nature of the numerical-dissipation approach, which demonstrate why this methods is not recommended in high fidelity turbulence simulations. In conclusion, Figures 4.1-4.3 demonstrate the reliability and superiority of the 4^{th} order central scheme with 10^{th} order explicit filtering for stabilization. This global spatial scheme, referred from now on as 4CSD10EF (4^{th} order central scheme in divergence form with 10^{th} order explicit filter), is used on the rest of this work.

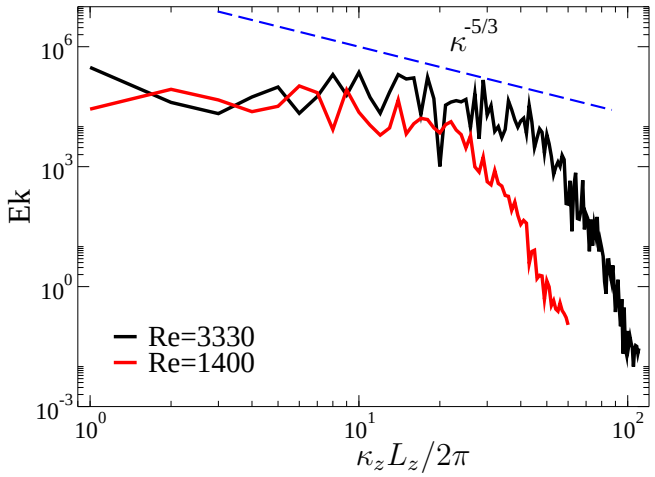

Figure 4.6: Computed one-dimensional LES energy spectra for $Re_\theta = 1400$ and $Re_\theta = 3330$ cases.

4.2.1 LES Validation

Having established the numerical approach to be implemented, it is applied it in Eqs. (2.40)-(2.48) to validate the LES solver. Figure 4.4 presents the computed mean velocity profile, normalized with wall-units [98], for $Re_\theta = 1400$ and $Re_\theta = 3330$. LES calculations accurately reproduce the law-of-the-wall and are found in excellent agreement with experimental data [2, 17], indicating that the friction coefficient is accurately reproduced. Here, it is important to mention that the friction coefficient obtained from experimental data is not directly measured, instead it is found by fiting the experimental results to the law-of-the-wall [2, 17]. In all the calculations, when required, the wall shear stress is directly computed demonstrating the accuracy of the predictions. Figure 4.5 presents the predicted velocity RMS and the Reynolds shear stress tensor. These second-order statistics are computed from the resolved and subgrid part (modeled turbulence) as follows [107]:

$$\overline{\rho u_i u_j} - \dot{\overline{\rho}}\dot{\widetilde{u}}_i\dot{\widetilde{u}}_j = \dot{\overline{\tau}}(\ddot{\widetilde{u}}_i, \ddot{\widetilde{u}}_j) + \dddot{\overline{\tau}}(u_i, u_j) \tag{4.1}$$

here, results are found in excellent agreement with experimental data. It is important to mention that when comparing LES calculations against experimental data or DNS data, the subgrid turbulent scales have to be accounted. This is of great importance

when assessing the quality of a LES grid. When the grid is coarsened, the intensity of the subgrid scales increase, due to the increase in the filter width. If only the resolved stresses are used to compare against reference data, wrong conclusions can be drawn, since the resolved turbulence may not present significant changes. However the contribution of the subgrid scales may significantly overshoot the predictions, especially if second order statistics are compared.

Thus far, the statistics of this flow have been predicted accurately. However, to fully validate the LES calculations, it is important to characterize some unsteady turbulence aspects in the predictions, to conclude that the simulated turbulence presents characteristics found in physical turbulence beyond statistics. To these end, the one-dimensional energy spectra computed, at $y^+ \sim 12$ over the spanwise direction $E(\kappa_z)$, from the resolved turbulence, for $Re_\theta = 1400$ and 3330, are present in Figure 4.6. The computed spectra suggest (since the spectrum is not normalized with Kolmogorov micro scales) an inertial range with a scaling of $k^{-5/3}$, this zone delimitates an equilibrium region where the turbulent kinetic energy is transfered from the large scales of the flow to the small viscous scales. It is expected that the extent of the suggested inertial range increase as the Re increases. This trend is reproduced in the results, which clearly predicts a longer suggested inertial range for the $Re = 3330$ case.

Figure 4.7 illustrates the wall-normal evolution of the streamwise velocity fluctuation u', for $Re = 1400$ case, at three locations, corresponding to the viscous $y^+ = 5$, buffer $y^+ = 11$, and logarithmic $y^+ = 100$ regions. Figure 7(a) indicates that at the viscous region, very close to the wall, the flow is not steady and small burst of intense velocity fluctuations can be found. However, as indicated by the second order statistics Figure 4.5, the peak of the turbulence generation is attained at the buffer layer $y^+ \sim 11$, this is observed in Figure 7(b) which present the highest distribution of unsteady fluctuation in all the domain. Finally, as we move away from the wall Figure 7(c), the velocity gradients become smaller reducing the production of turbulent

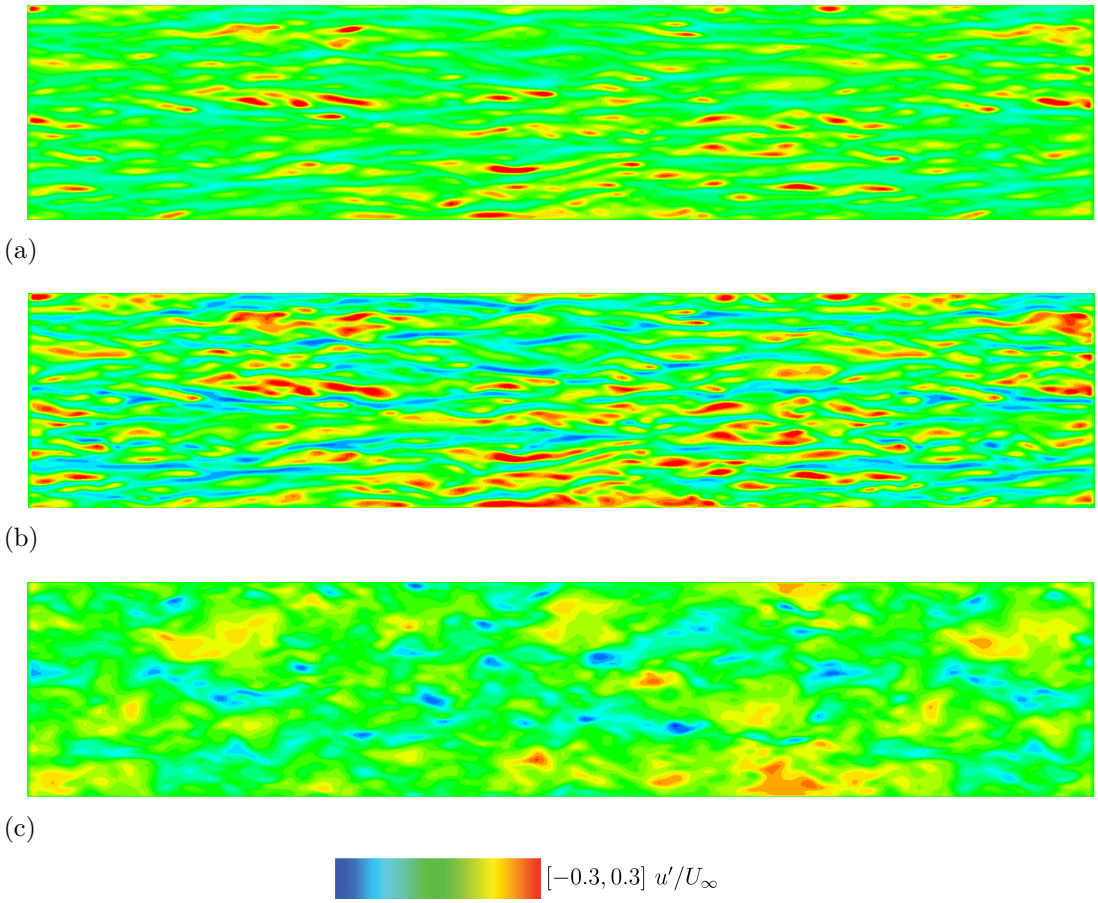

Figure 4.7: Wall-normal evolution of streamwise velocity fluctuations for $Re_\theta = 1400$: (a) viscous layer $y^+ = 5$; (b) buffer layer $y^+ = 11$; (c) logaritmic layer $y^+ = 100$.

kinetic energy, leading to the progressive dissipation of turbulence as the irrotational free stream region is approaches.

The fact that the turbulence simulated accurately reproduces the statistics and the distribution of energy over the turbulent scales, is a consequence of LES being able to resolve the driving forces that generate the turbulence in this flow. For the flat-plate boundary layer, the turbulence is produced by the high shear present at the wall, which generates coherent vortical-structures that are speculated to be of significant importance in the generation and transfer of turbulent kinetic energy [72]. Figure 4.8 presents isosurface of positive values of the second invariant of the velocity gradient, computed from the unsteady boundary layer field, known as $\mathcal{Q}$ criteria, which allows to identify the coherent structures in the boundary layer [21]:

$$\mathcal{Q} = \frac{1}{2}(R_{ij}R_{ij} - S_{ij}S_{ij}) \tag{4.2}$$

here, R_{ij} and S_{ij} are the antisymetric and symmetric velocity gradient tensors. The coherent structures visualized illustrate the unsteady near-wall dynamics present in this flow. Here, it can be observed how vortical structures, generated in the near-wall region, are ejected towards the outer layer transporting momentum from the wall to the outer regions of the boundary layer. The coherent structures are colored with values of streamwise velocity, which is also used in the gray contours. The use of the streamwise velocity on the contours and in the coherent structures allow to visualize the boundary layer thickness and the effect of the Re in the near wall dynamics. Here, by comparing Figures 8(a) and 8(b) it is clear that the increase in the Re number generate finer structures, which are closer concentrated in the near-wall region (observed by the reduction in red color, which represent the free stream velocity). The fast reduction in size of the near-wall structures and their closer location to the near-wall region, impose demanding grid requirements for simulations $N_x N_y N_z \propto Re^{1.8}$, since these structures scale with viscous units. On the other hand, the resolution required to resolve the large scale structures of the boundary layer is significant inferior

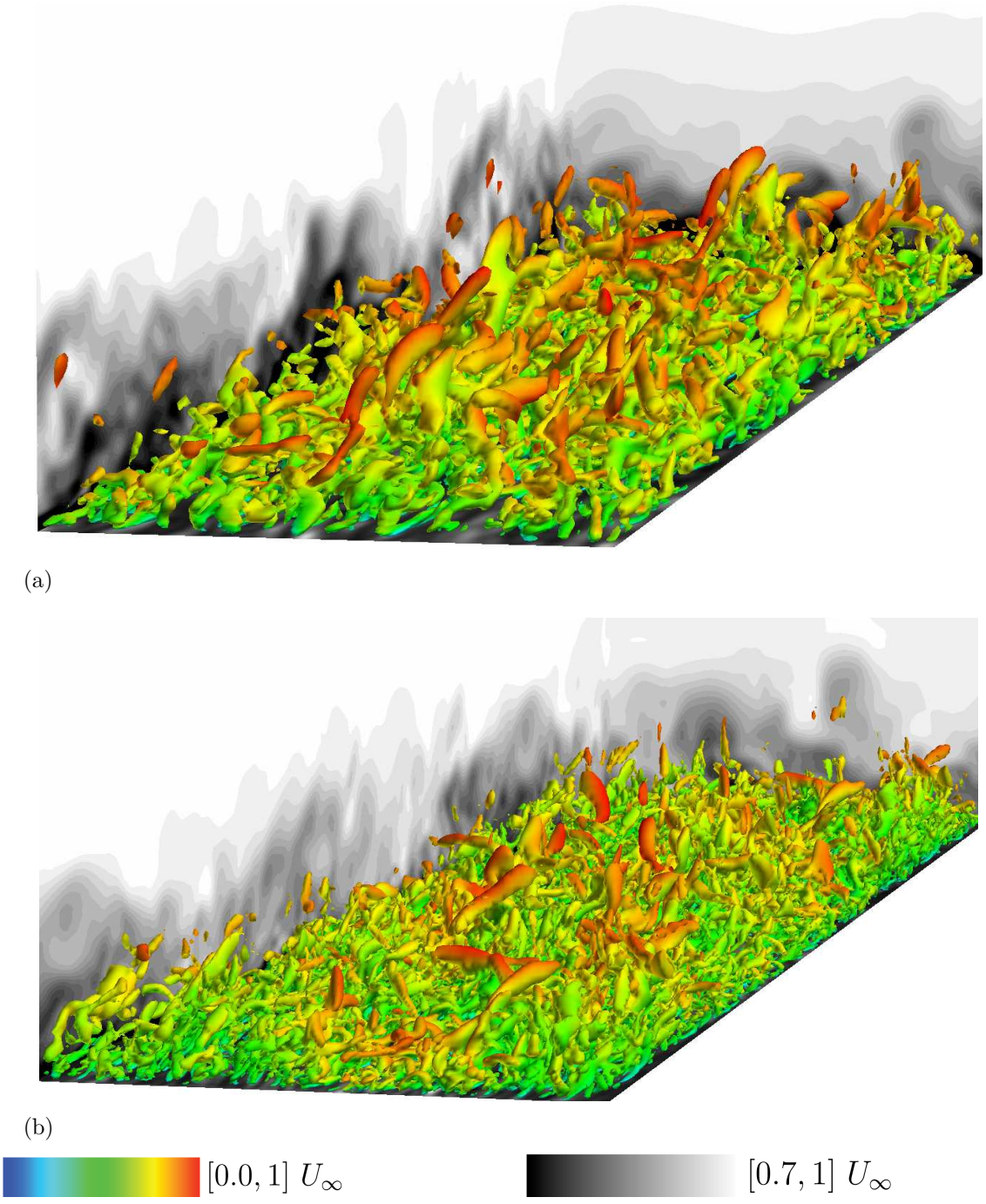

Figure 4.8: Isosurfaces of second invariant of the velocity gradient tensor ($\mathcal{Q}\theta/U_\infty = 1 \times 10^3$) colored with values of streamwise velocity, side contours streamwise velocity: (a) $Re_\theta = 1400$; (b) $Re_\theta = 3330$.

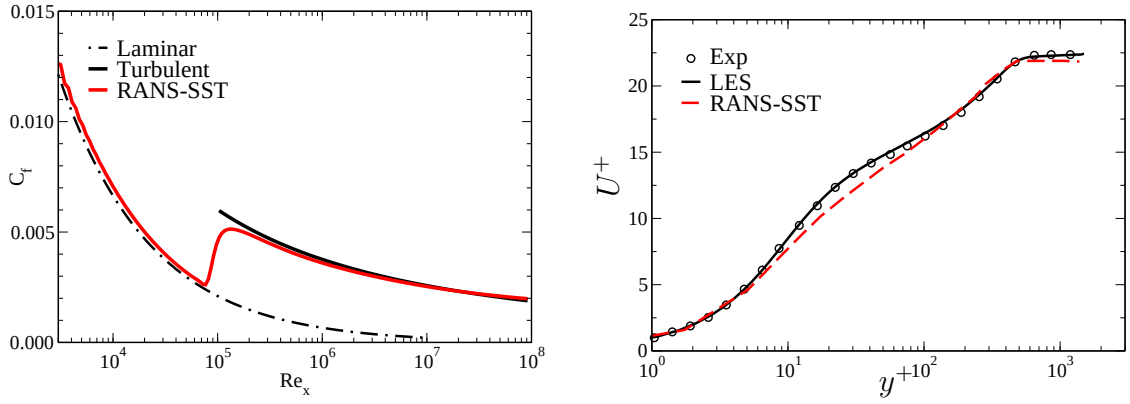

(a) (b)

Figure 4.9: Friction coefficient and mean streamwise velocity profile, normalized with wall-units, for $Re_\theta = 1400$, RANS-SST calculation: (a) friction coefficient transition from laminar to turbulent regime; (b) mean streamwise velocity profile.

$N_x N_y N_z \propto Re^{0.4}$, since these structures scales with the boundary layer thickness [69]. Overall Fig 4.8 clearly illustrates why wall-bounded flow turbulence simulations are so demanding.

4.2.2 RANS Validation

The ability of the numerical scheme to resolve the RANS equations (2.21)-(2.31) is validated by simulating the transition from laminar to turbulent flow in a flat-plate boundary layer. Figure 9(a) shows the evolution of the friction coefficient (C_f), results perfectly match the laminar C_f computed from laminar theory $c_f^L = 0.664/\sqrt{Re_x}$, more importantly RANS match the turbulent C_f predicted from law-of-the-wall estimations $c_f^T = 0.455/\ln^2(0.06Re_x)$ [104]. Here, the transition from laminar to turbulent flow is predicted around $Re_x \sim 10^5$. The mean velocity profile, normalized with wall-units, is compared against experiments at $Re_\theta = 1400$. Overall good agreement is obtained with LES calculations and with experimental data. However, a slight underprediction is reproduced at the buffer layer. This results are in agreement with previous RANS simulations, here the results did not present any dependency in the Ω free-stream boundary condition, in agreement with the original RANS-SST

reference [63].

Finally, these results validate the LES and RANS solver in flat-plate turbulent boundary layer, therefore it can be concluded that the solver is robust to conduct further studies.

CHAPTER V

GENERIC ADDITIVE FILTER FORMULATION

In the present Chapter, the compressible governing equations for the hybrid Reynolds-averaged/large-eddy simulations are formally derived by applying a hybrid filter to the Navier-Stokes equations. This filter is constructed by linearly combining the Reynolds-average (RANS) and large-eddy simulation (LES) operators with a continuous blending function. The derived hybrid equations include additional terms that represent the interactions between RANS and LES formulations. The importance of these terms is investigated in flat-plate turbulent boundary layer simulations. Further more, a model for the new hybrid terms predicted in the governing equations is proposed to reduce the cost of the exact hybrid RANS/LES formulation. Here, it is important to stress that the hybrid formulation derived is generic in the sense that it does not depend on the characteristics of the constitutive operators. Thus, the derived equations can be used with arbitrary operators by just changing their definitions. Here, the equations are derived using the RANS and LES operators due to the importance that hybrid RANS/LES turbulence models have achieved in engineering applications.

5.1 Formulation

The properties of additive filters, constructed by blending two or more independent operators in the framework of computational fluid dynamics were formally described by Germano [31]. In particular, he defined a hybrid RANS/LES filter by blending the RANS statistical operator and the LES filter operator and went on to derive the hybrid incompressible Navier-Stokes equations. The resulting differential equations depend explicitly on the hybrid variables, on the statistically operated, and on the

filtered quantities, increasing the number of independent variables. To close the equations, Germano introduced a simple reconstruction procedure, which in theory allows the calculation of the statistical and the filtered field from the hybrid variables. Germano did not conduct any numerical simulation to support the importance of the new formulation, which was only speculated. Therefore, his work is continued by extending the hybrid formulation to compressible flows and conducting numerical calculations to prove the importance of the exact formulation.

5.1.1 Operators

Having defined the RANS and the LES operators, a hybrid additive operator, and its Favre representation can be constructed by combining equations (2.19) and (2.35) with a blending function

$$\overline{\phi}(X,t) = \mathcal{F}\dot{\overline{\phi}}(X,t) + (1-\mathcal{F})\ddot{\overline{\phi}}(X,t) \tag{5.1}$$

$$\widetilde{\phi}(X,t) = \frac{\overline{\rho\phi}}{\overline{\rho}}. \tag{5.2}$$

Here, $\mathcal{F}$ is a normalized function that in general, depends on time and space. It is defined as $\mathcal{F} : \left\{ \; (\parallel X \parallel, t) \; \in \; [0,\infty) \rightarrow \mathcal{F}(X,t) \; \in \; [0,1] \; \right\}$. Furthermore, it must have continuous derivatives to at least second order in space and first order in time, i.e., $\mathcal{F}(X,t)$ is a $C^2(x_i)$ and $C^1(t)$ function (this will be evident when the hybrid equations are derived). Under this hybrid definition, Eq. (5.1) recovers RANS and LES variables when $\mathcal{F} = 1$ and $\mathcal{F} = 0$, respectively. Similar to RANS and LES, the unsteady variable (ϕ) can be constructed using the hybrid variables with the standard decomposition:

$$\phi = \overline{\phi} + \phi', \quad \phi = \widetilde{\phi} + \phi''. \tag{5.3}$$

Here, the hybrid fluctuations can be easily shown to be related to the RANS and LES fluctuations as

$$\phi' = \mathcal{F}\dot{\phi'} + (1-\mathcal{F})\ddot{\phi'} \tag{5.4}$$

and

$$\phi'' = \mathcal{F}\frac{\dot{\overline{\rho}}}{\overline{\rho}}\dot{\overline{\phi''}} + (1-\mathcal{F})\frac{\ddot{\overline{\rho}}}{\overline{\rho}}\ddot{\overline{\phi''}}. \tag{5.5}$$

It can also be shown that, in general, the hybrid filter Eq. (5.1) does not commute with differentiation and does not satisfy all the Reynolds rules of averaging regardless the properties of the constitutive operators. Thus,

$$\overline{\frac{\partial\phi}{\partial x_i}} = \frac{\partial\overline{\phi}}{\partial x_i} + \frac{\partial\mathcal{F}}{\partial x_i}(\ddot{\overline{\phi}} - \dot{\overline{\phi}}) \tag{5.6a}$$

$$\overline{\frac{\partial\phi}{\partial t}} = \frac{\partial\overline{\phi}}{\partial t} + \frac{\partial\mathcal{F}}{\partial t}(\ddot{\overline{\phi}} - \dot{\overline{\phi}}) \tag{5.6b}$$

$$\overline{\phi+\psi} = \overline{\phi} + \overline{\psi}, \tag{5.7a}$$

$$\overline{\alpha} = \alpha, \tag{5.7b}$$

$$\overline{\alpha\phi} = \alpha\overline{\phi}, \tag{5.7c}$$

$$\overline{\phi\overline{\psi}} \neq \overline{\phi}\,\overline{\psi}, \tag{5.7d}$$

$$\overline{\overline{\phi}} \neq \overline{\phi}, \qquad \widetilde{\widetilde{\phi}} \neq \widetilde{\phi}, \tag{5.7e}$$

$$\overline{\phi'} \neq 0, \qquad \overline{\phi''} \neq 0, \tag{5.7f}$$

$$\overline{\rho\phi'} \neq 0, \qquad \overline{\rho\phi''} \neq 0, \tag{5.7g}$$

since

$$\overline{\overline{\phi}} = (2-\mathcal{F})\mathcal{F}\dot{\overline{\phi}} + (1-\mathcal{F})^2\ddot{\overline{\phi}}. \tag{5.8}$$

Here, α and ψ are a constant and an unsteady function similar to ϕ, respectively. Equations (5.6) and (5.8) indicate that the hybrid filter does not commute with differentiation, and the application of the hybrid operator on the hybrid variable does not recover the same hybrid variable, i.e., $\overline{\overline{\phi}} \neq \overline{\phi}$. These are general properties of this hybrid operator, and do not depend on the constitutive operators.

The last relevant property of the hybrid operator is related to its ability to reconstruct the RANS and the LES variables if the hybrid field is known. Germano [31]

showed that by applying Eq. (2.19) in Eq. (5.1), and invoking Eq. (2.39), the RANS variable can be calculated directly from the hybrid variable as

$$\dot{\overline{\phi}} = \dot{\overline{\phi}}. \tag{5.9}$$

Once the RANS field is known, the LES variable can be obtained by substituting Eq. (5.9) in Eq. (5.1)

$$\ddot{\widetilde{\phi}} = \frac{\overline{\phi} - \mathcal{F}\dot{\overline{\phi}}}{1-\mathcal{F}}. \tag{5.10}$$

To extend Germano's original incompressible formulation to compressible flow, the governing equations have to be derived using the generalized second-order central-moments [30]. This give a better representation of the unclosed terms that appears when the operator is applied in the non-linear terms. This way, the final equations are invariant with respect to the operators employed. For the compressible formulation, the generalized second-order central-moments are defined as

$$\overline{\tau}(a,b) = \overline{\rho}(\widetilde{ab} - \widetilde{a}\widetilde{b}), \quad \overline{\chi}(a,b) = \overline{ab} - \widetilde{a}\overline{b}, \quad \overline{\zeta}(a,b) = \overline{ab} - \widetilde{a}\widetilde{b} \tag{5.11}$$

here, a and b are dummy variables and τ, χ, and ζ represent, the compressible operators required by the RANS, the LES, and the hybrid formulation. It is important to highlight that τ and ζ are symmetric operators while χ is not. Additionally, both χ and ζ operators are required to account for the additional non-linear terms present in the energy equation, and therefore they do not appear in Germano's [31] incompressible formulation. By substituting Eqs. (5.1) and (5.2) in Eq. (5.11), the dependency of the hybrid central-moments on the RANS and LES variables can be shown to be

$$\begin{aligned}
\overline{\tau}(a,b) =& \mathcal{F}\dot{\overline{\tau}}(a,b) + (1-\mathcal{F})\ddot{\widetilde{\tau}}(a,b) \\
&+ \overline{\rho}\Big[\mathcal{F}\Big(1-\mathcal{F}\frac{\dot{\overline{\rho}}}{\overline{\rho}}\Big)\frac{\dot{\overline{\rho}}}{\overline{\rho}}\dot{\widetilde{a}}\dot{\widetilde{b}} - \mathcal{F}(1-\mathcal{F})\frac{\dot{\overline{\rho}}\,\ddot{\overline{\rho}}}{\overline{\rho}^2}\dot{\widetilde{a}}\ddot{\widetilde{b}}\Big] \\
&+ \overline{\rho}\Big[(1-\mathcal{F})\Big(1-(1-\mathcal{F})\frac{\ddot{\overline{\rho}}}{\overline{\rho}}\Big)\frac{\ddot{\overline{\rho}}}{\overline{\rho}}\ddot{\widetilde{a}}\ddot{\widetilde{b}} - \mathcal{F}(1-\mathcal{F})\frac{\dot{\overline{\rho}}\,\ddot{\overline{\rho}}}{\overline{\rho}^2}\ddot{\widetilde{a}}\dot{\widetilde{b}}\Big]
\end{aligned} \tag{5.12}$$

$$
\begin{aligned}
\overline{\chi}(a,b) =& \mathcal{F}\dot{\overline{\chi}}(a,b) + (1-\mathcal{F})\ddot{\overline{\chi}}(a,b) \\
&+ \Big[\mathcal{F}\Big(1-\mathcal{F}\frac{\dot{\overline{\rho}}}{\overline{\rho}}\Big)\dot{\widetilde{a}}\dot{\widetilde{b}} - \mathcal{F}(1-\mathcal{F})\frac{\dot{\overline{\rho}}}{\overline{\rho}}\dot{\widetilde{a}}\ddot{\widetilde{b}}\Big] \\
&+ \Big[(1-\mathcal{F})\Big(1-(1-\mathcal{F})\frac{\ddot{\overline{\rho}}}{\overline{\rho}}\Big)\ddot{\widetilde{a}}\ddot{\widetilde{b}} - \mathcal{F}(1-\mathcal{F})\frac{\ddot{\overline{\rho}}}{\overline{\rho}}\ddot{\widetilde{a}}\dot{\widetilde{b}}\Big]
\end{aligned}
\tag{5.13}
$$

$$
\begin{aligned}
\overline{\zeta}(a,b) =& \mathcal{F}\dot{\overline{\zeta}}(a,b) + (1-\mathcal{F})\ddot{\overline{\zeta}}(a,b) \\
&+ \Big[\mathcal{F}\Big(1-\mathcal{F}\frac{\dot{\overline{\rho}}^2}{\overline{\rho}^2}\Big)\dot{\widetilde{a}}\dot{\widetilde{b}} - \mathcal{F}(1-\mathcal{F})\frac{\dot{\overline{\rho}}\,\ddot{\overline{\rho}}}{\overline{\rho}^2}\dot{\widetilde{a}}\ddot{\widetilde{b}}\Big] \\
&+ \Big[(1-\mathcal{F})\Big(1-(1-\mathcal{F})\frac{\ddot{\overline{\rho}}^2}{\overline{\rho}^2}\Big)\ddot{\widetilde{a}}\ddot{\widetilde{b}} - \mathcal{F}(1-\mathcal{F})\frac{\dot{\overline{\rho}}\,\ddot{\overline{\rho}}}{\overline{\rho}^2}\ddot{\widetilde{a}}\dot{\widetilde{b}}\Big]
\end{aligned}
\tag{5.14}
$$

It is trivial to show that these equations recover RANS and LES central moments when $\mathcal{F}=1$ and $\mathcal{F}=0$, respectively. Using the above operator, the hybrid Reynolds stress tensor is constructed by operating Eq. (5.12) on u_i and u_j:

$$
\begin{aligned}
\overline{\tau}(u_i,u_j) =& \mathcal{F}\dot{\overline{\rho}}(\dot{\widetilde{u_iu_j}} - \dot{\widetilde{u}}_i\dot{\widetilde{u}}_j) + (1-\mathcal{F})\ddot{\overline{\rho}}(\ddot{\widetilde{u_iu_j}} - \ddot{\widetilde{u}}_i\ddot{\widetilde{u}}_j) \\
&+ \overline{\rho}\Big[\mathcal{F}\Big(1-\mathcal{F}\frac{\dot{\overline{\rho}}}{\overline{\rho}}\Big)\frac{\dot{\overline{\rho}}}{\overline{\rho}}\dot{\widetilde{u}}_i\dot{\widetilde{u}}_j - \mathcal{F}(1-\mathcal{F})\frac{\dot{\overline{\rho}}\,\ddot{\overline{\rho}}}{\overline{\rho}^2}\dot{\widetilde{u}}_i\ddot{\widetilde{u}}_j\Big] \\
&+ \overline{\rho}\Big[(1-\mathcal{F})\Big(1-(1-\mathcal{F})\frac{\ddot{\overline{\rho}}}{\overline{\rho}}\Big)\frac{\ddot{\overline{\rho}}}{\overline{\rho}}\ddot{\widetilde{u}}_i\ddot{\widetilde{u}}_j - \mathcal{F}(1-\mathcal{F})\frac{\dot{\overline{\rho}}\,\ddot{\overline{\rho}}}{\overline{\rho}^2}\ddot{\widetilde{u}}_i\dot{\widetilde{u}}_j\Big].
\end{aligned}
\tag{5.15}
$$

It is clear that the compressible generic central-moments in their explicit form include density ratios induced by the Favre formulation that do not appear in the incompressible formulation of Germano [31]. However, it is easy to show, and it will be shown, that for incompressible flow, Eq. (5.15) reduces to the incompressible hybrid Reynolds stress tensor derived by Germano.

5.1.2 Compressible Hybrid RANS/LES Navier-Stokes Equations

Having established the required hybrid operators, Eqs. (5.1)-(5.14), they are applied to the compressible Navier-Stokes equations Eqs. (2.5)-(2.7).

$$
\frac{\partial\overline{\rho}}{\partial t} + \frac{\partial}{\partial x_j}(\widetilde{\overline{\rho}u_j}) = \frac{\partial\mathcal{F}}{\partial x_j}\big[\dot{\overline{\rho}}\dot{\widetilde{u}}_j - \ddot{\overline{\rho}}\ddot{\widetilde{u}}_j\big] + \frac{\partial\mathcal{F}}{\partial t}\big[\dot{\overline{\rho}} - \ddot{\overline{\rho}}\big] \tag{5.16}
$$

$$
\begin{aligned}
\frac{\partial \overline{\rho}\widetilde{u}_i}{\partial t} + \frac{\partial}{\partial x_j}(\overline{\rho}\widetilde{u}_i\widetilde{u}_j + \overline{p}\delta_{ij} - \widetilde{\tau}_{ij} + \overline{\tau}(u_i,u_j)) = \\
&\frac{\partial \mathcal{F}}{\partial x_j}\Big[\dot{\overline{\rho}}\dot{\widetilde{u}}_i\dot{\widetilde{u}}_j - \ddot{\overline{\rho}}\ddot{\widetilde{u}}_i\ddot{\widetilde{u}}_j + \dot{\overline{\tau}}(u_i,u_j) - \ddot{\overline{\tau}}(u_i,u_j) \\
&+ (\dot{\overline{p}} - \ddot{\overline{p}})\delta_{ij} - (\dot{\widetilde{\tau}}_{ij} - \ddot{\widetilde{\tau}}_{ij})\Big] \\
&- \frac{\partial}{\partial x_j}\Bigg\{\frac{\partial \mathcal{F}}{\partial x_j}(\dot{\overline{\mu}}\dot{\widetilde{u}}_i - \ddot{\overline{\mu}}\ddot{\widetilde{u}}_i) + \frac{\partial \mathcal{F}}{\partial x_i}(\dot{\overline{\mu}}\dot{\widetilde{u}}_j - \ddot{\overline{\mu}}\ddot{\widetilde{u}}_j) \\
&- \frac{2}{3}\frac{\partial \mathcal{F}}{\partial x_k}(\dot{\overline{\mu}}\dot{\widetilde{u}}_k - \ddot{\overline{\mu}}\ddot{\widetilde{u}}_k)\delta_{ij}\Bigg\} + \frac{\partial \mathcal{F}}{\partial t}\big[\dot{\overline{\rho}}\dot{\widetilde{u}}_i - \ddot{\overline{\rho}}\ddot{\widetilde{u}}_i\big]
\end{aligned} \tag{5.17}
$$

$$
\begin{aligned}
\frac{\partial \overline{\rho}\widetilde{E}}{\partial t} + \frac{\partial}{\partial x_j}\Bigg(&\overline{\rho}\widetilde{E}\widetilde{u}_j + \overline{p}\widetilde{u}_j - \overline{\kappa}\frac{\partial \widetilde{T}}{\partial x_j} - \widetilde{\tau}_{ij}\widetilde{u}_i + \overline{\tau}(E,u_j) \\
&+ \overline{\chi}(u_j,p) - \overline{\chi}\Big(\frac{\partial T}{\partial x_j},\kappa\Big) - \overline{\zeta}(\tau_{ij},u_i)\Bigg) = \\
&\frac{\partial \mathcal{F}}{\partial x_j}\Bigg\{\dot{\overline{\rho}}\dot{\widetilde{u}}_j\dot{\widetilde{E}} - \ddot{\overline{\rho}}\ddot{\widetilde{u}}_j\ddot{\widetilde{E}} + \dot{\overline{\tau}}(E,u_j) - \ddot{\overline{\tau}}(E,u_j) \\
&+ \dot{\widetilde{u}}_j\dot{\overline{p}} - \ddot{\widetilde{u}}_j\ddot{\overline{p}} + \dot{\overline{\chi}}(u_j,p) - \ddot{\overline{\chi}}(u_j,p) \\
&- \Big(\dot{\overline{\kappa}}\frac{\partial \dot{\widetilde{T}}}{\partial x_j} - \ddot{\overline{\kappa}}\frac{\partial \ddot{\widetilde{T}}}{\partial x_j} + \dot{\overline{\chi}}\Big(\frac{\partial T}{\partial x_j},\kappa\Big) - \ddot{\overline{\chi}}\Big(\frac{\partial T}{\partial x_j},\kappa\Big)\Big) \\
&- \Big(\dot{\widetilde{\tau}}_{ij}\dot{\widetilde{u}}_i - \ddot{\widetilde{\tau}}_{ij}\ddot{\widetilde{u}}_i + \dot{\overline{\zeta}}(\tau_{ij},u_i) - \ddot{\overline{\zeta}}(\tau_{ij},u_i)\Big)\Bigg\} \\
&+ \frac{\partial \mathcal{F}}{\partial t}\big[\dot{\overline{\rho}}\dot{\widetilde{E}} - \ddot{\overline{\rho}}\ddot{\widetilde{E}}\big]
\end{aligned} \tag{5.18}
$$

with the pressure, shear stress tensor, and total energy defined as

$$
\overline{p} = \overline{\rho}R\widetilde{T} \tag{5.19}
$$

$$
\widetilde{\tau}_{ij} = 2\overline{\mu}\big(\widetilde{S}_{ij} - \frac{1}{3}\widetilde{S}_{kk}\delta_{ij}\big), \quad \widetilde{S}_{ij} = \frac{1}{2}\Big(\frac{\partial \widetilde{u}_i}{\partial x_j} + \frac{\partial \widetilde{u}_j}{\partial x_i}\Big), \tag{5.20a}
$$

$$
\dot{\widetilde{\tau}}_{ij} = 2\dot{\overline{\mu}}\big(\dot{\widetilde{S}}_{ij} - \frac{1}{3}\dot{\widetilde{S}}_{kk}\delta_{ij}\big), \quad \dot{\widetilde{S}}_{ij} = \frac{1}{2}\Big(\frac{\partial \dot{\widetilde{u}}_i}{\partial x_j} + \frac{\partial \dot{\widetilde{u}}_j}{\partial x_i}\Big), \tag{5.20b}
$$

$$
\ddot{\widetilde{\tau}}_{ij} = 2\ddot{\overline{\mu}}\big(\ddot{\widetilde{S}}_{ij} - \frac{1}{3}\ddot{\widetilde{S}}_{kk}\delta_{ij}\big), \quad \ddot{\widetilde{S}}_{ij} = \frac{1}{2}\Big(\frac{\partial \ddot{\widetilde{u}}_i}{\partial x_j} + \frac{\partial \ddot{\widetilde{u}}_j}{\partial x_i}\Big) \tag{5.20c}
$$

$$\overline{\rho}\widetilde{E} = \overline{\rho}C_v\widetilde{T} + \frac{\overline{\rho}}{2}\widetilde{u}_i\widetilde{u}_i + \frac{1}{2}\overline{\tau}(u_i, u_i) \tag{5.21a}$$

$$\dot{\overline{\rho}}\dot{\widetilde{E}} = \dot{\overline{\rho}}C_v\dot{\widetilde{T}} + \frac{\dot{\overline{\rho}}}{2}\dot{\widetilde{u}}_i\dot{\widetilde{u}}_i + \frac{1}{2}\dot{\overline{\tau}}(u_i, u_i) \tag{5.21b}$$

$$\ddot{\overline{\rho}}\ddot{\widetilde{E}} = \ddot{\overline{\rho}}C_v\ddot{\widetilde{T}} + \frac{\ddot{\overline{\rho}}}{2}\ddot{\widetilde{u}}_i\ddot{\widetilde{u}}_i + \frac{1}{2}\ddot{\overline{\tau}}(u_i, u_i) \tag{5.21c}$$

As expected, the application of the hybrid operator to the Navier-Stokes equations results in unclosed terms that need to be modeled. Furthermore, the hybrid operator introduces new terms into the final equations. These terms are:

$$\sigma_\rho = \frac{\partial \mathcal{F}}{\partial x_j}\left[\dot{\overline{\rho}}\dot{\widetilde{u}}_j - \ddot{\overline{\rho}}\ddot{\widetilde{u}}_j\right] + \frac{\partial \mathcal{F}}{\partial t}\left[\dot{\overline{\rho}} - \ddot{\overline{\rho}}\right] \tag{5.22}$$

$$\begin{aligned}
\sigma_{\rho u_i} =& \frac{\partial \mathcal{F}}{\partial x_j}\Big[\dot{\overline{\rho}}\dot{\widetilde{u}}_i\dot{\widetilde{u}}_j - \ddot{\overline{\rho}}\ddot{\widetilde{u}}_i\ddot{\widetilde{u}}_j + \dot{\overline{\tau}}(u_i, u_j) - \ddot{\overline{\tau}}(u_i, u_j) \\
&+ (\dot{\overline{p}} - \ddot{\overline{p}})\delta_{ij} - (\dot{\widetilde{\tau}}_{ij} - \ddot{\widetilde{\tau}}_{ij})\Big] \\
&- \frac{\partial}{\partial x_j}\Bigg\{\frac{\partial \mathcal{F}}{\partial x_j}(\dot{\overline{\mu}}\dot{\widetilde{u}}_i - \ddot{\overline{\mu}}\ddot{\widetilde{u}}_i) + \frac{\partial \mathcal{F}}{\partial x_i}(\dot{\overline{\mu}}\dot{\widetilde{u}}_j - \ddot{\overline{\mu}}\ddot{\widetilde{u}}_j) \\
&- \frac{2}{3}\frac{\partial \mathcal{F}}{\partial x_k}(\dot{\overline{\mu}}\dot{\widetilde{u}}_k - \ddot{\overline{\mu}}\ddot{\widetilde{u}}_k)\delta_{ij}\Bigg\} + \frac{\partial \mathcal{F}}{\partial t}\left[\dot{\overline{\rho}}\dot{\widetilde{u}}_i - \ddot{\overline{\rho}}\ddot{\widetilde{u}}_i\right]
\end{aligned} \tag{5.23}$$

$$\begin{aligned}
\sigma_{\rho E} =& \frac{\partial \mathcal{F}}{\partial x_j}\Bigg\{\dot{\overline{\rho}}\dot{\widetilde{u}}_j\dot{\widetilde{E}} - \ddot{\overline{\rho}}\ddot{\widetilde{u}}_j\ddot{\widetilde{E}} + \dot{\overline{\tau}}(E, u_j) - \ddot{\overline{\tau}}(E, u_j) \\
&+ \dot{\widetilde{u}}_j\dot{\overline{p}} - \ddot{\widetilde{u}}_j\ddot{\overline{p}} + \dot{\overline{\chi}}(u_j, p) - \ddot{\overline{\chi}}(u_j, p) \\
&- \left(\dot{\overline{\kappa}}\frac{\partial \dot{\widetilde{T}}}{\partial x_j} - \ddot{\overline{\kappa}}\frac{\partial \ddot{\widetilde{T}}}{\partial x_j} + \dot{\overline{\chi}}\Big(\frac{\partial T}{\partial x_j}, \kappa\Big) - \ddot{\overline{\chi}}\Big(\frac{\partial T}{\partial x_j}, \kappa\Big)\right) \\
&- \left(\dot{\widetilde{\tau}}_{ij}\dot{\widetilde{u}}_i - \ddot{\widetilde{\tau}}_{ij}\ddot{\widetilde{u}}_i + \dot{\overline{\zeta}}(\tau_{ij}, u_i) - \ddot{\overline{\zeta}}(\tau_{ij}, u_i)\right)\Bigg\} \\
&+ \frac{\partial \mathcal{F}}{\partial t}\left[\dot{\overline{\rho}}\dot{\widetilde{E}} - \ddot{\overline{\rho}}\ddot{\widetilde{E}}\right]
\end{aligned} \tag{5.24}$$

and

$$\begin{aligned}\sigma_{\overline{\tau}(a,b)} =&\overline{\rho}\Big[\mathcal{F}\Big(1-\mathcal{F}\frac{\dot{\overline{\rho}}}{\overline{\rho}}\Big)\frac{\dot{\overline{\rho}}}{\overline{\rho}}\dot{\widetilde{a}}\dot{\widetilde{b}}-\mathcal{F}(1-\mathcal{F})\frac{\dot{\overline{\rho}}\,\ddot{\overline{\rho}}}{\overline{\rho}^2}\dot{\widetilde{a}}\ddot{\widetilde{b}}\Big]\\&+\overline{\rho}\Big[(1-\mathcal{F})\Big(1-(1-\mathcal{F})\frac{\ddot{\overline{\rho}}}{\overline{\rho}}\Big)\frac{\ddot{\overline{\rho}}}{\overline{\rho}}\ddot{\widetilde{a}}\ddot{\widetilde{b}}-\mathcal{F}(1-\mathcal{F})\frac{\dot{\overline{\rho}}\,\ddot{\overline{\rho}}}{\overline{\rho}^2}\ddot{\widetilde{a}}\dot{\widetilde{b}}\Big]\end{aligned}\tag{5.25}$$

$$\begin{aligned}\sigma_{\overline{\chi}(a,b)} =&\Big[\mathcal{F}\Big(1-\mathcal{F}\frac{\dot{\overline{\rho}}}{\overline{\rho}}\Big)\dot{\widetilde{a}}\dot{\widetilde{b}}-\mathcal{F}(1-\mathcal{F})\frac{\dot{\overline{\rho}}}{\overline{\rho}}\dot{\widetilde{a}}\ddot{\widetilde{b}}\Big]\\&+\Big[(1-\mathcal{F})\Big(1-(1-\mathcal{F})\frac{\ddot{\overline{\rho}}}{\overline{\rho}}\Big)\ddot{\widetilde{a}}\ddot{\widetilde{b}}-\mathcal{F}(1-\mathcal{F})\frac{\ddot{\overline{\rho}}}{\overline{\rho}}\ddot{\widetilde{a}}\dot{\widetilde{b}}\Big]\end{aligned}\tag{5.26}$$

$$\begin{aligned}\sigma_{\overline{\zeta}(a,b)} =&\Big[\mathcal{F}\Big(1-\mathcal{F}\frac{\dot{\overline{\rho}}^2}{\overline{\rho}^2}\Big)\dot{\widetilde{a}}\dot{\widetilde{b}}-\mathcal{F}(1-\mathcal{F})\frac{\dot{\overline{\rho}}\,\ddot{\overline{\rho}}}{\overline{\rho}^2}\dot{\widetilde{a}}\ddot{\widetilde{b}}\Big]\\&+\Big[(1-\mathcal{F})\Big(1-(1-\mathcal{F})\frac{\ddot{\overline{\rho}}^2}{\overline{\rho}^2}\Big)\ddot{\widetilde{a}}\ddot{\widetilde{b}}-\mathcal{F}(1-\mathcal{F})\frac{\dot{\overline{\rho}}\,\ddot{\overline{\rho}}}{\overline{\rho}^2}\ddot{\widetilde{a}}\dot{\widetilde{b}}\Big]\end{aligned}\tag{5.27}$$

Equations (5.22)-(5.24) represent turbulent terms that contribute to the governing equations during the RANS to LES transition (RTLT) zone. They occur due to the incommutability between hybrid operator and differentiation. Similarly, the hybrid terms (Eqs. (5.25)-(5.27)) are also only relevant in the RTLT zone and originate due to the nonlinearity of the hybrid central-moments, and consist of products between RANS and LES variables. In the following, Eqs. (5.22)-(5.27) will be referred to as "hybrid contributions" or "hybrid terms" indistinctly. Note that these terms become infinite if the blending function implemented in the hybrid operator is discontinuous. Therefore, a well defined hybrid formulation requires at least a $C^2(x_i)$ and $C^1(t)$ "$\mathcal{F}$" function.

The hybrid contributions provide the mechanism that keeps the balance between modeled and resolved scales in the RTLT zone, where neither RANS nor LES completely models nor resolves the turbulence of the flow. In order to demonstrate this point, let us further analyze the hybrid contributions. To simplify the analysis, Eqs. (2.24) and (2.43) are substituted in Eqs. (5.22)-(5.24), and additionally it is assumed that the turbulence is only weakly affected by compressibility effects, which is a valid

assumption provided that the fluctuating Mach number is $Ma' < 0.3$ [91]. Therefore, all density ratios appearing in Eqs. (5.25)-(5.27) can be assumed as unity for this discussion. It is also assumed that the blending function $\mathcal{F}$ is continous and function of space only, with bounded first and second order derivatives. Under these conditions Eqs. (5.22)-(5.27) reduce to

$$\sigma_\rho = \frac{\partial \mathcal{F}}{\partial x_j}\left[\dot{\overline{\rho}}\dot{\widetilde{u}}_j - \ddot{\overline{\rho}}\ddot{\widetilde{u}}_j\right] \tag{5.28}$$

$$\begin{aligned}\sigma_{\rho u_i} = {} & \frac{\partial \mathcal{F}}{\partial x_j}\left[\dot{\overline{\rho u_i u_j}} - \ddot{\overline{\rho u_i u_j}} + (\dot{\overline{p}} - \ddot{\overline{p}})\delta_{ij} - (\dot{\tilde{\tau}}_{ij} - \ddot{\tilde{\tau}}_{ij})\right] \\ & - \frac{\partial}{\partial x_j}\left\{\frac{\partial \mathcal{F}}{\partial x_j}(\dot{\overline{\mu}}\dot{\widetilde{u}}_i - \ddot{\overline{\mu}}\ddot{\widetilde{u}}_i) + \frac{\partial \mathcal{F}}{\partial x_i}(\dot{\overline{\mu}}\dot{\widetilde{u}}_j - \ddot{\overline{\mu}}\ddot{\widetilde{u}}_j) - \frac{2}{3}\frac{\partial \mathcal{F}}{\partial x_k}(\dot{\overline{\mu}}\dot{\widetilde{u}}_k - \ddot{\overline{\mu}}\ddot{\widetilde{u}}_k)\delta_{ij}\right\}\end{aligned} \tag{5.29}$$

$$\sigma_{\rho E} = \frac{\partial \mathcal{F}}{\partial x_j}\left\{\dot{\overline{\rho u_j E}} - \ddot{\overline{\rho u_j E}} + \dot{\overline{u_j p}} - \ddot{\overline{u_j p}} - \left(\dot{\overline{\kappa \frac{\partial T}{\partial x_j}}} - \ddot{\overline{\kappa \frac{\partial T}{\partial x_j}}}\right) - \left(\dot{\widetilde{\tau_{ij}u_i}} - \ddot{\widetilde{\tau_{ij}u_i}}\right)\right\} \tag{5.30}$$

$$\sigma_{\overline{\tau}(a,b)} = \frac{\mathcal{F}(1-\mathcal{F})}{\overline{\rho}}\left(\dot{\overline{\rho a}} - \ddot{\overline{\rho a}}\right)\left(\dot{\overline{\rho b}} - \ddot{\overline{\rho b}}\right) \tag{5.31}$$

$$\sigma_{\overline{\chi}(a,b)} = \frac{\mathcal{F}(1-\mathcal{F})}{\overline{\rho}}\left(\dot{\overline{\rho a}} - \ddot{\overline{\rho a}}\right)\left(\dot{\overline{b}} - \ddot{\overline{b}}\right) \tag{5.32}$$

$$\sigma_{\overline{\zeta}(a,b)} = \frac{\mathcal{F}(1-\mathcal{F})}{\overline{\rho}^2}\left(\dot{\overline{\rho a}} - \ddot{\overline{\rho a}}\right)\left(\dot{\overline{\rho b}} - \ddot{\overline{\rho b}}\right) \tag{5.33}$$

Equations (5.28)-(5.33) indicate that the hybrid contributions are directly proportional to difference between RANS and LES variables. In order to extract additional information, the RANS and the LES differences can be approximated with the instantaneous turbulent fluctuation $\phi^{\dot{\prime}} = \phi - \dot{\overline{\phi}} = \mathcal{C}(\ddot{\overline{\phi}} - \dot{\overline{\phi}})$, since $\ddot{\overline{\phi}} \to \phi$ for $\Delta \to 0$ and $\dot{\phi^{\dot{\prime}}} = \mathcal{C}(\dddot{\overline{\phi}} - \ddot{\overline{\phi}}) = 0$. Here, ϕ is the instantaneous variable and $\mathcal{C}$ is an order one coefficient. Therefore, by substituting $\phi^{\dot{\prime}} = \mathcal{C}(\ddot{\overline{\phi}} - \dot{\overline{\phi}})$ in Eqs. (5.28)-(5.33), and assuming $\mathcal{C} = 1$ the hybrid contributions can be expressed as

$$\sigma_\rho = -\frac{\partial \mathcal{F}}{\partial x_j}(\rho u_j)^{\dot{\prime}} \tag{5.34}$$

$$\begin{aligned}\sigma_{\rho u_i} = &- \frac{\partial \mathcal{F}}{\partial x_j}\left[(\rho u_i u_j)^{\dot{\overline{\tau}}} + p^{\dot{\overline{\tau}}}\delta_{ij} - \tau_{ij}^{\dot{\overline{\tau}}}\right] \\ &+ \frac{\partial}{\partial x_j}\left\{\frac{\partial \mathcal{F}}{\partial x_j}(\mu u_i)^{\dot{\overline{\tau}}} + \frac{\partial \mathcal{F}}{\partial x_i}(\mu u_j)^{\dot{\overline{\tau}}} - \frac{2}{3}\frac{\partial \mathcal{F}}{\partial x_k}(\mu u_k)^{\dot{\overline{\tau}}}\delta_{ij}\right\}\end{aligned} \tag{5.35}$$

$$\sigma_{\rho E} = - \frac{\partial \mathcal{F}}{\partial x_j}\left\{(\rho u_j E)^{\dot{\overline{\tau}}} + (u_j p)^{\dot{\overline{\tau}}} - \left(\kappa \frac{\partial T}{\partial x_j}\right)^{\dot{\overline{\tau}}} - (\tau_{ij} u_i)^{\dot{\overline{\tau}}}\right\} \tag{5.36}$$

$$\sigma_{\overline{\tau}(a,b)} = \frac{\mathcal{F}(1-\mathcal{F})}{\overline{\rho}}(\rho a)^{\dot{\overline{\tau}}}(\rho b)^{\dot{\overline{\tau}}} \tag{5.37}$$

$$\sigma_{\overline{\chi}(a,b)} = \frac{\mathcal{F}(1-\mathcal{F})}{\overline{\rho}}(\rho a)^{\dot{\overline{\tau}}}(b)^{\dot{\overline{\tau}}} \tag{5.38}$$

$$\sigma_{\overline{\zeta}(a,b)} = \frac{\mathcal{F}(1-\mathcal{F})}{\overline{\rho}^2}(\rho a)^{\dot{\overline{\tau}}}(\rho b)^{\dot{\overline{\tau}}} \tag{5.39}$$

Equations (5.34)-(5.39) demonstrate that the hybrid contributions represent physical turbulent scales that are not directly accounted by either RANS or LES. Therefore, if Eqs. (5.22)-(5.27) cannot be reconstructed from the hybrid field, they have to be either modeled or prescribed. Here, it is important to stress that Eqs. (5.34)-(5.39) are just an approximation of the hybrid terms and serve the only purpose to illustrate the physical meaning of the hybrid therms. Therefore, Eqs. (5.34)-(5.39) should not be used to compute or model the hybrid terms, here Eqs. (5.22)-(5.27) have to be used instead. It will be shown that the hybrid contribution plays an important role keeping in equilibrium the transition from RANS to LES, and in compensating the turbulence that RANS does not model and that LES does not yet resolve.

Here, it is important to mention, that current hybrid RANS/LES approaches assumes that the transition from RANS to LES is only obtained through the turbulent model equations. However, some of the existent hybrid RANS/LES models can be obtained by simplifying Eqs. (5.12)-(5.14) and (5.16)-(5.18), for instances:

Speziale VLES model: This approach scales the Reynolds stress tensor to bridge DNS with RANS $\tau_{ij}^s = \alpha \tau_{ij}^R$, here the scaling function $\alpha = [1-\exp(-\beta\Delta/\eta)]^n$ depends on the grid resolution (Δ), the Kolmolgorov length scale (η), and model coefficients β and n [90]. This approach can be recovered if the LES operator in Eqs. (5.16)-(5.15)

is replaced by the identity operator $\overline{\overline{\phi}} = \phi$ and the HT are neglected. Under these conditions Eq. (5.15) simplifies to $\overline{\tau}(u_i, u_j) = \mathcal{F}\dot{\overline{\tau}}(u_i, u_j)$, since the central-moments for the identity operator are zero $\ddot{\overline{\tau}}(a, b) = 0$. Hence, the blending function can be directly related with the scaling factor $\mathcal{F} = \alpha$. Thus, what is left is to provide a closure for α for which different methods have been proposed [5, 18, 33, 58]. The equations indicate, that the model transits from RANS to DNS. However, it is not clear how this approach could formally fit LES in between, as stated originally by Speziale [90].

Zonal RANS/LES approach: In this approach the RANS and LES governing equations are usually solved in different flow domains with a discontinuous model transition [13, 14, 29, 34, 35, 69, 77, 97, 100, 111]. This approach can be recovered from Eqs. (5.16)-(5.15) by neglecting the HT and implementing a discontinuous function in $\mathcal{F}$.

Blended hybrid RANS/LES approaches: In this approach the RANS and LES model equations are usually combined using a blending function [3, 6, 25, 46, 76, 108, 109], inducing a RTLT region. This approach is obtained from Eqs. (5.16)-(5.15) by neglecting the hybrid terms and implementing a continuous blending function $\overline{\tau}(u_i, u_j) = \mathcal{F}\dot{\overline{\tau}}(u_i, u_j) + (1 - \mathcal{F})\ddot{\overline{\tau}}(u_i, u_j)$. In particular, if the same closure equations are used for both RANS and LES central-moments Eqs. (2.24) and (2.43), the hybrid formulation reduces to a blending of turbulence viscosities $\overline{\tau}(u_i, u_j) - \frac{2}{3}\delta_{ij}\overline{\tau}(u_k, u_k) = 2[\mathcal{F}\mu_{rans} + (1 - \mathcal{F})\mu_{sgs}](\widetilde{S}_{ij} - \frac{1}{3}\widetilde{S}_{kk})$, which is one of the most common form of hybrid models. In fact, the Detached Eddy Simulation approach [86, 88] can be presented in this form where $\mu_{DES} = \mathcal{F}\mu_{rans} + (1 - \mathcal{F})\mu_{sgs}$, with the transition from RANS to LES built in the model equation of μ_{DES}.

5.1.3 Time Dependent Hybrid RANS/LES Formulation

Although it will not be pursued any further numerically in this work, it is worth mentioning the case when the hybridization is conducted over time, i.e., $\mathcal{F} = f(t)$, which is relevant for LES simulations that are conducted from an initial steady RANS field.

$$\frac{\partial \overline{\rho}}{\partial t} + \frac{\partial}{\partial x_j}(\overline{\rho}\widetilde{u}_j) = \frac{\partial \mathcal{F}}{\partial t}\left[\dot{\overline{\rho}} - \ddot{\overline{\rho}}\right] = -\frac{\partial \mathcal{F}}{\partial t}(\rho)^{\dot{\mathcal{F}}} \tag{5.40}$$

$$\frac{\partial \overline{\rho}\widetilde{u}_i}{\partial t} + \frac{\partial}{\partial x_j}(\overline{\rho}\widetilde{u}_i\widetilde{u}_j + \overline{p}\delta_{ij} - \widetilde{\tau}_{ij} + \overline{\tau}(u_i, u_j)) = \frac{\partial \mathcal{F}}{\partial t}\left[\dot{\overline{\rho}}\dot{\widetilde{u}}_i - \ddot{\overline{\rho}}\ddot{\widetilde{u}}_i\right] = -\frac{\partial \mathcal{F}}{\partial t}(\rho u_i)^{\dot{\mathcal{F}}} \tag{5.41}$$

$$\begin{aligned}\frac{\partial \overline{\rho}\widetilde{E}}{\partial t} + \frac{\partial}{\partial x_j}\Bigg(&\overline{\rho}\widetilde{E}\widetilde{u}_j + \overline{p}\widetilde{u}_j - \overline{\kappa}\frac{\partial \widetilde{T}}{\partial x_j} - \widetilde{\tau}_{ij}\widetilde{u}_i + \overline{\tau}(E, u_j) \\ &+ \overline{\chi}(u_j, p) - \overline{\chi}\Big(\frac{\partial T}{\partial x_j}, \kappa\Big) - \overline{\zeta}(\tau_{ij}, u_i)\Bigg) = \frac{\partial \mathcal{F}}{\partial t}\left[\dot{\overline{\rho}}\dot{\widetilde{E}} - \ddot{\overline{\rho}}\ddot{\widetilde{E}}\right] = -\frac{\partial \mathcal{F}}{\partial t}(\rho E)^{\dot{\mathcal{F}}}\end{aligned} \tag{5.42}$$

Equations (5.40)-(5.42) indicate that the transition from a steady RANS to an unsteady LES simulation is promoted by unsteady sources that help to trigger instabilities in the flow that will develop into resolved turbulence. Here, it is only speculated that the inclusion of these terms would help to reduce the time it takes for a steady field (used for initialization or used for forced studies) to develop realistic unsteady turbulence.

Note that for time dependent blending functions, Eq. (5.9) will not be valid if the RANS operator represents a time-averaged operator, since in this case the blending function will not commute with the time-averaging operator $\overline{\dot{\mathcal{F}}\phi} \neq \mathcal{F}\dot{\overline{\phi}}$. Nevertheless, even in this case, Eqs. (5.40)-(5.42) are still valid.

5.1.4 Incompressible Hybrid Navier-Stokes Equations

Although the incompressible hybrid RANS/LES Navier-Stokes equations for an additive hybrid operator were first presented by Germano [31], these equations are repeated and expanded here to highlight the hybrid contributions, and to establish

our new notation. The incompressible formulation is derived from the compressible hybrid approach (described in section 5.1) by assuming incompressibility and by eliminating the energy and the state equations.

$$\frac{\partial \overline{u}_j}{\partial x_j} = \frac{\partial \mathcal{F}}{\partial x_j}\big[\dot{\overline{u}}_j - \ddot{\overline{u}}_j\big] \tag{5.43}$$

$$\begin{aligned}\frac{\partial \overline{u}_i}{\partial t} + \overline{u}_j\frac{\partial \overline{u}_i}{\partial x_j} + \frac{\partial}{\partial x_j}(\overline{p}/\rho\delta_{ij} - \overline{\tau}_{ij}/\rho + \overline{\tau}(u_i,u_j)/\rho) = \\ \frac{\partial \mathcal{F}}{\partial x_j}\Big[\dot{\overline{u}}_i\dot{\overline{u}}_j - \ddot{\overline{u}}_i\ddot{\overline{u}}_j + \dot{\overline{\tau}}(u_i,u_j)/\rho - \ddot{\overline{\tau}}(u_i,u_j)/\rho \\ + (\dot{\overline{p}} - \ddot{\overline{p}})/\rho\delta_{ij} - (\dot{\overline{\tau}}_{ij} - \ddot{\overline{\tau}}_{ij})/\rho\Big] \\ - \nu\frac{\partial}{\partial x_j}\left\{\frac{\partial \mathcal{F}}{\partial x_j}(\dot{\overline{u}}_i - \ddot{\overline{u}}_i) + \frac{\partial \mathcal{F}}{\partial x_i}(\dot{\overline{u}}_j - \ddot{\overline{u}}_j)\right\} \\ + \frac{\partial \mathcal{F}}{\partial t}\big[\dot{\overline{u}}_i - \ddot{\overline{u}}_i\big]\end{aligned} \tag{5.44}$$

$$\overline{\tau}_{ij} = \mu\Big(\frac{\partial \overline{u}_i}{\partial x_j} + \frac{\partial \overline{u}_j}{\partial x_i}\Big), \quad \dot{\overline{\tau}}_{ij} = \mu\Big(\frac{\partial \dot{\overline{u}}_i}{\partial x_j} + \frac{\partial \dot{\overline{u}}_j}{\partial x_i}\Big), \quad \ddot{\overline{\tau}}_{ij} = \mu\Big(\frac{\partial \ddot{\overline{u}}_i}{\partial x_j} + \frac{\partial \ddot{\overline{u}}_j}{\partial x_i}\Big). \tag{5.45}$$

$$\dot{\overline{\tau}}(a,b) = \rho(\dot{\overline{ab}} - \dot{\overline{a}}\dot{\overline{b}}) \tag{5.46}$$

$$\ddot{\overline{\tau}}(a,b) = \rho(\ddot{\overline{ab}} - \ddot{\overline{a}}\ddot{\overline{b}}) \tag{5.47}$$

$$\overline{\tau}(a,b) = \rho(\overline{ab} - \overline{a}\overline{b}) \tag{5.48}$$

Equations (5.43), (5.44), and (5.48) represent the incompressible hybrid Navier-Stokes equations and the hybrid second order central-moment. The explicit expression for the hybrid central-moment is obtained by substituting Eq. (5.1) in Eq. (5.48)

$$\overline{\tau}(a,b) = \mathcal{F}\dot{\overline{\tau}}(a,b) + (1-\mathcal{F})\ddot{\overline{\tau}}(a,b) + \rho\mathcal{F}(1-\mathcal{F})(\dot{\overline{a}} - \ddot{\overline{a}})(\dot{\overline{b}} - \ddot{\overline{b}}) \tag{5.49}$$

and by operating Eq. (5.49) in u_i and u_j, the hybrid Reynolds stress tensor is directly obtained as

$$\begin{aligned}\overline{\tau}(u_i,u_j) = \rho\big[\mathcal{F}(\dot{\overline{u_iu_j}} - \dot{\overline{u}}_i\dot{\overline{u}}_j) + (1-\mathcal{F})(\ddot{\overline{u_iu_j}} - \ddot{\overline{u}}_i\ddot{\overline{u}}_j) \\ + \mathcal{F}(1-\mathcal{F})(\dot{\overline{u}}_i - \ddot{\overline{u}}_i)(\dot{\overline{u}}_j - \ddot{\overline{u}}_j)\big].\end{aligned} \tag{5.50}$$

The momentum equation derived here is slightly different from Germano's original derivation since the definition for the viscous stress tensor (5.45) is maintained, while Germano applied continuity to simplify the momentum equation. Nevertheless, it can be shown that both equations are consistent.

Finally, by substituting Eqs. (5.46) and (5.47) in Eq. (5.44), and the differences beten RANS and LES variables with the turbulence fluctuations ($\phi^{\dot{\prime}} = \phi - \dot{\overline{\phi}} = \mathcal{C}(\ddot{\overline{\phi}} - \dot{\overline{\phi}})$, with $\mathcal{C} = 1$) it can be shown that the hybrid contributions take the following form:

$$\sigma_\rho = -\frac{\partial \mathcal{F}}{\partial x_j} u_j^{\dot{\prime}} \tag{5.51}$$

$$\begin{aligned} \sigma_{\rho u_i} = &- \frac{\partial \mathcal{F}}{\partial x_j}\Big[(u_i u_j)^{\dot{\prime}} + p^{\dot{\prime}}/\rho\delta_{ij} - \tau_{ij}{}^{\dot{\prime}}/\rho\Big] \\ &+ \nu \frac{\partial}{\partial x_j}\left\{\frac{\partial \mathcal{F}}{\partial x_j} u_i^{\dot{\prime}} + \frac{\partial \mathcal{F}}{\partial x_i} u_j^{\dot{\prime}}\right\} - \frac{\partial \mathcal{F}}{\partial t} u_i^{\dot{\prime}} \end{aligned} \tag{5.52}$$

$$\sigma_{\overline{\tau}(u_i,u_j)} = \rho\mathcal{F}(1-\mathcal{F}) u_i^{\dot{\prime}} u_j^{\dot{\prime}} \tag{5.53}$$

Similar to the compressible formulation, the incompressible hybrid contributions represent turbulence scales and need to be included.

5.1.5 Hybrid RANS/LES Turbulence Model

In order to solve the governing equations, the generic hybrid central-moments have to be defined using RANS and LES equations. For RANS, the closure model implemented at present uses a standard eddy viscosity and a gradient diffusion assumption.

$$\dot{\overline{\tau}}(u_k, u_k) = 2\overline{\rho}k \tag{5.54}$$

$$\dot{\overline{\tau}}(u_i, u_j) = -2\overline{\rho}\nu_t(\widetilde{S}_{ij} - \frac{1}{3}\widetilde{S}_{kk}\delta_{ij}) + \frac{2}{3}\overline{\rho}k\delta_{ij} \tag{5.55}$$

$$\begin{aligned} \dot{\overline{\chi}}\Big(\frac{\partial T}{\partial x_j}, \kappa\Big) + \dot{\overline{\zeta}}(\tau_{ij}, u_i) - \dot{\overline{\tau}}(E, u_j) - \dot{\overline{\chi}}(u_j, p) = &\frac{\overline{\rho} C_p \nu_t}{\mathrm{Pr}_T} \frac{\partial \widetilde{T}}{\partial x_j} \\ &+ \overline{\rho}(\overline{\nu} + \nu_t\sigma^*)\frac{\partial k}{\partial x_j} - \dot{\overline{\tau}}(u_i, u_j)\widetilde{u}_i. \end{aligned} \tag{5.56}$$

(5.57)

Here, k is the turbulent kinetic energy (TKE), ν is the kinematic viscosity, ν_t is the turbulent eddy viscosity, C_p is the heat capacity at constant pressure, and σ^* and Pr_T are constants set to 1/2 and 1, respectively [105]. Similarly, the same assumptions are used to construct the LES closures defined as

$$\ddot{\overline{\tau}}(u_k, u_k) = 2\overline{\rho}k^{ksgs} \tag{5.58}$$

$$\ddot{\overline{\tau}}(u_i, u_j) = -2\overline{\rho}\nu_{sgs}(\widetilde{S}_{ij} - \frac{1}{3}\widetilde{S}_{kk}\delta_{ij}) + \frac{2}{3}\overline{\rho}k^{sgs}\delta_{ij} \tag{5.59}$$

$$\ddot{\overline{\chi}}\Big(\frac{\partial T}{\partial x_j}, \kappa\Big) + \ddot{\overline{\zeta}}(\tau_{ij}, u_i) - \ddot{\overline{\tau}}(E, u_j) - \ddot{\overline{\chi}}(u_j, p) = \frac{\overline{\rho}C_p\nu_{sgs}}{\mathrm{Pr}_t}\frac{\partial \widetilde{T}}{\partial x_j} + \overline{\rho}\frac{\nu_{sgs}}{Pr_t}\frac{\partial \widetilde{E}}{\partial x_j} \tag{5.60}$$

$$+ \frac{\nu_{sgs}}{Pr_t}\frac{\partial \widetilde{p}}{\partial x_j} - \ddot{\overline{\tau}}(u_i, u_j)\widetilde{u}_i. \tag{5.61}$$

Here, k^{sgs} is the subgrid kinetic energy, ν_{sgs} is the subgrid eddy viscosity, and Pr_t is a coefficient assumed unity [62]. Finally, model equations for ν_t, k, ν_{sgs}, and k^{sgs} have to be defined to close the system of equations.

In this work, RANS and LES turbulence models are coupled in the hybrid formulation by blending equivalent RANS and LES models. Here, the two-equation RANS-SST model [63] and the one-equation localized dynamic k^{sgs} (LDKM) LES model [62] were selected to compute ν_t, k, ν_{sgs}, and k^{sgs}, since both methods have transport equations for the kinetic energy of the turbulence (k for RANS and k^{sgs} for LES), which are used to design the hybrid model equation. The RANS-SST model is selected due to its well-documented success predicting complex flows [41,63,105,106].

An equation for the hybrid turbulent kinetic energy ($\mathcal{K} = \mathcal{F}k + (1-\mathcal{F})k^{sgs}$) can be derived formally by merging RANS and LES transport equations following the same procedure used to derive the hybrid Navier-Stokes equations. However, this approach would yield an equation with extra terms that cannot be readily computed, and unlike the hybrid Navier-Stokes equations, it is not possible to demonstrate any physical significance for all the additional terms derived in the hybrid *model* equation. The formal combination of two model equations does not guarantee that the physics

of the flow is modeled any better. Here, a model equation that identically recovers the RANS k and LES k^{sgs} equations is proposed in such a way that its structure resembles Eqs. (5.16)-(5.18) without the hybrid contributions. This model equation is:

$$\frac{\partial \overline{\rho}\mathcal{K}}{\partial t} + \frac{\partial}{\partial x_j}\Big(\overline{\rho}\widetilde{u}_j\mathcal{K} - KT_j\Big) = KS \tag{5.62}$$

where

$$KT_j = \mathcal{F}\bigg(\overline{\rho}(\overline{\nu} + \sigma_k\nu_t)\frac{\partial \mathcal{K}}{\partial x_j}\bigg) + (1-\mathcal{F})\bigg(\overline{\rho}(\frac{\overline{\nu}}{Pr} + \nu_{sgs})\frac{\partial \mathcal{K}}{\partial x_j}\bigg) \tag{5.63a}$$

$$KS = \mathcal{F}\bigg(-\dot{\overline{\tau}}(u_i,u_j)\frac{\partial \widetilde{u}_i}{\partial x_j} - \beta^*\overline{\rho}\mathcal{K}\omega\bigg) + (1-\mathcal{F})\bigg(-\ddot{\overline{\tau}}(u_i,u_j)\frac{\partial \widetilde{u}_i}{\partial x_j} - C_\varepsilon\overline{\rho}\frac{\mathcal{K}}{\Delta}^{3/2}\bigg). \tag{5.63b}$$

Equation (5.62) is the model equation for the hybrid turbulent kinetic energy ($\mathcal{K}$). The model equation is constructed by directly blending the source and the transport terms of the RANS-SST "k" and the LES "k^{sgs}" equations. An additional modification is required in Eqs. (5.55) and (5.59) to eliminate their explicit dependence on k and k^{sgs}. Both turbulence variables are substituted by $\mathcal{K}$ so that.

$$\dot{\overline{\tau}}(u_i,u_j) = -2\overline{\rho}\nu_t(\widetilde{S}_{ij} - \frac{1}{3}\widetilde{S}_{kk}\delta_{ij}) + \frac{2}{3}\overline{\rho}\mathcal{K}\delta_{ij} \tag{5.64}$$

$$\ddot{\overline{\tau}}(u_i,u_j) = -2\overline{\rho}\nu_{sgs}(\widetilde{S}_{ij} - \frac{1}{3}\widetilde{S}_{kk}\delta_{ij}) + \frac{2}{3}\overline{\rho}\mathcal{K}\delta_{ij} \tag{5.65}$$

This additional modification does not alter the original RANS-SST and LES-LDKM equations, which are identically recovered when $\mathcal{F}=1$ and $\mathcal{F}=0$, respectively. The RANS-SST model requires an additional equation for the specific energy dissipation rate "ω" defined by

$$\begin{aligned}\frac{\partial}{\partial t}(\overline{\rho}\omega) + \frac{\partial}{\partial x_j}(\overline{\rho}\widetilde{u}_j\omega) = -\frac{\gamma}{\nu_t}\dot{\overline{\tau}}(u_i,u_j)\frac{\partial \widetilde{u}_i}{\partial x_j} - \beta\overline{\rho}\omega^2 + \frac{\partial}{\partial x_j}\Big[\overline{\rho}(\overline{\nu}+\sigma_\omega\nu_t)\frac{\partial\omega}{\partial x_j}\Big] \\ + 2(1-F_1)\overline{\rho}\sigma_{\omega 2}\frac{1}{\omega}\frac{\partial \mathcal{K}}{\partial x_j}\frac{\partial\omega}{\partial x_j}\end{aligned} \tag{5.66}$$

$$F_1 = \tanh(\chi^4), \quad \chi = \min\left(\max\left(\frac{\sqrt{\mathcal{K}}}{0.09\omega y}; \frac{500\overline{\nu}}{y^2\omega}\right); \frac{4\overline{\rho}\sigma_{\omega 2}\mathcal{K}}{CDy^2}\right) \tag{5.67a}$$

$$CD = \max\left(2\overline{\rho}\sigma_{\omega 2}\frac{1}{\omega}\frac{\partial \mathcal{K}}{\partial x_j}\frac{\partial \omega}{\partial x_j}; 10^{-20}\right) \tag{5.67b}$$

here Ω, F_1, and y are the vorticity magnitude, a blending function, and the wall-normal distance, respectively. Here, it is stressed that the equation for ω is not explicitly hybridized since there is no equivalent equation in the LES model implemented here. The constants for the RANS-SST model, here represented as ψ, are computed from two set of constants ψ_1 and ψ_2 as $\psi = F_1\psi_1 + (1 - F_1)\psi_2$. Here, the values of these two sets were previously defined. Finally, the RANS and the LES eddy viscosities are defined by

$$\nu_t = \frac{a_1\mathcal{K}}{\max(a_1\omega; \Omega F_2)} \tag{5.68}$$

and

$$\nu_{sgs} = C_\nu \Delta\sqrt{\mathcal{K}} \tag{5.69}$$

where

$$F_2 = \tanh(\eta^2), \quad \eta = \max\left(2\frac{\sqrt{\mathcal{K}}}{0.09\omega y}; \frac{500\overline{\nu}}{y^2\omega}\right). \tag{5.70}$$

This hybrid RANS/LES turbulent model has been successfully applied to simulate complex unsteady flow separation [60, 76].

5.2 Validation of The Hybrid RANS/LES Formulation

In order to evaluate the importance of the hybrid terms, Eqs. (5.22)-(5.27), LES and hybrid RANS/LES simulations are conducted for the turbulent attached flow over a flat-plate at $Re_\theta = 1400$ and $Re_\theta = 3330$, based on the boundary layer momentum thickness (θ) and free stream velocity (U_∞). The experimental data from DeGraaff and Eaton [17] and Aubertine and Eaton [2] are used to compare with the calculations.

The main objective here is to demonstrate the importance of the hybrid terms. Therefore, when needed, these terms are a priori computed from the LES simulation. Here it is important to stress, that even if in theory the LES field could be computed with Eq. (5.10) and from it the hybrid terms, it is very likely that Eq. (5.10) could become ill-conditioned, and thus, numerically intractable [31]. Even if Eq. (5.10) converges in all the domain, the LES field could not be correctly recovered since the grid resolution expected to be used in engineering applications would be too coarse to allow the LES reconstruction. Therefore, for practical applications, the only way to include Eqs. (5.22)-(5.27) is through modeling.

Accurate LES simulations require high order discretization in both time and space. Therefore, the governing equations and the turbulence models are solved with a parallel code consisting of a fully coupled explicit compressible finite volume formulation, where time integration is conducted using a five stage Runge-Kutta scheme [44] and space discretization uses a fourth-order scheme in divergence form [24]. Additionally, to prevent spurious numerical oscillations, an explicit tenth-order low-pass filter is applied periodically to the flow variables based on an approach demonstrated earlier [28].

Boundary conditions are applied explicitly for the flow and the turbulence variables. At the wall, no-slip and adiabatic conditions are imposed. At the free stream boundary, the variables are computed from the one-dimensional Riemann invariants [38]. In the spanwise direction, periodic boundary conditions are implemented, and at the outflow, a zero gradient condition is enforced. For the LES simulation, realistic turbulence is provided at the inflow boundary by using the rescaling method of Lund et al. [59]. For the hybrid RANS/LES simulations, the turbulent inflow is obtained from a LES simulation that is conducted simultaneously. Here, no significant difference is observed when the rescaling approach of Lund was implemented in the hybrid field.

Table 5.1: Summary of grids implemented

Grid name	Re_θ	Number of grid points $n_x \times n_y \times n_z$	Grid resolution Δx^+	Δy^+	Δz^+
Fine	1400	$201 \times 91 \times 121$	30	$0.5 - 63$	10
Medium	1400	$201 \times 45 \times 121$	30	$0.5 - 147$	10
Coarse	1400	$201 \times 45 \times 65$	30	$0.5 - 147$	20
Coarsest	1400	$151 \times 25 \times 65$	40	$0.5 - 300$	20
Fine	3300	$361 \times 91 \times 221$	36	$0.5 - 190$	12
Coarse	3300	$201 \times 91 \times 121$	66	$0.5 - 190$	22

Based on previous LES [59] and DNS [26] studies, four grids, summarized on Table 5.1, extending over a domain of $L_x = 10\delta$ (streamwise), $L_y^{Re_\theta=1400} = 3\delta$ and $L_y^{Re_\theta=3330} = 3.5\delta$ (wall-normal), and $L_z = 2\delta$ (spanwise) are evaluated. Here, δ is the boundary layer thickness. For all the grids, the grid-points are distributed uniformly in the streamwise and in the spanwise directions, while in the wall-normal direction, a hyperbolic tangent stretching is implemented [99]. The benchmark LES simulation is conducted using the fine grid only to capture the near-wall structures [69], while the hybrid RANS/LES simulations are conducted with the four grids.

5.2.1 Hybrid RANS/LES Blending Functions

The LES and hybrid RANS/LES simulations are conducted by solving the hybrid governing equations (5.16)-(5.21), the generic central-moments Eqs. (5.12)-(5.14), and the turbulent hybrid model with a hybrid blending function $\mathcal{F}$. For LES, $\mathcal{F} \equiv 0$. However, for the hybrid formulation, a general specification of the blending function for different flows remains an open issue. Fortunately, for the turbulent boundary layer, it is possible to implement simple blending functions that depend only on the wall-normal distance (thus, principally one-dimensional). Therefore, the sensibility of the model to the blending function can be evaluated without complicating the problem any further. Here, it is important to evaluate the effect of the functional form and the location of the RTLT zone. Therefore, the blending functions here

analyzed are designed to address the effect of continuos over discontinuous functions and how the location of the RTLT zone affects the formulation. For the last point, it is important to address how the production of turbulence is affected by the hybrid region depending on whether the RTLT zone is in the inner or outer layers.

Five blending functions, summarized in Table 5.2, are evaluated. The first and second blending functions are constructed using a smooth function to transit from RANS to LES [46].

$$F(y) = \frac{1}{2}\Big[1 - \tanh\Big(\frac{C_1(y/d - C_2)}{(1-2C_2)y/d + C_2}\Big)/\tanh(C_1)\Big] \tag{5.71}$$

here, C_1 and C_2 are constants, selected to be 2 and 0.2, respectively. Also, the distance d represents the location at which the blending function is zero, $F(d) = 0$. The first blending function implements Eq. (5.71) over one-quarter of the wall-normal length $d = L_y/4$, so that the boundary layer buffer-layer is within the RTLT zone (this zone is more precisely defined here as the range where $0.9 < \mathcal{F} < 0.1$).

$$\mathcal{F}1(y) = \begin{cases} F(y) & \text{for } y \le d = L_y/4 \\ 0 & \text{for } y > d \end{cases} \tag{5.72}$$

The second blending function is designed to use Eq. (5.71) throughout the domain $d = L_y$, to set the outer layer within the RTLT zone, so that

$$\mathcal{F}2(y) = F(y), \quad d = L_y. \tag{5.73}$$

The third blending function consists of a linear function with limits $L_1 = L_y/100$ and $L_2 = L_y/3$ which bounds a RANS zone between $0 \le y^+ < 20$, the RTLT region between $20 \le y^+ \le 580$ and the LES zone beyond $y^+ > 580$.

$$\mathcal{F}3(y) = \begin{cases} 1 & \text{for } y \le L_1 \\ 1 - (y - L_1)/(L_2 - L_1) & \text{for } L_1 \le y \le L_2 \\ 0 & \text{for } y > L_2 \end{cases} \tag{5.74}$$

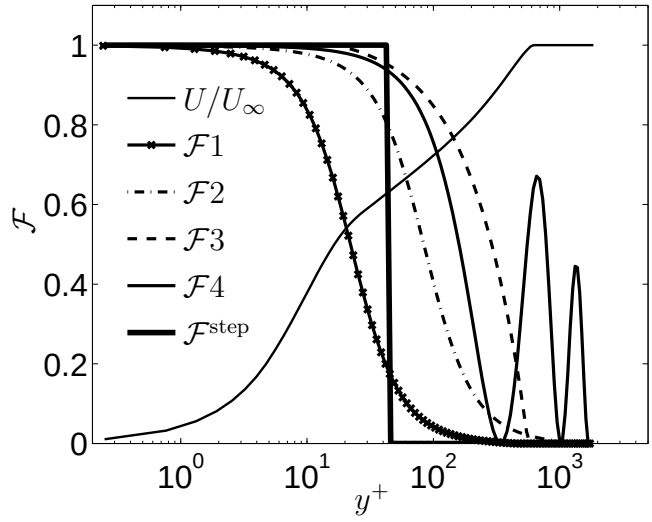

Figure 5.1: Law-of-the-wall profile and hybrid RANS/LES blending functions.

The fourth blending function consists of an exponentially decaying cosine function. This function completes 2.5 cycles throughout the domain inducing 5 RTLT zones, the objective is to evaluate the effect of non-monotonic function which induces multiples RTLT regions in the domain.

$$\mathcal{F}4(y) = e^{-y/L_y}[\cos(5\pi y/L_y) + 1]/2. \tag{5.75}$$

Finally, the fifth blending function consists of a step function, which leads to the classic zonal RANS/LES approach [13, 14, 34, 35, 69, 97, 100, 111]. Here, the interface between RANS and LES is specified at $y^+ = 45$, in order to model the inner layer with RANS, while the outer layer is resolved with LES. This is consistent with past studies [13, 14, 34, 35], the function is defined as:

$$\mathcal{F}^{\text{step}}(y^+) = \begin{cases} 1 & \text{if } y^+ < 45 \\ 0 & \text{if } y^+ \geq 45 \end{cases} \tag{5.76}$$

The five blending functions and the law-of-the-wall, are shown in Figure 5.1 normalized by wall-units, $U^+ = U/u_\tau$, $y^+ = yu_\tau/\nu$, where $u_\tau = \sqrt{\tau_w/\rho}$ is the friction velocity. This figure illustrates how the different transition functions blend RANS and LES formulations, and more importantly, Figure 5.1 shows the location of RTLT zone

Table 5.2: Summary of hybrid RANS/LES blending functions

Formulation	Blending function $\mathcal{F}$	RTLT zone $0.1 < \mathcal{F} < 0.9$	Equation
RANS	1	Does not apply	-
LES	0	Does not apply	-
Hybrid RANS/LES	$\mathcal{F}1$	$8 < y^+ < 40$	(5.72)
Hybrid RANS/LES	$\mathcal{F}2$	$30 < y^+ < 240$	(5.73)
Hybrid RANS/LES	$\mathcal{F}3$	$20 < y^+ < 580$	(5.74)
Hybrid RANS/LES	$\mathcal{F}4$	$50 < y^+ < 1100$	(5.75)
Zonal RANS/LES	$\mathcal{F}^{step}$	Discontinuous	(5.76)

superimposed in the law-of-the-wall velocity profile. For $\mathcal{F} \equiv \mathcal{F}1$, the RTLT zone is designed to cover most of the inner layer $8 < y^+ < 40$ to allow LES to resolve part of the energy produced in the buffer layer. For $\mathcal{F} \equiv \mathcal{F}2$, the RTLT zone is located in the outer layer $30 < y^+ < 240$ to guarantee that most of the inner layer is modeled with RANS with a well defined RTLT zone. For $\mathcal{F} \equiv \mathcal{F}3$, the RANS region is extended up to $y^+ \sim 20$ to warrant that most of the near-wall turbulence is modeled with RANS, additionally, the RTLT is designed to cover the outer layer $20 \leq y^+ \leq 580$ to ensure that most of the boundary layer is simulated with the model in the hybrid mode i.e., $0 < \mathcal{F} < 1$. For $\mathcal{F} \equiv \mathcal{F}4$, the RTLT zone extends from $y^+ = 55$ up to the free stream boundary, in addition, this function reach LES ($\mathcal{F} = 0$) at three locations $y^+ \sim 330$, $y^+ \sim 1000$, and $y^+ \sim 1700$. Finally, for $\mathcal{F} \equiv \mathcal{F}^{\text{step}}$, the RANS to LES transition point is located at the end of the inner layer to guarantee that RANS can completely model this region, this function does not have a RTLT zone.

5.2.2 Results and Discussion

The initial conditions chosen for $Re_\theta = 1430$ consist of random noise superimposed on the law-of-the-wall profile. This artificial flow field is evolved using periodic boundary conditions in the streamwise direction to promote transition to turbulence. Once realistic turbulence develops, the flow field is rescaled and then used to initialize the

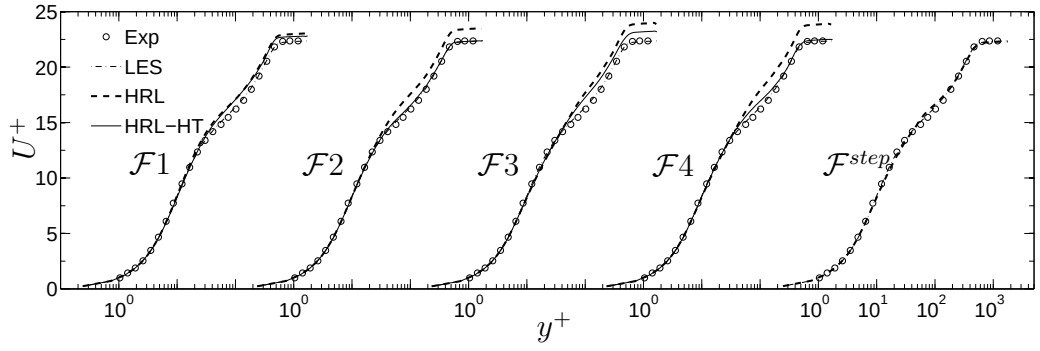

(a)

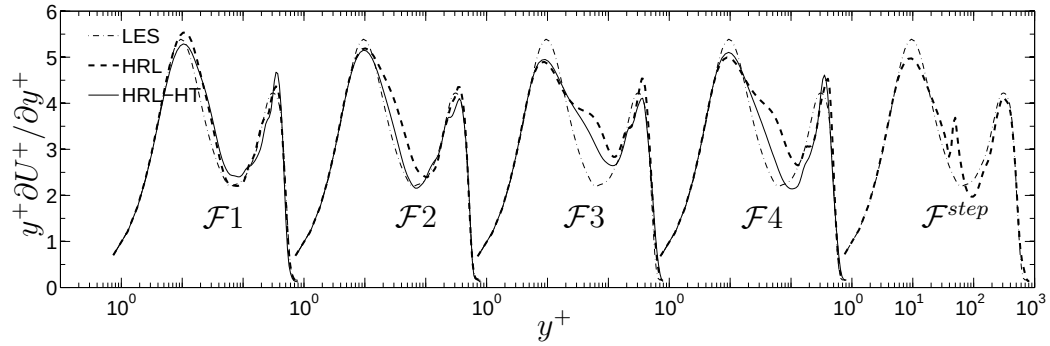

(b)

Figure 5.2: Wall-normal distribution of mean streamwise-velocity profile and $y^+\partial U^+/\partial y^+$ for LES, HRL, HRL-HT, and Zonal RANS/LES ($\mathcal{F}^{step}$) fine grid simulations: (a) U^+; (b) $y^+\partial U^+/\partial y^+$.

LES and hybrid simulations. It is at this point that the rescaling approach of Lund et al. [59] is used to provide turbulent inflow conditions. All the simulations are run initially for a non-dimensional period of $t_{\text{trans}}u_\tau^2/\nu_{\text{wall}} \sim 1000$ to eliminate the transient conditions [59]. Here, ν_{wall} is the kinematic viscosity evaluated at the wall. After the flow reach a stationary state, flow statistics are collected for a non-dimensional period of $t_{\text{aver}}u_\tau^2/\nu_{\text{wall}} \sim 1800$ [59].

All simulations conducted with the fine grid are summarized in Table 5.3. The main differences among hybrid RANS/LES simulations are in the blending functions implemented, and whether or not the hybrid contributions are included (hereafter, denoted HRL when the hybrid terms are not considered and HRL-HT when the hybrid terms are included). These terms are computed from the available LES and

Table 5.3: Simulation description and predicted friction coefficient for turbulent boundary layer $R_\theta = 1430$, fine grid

Simulation	Blending function $\mathcal{F}$	$C_f \times 10^3$	Deviation from LES (%)
Experiments	-	3.96[†]	-
1 LES	0	4.00	-
2 Zonal RANS/LES	$\mathcal{F}^{step}$	3.92	-2.0
3 HRL	$\mathcal{F}1$	3.81	-4.8
4 HRL	$\mathcal{F}2$	3.44	-14.0
5 HRL	$\mathcal{F}3$	3.46	-13.5
6 HRL	$\mathcal{F}4$	3.50	-12.5
7 HRL-HT	$\mathcal{F}1$	3.77	-5.8
8 HRL-HT	$\mathcal{F}2$	3.88	-3.0
9 HRL-HT	$\mathcal{F}3$	3.73	-6.8
10 HRL-HT	$\mathcal{F}4$	3.94	-1.5

[†] Obtained by best fitting the law of the wall to the experimental data.

its time-averaged fields using Eqs. (5.22)-(5.27). For the coarse grids, the hybrid terms are still computed from the LES simulation conducted in the fine grid and then interpolated into the coarse grids.

The mean streamwise velocity profiles (normalized with wall-units) and its wall normal gradient are presented in Figure 5.2. Here, the LES prediction is found in excellent agreement with experiments as expected. It is interesting to note that Figure 2(a) apparently indicates that for the fine grid, the zonal RANS/LES approach (simulation 2 with $\mathcal{F} \equiv \mathcal{F}^{step}$) predicts accurately the mean velocity profile. This high accuracy of the zonal RANS/LES simulation is explained first by the high resolution used in the fine grid, and second, by the fact that RANS, which is calibrated to predict correctly this kind of flows, completely models the inner layer, whereas LES is able to resolve the turbulence located in the outer-layer region. However, if the velocity normal gradient is analyzed, Figure 2(b), it is evident that the zonal RANS/LES approach predicts an unphysical flow field, which is indicated by the spike located at the models interface ($y^+ = 45$). Here, the anomalous region is bounded within

a small region, in the order of 10 wall-units, neighboring the models interface, set at $y^+ = 45$ for this study. However, as will be shown later, if the grid resolution is reduced, the error region will be significantly magnified [13, 14, 34, 35, 70]. This is a well-documented anomaly observed in all zonal RANS/LES approaches [34, 70], and it is due to the abrupt switch from RANS to LES. This abrupt switch induces a transition from RANS to LES out of equilibrium, such that the turbulence is neither completely modeled by RANS nor completely resolved by LES [70].

For HRL-HT simulations, Figure 5.2 demonstrates that the predicted mean velocity profiles are again in excellent agreement with experiments and the LES simulation. Here, only the line function, simulation 9, presents slight deviations compared with the other functions. However, here it is recalled that $\mathcal{F}3$ sets RANS modeling at the inner layer and extends the RTLT zone throughout the boundary layer completing the transition to LES at the free stream region. Consequently, $\mathcal{F}3$ is the most stringent function here implemented since for most of the boundary layer, the turbulence model is acting in the hybrid mode $0 < \mathcal{F} < 1$. Nevertheless, it can be concluded from these results, that as long as the hybrid terms are included, the predicted velocity profiles are not very sensitive to the blending function implemented, even when non-monotonic functions with multiples RTLT zones are considered. This implies that during RTLT zone, the turbulence that is not modeled by RANS and is not yet resolved by LES, is explicitly accounted for by Eqs. (5.22)-(5.27). Therefore, the mean transfer of turbulence throughout the boundary layer is correctly reproduced, and the transition from RANS to LES in the mean velocity profile occurs nearly independent of the blending function implemented.

Figure 5.2 also demonstrates that by not including the hybrid contributions (simulations 3 to 6), the predicted velocity profile becomes very sensitive to the blending function implemented. This is explained by the fact that the amount of modeled and resolved turbulence provided by the hybrid model depends primarily on the blending

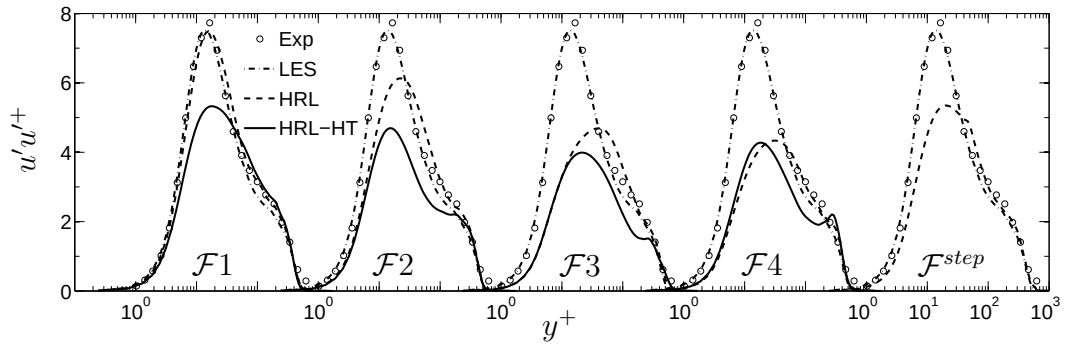

(a)

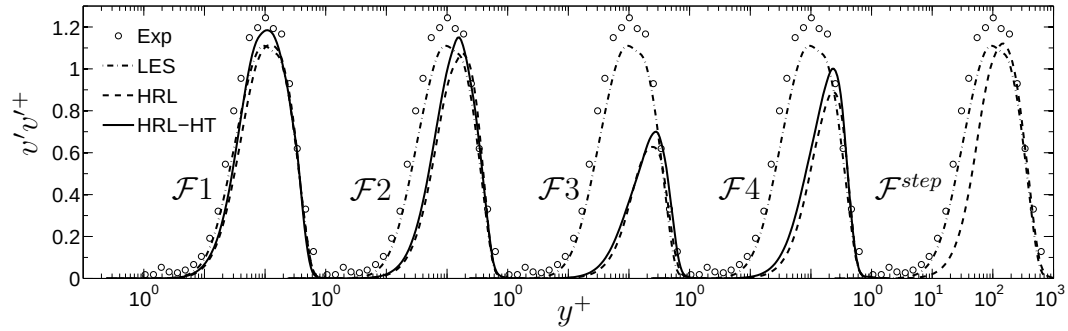

(b)

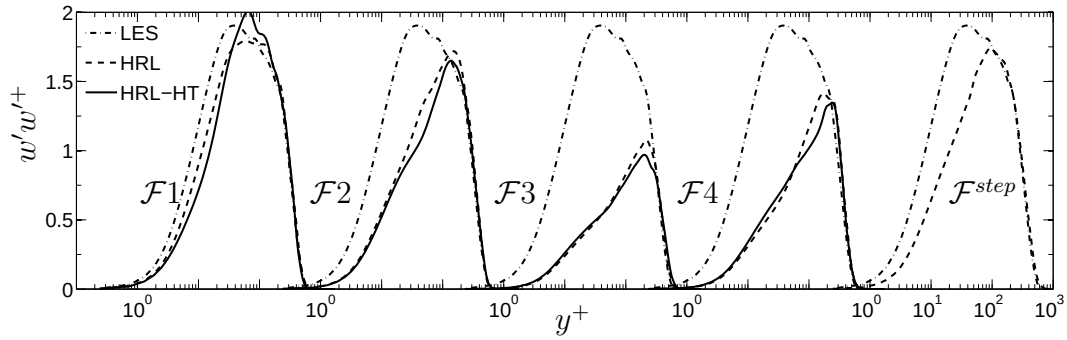

(c)

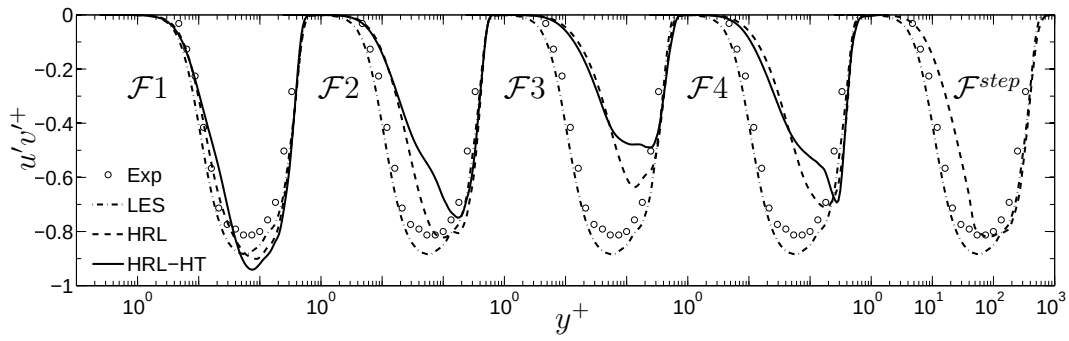

(d)

Figure 5.3: Wall-normal distribution of resolved Reynolds stresses for LES, HRL, HRL-HT, and Zonal RANS/LES ($\mathcal{F}^{step}$) fine grid simulations: (a) $u'u'^+$; (b) $v'v'^+$; (c) $w'w'^+$; (d) $u'v'^+$.

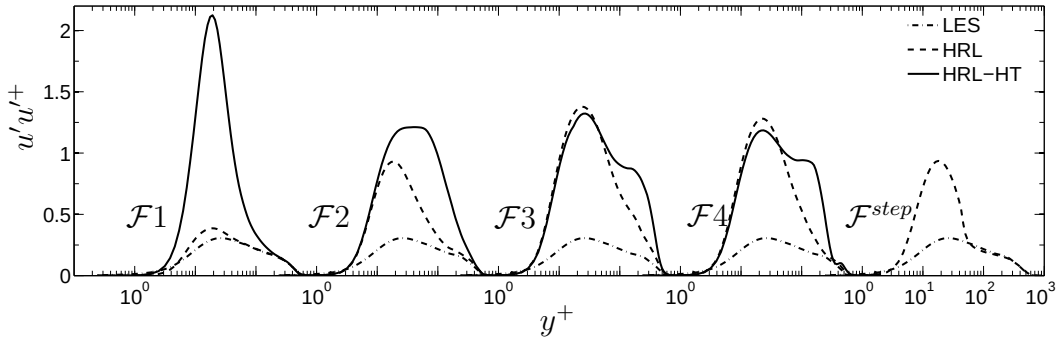

(a)

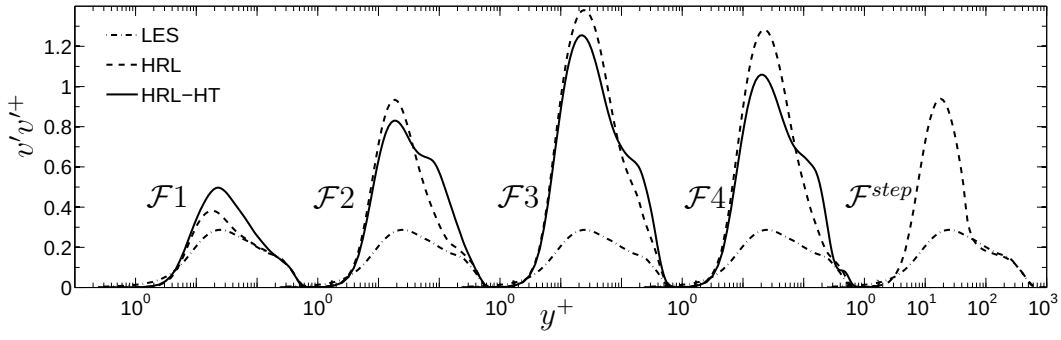

(b)

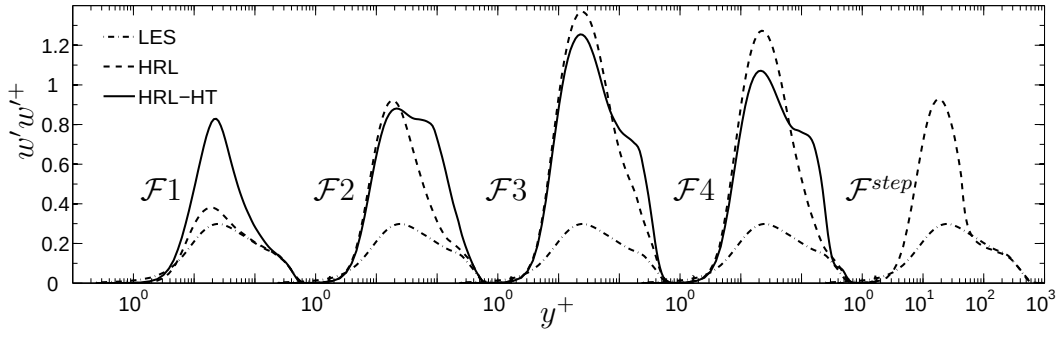

(c)

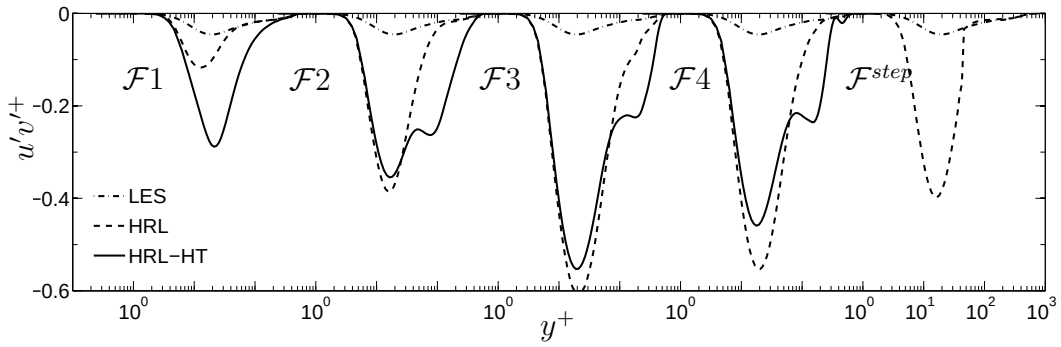

(d)

Figure 5.4: Wall-normal distribution of modeled Reynolds stresses for LES, HRL, HRL-HT, and Zonal RANS/LES ($\mathcal{F}^{step}$) fine grid simulations: (a) $u'u'^+$; (b) $v'v'^+$; (c) $w'w'^+$; (d) $u'v'^+$.

function. Simulation 3 uses a blending function that sets the RTLT in the inner layer. Therefore, the turbulence not accounted by the hybrid contributions is partially resolved by the LES part of the hybrid model, yielding results in close agreement to LES and simulation 7. On the other hand, simulations 4 to 6 implement blending functions that set the RTLT deeper in the outer layer, precluding the LES part of the hybrid model to resolve a significant amount of the turbulence that Eqs. (5.22)-(5.27) represent, resulting in the underprediction of the velocity profiles in Figure 2(a).

Table 5.3 shows the friction coefficient (C_f) predicted with the five blending functions using the fine grid. In particular, the friction coefficient computed with LES is found in excellent agreement with the experimental data, previous LES simulations have reported similar accuracy in their calculations [59]. Consequently, these LES results are used as a benchmark reference to analyze the hybrid simulations results.

The zonal approach, simulation 2, predicts a C_f in close agreement with LES. This is an expected result, as mentioned before, since the inner layer is completely modeled by RANS, which is calibrated to reproduce the law of the wall [63, 105]. For HRL-HT, simulations 7 to 10, the predicted friction coefficients are found within -1.5% to -6.8% error with respect to LES. The difference among HRL-HT simulations is caused by the different blending functions, which indicates that even when the hybrid terms are included, small variations in the predicted C_f can be reproduced with different blending functions. However, when the hybrid contributions are not included, significant deviations in the predicted C_f are reproduced among blending functions. Simulation 3 predicts an error with respect to LES (here, the inner layer of the boundary layer is partially resolved) in close agreement with the error predicted when the hybrid contributions are included (simulation 7). However, if the blending function locates the RTLT away from the inner layer, the hybrid model is not able to significantly compensate for the lost turbulence magnifying the deviations in the

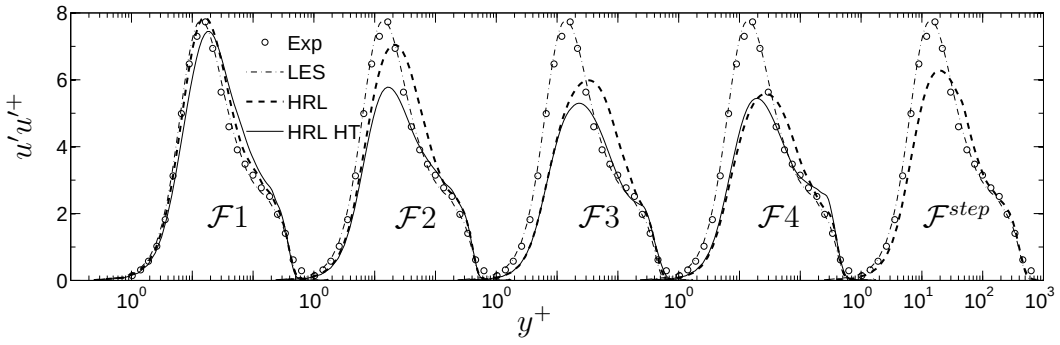

(a)

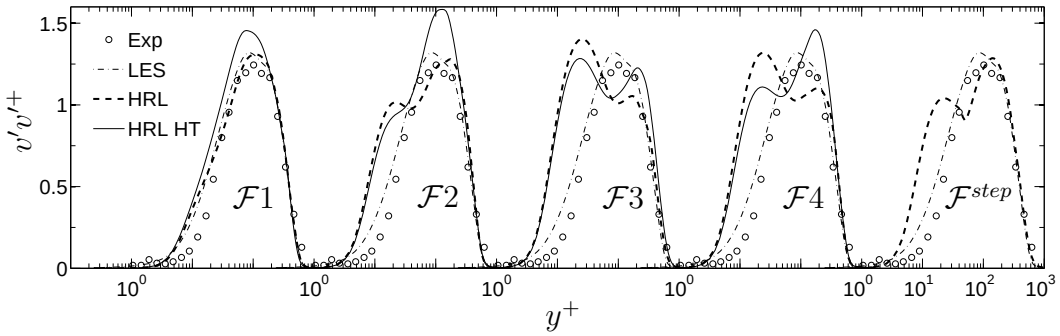

(b)

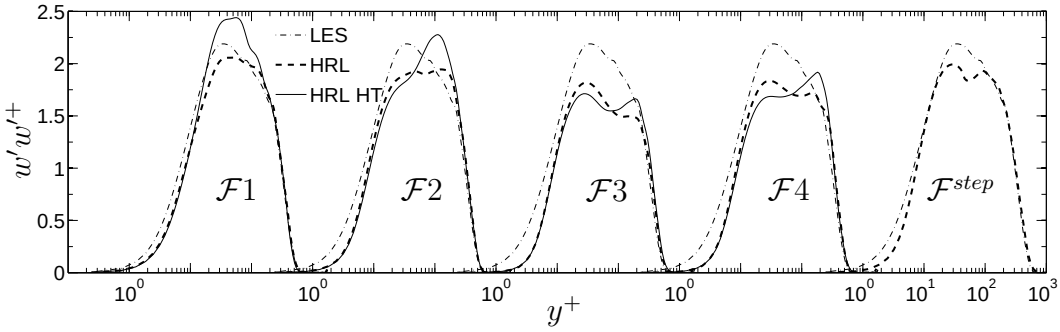

(c)

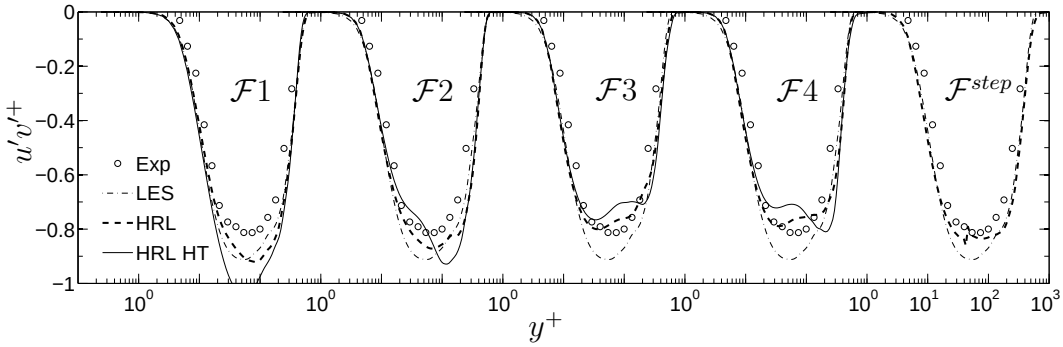

(d)

Figure 5.5: Wall-normal distribution of total (resolved plus modeled) Reynolds stresses for LES, HRL, HRL-HT, and Zonal RANS/LES ($\mathcal{F}^{step}$) fine grid simulations: (a) $u'u'^+$; (b) $v'v'^+$; (c) $w'w'^+$; (d) $u'v'^+$.

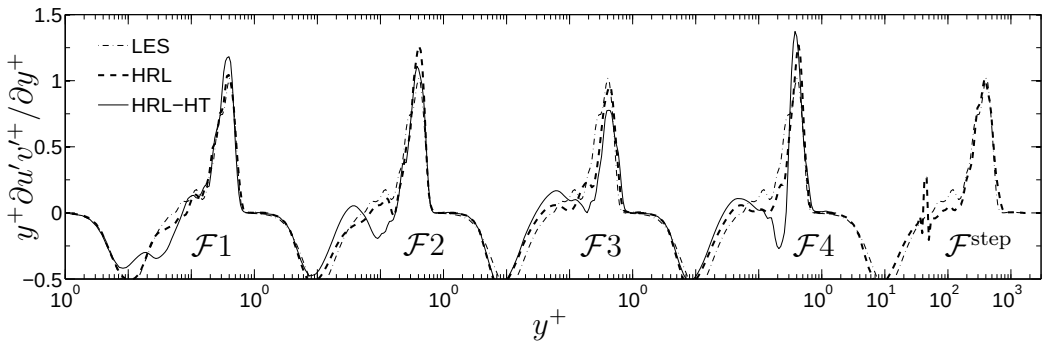

Figure 5.6: Wall-normal distribution of $y^+\partial u'v'^+/\partial y^+$ (for the total Reynolds stress, modeled plus resolved) for LES, HRL, HRL-HT, and Zonal RANS/LES ($\mathcal{F}^{step}$) simulations, fine grid results.

predicted friction coefficient. For simulation 4, the $\mathcal{F}2$ sets the RTLT zone in $30 < y^+ < 240$ inducing an error, with respect to LES, 4.6 times higher that the error predicted when the hybrid terms are included. For simulation 5, the $\mathcal{F}3$ sets the RTLT zone in $20 < y^+ < 580$, in this case the error is doubled. Here, it is pointed out that this apparent good response of $\mathcal{F}3$ to not include the hybrid terms is misleading, since overall, the accuracy of C_f predicted with this function is the lowest for both HRL and HRL-HT simulations. Nevertheless, including the hybrid contributions with this function does have a positive effect improving the accuracy of C_f. For simulation 6 the $\mathcal{F}4$, induces five RTLT regions and yields an error about 8 times higher than when the hybrid terms are included. This drastic drop in accuracy is related with the fact that the multiple RTLT zones make the accuracy of the hybrid formulation more dependent on the hybrid contributions, thus neglecting Eqs. (5.22)-(5.27) has a major effect in the accuracy of C_f. Here, it is pointed out that the behaviour previously described is induced only by the turbulent modeling approach here described, since the grid implemented is fine enough for both LES and RANS simulations. However, a similar trend is observed in the predicted C_f computed with the medium and coarse grids, which are not reported here for the sake of brevity.

In order to further elucidate the effect of the blending function and the hybrid

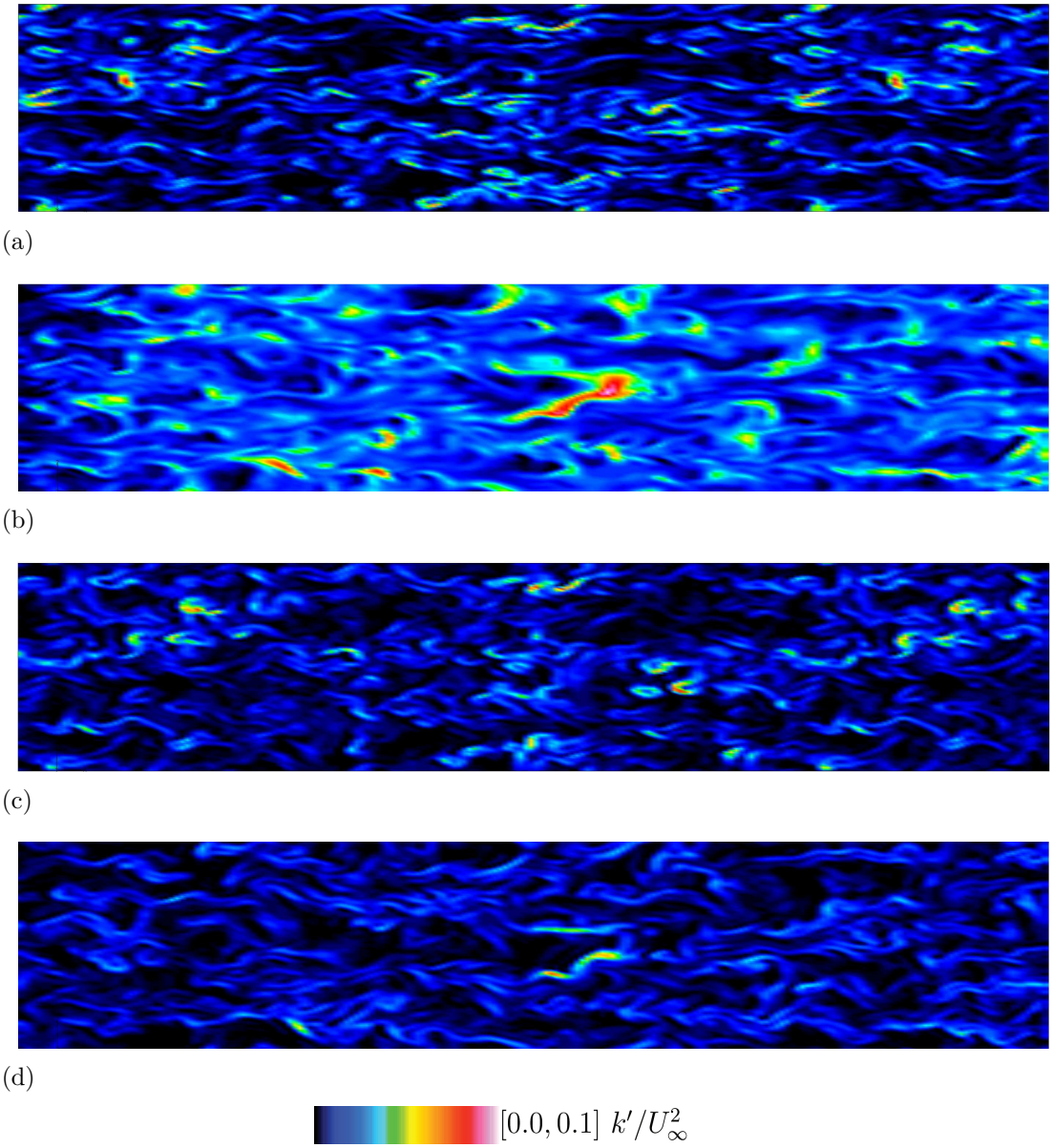

Figure 5.7: Contours of subgrid kinetic energy (k^{sgs}) and hybrid turbulent kinetic energy ($\mathcal{K}$) for $Re_\theta = 1400$: (a) LES $y^+ = 40$; (b) HRL $\mathcal{F}^{stp} = 1.0$ (RANS) $y^+ = 40$; (c) LES $y^+ = 50$; (d) HRL $\mathcal{F}^{stp} = 0.0$ (LES) $y^+ = 50$.

contribution in the boundary layer turbulence, the second-order statistics are computed and analyzed. Figures 5.3 and 5.4 presents the resolved Reynolds stresses $\dot{\overline{\tau}}(\overline{u}_i, \overline{u}_j)/\dot{\overline{\rho}}$ and the time average of the modeled Reynolds stresses (here after referred just as modeled) $\dot{\overline{\overline{\tau}}}(u_i, u_j)/\dot{\overline{\rho}}$, respectively, while Figure 5.5 presents the total stresses $u_i' u_j'^{tot} = (\dot{\overline{\tau}}(\overline{u}_i, \overline{u}_j) + \dot{\overline{\overline{\tau}}}(u_i, u_j))/\dot{\overline{\rho}}$ (hereafter the notation $u_i' u_j'$ is used to refer the components of the Reynolds stress tensor indistinctly), for both figures, the statistics are computed from the LES and the hybrid RANS/LES formulation on the fine grid. Here, it is pointed out that for the HRL-HT simulations, only a fraction, Eq. (5.25), of the hybrid terms Eqs. (5.22)-(5.27) can be included in the modeled stresses. Nevertheless, the rest of the hybrid terms play their part in the governing equations.

As expected, the fine grid allows LES to resolve the near-wall turbulence without any special wall-treatment. Consequently, the LES predictions are found in very-good agreement with the experimental data, as shown in Figures 5.3-5.5, and will be used as our benchmark case. For hybrid RANS/LES simulations, Figures 5.3 and 5.4 demonstrate the effect that the blending function has on the resolved and modeled Reynolds stresses. Although it is an expected result, Figures 5.3 and 5.4 demonstrate that as the RTLT region gets closer to the wall ($\mathcal{F}4 \rightarrow \mathcal{F}1$), the levels of modeled turbulence drops while the resolved increases, with or without the hybrid terms. This is explained by the fact that LES takes over the hybrid formulation as the RTLT zone completes closer and closer to the near-wall region, replacing modeled by resolved stresses.

Figures 5.3-5.5 indicate that if discontinuous blending functions are implemented, as in simulation 2, the sharp transition from RANS to LES induces nonphysical discontinuities in the modeled and resolved statistics. Figure 5.6 presents the wall-normal derivative of the total principal Reynolds stress $y^+ \partial u' v'^+ / \partial y^+$ (the other stresses present similar trends). The figure clearly shows, similar to Figure 2(b), that only with the step function anomalous profiles, indicated by a spike located

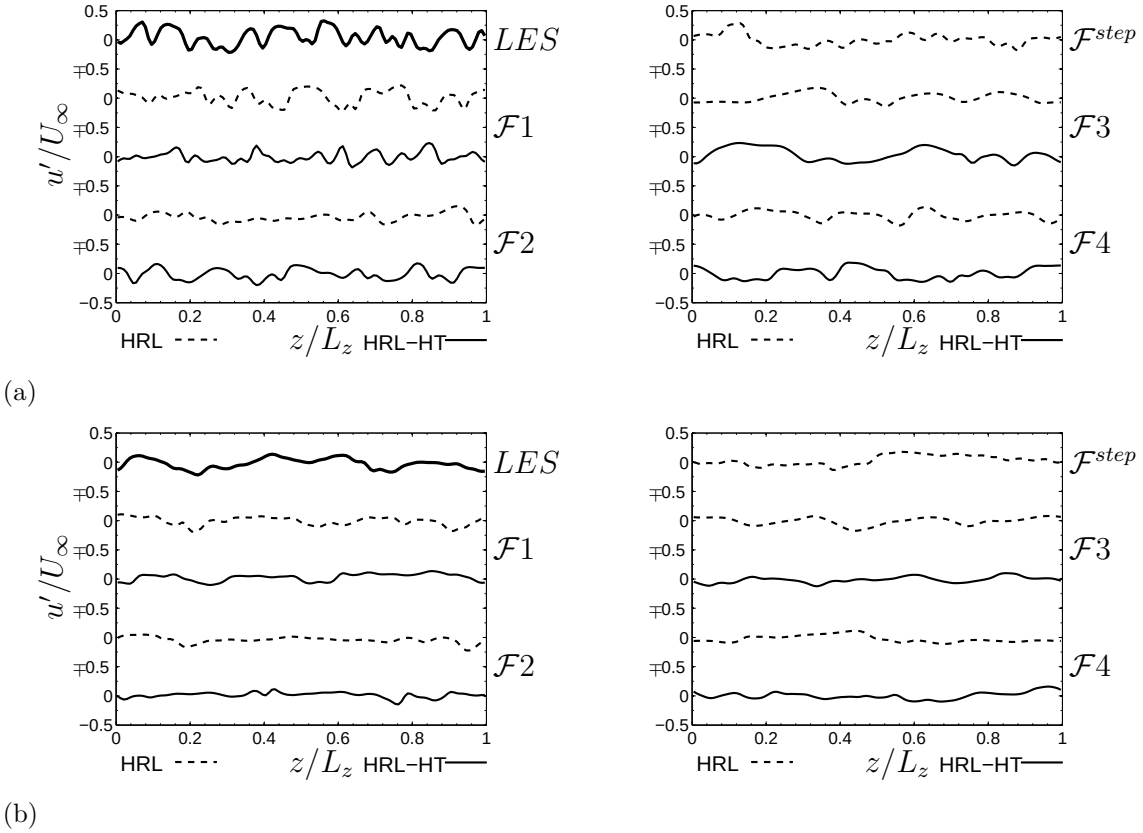

(a)

(b)

Figure 5.8: Spanwise distribution of normalized unsteady streamwise-velocity fluctuations u'/U_∞ for LES, HRL, HRL-HT, and Zonal RANS/LES ($\mathcal{F}^{step}$) fine grid simulations: (a) wall-normal location $y^+ = 11$, RANS-dominated region for all blending functions; (b) wall-normal location $y^+ = 100$, RANS-dominated region for $\mathcal{F}3$ and $\mathcal{F}4$ functions. Here the y axis is shifted to show all the plots.

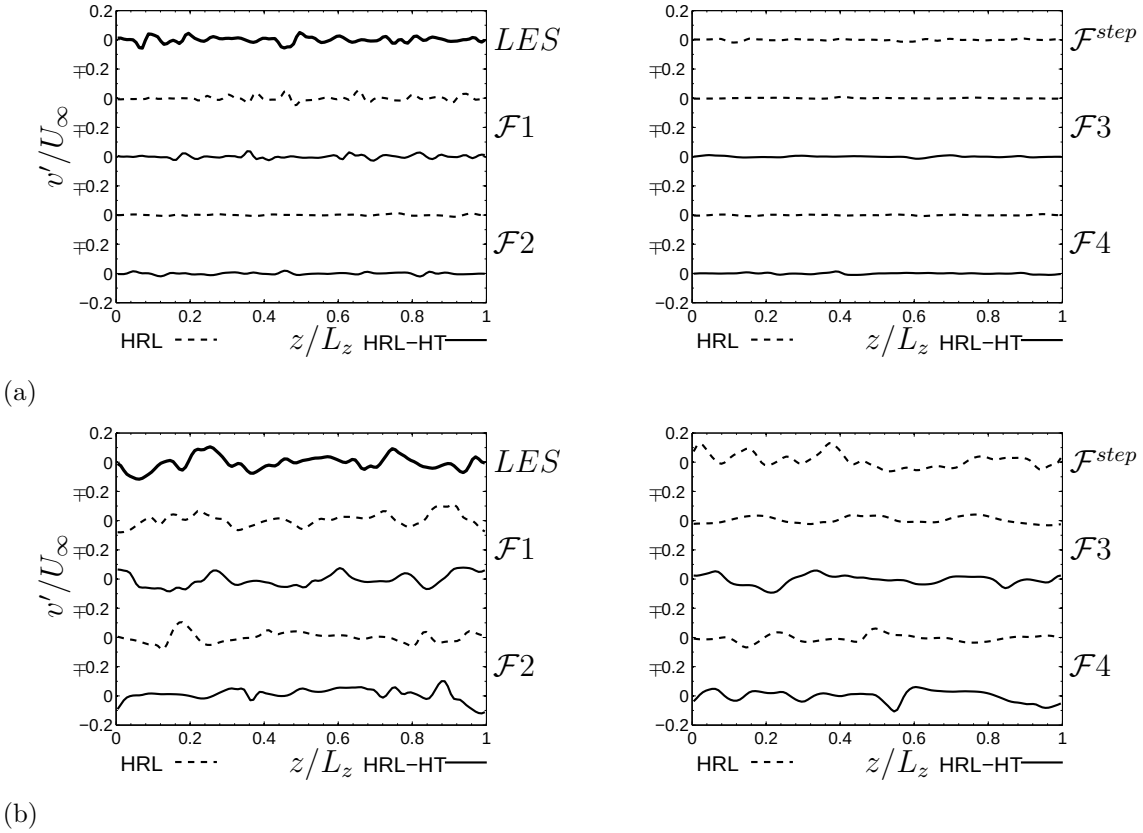

(a)

(b)

Figure 5.9: Spanwise distribution of normalized unsteady wall-normal-velocity fluctuations v'/U_∞ for LES, HRL, HRL-HT, and Zonal RANS/LES ($\mathcal{F}^{step}$) fine grid simulations: (a) wall-normal location $y^+ = 11$, RANS-dominated region for all blending functions; (b) wall-normal location $y^+ = 100$, RANS-dominated region for $\mathcal{F}3$ and $\mathcal{F}4$ functions. Here the y axis is shifted to show all the plots.

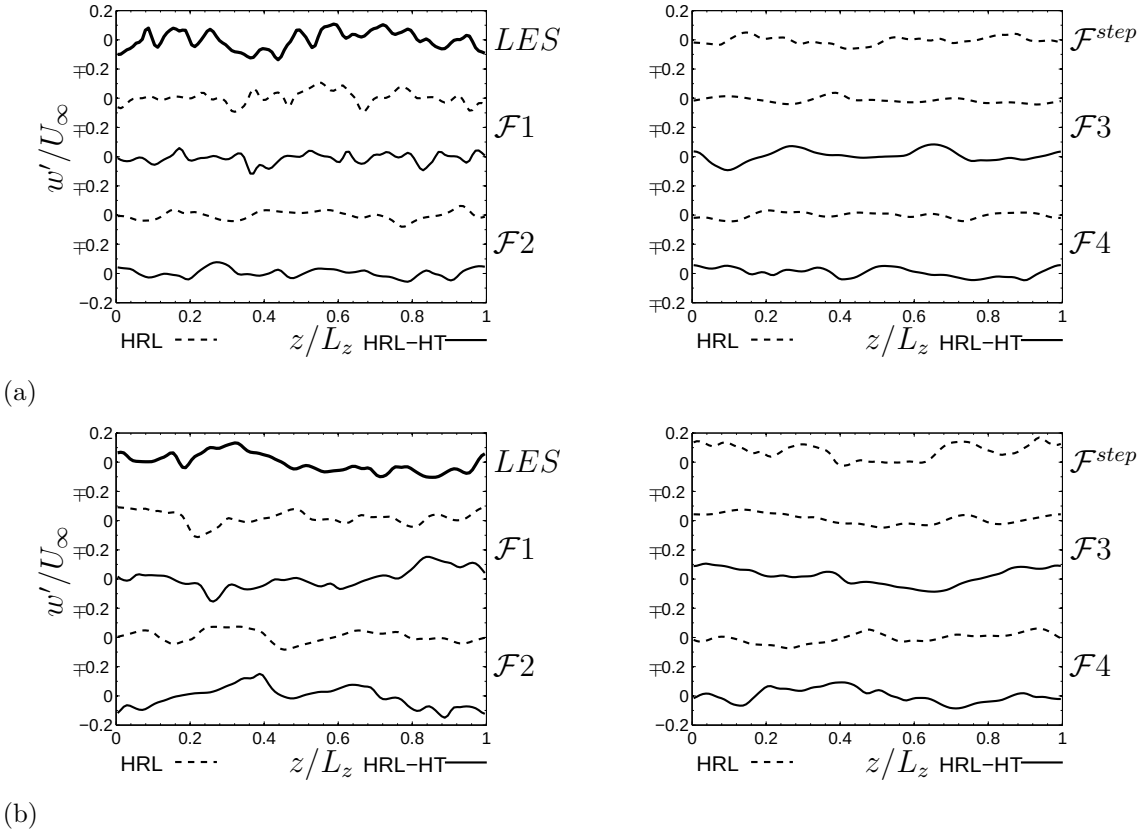

(a)

(b)

Figure 5.10: Spanwise distribution of normalized unsteady spanwise-velocity fluctuations w'/U_∞ for LES, HRL, HRL-HT, and Zonal RANS/LES ($\mathcal{F}^{step}$) fine grid simulations: (a) wall-normal location $y^+ = 11$, RANS-dominated region for all blending functions; (b) wall-normal location $y^+ = 100$, RANS-dominated region for $\mathcal{F}3$ and $\mathcal{F}4$ functions. Here the y axis is shifted to show all the plots.

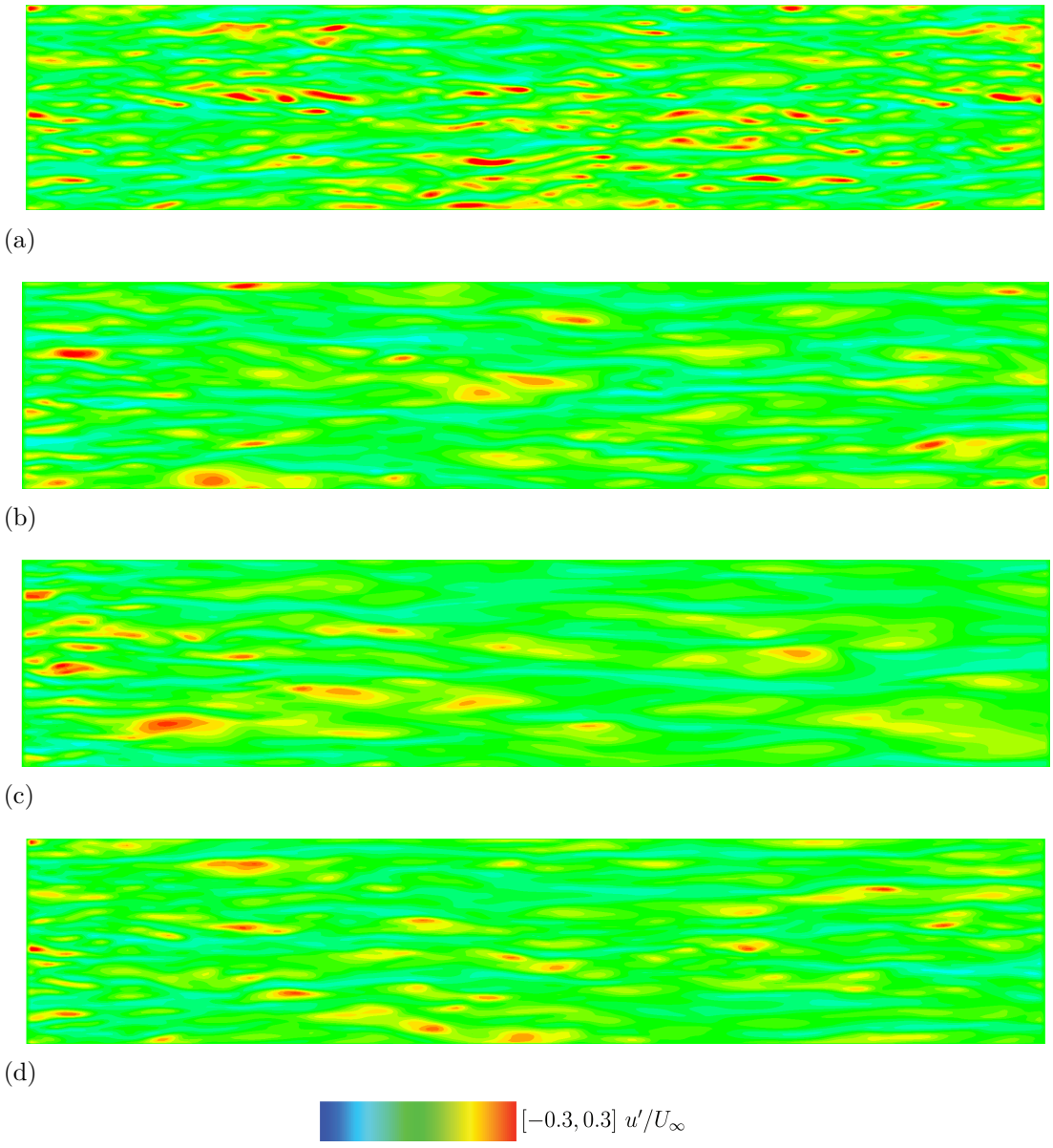

Figure 5.11: Contours of streamwise velocity fluctuations for $Re_\theta = 1400$ at $y^+ = 5$: (a) LES; (b) HRL $\mathcal{F}^{stp} = 1.0$; (c) HRL $\mathcal{F}2 = 0.99$; (d) HRL-HT $\mathcal{F}2 = 0.99$.

precisely at the model interface, are reproduced. Similar discontinuities have been reported in previous hybrid zonal approaches [15, 34, 70]. The discontinuities in the modeled stresses can be also observed in Figures 5.4 and 5.7, which show the sharp drop of modeled stresses occurring at $y^+ = 45$ when $\mathcal{F}^{step}$ is used. In particular, Figure 5.7 presents contours of k^{sgs} and $\mathcal{K}$ computed from LES and HRL-$\mathcal{F}^{stp}$ simulations. Results clearly illustrate the dramatic change in the magnitude of the modeled turbulence around the model interface ($y^+ = 45$), while k^{sgs} shows no variation in the LES calculations, $\mathcal{K}$ presents a dramatic change in magnitude when it abruptly switches from RANS to LES formulation in the HRL simulation that uses the $\mathcal{F}^{stp}$ function.

On the other hand, when continuous blending functions are implemented in the hybrid formulation, with and without hybrid terms, the modeled stresses smoothly transit from RANS to LES. Similarly, when $\mathcal{F}^{step}$ is used, the resolved stresses, Figure 5.3, also present discontinuities. However, they do not go from resolved LES levels to zero at the RANS region as could be expected. In fact, at the RANS region the resolved unsteady structures are not entirely dissipated as indicated by the low, yet not zero, levels of resolved turbulence below $y^+ < 45$. This indicates that for the zonal RANS/LES approach, LES feeds in turbulent unsteady structures, which transforms the otherwise steady RANS region, into a quasi-steady zone. Similarly, nonzero levels of resolved stresses are reproduced within the RANS region with other blending functions, indicating that the existence of a quasi-steady RANS field is not exclusive of zonal RANS/LES approaches.

For HRL and HRL-HT simulations, Figures 5.3-5.6 indicate that whether or not the hybrid terms are included, the modeled and resolved statistics do not present any discontinuities in their profiles as long as the blending function is continuous. Figures 5.3 and 5.4 illustrate the distribution of modeled and resolved stresses, which

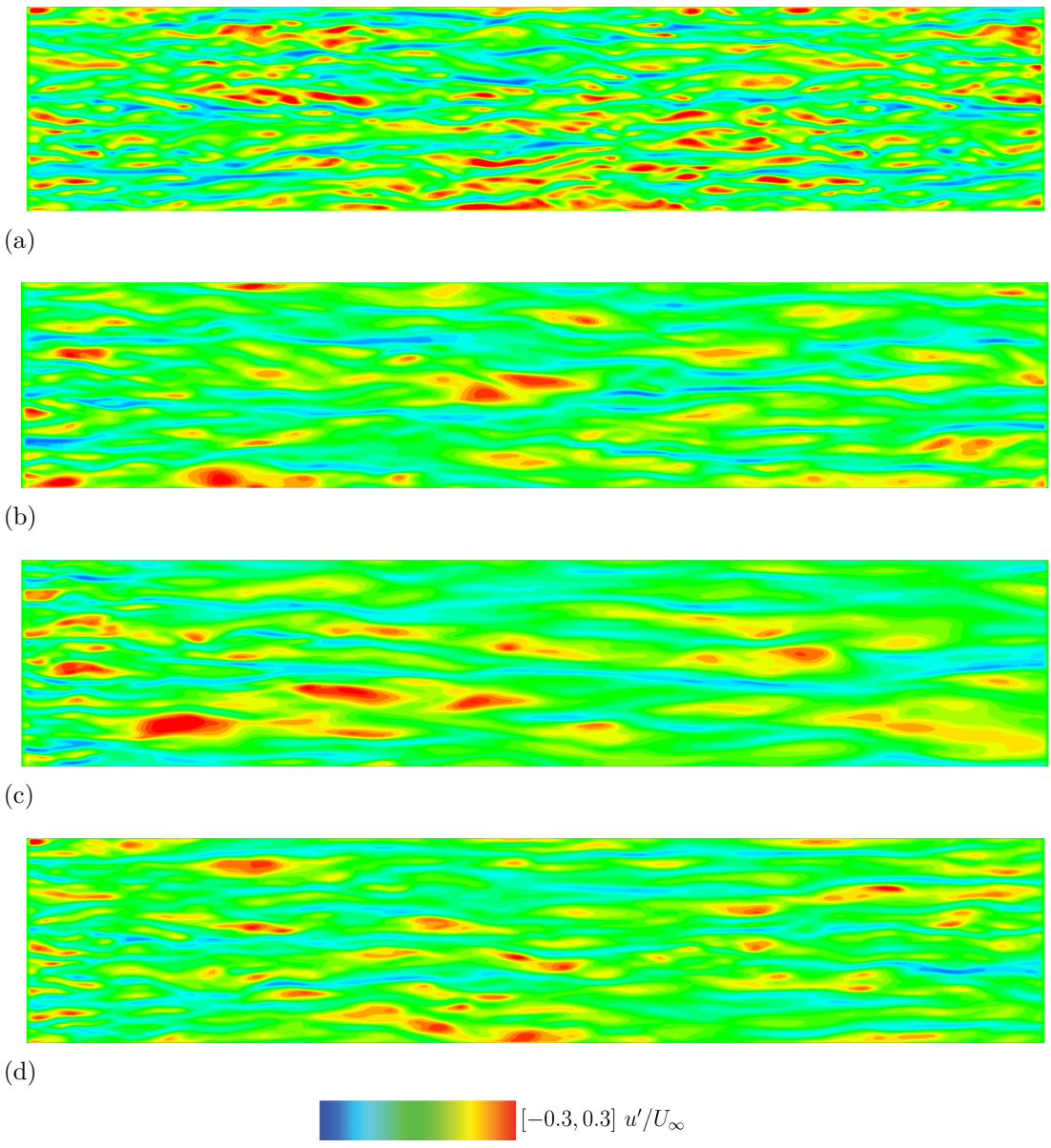

Figure 5.12: Contours of streamwise velocity fluctuations for $Re_\theta = 1400$ at $y^+ = 10$: (a) LES; (b) HRL $\mathcal{F}^{stp} = 1.0$; (c) HRL $\mathcal{F}2 = 0.97$; (d) HRL-HT $\mathcal{F}2 = 0.97$.

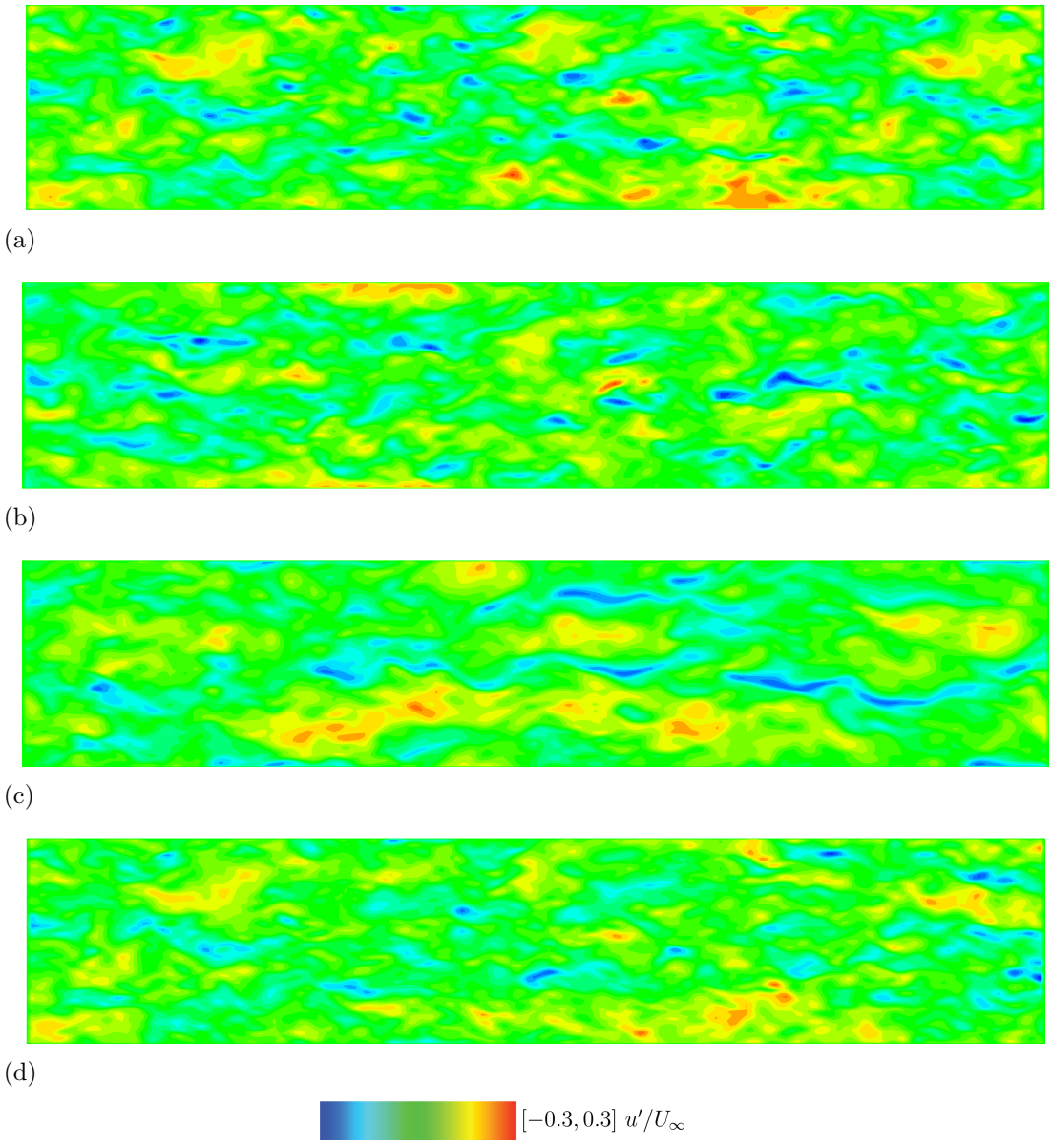

Figure 5.13: Contours of streamwise velocity fluctuations for $Re_\theta = 1400$ at $y^+ = 100$: (a) LES; (b) HRL $\mathcal{F}^{stp} = 0.0$; (c) HRL $\mathcal{F}2 = 0.4$; (d) HRL-HT $\mathcal{F}2 = 0.4$.

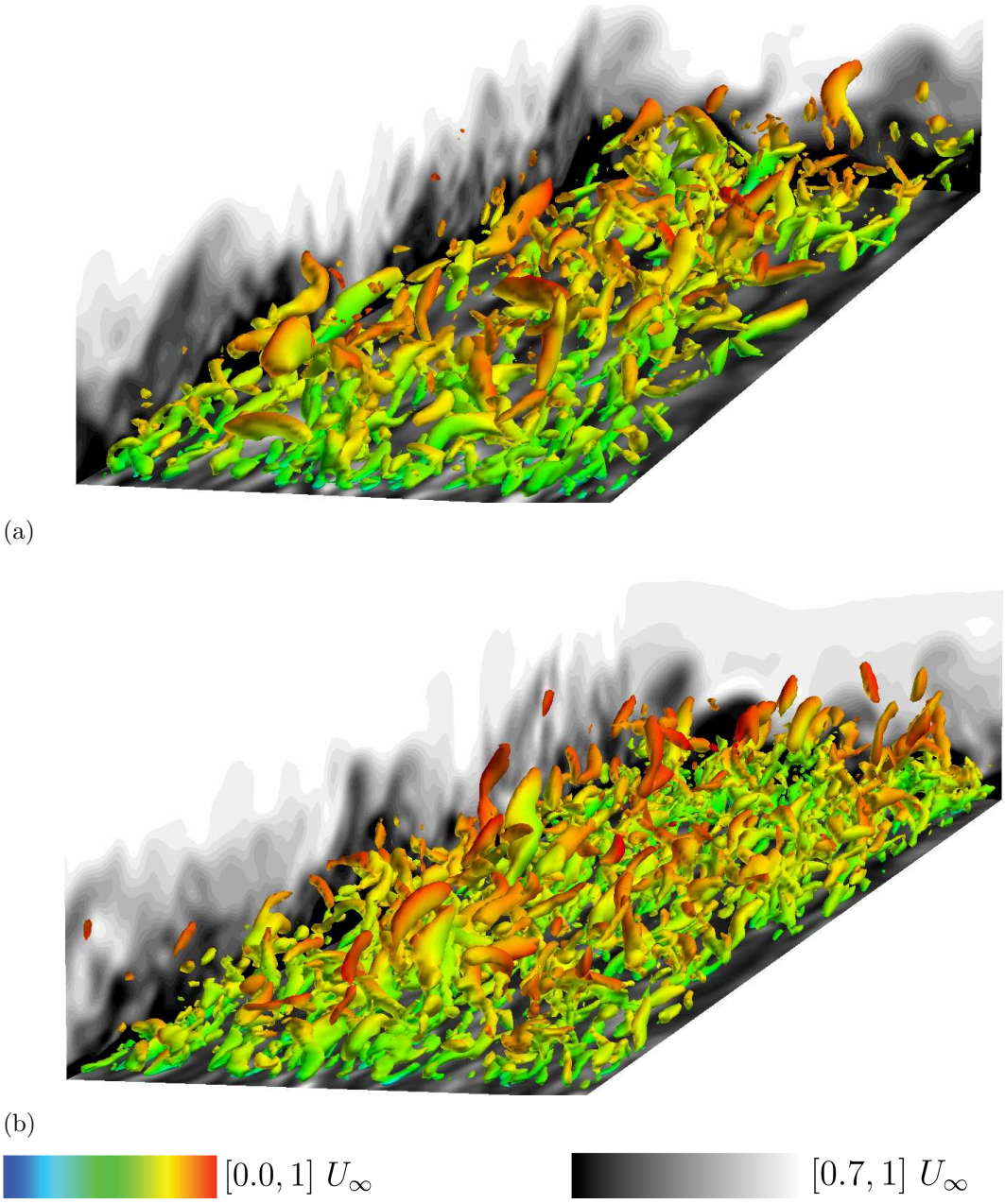

Figure 5.14: Isosurfaces of second invariant of the velocity gradient tensor ($\mathcal{Q}\theta/U_\infty = 1 \times 10^3$) colored with values of streamwise velocity, side contours streamwise velocity, for hybrid RANS/LES simulations using $\mathcal{F}2$ function, $Re_\theta = 1400$: (a) HRL; (b) HRL-HT.

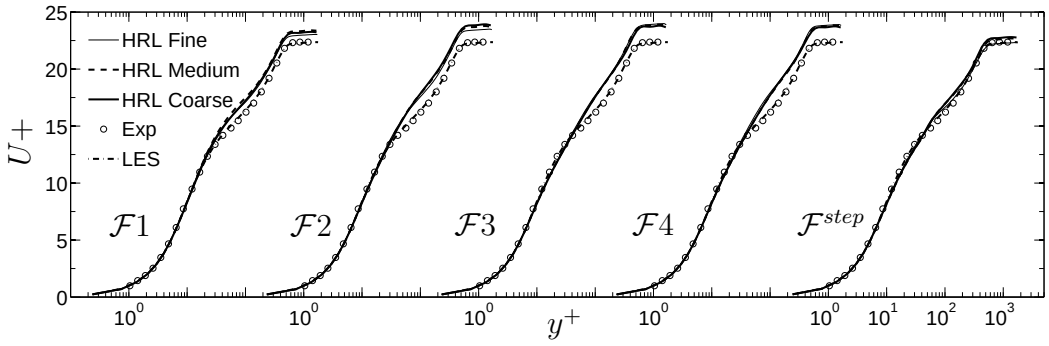

(a)

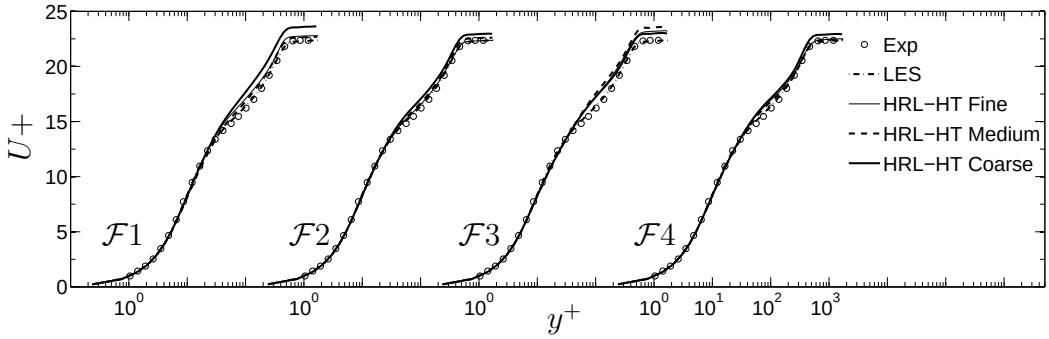

(b)

Figure 5.15: Grid sensitivity studies, mean streamwise velocity profile U^+, for hybrid and Zonal RANS/LES ($\mathcal{F}^{step}$) simulations conducted on fine, medium, and coarse grids: (a) hybrid simulations not including the hybrid terms; (b) hybrid simulations including the hybrid terms.

depend on the blending function implemented and whether or not the hybrid contributions are included. However, for the total stresses, shown in Figure 5.5, the dependency on blending function and hybrid contribution is not that evident, and only quantitative differences can be distinguished.

It is important to mention that the total stresses computed with and without hybrid contributions, with the exception of $u'u'$, present inflection points and a local minimum at the RTLT zone. The inflection point and local minimum are generated because the resolved and modeled stresses do not peak around the same location. Figure 5.5 indicates that the peaks separation distance is found to be in the order of 100 wall units for all blending functions. For the $u'u'$ stress, the modeled and resolved stresses peak around the same location with all blending functions. Therefore, no

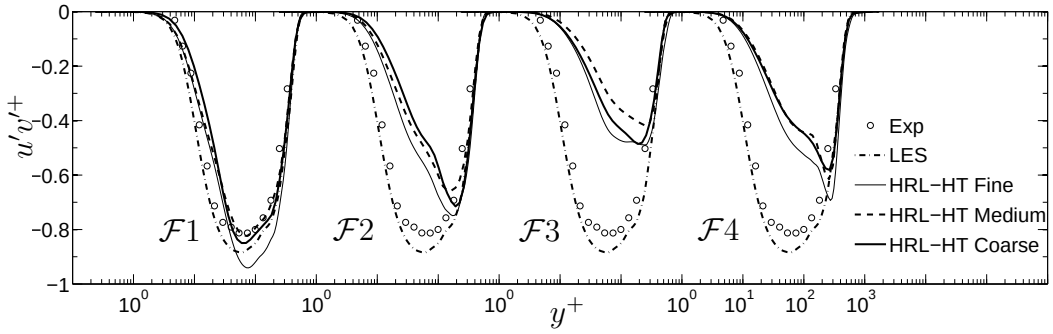

(a)

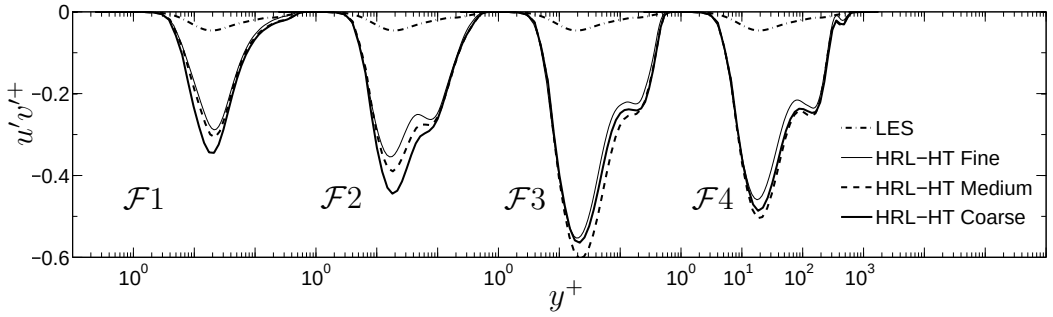

(b)

Figure 5.16: Grid sensitivity studies for hybrid simulations including the hybrid terms conducted on fine, medium, and coarse grids: (a) resolved $u'v'^+$ Reynolds stress; (b) modeled $u'v'^+$ Reynolds stress.

local minimum or inflection point is reproduced in this stress. It is important to point out that when the RTLT zone is in the inner layer, $\mathcal{F}1$, the total stresses do not present any inflection points and local minimum, since the modeled stresses are not that significant when compared with the resolved stresses for this blending function. Finally, current results indicate that the local minimum and inflection point observed in the total stresses, computed with and without the hybrid contributions, cannot be avoided when blending functions with RTLT in the outer layer are implemented.

Figure 5.3 shows that for blending functions with RTLT zone close to the inner layer, $\mathcal{F}1$, the LES part of the hybrid model is able to resolve a significant amount of the near-wall turbulence yielding resolved stresses in close agreement when the hybrid contributions are included or neglected ($u'u'$ is the only stress that shows slight

differences when the hybrid terms are included). On the other hand, Figure 5.4 shows that the modeled stresses reach higher values when the hybrid terms are included than when these terms are neglected, slightly increasing the total stresses as seen in Figure 5.5. Nonetheless, it can be concluded that for blending functions with RTLT zones located very close to the near-wall region, the effect of the hybrid terms is reduced, as indicated by Figures 5.2-5.5, and it is expected that their effect become negligible as $\mathcal{F} \to 0$ everywhere. Contrary, if the blending function locates the RTLT zone in the outer layer, the hybrid contributions become more relevant. Figure 5.4 shows that for blending functions $\mathcal{F}2$, $\mathcal{F}3$, and $\mathcal{F}4$, the hybrid contributions indeed increase the modeled stresses in the RTLT zone. This demonstrates that the hybrid terms represent modeled scales that should not be neglected. In fact, if these terms are neglected, the levels of modeled stresses drops and the hybrid model is forced to compensate this deficit by resolving more scales as seen, specially with $u'u'$ and $u'v'$, in Figure 5.3. Unfortunately, for RTLT zones deep in the outer layer, the LES part of the hybrid model is not able to correctly compensate Eqs. (5.22)-(5.27) yielding levels of resolved and modeled stresses that differs from those computed with the hybrid contributions, which eventually leads to the inaccurate predictions in the mean velocity profile and C_f.

Whether or not the blending function allows the hybrid model to resolve part of the turbulence contained in the hybrid contributions, these terms cannot be completely resolved by the LES part of the hybrid formulation, unless the blending function reduces to $\mathcal{F} \equiv 0$ everywhere, which obviously reduces the hybrid RANS/LES formulation to LES. Therefore, if Eqs. (5.22)-(5.27) are neglected and $\mathcal{F}$ is not always zero, some amount of turbulence that cannot be resolved nor modeled is lost leading to ATD. How much turbulence is not accounted for in the hybrid simulations and how this impacts the accuracy of the calculations strongly depends on the blending function implemented. This is the main reason why the flow statistics predicted with

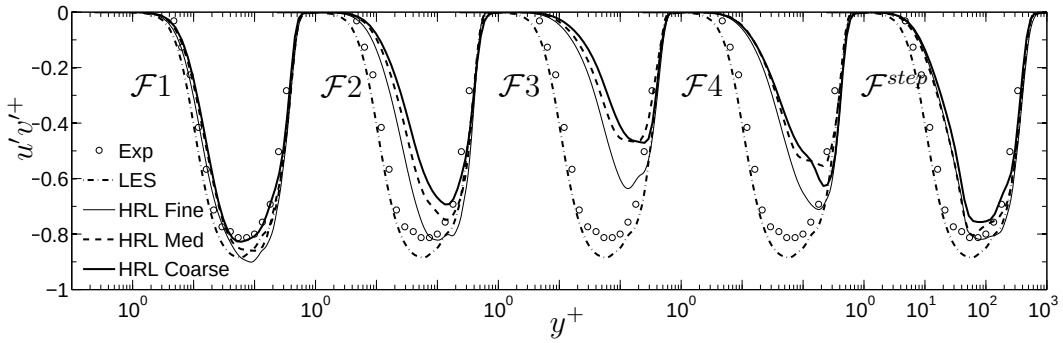

(a)

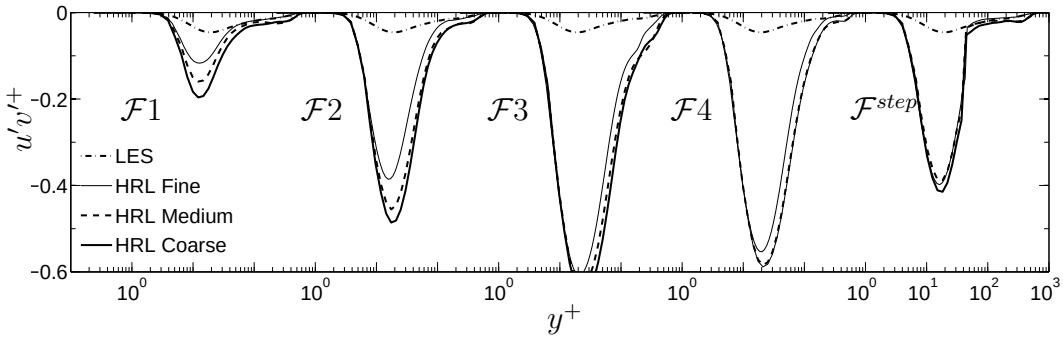

(b)

Figure 5.17: Grid sensitivity studies for hybrid simulations not including the hybrid terms conducted on fine, medium, and coarse grids: (a) resolved $u'v'^+$ Reynolds stress; (b) modeled $u'v'^+$ Reynolds stress.

the five blending functions here implemented (simulations 2 to 6) differ from each others.

Figures 5.8-5.10 shows the effect of the hybrid formulation in the instantaneous velocity field. It presents the velocity fluctuations, plotted over the span-wise direction, normalized with the free stream velocity, sampled at the buffer layer $y^+ = 11$ and at the outer layer $y^+ = 100$. As indicated by Figure 5.3 and corroborated by Figures 5.8-5.10, for all simulations, the intensity in the fluctuations are higher at $y^+ = 11$ than at $y^+ = 100$ for the streamwise velocity, while they are higher at $y^+ = 100$ than at $y^+ = 11$ for the spanwise and wall-normal velocities. However, in all simulations, the wavelengths of the fluctuations are smaller at $y^+ = 11$ than at

$y^+ = 100$, indicating the presence of finer structures at the buffer layer. Overall, Figures 5.8-5.10 demonstrate that the dissipation of the turbulent scales, due to RANS modeling, depends on the blending function implemented. At $y^+ = 11$, the highest reduction in velocity fluctuations, yet not complete dissipation, is obtained with the functions that set RANS modeling at the inner layer $\mathcal{F}2$, $\mathcal{F}3$, $\mathcal{F}4$, and $\mathcal{F}^{step}$, whereas $\mathcal{F}1$ simulations predict unsteady structures close to those of LES. This strengthens the observation that the turbulent scales, fed in the RANS region by LES, are significantly reduced, but are not dissipated entirely by RANS. On the other hand, as the hybrid formulation becomes more dominated by LES, the hybrid simulations resolve more unsteady turbulent content, as seen in all velocity fluctuations at $y^+ = 100$.

Figures 5.8-5.10 shows the importance of the unsteady nature of the HT, Eqs. (5.34)-(5.39), in promoting unsteady structures in hybrid calculations. This point is highlighted by Figures 5.11-5.13, which present contours of streamwise velocity fluctuations at three wall-normal locations $y^+ = 5$, 11, and 100. Here, only results obtained with the $\mathcal{F}2$ and $\mathcal{F}^{stp}$ functions are compared against LES simulations, since the other blending functions yield similar trends. Figures. 5.11 and 5.12 demonstrate that in the region where the hybrid model is dominated by RANS $y^+ < 100$ (for these functions), HRL calculations that neglect the hybrid terms predict quite elongated streaks of velocity fluctuations, in disagreement with LES predictions. However, by including the hybrid terms in the calculations (HRL-HT), these anomalous elongated streaks are broken into smaller structures, in better agreement with the physical picture predicted by LES. As we move away from the wall, the hybrid model become dominated by LES, reducing the effect of the HT on the calculations Figure 5.13, here HRL and HRL-HT simulations predict structures in close agreement with LES.

The effect of the hybrid terms in preventing ATD (lost of modeled or resolved turbulence) in the RTLT zone is further illustrated by visualizing the coherent structures of the flow in Figure 5.14. Here, it is evident that by including the HT, their unsteady

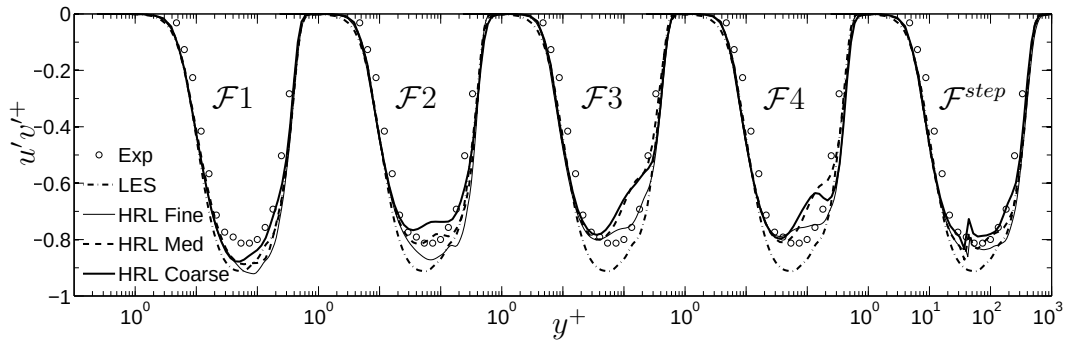

(a)

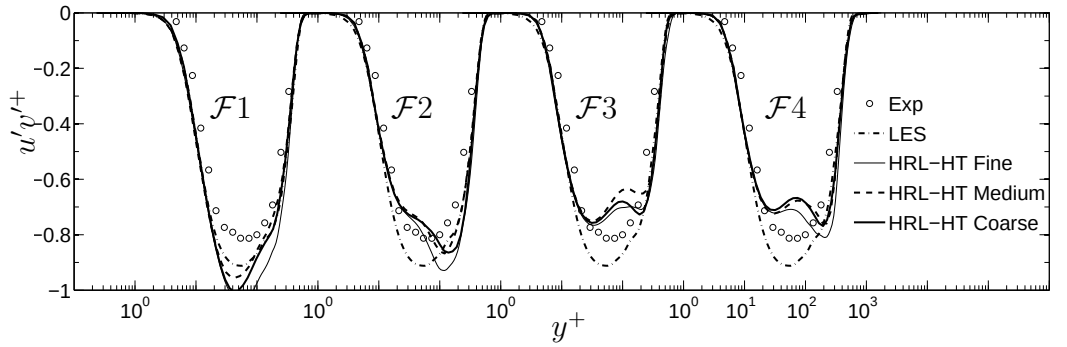

(b)

Figure 5.18: Grid sensitivity studies, total $u'v'^{+}$ Reynolds stress (modeled plus resolved), for HRL, HRL-HT, and Zonal RANS/LES ($\mathcal{F}^{step}$) simulations conducted on fine, medium, and coarse grids: (a) hybrid simulations not including the hybrid terms; (b) hybrid simulations including the hybrid terms.

nature promotes the generation of unsteady near-wall vortices, which are dissipated if the HT are not included. These results further demonstrate the importance of resolving the exact equations in hybrid RANS/LES simulations.

Results indicate that the blending function plays a fundamental roll in the hybrid RANS/LES formulation. However, by including the hybrid terms it is possible to reduce the effect of this function in the accuracy of the calculations. In fact, as long as the blending function is smooth and the RTLT zone located in the outer layer, the calculations will be only weakly affected by the blending function.

Thus far, the importance of the hybrid formulation has been demonstrated in a grid fine enough to conduct both LES (wall-resolving) and RANS simulations (solutions are grid independent). Nevertheless, it is pertinent to illustrate, up to some

extent, the behavior of the hybrid formulation, when none-wall resolving LES grids are implemented. Due to limited computational resources, only the medium and coarse grids are evaluated with all the blending functions, while the coarsest grid is evaluated only with the $\mathcal{F}^{step}$ and $\mathcal{F}2$ functions, which are selected to illustrate the effect of discontinuous and continuous functions with RTLT zone in the outer layer.

Figure 5.15 presents the mean velocity profile computed with all blending functions using the fine, medium, and coarse grids. The figure indicates that for the blending function with RTLT zone close to the inner layer, $\mathcal{F}1$, coarsening the grid to none wall-resolving resolutions, coarse grid, has a negative impact on the mean velocity profile even when the hybrid terms are included. Since the hybrid model is quickly dominated by LES at the near-wall region where the grid does not allow LES to resolve the near wall dynamics. However, when the RTLT zone is in the outer layer, RANS dominates the hybrid formulation at the near-wall region, thus the effect of reducing the grid resolution is not as negative as in the previous case, as long as the hybrid terms are included. When these terms are included, the predicted velocity profiles do not change drastically even with the coarse grid. On the contrary, if the hybrid terms are neglected, a drop in accuracy in the predicted mean profile is observed for all blending functions. For the zonal RANS/LES simulation, $\mathcal{F}^{step}$, the medium and coarse grids predict results in close agreement to those obtained in the fine grid, mainly because the near-wall zone is completely modeled with RANS for this function. However, the velocity profiles still present similar discontinuities (results not shown) as those shown in Figure 2(b).

The resolved, modeled, and total Reynolds stress $u'v'$, are shown in Figures 5.16-5.18, respectively. The figures demonstrate that, for all blending functions with and without hybrid contributions, coarsening the grid tends to slightly increase and decrease the modeled and resolved stresses, respectively. However, the net effect in the total Reynolds stress is not very significant. Here, the zonal RANS/LES approach

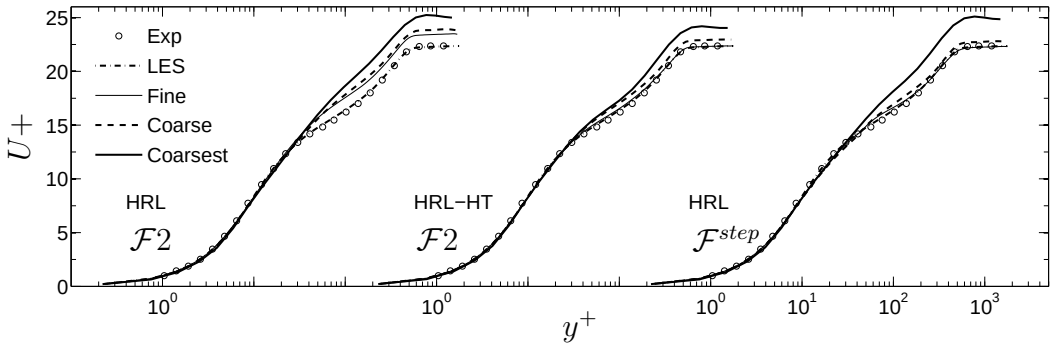

Figure 5.19: Grid sensitivity studies, mean streamwise velocity profile U^+, for hybrid ($\mathcal{F}2$) and Zonal RANS/LES ($\mathcal{F}^{step}$) simulations conducted on fine, coarse, and coarsest grids.

$\mathcal{F}^{step}$ is the less sensible to the reduction in grid resolution.

Overall, results obtained with all blending functions in the medium and coarse grids are quite good when the hybrid terms are included. This responds to the fact that those grids are still fine for hybrid simulations i.e., the near-wall grid-resolution is good for RANS modeling and the outer-layer resolution is fine enough for LES. However, if the grid resolution is further reduced to levels not appropriated for LES, yet good for RANS, the predictions start to present significant anomalies. Figure 5.19 presents the computed mean velocity profile using the fine, coarse, and coarsest grids with the $\mathcal{F}2$ and $\mathcal{F}^{step}$ blending functions. From the results, it is clear that the coarsest grid is not adequate for LES, and consequently hybrid simulations, as demonstrated by the significant deviations predicted in the velocity profiles. However, by including the hybrid terms, the mean velocity profile is slightly improved, demonstrating once more that Eqs. (5.22)-(5.27) have a positive effect in the hybrid formulation.

Figures 20(a) and 20(b) present the resolved and modeled Reynolds stress $u'v'$, it shows a drastic drop in the resolved stress and an important increase in the modeled stress for the $\mathcal{F}2$ function with respect to the fine and coarse grid results, specially when the hybrid terms are neglected. The increase in modeled stress at the RTLT zone is induced by the modeled stress coming from LES, which increases as the grid-resolution decreases. On the other hand, for the zonal RANS/LES simulation, the

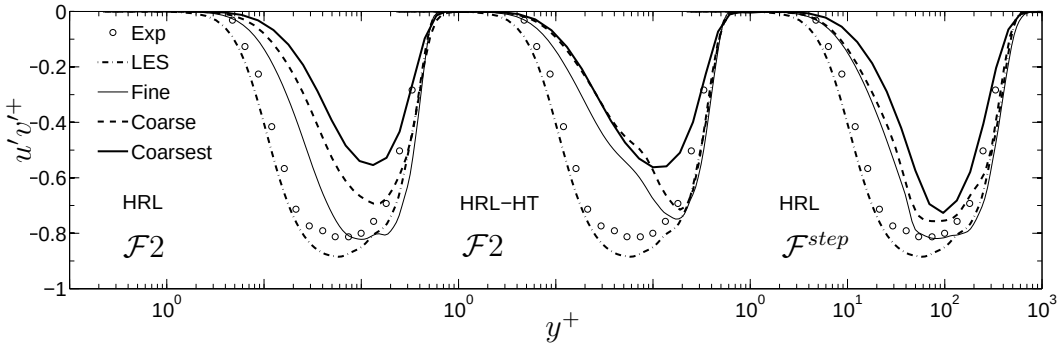

(a)

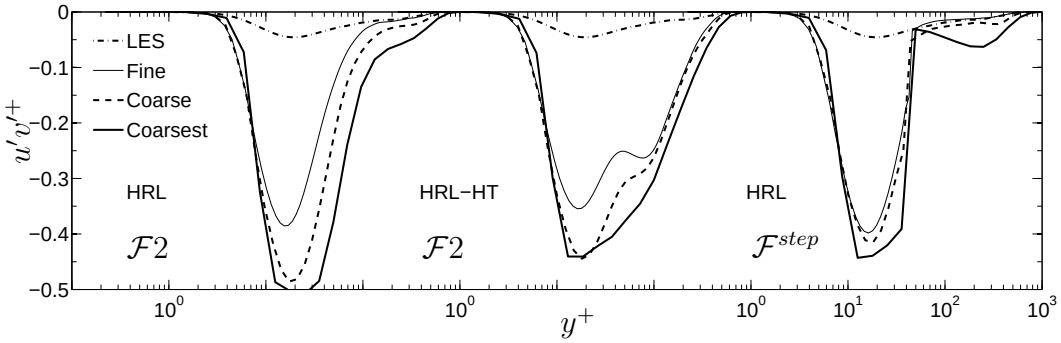

(b)

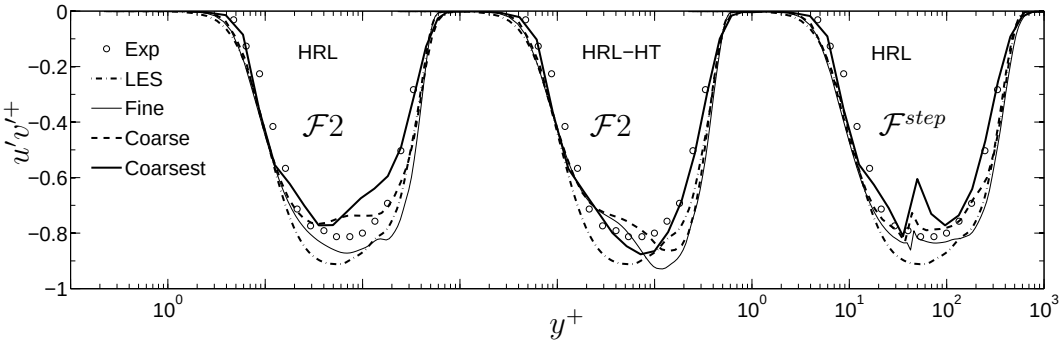

(c)

Figure 5.20: Grid sensitivity studies for hybrid ($\mathcal{F}2$) and Zonal RANS/LES ($\mathcal{F}^{step}$) simulations conducted on fine, coarse, and coarsest grids: (a) resolved $u'v'^{+}$ Reynolds stress; (b) modeled $u'v'^{+}$ Reynolds stress; (c) total (modeled plus resolved) $u'v'^{+}$ Reynolds stress.

modeled stress, which is purely RANS below $y^+ = 45$, is virtually grid independent. However, in the LES region, the resolved and modeled stresses drop and increase, respectively, due to the low grid resolution attained in the outer layer.

The computed total stress shown in Figure 20(c), shows an important drop at the RTLT zone when the hybrid contributions are neglected. This occurs because the grid is not fine enough there to resolve the turbulence and the modeled stresses drops because the hybrid terms are not included. However, when Eqs. (5.22)-(5.27) are included, fair agreement is reproduced with respect to the fine and coarse grids results, demonstrating once more the importance of the hybrid terms in this RANS/LES approach. The figure also indicates that the discontinuities reproduced with the zonal RANS/LES approach are dramatically amplified when the grid resolution is significantly reduced, proving that zonal RANS/LES approaches will always predict nonphysical results and thus this approach should be avoided.

5.3 Proposed Model for the Hybrid RANS/LES Governing Equations

The importance of the HT terms in attached turbulent boundary layer has been demonstrated. However, requiring a LES simulation to compute the HT terms is not, evidently, an option. Therefore, an alternative approach to model those terms has to be devised. The main problem faced to include the HT terms is the reconstruction of the LES out of the hybrid variables in the RTLT zone. On the other hand, the RANS field can be easily computed using Eq. (5.9). Although, Germano introduced a simple reconstruction procedure to compute the LES field Eq. (5.10), the operation easily becomes ill-conditioned. Another theoretical inconvenience is, that reconstructing the LES field from the hybrid variables is equivalent to defiltering, which is mathematically ill-posed [90]. Consequently, to include the HT terms, the LES field at the RTLT zone has to be invariably approximated.

In the literature, different methods to explicitly reconstruct the LES subgrid turbulent field have been proposed [19, 22, 48, 50, 53, 55]. However, they usually incur additional complexities that need to be avoided, if the modeling approach is to remain simple and computationally inexpensive. Specially if it is considered that including the HT terms already incur in additional costs. Therefore, with the only purpose of computing the HT terms, the LES field is reconstructed from the hybrid field using a similarity model as follows [61]:

$$\overline{\overline{\phi}} = \overline{\phi} + G_{(0,1)}\left(\overline{\overline{\phi}}\,\dot{\overline{\phi}} - \dot{\overline{\phi}}\,\dot{\overline{\phi}}\right)^{1/2} \tag{5.77}$$

here, $G_{(0,1)}$ is a random number from a Gaussian distribution with zero mean and unit variance. For convenience, it was decided to compute the turbulence intensity using the RANS operator. However, a more general procedure can be obtained by computing the turbulence intensity using a test filter procedure [61], here denoted as $< \cdot >$:

$$\overline{\overline{\phi}} = \overline{\phi} + G_{(0,1)}\left(< \overline{\phi}\,\overline{\phi} > - < \overline{\phi} >< \overline{\phi} > \right)^{1/2}. \tag{5.78}$$

Equation (5.77) indicates that the difference between the approximated LES field and the hybrid variable is $G_{(0,1)}\left(\overline{\overline{\phi}}\,\dot{\overline{\phi}} - \dot{\overline{\phi}}\,\dot{\overline{\phi}}\right)^{1/2}$, which does not vanish when $\mathcal{F} \to 0$. This vanishing condition could be enforced by including the blending function in the HT-model as $\mathcal{F}G_{(0,1)}\left(\overline{\overline{\phi}}\,\dot{\overline{\phi}} - \dot{\overline{\phi}}\,\dot{\overline{\phi}}\right)^{1/2}$. Nevertheless, it is considered that this is not necessary, since the hybrid terms already include the effects of the blending function since $HT \to 0$ when $\mathcal{F} \to 0$. Therefore, the blending function is not included in Eq. (5.77).

5.3.1 Results and Discussion

The model is evaluated using the five transition functions, summarized in Table 5.2 and Figure 5.1. These functions depend only on the wall-normal distance to avoid including the time-derivative of the blending function. However, if a time dependent transition function is implemented, the unsteady HT must be included, since the flow

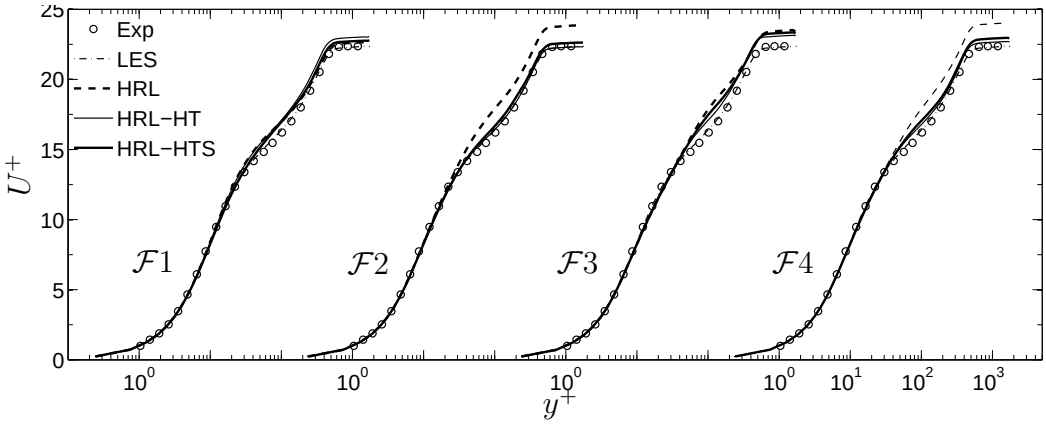

Figure 5.21: Law-of-the-wall for LES, HRL, HRL-HT, and HRL-HTS simulations $Re_\theta = 1400$.

cannot adapt instantaneously to the new modeling conditions, as indicated by Eqs (5.16)-(5.18). The case simulated is the $Re_\theta = 1400$, here the fine grid is implemented Table 5.1.

Figure 5.21 presents the predicted mean velocity profile normalized with wall-units for LES simulations, hybrid RANS/LES simulations without hybrid terms (HRL), hybrid RANS/LES simulations computing the hybrid terms using the parallel LES field (HRL-HT), and hybrid RANS/LES simulations computing the hybrid terms using the model Eq. (5.77) (HRL-HTS). Results indicate that for all blending functions implemented, the model for the hybrid terms, Eq. (5.77), is able to mimic the effect of the exact hybrid terms. The positive effect of the stochastic model is not surprising, since previous stochastic forcing approaches implemented in hybrid RANS/LES calculations have also shown significant improvements in the modeling of near-wall turbulence, even when they could be considered ad hoc [13, 14, 47, 70]. However, the exact hybrid RANS/LES equations provide fundamental justification to the stochastic forcing approaches proving that their success is related to the fact that they mimic the terms that represent the interactions between RANS and LES formulations.

Figure 5.22 compares the resolved second-order statistics. Results indicate that the levels of resolved stresses are in close agreement to the predictions when the

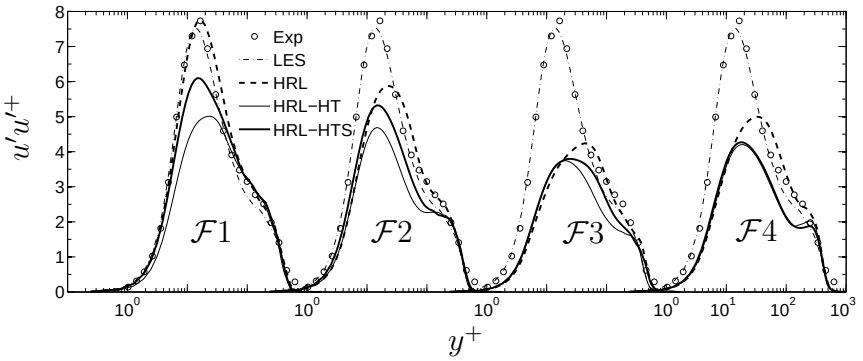

(a)

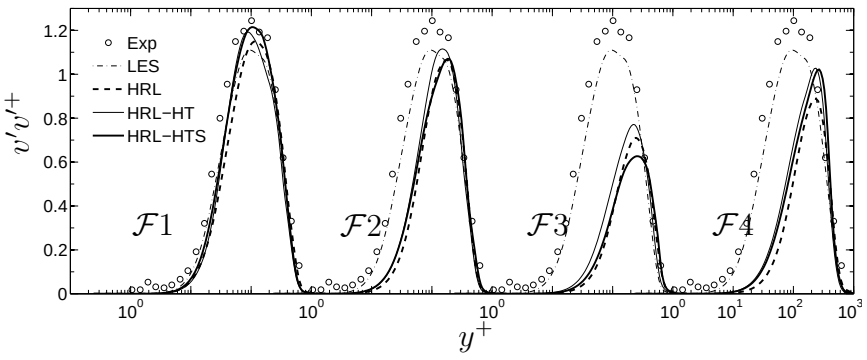

(b)

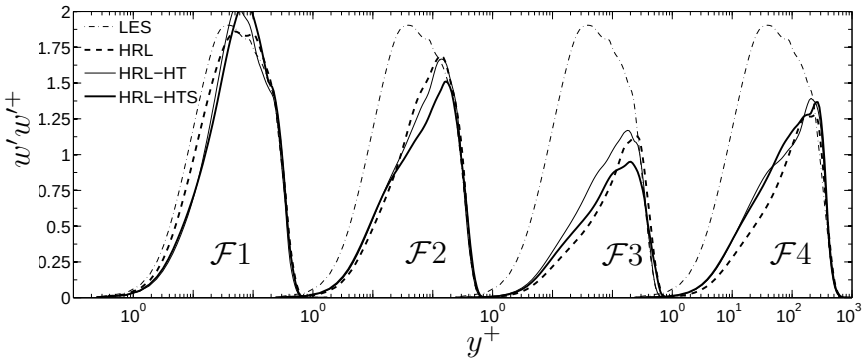

(c)

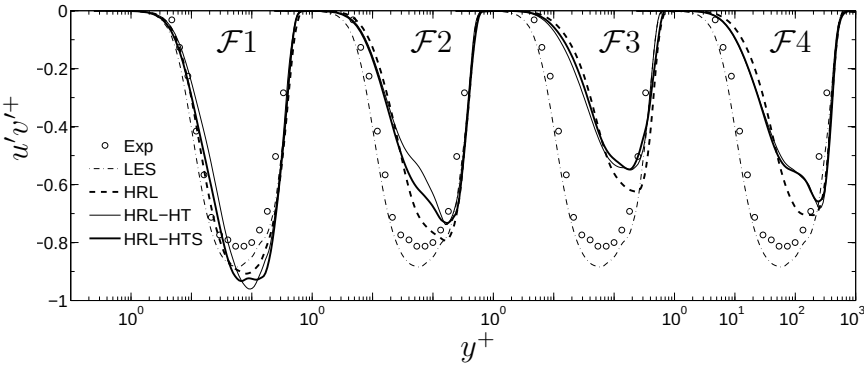

(d)

Figure 5.22: Wall-normal distribution of resolved Reynolds stresses for LES, HRL, HRL-HT, and HRL-HTS simulations $Re_\theta = 1400$: (a) $u'u'^+$; (b) $v'v'^+$; (c) $w'w'^+$; (d) $u'v'^+$.

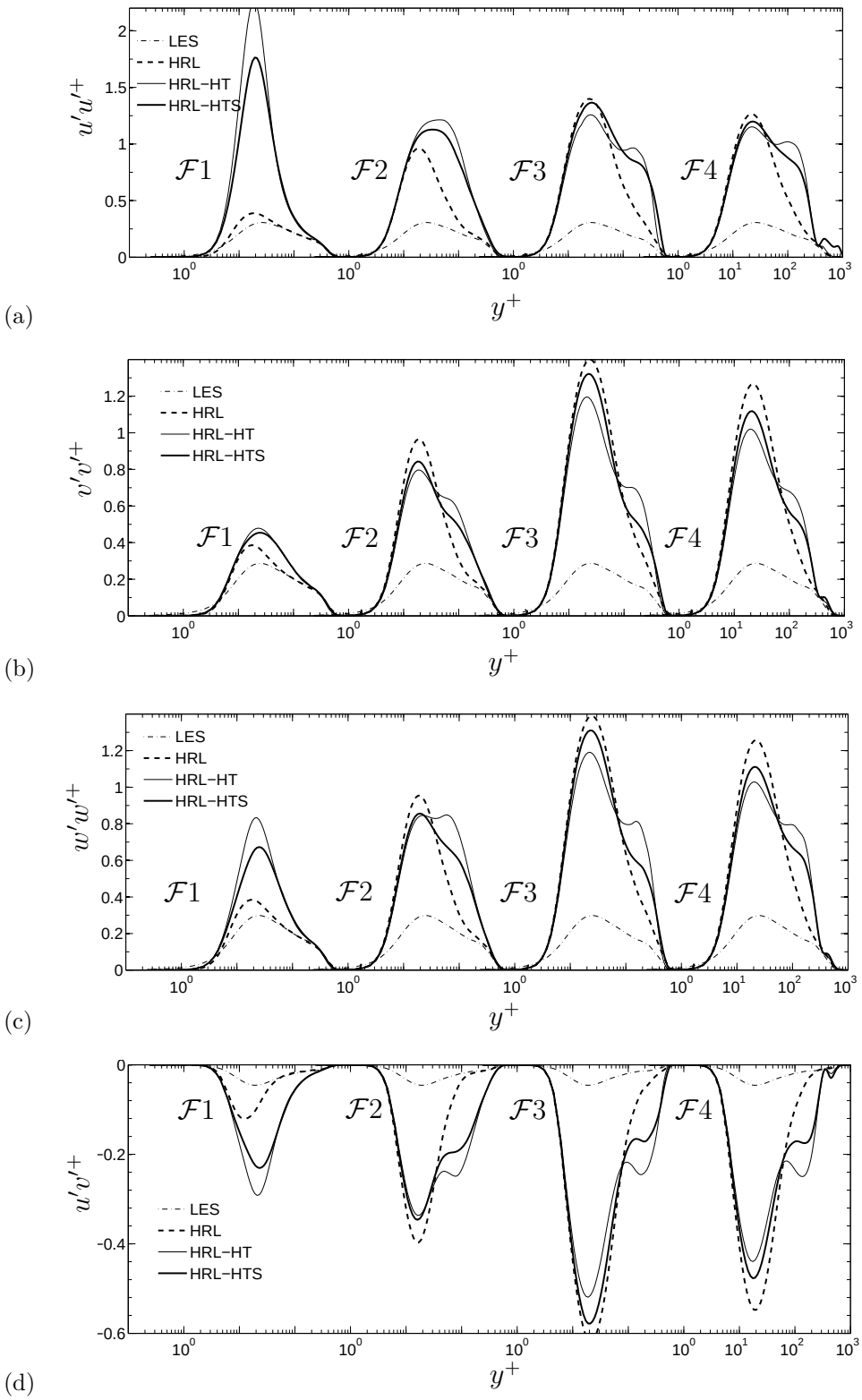

Figure 5.23: Wall-normal distribution of modeled Reynolds stresses for LES, HRL, HRL-HT, and HRL-HTS simulations $Re_\theta = 1400$: (a) $u'u'^+$; (b) $v'v'^+$; (c) $w'w'^+$; (d) $u'v'^+$.

exact HT are included. Similarly, the modeled stresses predicted by the HT-model are found in agreement with the exact HRL-HT contributions, Figure 5.23. Although the agreement between the modeled stresses obtained from the exact and the modeled HT is qualitative for some cases, the HT-model does, in general, increase the modeling contributions in the RTLT zone when compared with the modeled stresses from HRL calculations, which ignore the HT. This is a key aspect of the HT-model, since the increase in modeled stresses is what prevents the ATD in the RTLT zone. Figure 5.25 presents contours of k^{sgs} and $\mathcal{K}$ at a plane located in the RTLT zone $y^+ = 50$. The contours show the effect of the hybrid terms on the modeled turbulence, while LES predicts very small k^{sgs} structures, the HRL simulations predict quite elongated structures. These long structures are broken into smaller structures by including the HT either in its exact or modeled form.

The ability of the HT-model to maintain the unsteady near-wall structures is demonstrated in Figure 5.26. Here, coherent vortical structures are visualized in the near wall-region. Although, some dissipation in the HT-model calculation is observed, results indicate that the HT-model is able to reproduce more near-wall unsteady structures than calculations that neglect the HT.

The sensitivity of the formal hybrid RANS/LES formulation to grid resolution has been already addressed using different blending functions; therefore, this study will not be repeated for the HT-model. However, the effect of the grid resolution is evaluated by conducting calculations for a Re that slightly doubles the Re previously simulated. Here, by doubling the $Re = 3330$, the grid required by LES, Fine-3330 grid on Table 5.1, has to be increased about three times [69]. On the other hand, for the hybrid RANS/LES calculation, with the HT-model, a grid about three times coarser than the required in the LES calculation is implemented, Coarse-3330 in Table 5.1. For this calculation, only the $\mathcal{F}4$ blending function is implemented, since it extends the RTLT over all the domain, which imposes the most stringent condition

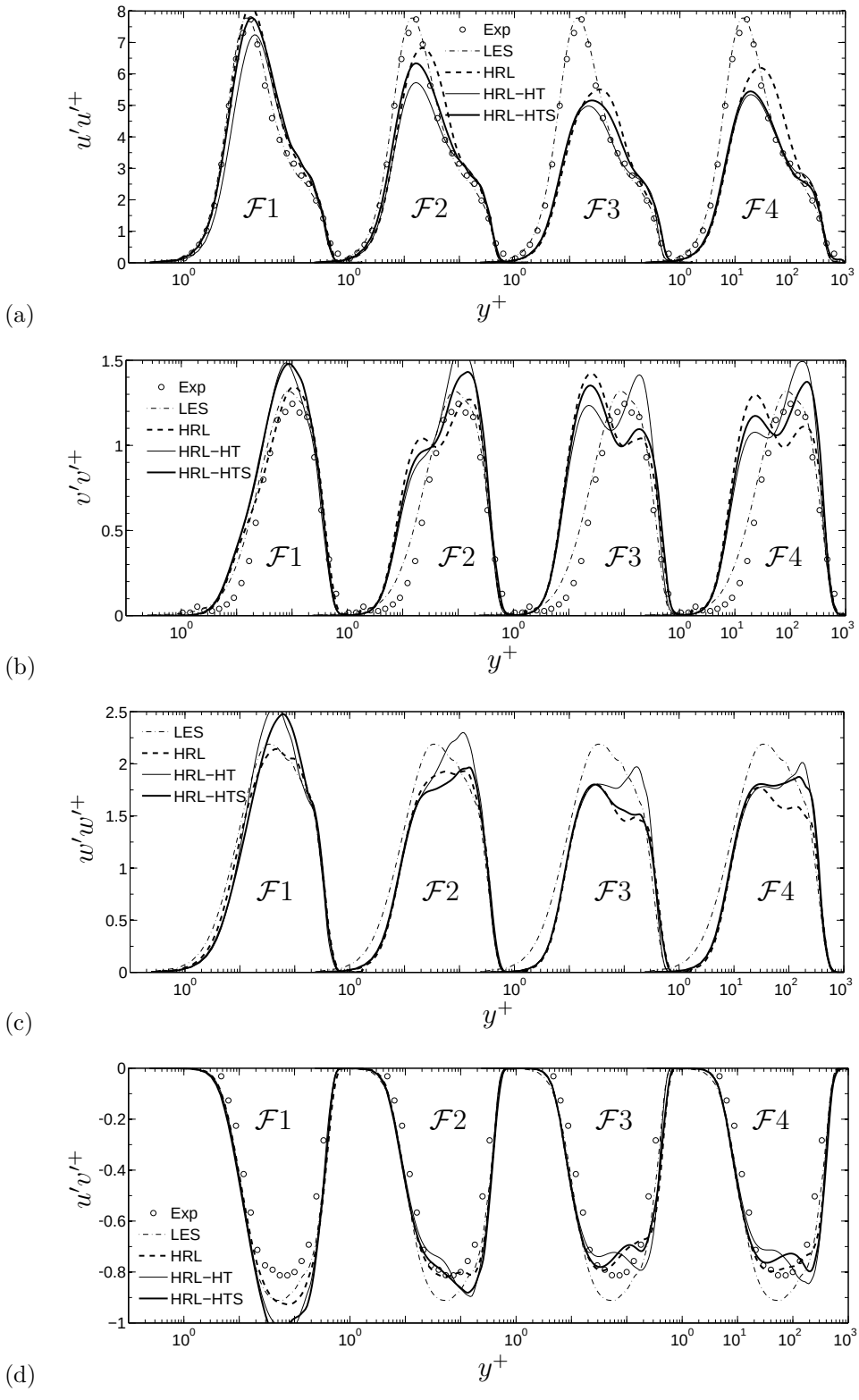

Figure 5.24: Wall-normal distribution of total, resolved plus modeled, Reynolds stresses for LES, HRL, HRL-HT, and HRL-HTS simulations $Re_\theta = 1400$: (a) $u'u'^+$; (b) $v'v'^+$; (c) $w'w'^+$; (d) $u'v'^+$.

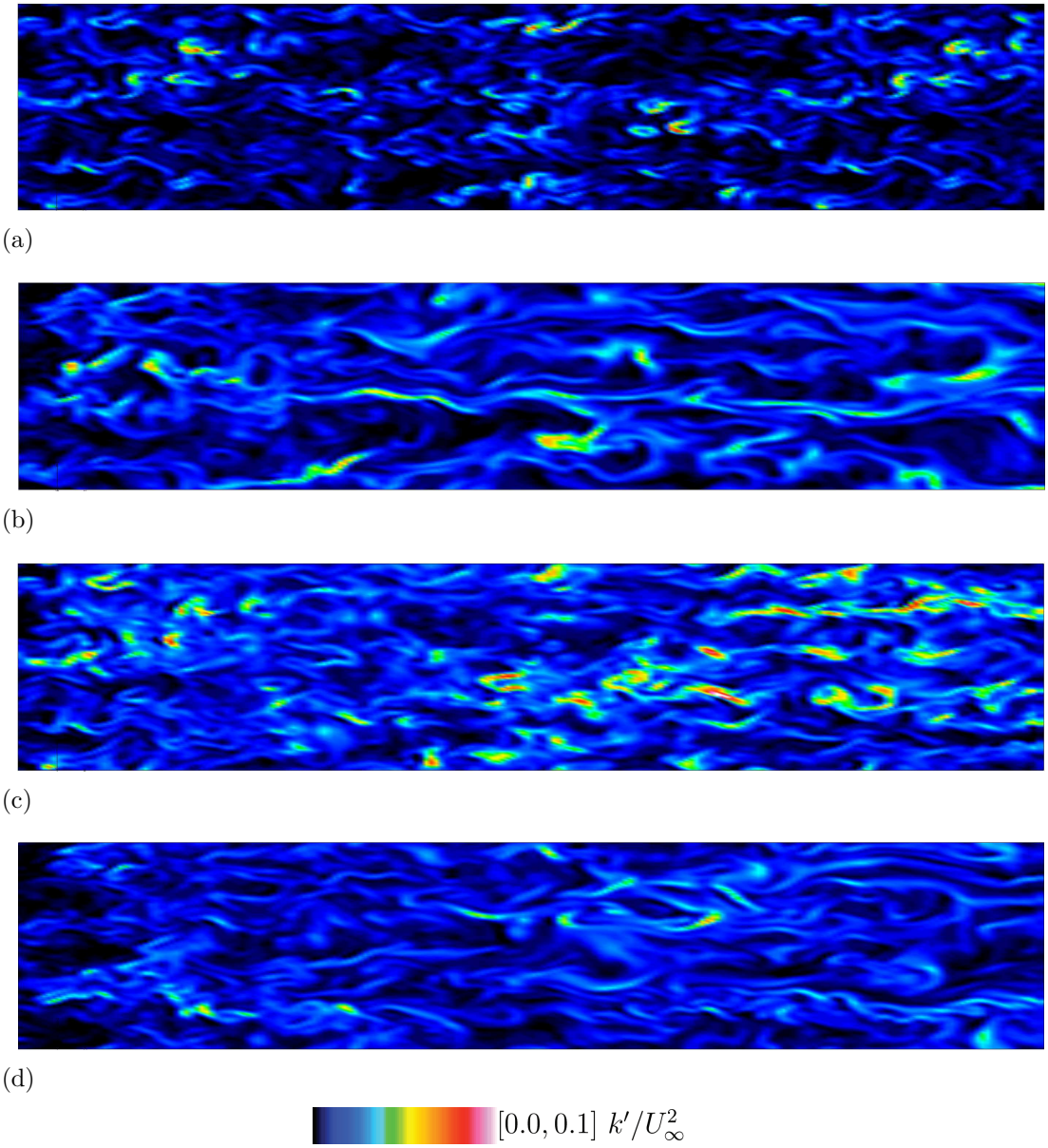

Figure 5.25: Contours of subgrid kinetic energy (k^{sgs}) and hybrid kinetic energy ($\mathcal{K}$) for $Re_\theta = 1400$ at $y^+ = 50$, ($\mathcal{F}2 = 0.74$): (a) LES; (b) HRL $\mathcal{F}2$; (c) HRL-HT $\mathcal{F}2$; (d) HRL-HTS $\mathcal{F}2$.

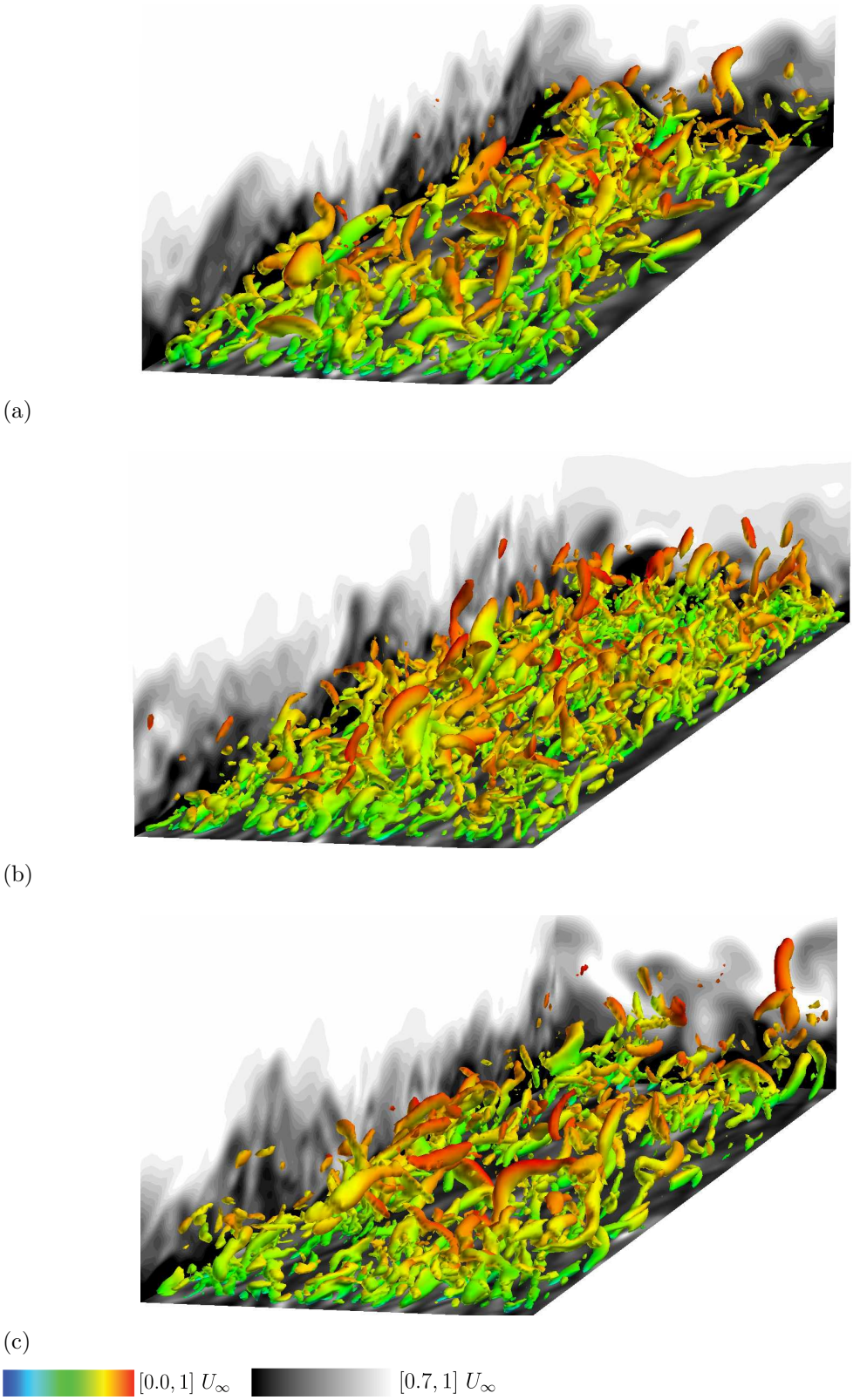

Figure 5.26: Isosurfaces of second invariant of the velocity gradient tensor ($\mathcal{Q}\theta/U_\infty = 1 \times 10^3$) colored with values of streamwise velocity, side contours streamwise velocity, for hybrid RANS/LES simulations using $\mathcal{F}2$ function, $Re_\theta = 1400$: (a) HRL (no HT); (b) HRL-HT (exact HT);(c) HRL-HTS (modeled HT).

to the HT-model. Additionally, to reduce the cost of the simulation, for this higher Re number case, the turbulent inflow is obtained by applying the boundary layer rescaling approach in the hybrid field. Consequently, the effect of the grid resolution and the ability to predict a higher Re number turbulent boundary layer flow can be addressed with one simulation.

The predicted mean velocity profile is presented in Figure 27(a). LES predictions are found in excellent agreement with experimental data, which is expected since the grid resolution is kept constant when compared with the $Re = 1400$ case. Similarly, the HRL-HTS calculations are found in good agreement with experimental data and LES calculations, here a slight departure from the experimental data at the free-stream region is reproduced. Nevertheless, it can be concluded that the HT-model is able to reproduce the law-of-the-wall at this Re number with a grid coarser than the one used in the LES calculation.

The total, resolved plus modeled, Reynolds shear stress is presented in Figure 27(b). Here, HRL-HTS predictions are found in close agreement with LES calculations and experimental data, especially in the near-wall region. Results show that ATD is not observed in this high Re number calculation, since the law-of-the-wall and the total Reynolds shear stress are predicted in close agreement with reference data. This indicates that the HT-model is robust enough to maintain the levels of modeled turbulence in the RTLT zone, even when this region completely covers the boundary layer.

The approximated cost of the simulations (required to obtain statistics for a non-dimensional time of $t_{\text{aver}} u_\tau^2/\nu_{\text{wall}} \sim 1800$ using the fine grid) given in single-processor hours on a Cray XT3 machine are the following: (a) Simulation 1 required around $6,800$ hrs., (b) Simulations 2-6 required around $13,000$ hrs., and (c) Simulation 7-10 required around $15,000$ hrs. Here, the cost of the hybrid simulations is about twice the cost of the LES simulations because each HRL-HT simulation runs simultaneously

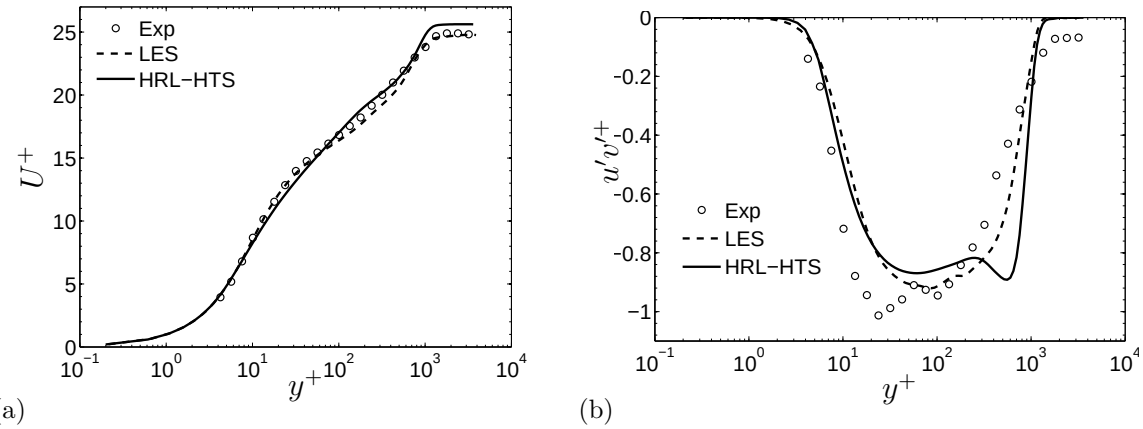

Figure 5.27: Wall-normal distribution of Mean velocity profile and total, resolved plus modeled, Reynolds-shear stress for LES and HRL-HTS simulations $Re_\theta = 3330$: (a) U^+; (b) $u'v'^+$.

a LES simulation to provide the turbulent inflow and to explicitly compute the hybrid terms. However, when the hybrid term model (HT-model) is implemented, the cost of the HRL-HTS simulation increases roughly 30% compared when the HT are neglected.

CHAPTER VI

COMPRESSIBLE TWO LEVEL SIMULATION

In this Chapter the explicit modeling approach known as Two Level Simulation, recently developed by Kemenov and Menon [48], is extended to compressible flows. In particular, the small-scale governing equations for the flow and thermodynamic variables are derived. The derived set of equations is simplified following the original assumptions of TLS. Here, the main focus is to demonstrate the potential of the TLS formulation as a near-wall model for LES. To this end turbulent boundary layer simulations are conducted to asses the potential of this new approach.

6.1 Mathematical Formulation

In order to develop the TLS governing equations the flow variables, here denoted in general as ϕ, have to be scale-separated. To this end, the approach of Kemenov and Menon [48] is followed, which splits the flow variables into two classes, large-scale $\phi^L \in \mathscr{F}^L$ and small-scale $\phi^S \in \mathscr{F}^S$, variables. Consequently, any variable that belongs to either the large-scale or small-scale class is identified with the "L" and "S" superscripts, respectively. An example of this scale-decomposition is the LES formulation, which applies a space filter to separate the flow variables into space filtered variables $\ddot{\tilde{\phi}}$ (large-scale class) and subgrid fluctuation $\phi^{\ddot{\overline{\prime\prime}}} = \phi - \ddot{\tilde{\phi}}$ (small-scale class). Another example considered by Kemenov and Menon, is to construct the large-scale field based on the underlying large-scale grid G^{Δ} and the total variable

using of the large-scale operator:

$$\phi^L(x) = \mathscr{L}^\Delta \phi(x) = \mathscr{I}^\Delta \circ \mathscr{G}^\Delta[\phi(x)] \tag{6.1a}$$

$$\mathscr{G}^\Delta : \phi(x) \rightarrow \phi^L(x_k) \tag{6.1b}$$

$$\mathscr{I}^\Delta : \phi^L(x_k) \rightarrow \phi^L(x) \tag{6.1c}$$

$$x_k \in G^\Delta \equiv \{x_1, \ldots, x_N\} \subset \Omega \tag{6.1d}$$

where, $\mathscr{G}^\Delta$ is a local averaging operator, $\mathscr{I}$ is an interpolation operator which acts on the discrete function $\phi^L(x_k)$ by mapping it to the continuous large-scale variable $\phi^L(x)$, x is the continuous space variable, and x_k are the discrete locations at which the discrete $\phi^L(x_k)$ function is known[1]. The local averaging operator $\mathscr{G}^\Delta$ can be quite general and time dependent. It is a function of the large-scale grid G^Δ and the algorithm used to obtain $\phi^L(x_k)$, in reminiscence with the LES filter operator. Further discussion on this second TLS operator example can be found in the original reference [48].

Having defined the TLS operator, the derivation of the TLS equations is conducted by decomposing the unsteady variable in its large-scale and small-scale components. However, for the sake of consistency with the compressible LES formulation, in this derivation the large-scale operator is identified as the LES filter. Here, it is only assumed that the unsteady variable is decomposed into large-scale and small-scale components.

$$\phi = \overline{\phi}^L + \phi'^S \tag{6.2}$$

Additionally, for this compressible formulation and to keep pace with standard derivations of compressible formulations like RANS or LES, a Favre density-weighted operator is defined as

$$\widetilde{\phi}^L = \frac{\overline{\rho\phi}^L}{\overline{\rho}^L} \tag{6.3}$$

[1]This is the only time the subscript does not represent tensor notation.

such that the unsteady variable can also be split in a Favre-averaged large-scale part and a small-scale fluctuations

$$\phi = \widetilde{\phi}^L + \phi''^S. \tag{6.4}$$

Having defined the scale separation, the flow and thermodynamic variables can be decomposed as follows:

$$\rho = \overline{\rho}^L + \rho'^S \tag{6.5a}$$

$$u_i = \widetilde{u}_i^L + u_i''^S \tag{6.5b}$$

$$p = \overline{p}^L + p'^S \tag{6.5c}$$

$$T = \widetilde{T}^L + T''^S \tag{6.5d}$$

$$E = \widetilde{E}^L + E''^S. \tag{6.5e}$$

Similarly, the momentum can be decomposed into large and small scale parts

$$\rho u_i = \overline{\rho}^L \widetilde{u}_i^L + \rho u_i''^S + \rho'^S \widetilde{u}_i^L \tag{6.6}$$

$$\widetilde{m}_i^L = \overline{\rho}^L \widetilde{u}_i^L \tag{6.7}$$

$$m_i''^S = \rho u_i''^S + \rho'^S \widetilde{u}_i^L. \tag{6.8}$$

where, $\widetilde{m}_i^L$ and $m_i''^S$ are the large-scale and small-scale momentum components. For the pressure decomposition, the large-scale component is obtained by directly applying the Favre operator on the state equation

$$\overline{p}^L = R\overline{\rho T}^L = R\overline{\rho}^L \widetilde{T}^L \tag{6.9}$$

the small-scale pressure fluctuation, however, it is obtained from the state equation in its scale-separated form on which the large scale terms (in brackets) cancel

$$p = R\rho T \tag{6.10a}$$

$$\overline{p}^L + p'^S = R(\overline{\rho}^L \widetilde{T}^L + \rho'^S \widetilde{T}^L + \rho T''^S) \tag{6.10b}$$

$$p'^S = R(\rho'^S \widetilde{T}^L + \rho T''^S) + [R\overline{\rho}^L \widetilde{T}^L - \overline{p}^L] \tag{6.10c}$$

$$p'^S = R(\rho'^S \widetilde{T}^L + \rho T''^S). \tag{6.10d}$$

Similarly to pressure, in the temperature decomposition the large scale temperature is obtained by applying the Favre operator in the internal energy relation

$$\overline{\rho}^L \widetilde{e}^L = \overline{\rho C_v T}^L = \overline{\rho}^L C_v \widetilde{T}^L \tag{6.11a}$$

$$\widetilde{e}^L = C_v \widetilde{T}^L \tag{6.11b}$$

the small scale temperature fluctuation is obtained by applying the scale separation in the internal energy relation and canceling the large scale variables

$$\rho e = \rho C_v T \tag{6.12a}$$

$$\overline{\rho}^L \widetilde{e}^L + \rho'^S \widetilde{e}^L + \rho e''^S = C_v(\overline{\rho}^L \widetilde{T}^L + \rho'^S \widetilde{T}^L + \rho T''^S) \tag{6.12b}$$

$$\rho e''^S = C_v \rho T''^S + [\overline{\rho}^L C_v \widetilde{T}^L - \overline{\rho}^L \widetilde{e}^L] + [\rho'^S C_v \widetilde{T}^L - \rho'^S \widetilde{e}^L] \tag{6.12c}$$

here, the terms in brackets vanish leading to the small-scale internal energy relation

$$e''^S = C_v T''^S. \tag{6.13}$$

Here, e, R, and C_v are the internal energy, gas constant and the specific heat at constant volume, respectively. For the total energy $E = e + \frac{1}{2}u_i u_i$, it is important to point out that standard compressible LES and RANS formulations include an additional turbulence contribution, k^{sgs} for LES and k^{TKE} for RANS, in their total energy definition $\widetilde{E}^{LES} = \widetilde{e} + \frac{1}{2}\widetilde{u}_i\widetilde{u}_i + k^{sgs}$ and $\widetilde{E}^{RANS} = \widetilde{e} + \frac{1}{2}\widetilde{u}_i\widetilde{u}_i + k^{TKE}$. This is a direct consequence of applying the LES or RANS operator in the total energy definition. However, if the total energy is just expanded using Eq.(6.3) the following is obtained

$$\rho E = \overline{\rho}^L(\widetilde{e}^L + \frac{1}{2}\widetilde{u}_i^L\widetilde{u}_i^L) + \rho'^S(\widetilde{e}^L + \frac{1}{2}\widetilde{u}_i^L\widetilde{u}_i^L) + \rho(e''^S + \frac{1}{2}u_i''^S u_i''^S + \widetilde{u}_i^L u_i''^S) \tag{6.14}$$

which does not include any second-order moment like $\widetilde{u_i u_i}^L - \widetilde{u}_i^L\widetilde{u}_i^L$. Therefore, to keep consistency between LES and TLS formulations the TLS total energy definition

is manipulated to include this $k^{TLS} = \widetilde{u_i u_i}^L - \widetilde{u}_i^L \widetilde{u}_i^L$ second-order moment

$$\begin{aligned}\rho E = \overline{\rho}^L(\widetilde{e}^L + \frac{1}{2}\widetilde{u}_i^L\widetilde{u}_i^L + k^{TLS}) + \rho'^S(\widetilde{e}^L + \frac{1}{2}\widetilde{u}_i^L\widetilde{u}_i^L + k^{TLS}) \\ + \rho(e''^S + \frac{1}{2}u_i''^S u_i''^S + \widetilde{u}_i^L u_i''^S - k^{TLS})\end{aligned} \tag{6.15}$$

$$\widetilde{E}^L = \widetilde{e}^L + \frac{1}{2}\widetilde{u}_i^L\widetilde{u}_i^L + k^{TLS} \tag{6.16a}$$

$$E''^S = e''^S + \frac{1}{2}u_i''^S u_i''^S + \widetilde{u}_i^L u_i''^S - k^{TLS} \tag{6.16b}$$

such that the TLS large-scale total energy definition complies with the LES definition. Here, it has to be mentioned that the additional k^{TLS} term included in the total energy identically vanishes when the TLS operator is applied in Eq.(6.15). Additionally, if the TLS and LES operators are equivalent k^{sgs} and k^{TLS} represent the same quantity, here k^{sgs} is defined as

$$k^{sgs} = \frac{1}{2}(\widetilde{u_i u_i}^L - \widetilde{u}_i^L\widetilde{u}_i^L). \tag{6.17}$$

6.1.1 Derivation of TLS Governing Equations

Having defined the scale separation of the flow and thermodynamic variables, Eq.(6.5) is substituted in the Navier-Stokes equations (2.5)-(2.7) and collect the small and large scale variables into independent equations.

- Large scale continuity equation

$$\frac{\partial\overline{\rho}^L}{\partial t} + \frac{\partial}{\partial x_j}\big(\rho u_j\big) = -\frac{\partial\rho'^S}{\partial t} = \mathcal{F}_\rho^S(\rho'^S). \tag{6.18}$$

- Small scale continuity equation

$$\frac{\partial\rho'^S}{\partial t} + \frac{\partial}{\partial x_j}\big(\rho u_j\big) = -\frac{\partial\overline{\rho}^L}{\partial t} = \mathcal{F}_\rho^L(\overline{\rho}^L). \tag{6.19}$$

- Large scale momentum equation

$$\frac{\partial}{\partial t}\big(\overline{\rho}^L\widetilde{u}_i^L\big) + \frac{\partial}{\partial x_j}\big(\rho u_j u_i\big) = \frac{\partial}{\partial x_j}\big(-\overline{p}^L\delta_{ij} + \widetilde{\tau}_{ij}^L\big) + \mathcal{F}_{\rho u_i}^S\big(\rho'^S, \overline{\rho}^L, u_i''^S, \widetilde{u}_i^L, p'^S\big) \tag{6.20}$$

$$\mathcal{F}_{\rho u_i}^S\big(\rho'^S, \overline{\rho}^L, u_i''^S, \widetilde{u}_i^L, p'^S\big) = -\frac{\partial}{\partial t}\big(\rho u_i''^S + \rho'^S\widetilde{u}_i^L\big) + \frac{\partial}{\partial x_j}\big(-p'^S\delta_{ij} + \tau_{ij}''^S\big). \tag{6.21}$$

- Small scale momentum equation

$$\frac{\partial}{\partial t}\big(\rho u_i''^S + \rho'^S \widetilde{u}_i^L\big) + \frac{\partial}{\partial x_j}\big(\rho u_j u_i\big) = \frac{\partial}{\partial x_j}\big(-p'^S\delta_{ij} + \tau_{ij}''^S\big) + \mathcal{F}^L_{\rho u_i}\big(\overline{\rho}^L, \widetilde{u}_i^L, \overline{p}^L\big) \tag{6.22}$$

$$\mathcal{F}^L_{\rho u_i}\big(\overline{\rho}^L, \widetilde{u}_i^L, \overline{p}^L\big) = -\frac{\partial}{\partial t}\big(\overline{\rho}^L \widetilde{u}_i^L\big) + \frac{\partial}{\partial x_j}\big(-\overline{p}^L\delta_{ij} + \widetilde{\tau}_{ij}^L\big). \tag{6.23}$$

- Large scale energy equation

$$\begin{aligned}\frac{\partial}{\partial t}\big(\overline{\rho}^L \widetilde{E}^L\big) + \frac{\partial}{\partial x_j}\big(\rho u_j(E + p/\rho)\big) = \frac{\partial}{\partial x_j}\Big(-\widetilde{q}_j^L + \widetilde{u}_i^L\widetilde{\tau}_{ij}^L\Big) \\ + \mathcal{F}^S_{\rho E}\big(\rho'^S, \overline{\rho}^L, u_i''^S, \widetilde{u}_i^L, T''^S, \widetilde{T}^L, E''^S, \widetilde{E}^L\big)\end{aligned} \tag{6.24}$$

$$\begin{aligned}\mathcal{F}^S_{\rho E}\big(\rho'^S, \overline{\rho}^L, u_i''^S, \widetilde{u}_i^L, T''^S, \widetilde{T}^L, E''^S, \widetilde{E}^L\big) = -\frac{\partial}{\partial t}\big(\rho'^S\widetilde{E}^L + \rho E''^S\big) \\ + \frac{\partial}{\partial x_j}\big(-q''^S + \widetilde{u}_i^L\tau_{ij}''^S + u_i''^S\widetilde{\tau}_{ij}^L + u_i''^S\tau_{ij}''^S\big).\end{aligned} \tag{6.25}$$

- Small scale energy equation

$$\begin{aligned}\frac{\partial}{\partial t}\big(\rho'^S\widetilde{E}^L + \rho E''^S\big) + \frac{\partial}{\partial x_j}\big(\rho u_j(E + p/\rho)\big) = \frac{\partial}{\partial x_j}\Big(-q_j''^S + \widetilde{u}_i^L\tau_{ij}''^S \\ + u_i''^S\widetilde{\tau}_{ij}^L + u_i''^S\tau_{ij}''^S\Big) + \mathcal{F}^L_{\rho E}\big(\overline{\rho}^L, \widetilde{u}_i^L, \widetilde{T}^L, \widetilde{E}^L\big)\end{aligned} \tag{6.26}$$

$$\mathcal{F}^L_{\rho E}\big(\overline{\rho}^L, \widetilde{u}_i^L, \widetilde{T}^L, \widetilde{E}^L\big) = -\frac{\partial}{\partial t}\big(\overline{\rho}^L\widetilde{E}^L\big) + \frac{\partial}{\partial x_j}\big(-\widetilde{q}^L + \widetilde{u}_i^L\widetilde{\tau}_{ij}^L\big). \tag{6.27}$$

Additionally, the nonlinear convection terms can be split into small and large scale terms [48].

- Large scale continuity equation

$$\frac{\partial\overline{\rho}^L}{\partial t} + \frac{\partial}{\partial x_j}\big[\rho u_j\big]^L = \mathcal{G}^S_\rho(\rho'^S, \overline{\rho}^L, u_i'^S, \widetilde{u}_i^L) \tag{6.28}$$

$$\mathcal{G}^S_\rho\big(\rho'^S, \overline{\rho}^L, u_i''^S, \widetilde{u}_i^L\big) = \mathcal{F}^S_\rho(\rho'^S) - \frac{\partial}{\partial x_j}\big[\rho u_j\big]^S. \tag{6.29}$$

- Small scale continuity equation

$$\frac{\partial\rho'^S}{\partial t} + \frac{\partial}{\partial x_j}\big[\rho u_j\big]^S = \mathcal{G}^L_\rho(\rho'^S, \overline{\rho}^L, u_i'^S, \widetilde{u}_i^L) \tag{6.30}$$

$$\mathcal{G}^L_\rho(\rho'^S, \overline{\rho}^L, u_i'^S, \widetilde{u}_i^L) = \mathcal{F}^L_\rho(\overline{\rho}^L) - \frac{\partial}{\partial x_j}\big[\rho u_j\big]^L. \tag{6.31}$$

- Large scale momentum equation

$$\frac{\partial}{\partial t}\big(\overline{\rho}^L\widetilde{u}_i^L\big)+\frac{\partial}{\partial x_j}\big[\rho u_j u_i\big]^L=\frac{\partial}{\partial x_j}\big(-\overline{p}^L\delta_{ij}+\widetilde{\tau}_{ij}^L\big) \\ +\mathcal{G}_{\rho u_i}^S\big(\rho'^S,\overline{\rho}^L,u_i''^S,\widetilde{u}_i^L,p'^S\big) \tag{6.32}$$

$$\mathcal{G}_{\rho u_i}^S\big(\rho'^S,\overline{\rho}^L,u_i''^S,\widetilde{u}_i^L,p'^S\big)=\mathcal{F}_{\rho u_i}^S\big(\rho'^S,\overline{\rho}^L,u_i''^S,\widetilde{u}_i^L,p'^S\big)-\frac{\partial}{\partial x_j}\big[\rho u_j u_i\big]^S. \tag{6.33}$$

- Small scale momentum equation

$$\frac{\partial}{\partial t}\big(\rho u_i''^S+\rho'^S\widetilde{u}_i^L\big)+\frac{\partial}{\partial x_j}\big[\rho u_j u_i\big]^S=\frac{\partial}{\partial x_j}\big(-p'^S\delta_{ij}+\tau_{ij}''^S\big) \\ +\mathcal{G}_{\rho u_i}^L\big(\rho'^S,\overline{\rho}^L,u_i''^S,\widetilde{u}_i^L,\overline{p}^L\big) \tag{6.34}$$

$$\mathcal{G}_{\rho u_i}^L\big(\rho'^S,\overline{\rho}^L,u_i''^S,\widetilde{u}_i^L,\overline{p}^L\big)=\mathcal{F}_{\rho u_i}^L\big(\overline{\rho}^L,\widetilde{u}_i^L,\overline{p}^L\big)-\frac{\partial}{\partial x_j}\big[\rho u_j u_i\big]^L. \tag{6.35}$$

- Large scale energy equation

$$\frac{\partial}{\partial t}\big(\overline{\rho}^L\widetilde{E}^L\big)+\frac{\partial}{\partial x_j}\big[\rho u_j(E+p/\rho)\big]^L=\frac{\partial}{\partial x_j}\Big(-\widetilde{q}_j^L+\widetilde{u}_i^L\widetilde{\tau}_{ij}^L\Big) \\ +\mathcal{G}_{\rho E}^S\big(\rho'^S,\overline{\rho}^L,u_i''^S,\widetilde{u}_i^L,T''^S,p'^S,\overline{p}^L,E''^S,\widetilde{E}^L\big) \tag{6.36}$$

$$\mathcal{G}_{\rho E}^S\big(\rho'^S,\overline{\rho}^L,u_i''^S,\widetilde{u}_i^L,T''^S,\widetilde{T}^L,p'^S,\overline{p}^L,E''^S,\widetilde{E}^L\big)= \\ \mathcal{F}_{\rho E}^S\big(\rho'^S,\overline{\rho}^L,u_i''^S,\widetilde{u}_i^L,T''^S,\widetilde{T}^L,E''^S,\widetilde{E}^L\big)-\frac{\partial}{\partial x_j}\big[\rho u_j(E+p/\rho)\big]^S. \tag{6.37}$$

- Small scale energy equation

$$\frac{\partial}{\partial t}\big(\rho'^S\widetilde{E}^L+\rho E''^S\big)+\frac{\partial}{\partial x_j}\big[\rho u_j(E+p/\rho)\big]^S=\frac{\partial}{\partial x_j}\Big(-q_j''^S+\widetilde{u}_i^L\tau_{ij}''^S \\ +u_i''^S\widetilde{\tau}_{ij}^L+u_i''^S\tau_{ij}''^S\Big)+\mathcal{G}_{\rho E}^L\big(\rho'^S,\overline{\rho}^L,u_i''^S,\widetilde{u}_i^L,\widetilde{T}^L,p''^S,\widetilde{p}^L,E''^S,\widetilde{E}^L\big) \tag{6.38}$$

$$\mathcal{G}_{\rho E}^L\big(\rho'^S,\overline{\rho}^L,u_i''^S,\widetilde{u}_i^L,\widetilde{T}^L,p''^S,\widetilde{p}^L,E''^S,\widetilde{E}^L\big)=\mathcal{F}_{\rho E}^L\big(\overline{\rho}^L,\widetilde{u}_i^L,\widetilde{T}^L,\widetilde{E}^L\big) \\ -\frac{\partial}{\partial x_j}\big[\rho u_j(E+p/\rho)\big]^L. \tag{6.39}$$

These governing equations represent the exact Navier-Stokes equations and indicate that the large and small scales are mutually affected, through the forcing functions $\mathcal{G}_{\rho}^{S}$, $\mathcal{G}_{\rho}^{L}$, $\mathcal{G}_{\rho u_i}^{S}$, $\mathcal{G}_{\rho u_i}^{L}$, $\mathcal{G}_{\rho E}^{S}$, and $\mathcal{G}_{\rho E}^{L}$. However, it is important to stress, that the scale separation conducted previously doubled the number of governing equations, without bringing any additional information, complicating drastically the original problem. Thus some additional manipulations have to be conducted and additional assumptions have to be made to simplify this set of equations. First, it is trivial to demonstrate that the addition of the forcing functions in each large and small scale equations reduces identically to zero. Further more, this addition represent the original Navier-Stokes equations with all the terms arranged in the same side of the equal sign [48]:

$$\mathcal{G}_{\rho}^{L}(\rho'^{S}, \overline{\rho}^{L}, u_i'^{S}, \widetilde{u}_i^{L}) + \mathcal{G}_{\rho}^{S}\big(\rho'^{S}, \overline{\rho}^{L}, u_i''^{S}, \widetilde{u}_i^{L}\big) = 0 \tag{6.40}$$

$$\mathcal{G}_{\rho u_i}^{L}\big(\rho'^{S}, \overline{\rho}^{L}, u_i''^{S}, \widetilde{u}_i^{L}, \overline{p}^{L}\big) + \mathcal{G}_{\rho u_i}^{S}\big(\rho'^{S}, \overline{\rho}^{L}, u_i''^{S}, \widetilde{u}_i^{L}, p'^{S}\big) = 0 \tag{6.41}$$

$$\begin{aligned}\mathcal{G}_{\rho E}^{L}\big(\rho'^{S}, \overline{\rho}^{L}, u_i''^{S}, \widetilde{u}_i^{L}, \widetilde{T}^{L}, p''^{S}, \widetilde{p}^{L}, E''^{S}, \widetilde{E}^{L}\big) \\ + \mathcal{G}_{\rho E}^{S}\big(\rho'^{S}, \overline{\rho}^{L}, u_i''^{S}, \widetilde{u}_i^{L}, T''^{S}, \widetilde{T}^{L}, p'^{S}, \overline{p}^{L}, E''^{S}, \widetilde{E}^{L}\big) = 0.\end{aligned} \tag{6.42}$$

Second, the arguments presented by Kemenov and Menon [48] which argue with the properties of the large and small scales, regardless of the governing equations (these arguments are not reproduced here) are used to claim that the forcing functions $\mathcal{G}_{\rho}^{S}$, $\mathcal{G}_{\rho}^{L}$, $\mathcal{G}_{\rho u_i}^{S}$, $\mathcal{G}_{\rho u_i}^{L}$, $\mathcal{G}_{\rho E}^{S}$, and $\mathcal{G}_{\rho E}^{L}$ are independently equal to zero[2], such that the final TLS equations can be obtained in a much tractable form:

- Large scale continuity equation

$$\frac{\partial \overline{\rho}^{L}}{\partial t} + \frac{\partial}{\partial x_j}\big[\rho u_j\big]^{L} = 0. \tag{6.43}$$

[2]This condition can be also introduced as a model assumption required to simplify the small-scale equations, just like the commutativity assumption between the LES filter operator and differentiation which does not hold in general but it is assumed anyway, and its validity will be supported by the accuracy of the calculations.

- Small scale continuity equation

$$\frac{\partial \rho'^S}{\partial t} + \frac{\partial}{\partial x_j}(\rho u_j) = \frac{\partial}{\partial x_j}\big[\rho u_j\big]^L = \frac{\partial}{\partial x_j}(\overline{\rho}^L \widetilde{u}_j^L). \tag{6.44}$$

- Large scale momentum equation

$$\frac{\partial}{\partial t}(\overline{\rho}^L \widetilde{u}_i^L) + \frac{\partial}{\partial x_j}\big[\rho u_j u_i\big]^L = \frac{\partial}{\partial x_j}\big(- \overline{p}^L \delta_{ij} + \widetilde{\tau}_{ij}^L\big). \tag{6.45}$$

- Small scale momentum equation

$$\frac{\partial}{\partial t}(\rho u_i''^S + \rho'^S \widetilde{u}_i^L) + \frac{\partial}{\partial x_j}(\rho u_j u_i) = \frac{\partial}{\partial x_j}\big(- p'^S \delta_{ij} + \tau_{ij}''^S\big) + \frac{\partial}{\partial x_j}\big[\rho u_j u_i\big]^L. \tag{6.46}$$

- Large scale energy equation

$$\frac{\partial}{\partial t}(\overline{\rho}^L \widetilde{E}^L) + \frac{\partial}{\partial x_j}\big[\rho u_j (E + p/\rho)\big]^L = \frac{\partial}{\partial x_j}\Big(- \widetilde{q}_j^L + \widetilde{u}_i^L \widetilde{\tau}_{ij}^L\Big). \tag{6.47}$$

- Small scale energy equation

$$\begin{aligned}\frac{\partial}{\partial t}(\rho'^S \widetilde{E}^L + \rho E''^S) + \frac{\partial}{\partial x_j}\big(\rho u_j (E + p/\rho)\big) = \frac{\partial}{\partial x_j}\Big(& - q_j''^S + \widetilde{u}_i^L \tau_{ij}''^S \\ & + u_i''^S \widetilde{\tau}_{ij}^L + u_i''^S \tau_{ij}''^S\Big) + \frac{\partial}{\partial x_j}\big[\rho u_j (E + p/\rho)\big]^L.\end{aligned} \tag{6.48}$$

- The viscous stress

$$\tau_{ij} = \mu T_{ij} = (\overline{\mu}^L + \mu'^S)(\widetilde{T}_{ij}^L + T_{ij}''^S) \tag{6.49}$$

$$T_{ij} = 2(S_{ij} - \frac{1}{3} S_{kk} \delta_{ij}) \tag{6.50}$$

$$S_{ij} = \frac{1}{2}\Big(\frac{\partial u_i}{\partial x_j} + \frac{\partial u_j}{\partial x_i}\Big) = \frac{1}{2}\Big(\frac{\partial \widetilde{u}_i^L}{\partial x_j} + \frac{\partial \widetilde{u}_j^L}{\partial x_i}\Big) + \frac{1}{2}\Big(\frac{\partial u_i''^S}{\partial x_j} + \frac{\partial u_j''^S}{\partial x_i}\Big). \tag{6.51}$$

- Heat flux

$$q_i = \kappa \frac{\partial T}{\partial x_i} = (\overline{\kappa}^L + \kappa'^S)\Big(\frac{\partial \widetilde{T}^L}{\partial x_i} + \frac{\partial T''^S}{\partial x_i}\Big). \tag{6.52}$$

This final set of equations establishes the interactions between large and small scales in an explicit form. The equations indicate that the nonlinear convective terms

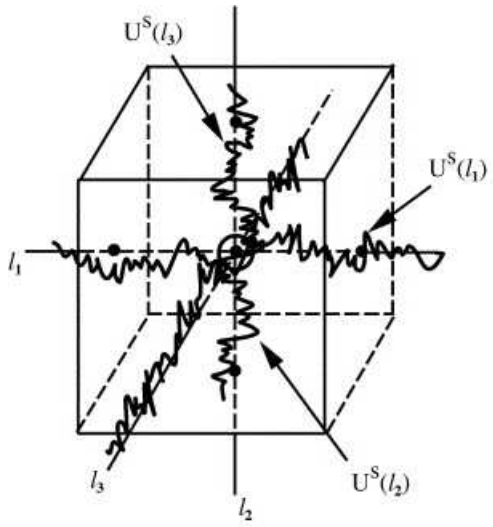

Figure 6.1: Arrangement of one-dimensional lines on the three dimensional domain. The small-scale velocity field is superimposed in the lines for illustration purposes, taken from Kemenov and Menon [48].

act as forcing function for the small-scale equations. This has physical consistency with spectral analysis, that establishes that the nonlinearities in the convective terms are responsible for the transfer of turbulent kinetic energy from the large to the small scales [72]. On the other hand, the large-scale equations are affected by the small scales through the turbulent unclosed terms, which are computed directly from the small scale field.

6.1.2 Treatment of The Small-Scale Equation

It is important to remark that the equations here derived are just another form of the Navier-Stokes equations (or in the computational sense the DNS equations) and they cannot be solved practically for high Reynolds number flows. Therefore, the equations have to be simplified if the method is going to be feasible.

The small-scale equations are simplified following the approach of Kemenov and Menon [48]. These equations are solved on a collection of one-dimensional lines embedded in the large-scale grid and parallel to each spatial direction (see Figure 6.1). This set of lines span the small-scale domain defined as $\Omega_l = \{l_k^j\}, k = 1, 2, 3, j =$

$1, \ldots, N_k$. Where, N_k represents the number of lines parallel to the spatial direction x_k. Here, the spatial coordinates of each line are defined as $l_1 = \{x_1, x_2 = C_2, x_3 = C_3\}$ (here the line l_1 is used for demonstrative purposes) , where x_1 is the only spatial variable and C_1 and C_2 are constants. This treatment of the small-scale equations require a total number grid points of $N_L^3 + 3N_L^2 N_s$, where N_L is the number of large-scale grid-points and N_s is the number of small-scale grid-points in the one-dimensional lines.

Having defined the small-scale lines, the small-scale field over each line is defined as $\phi'^S(x_i, t) \rightarrow \phi'^S_{l_k}(l_k, t)$, with $x_i \in l_k \subset \Omega$. What implies that the small-scale field is just function of a particular line in space, and it is not coupled with fields in other lines. However, at the lines intersections the small-scale field is overdetermined since it is provided by three independent lines. Here, the problem is resolved by defining the small-scale field as an average over the three lines at that point [48]. Further more, the one dimensional description of the small-scale field poses some problems in the definition of derivatives in the directions orthogonal to the lines. To avoid this problem, the assumptions demonstrated in free and wall-bounded flows by Kemenov and Menon [48, 49] are implemented:

(i) For each small-scale velocity component $u_i''^S$, the second derivative along the line l_k is equal to the averaged sum of the second derivatives along all three orthogonal directions:

$$\frac{\partial^2 u_i'^S}{\partial x_k^2} = \frac{1}{3} \sum_{j=1}^{3} \frac{\partial^2 u_i'^S}{\partial x_j^2}, \; i, k = 1, 2, 3. \tag{6.53}$$

(ii) Changes in the small-scale part of the convective derivatives are neglected in directions transverse ($j \neq k$) to the line l_k:

$$\begin{aligned} &\frac{\partial}{\partial x_j}\left[(\overline{\rho}^L + \rho'^S)(\widetilde{u}_j^L + u_j''^S)(\widetilde{\phi}^L + \phi''^S)\right]^S = \\ &\qquad \frac{\partial}{\partial x_j}\left[(\overline{\rho}^L + \rho'^S(l_k))(\widetilde{u}_j^L + u_j''^S(l_k))(\widetilde{\phi}^L + \phi''^S(l_k))\right]^S. \end{aligned} \tag{6.54}$$

Here, it is important to point out that assumption (ii) implies that the first derivatives of the small-scale variables are neglected in directions orthogonal to the small-scale line. Finally, with the only purpose of simplifying the notation in the final equations, the following shortcut is defined

$$\rho(l_k)u_j(l_k)\phi(l_k) = (\overline{\rho}^L + \rho'^S(l_k))(\widetilde{u}_j^L + u_j''^S(l_k))(\widetilde{\phi}^L + \phi''^S(l_k)). \tag{6.55}$$

By applying the previous assumptions in Eqs. (6.44), (6.46) and (6.48) the one-dimensional small-scale equations take the final form:

- Continuity:

$$\frac{\partial \rho'^S}{\partial t} + \frac{\partial}{\partial x_j}\big[\rho(l_k)u_j(l_k))\big] = \frac{\partial}{\partial x_j}\big[\rho u_j\big]^L = \frac{\partial}{\partial x_j}\big(\overline{\rho}^L\widetilde{u}_j^L\big). \tag{6.56}$$

- Momentum:

$$\begin{aligned}\frac{\partial}{\partial t}\big(\rho u_i''^S + \rho'^S\widetilde{u}_i^L\big) + \frac{\partial}{\partial x_j}\big[\rho(l_k)u_j(l_k)u_i(l_k)\big] =& \frac{\partial}{\partial x_j}\big(-p'^S(l_k)\delta_{ij} + \tau_{ij}''^S(l_k)\big) \\ &+ \frac{\partial}{\partial x_j}\big[\rho(l_k)u_j(l_k)u_i(l_k)\big]^L.\end{aligned} \tag{6.57}$$

- Energy:

$$\begin{aligned}\frac{\partial}{\partial t}\big(\rho'^S\widetilde{E}^L + \rho E''^S\big) + \frac{\partial}{\partial x_j}\big[\rho(l_k)u_j(l_k)(E(l_k) + p(l_k)/\rho(l_k))\big] = \\ \frac{\partial}{\partial x_j}\Big(-q_j''^S(l_k) + \widetilde{u}_i^L\tau_{ij}''^S(l_k) + u_i''^S(l_k)\widetilde{\tau}_{ij}^L + u_i''^S(l_k)\tau_{ij}''^S(l_k)\Big) \\ + \frac{\partial}{\partial x_j}\big[\rho(l_k)u_j(l_k)(E(l_k) + p(l_k)/\rho(l_k))\big]^L.\end{aligned} \tag{6.58}$$

Here, it is pertinent to expand the transport terms of the small-scale equations to show their final form, here $(l_1, l_2, l_3) \parallel (x_1, x_2, x_3)$.

- Convective terms in the continuity equation:

Line l_1

$$\frac{\partial}{\partial x_j}(\rho u_j) = \frac{\partial}{\partial x}\big(\rho u\big) + \frac{\partial}{\partial y}\big(\overline{\rho}^L \widetilde{v}^L\big) + \frac{\partial}{\partial z}\big(\overline{\rho}^L \widetilde{w}^L\big). \tag{6.59}$$

Line l_2

$$\frac{\partial}{\partial x_j}(\rho u_j) = \frac{\partial}{\partial x}\big(\overline{\rho}^L \widetilde{u}^L\big) + \frac{\partial}{\partial y}\big(\rho v\big) + \frac{\partial}{\partial z}\big(\overline{\rho}^L \widetilde{w}^L\big). \tag{6.60}$$

Line l_3

$$\frac{\partial}{\partial x_j}(\rho u_j) = \frac{\partial}{\partial x}\big(\overline{\rho}^L \widetilde{u}^L\big) + \frac{\partial}{\partial y}\big(\overline{\rho}^L \widetilde{v}^L\big) + \frac{\partial}{\partial z}\big(\rho w\big). \tag{6.61}$$

- Transport terms in the momentum equation:

Line l_1

$$\begin{aligned}\frac{\partial}{\partial x_j}(\rho u_j u_i + p'^S \delta_{ij} - \tau''^S_{ij}) = &\frac{\partial}{\partial x}(\rho u_i u) + \overline{\rho}^L v \frac{\partial \widetilde{u}_i^L}{\partial y} + \overline{\rho}^L w \frac{\partial \widetilde{u}_i^L}{\partial z} \\ &+ \widetilde{u}_i^L \big[\frac{\partial}{\partial y}(\overline{\rho}^L \widetilde{v}^L) + \frac{\partial}{\partial z}(\overline{\rho}^L \widetilde{w}^L)\big] \\ &+ m_i''^S \big[\frac{\partial \widetilde{v}^L}{\partial y} + \frac{\partial \widetilde{w}^L}{\partial z}\big] \\ &+ \frac{\partial p'^S}{\partial x}\delta_{i1} - \overline{\mu}^L \big(3\frac{\partial^2 u_i''^S}{\partial x^2} + \frac{1}{3}\frac{\partial^2 u''^S}{\partial x^2}\big).\end{aligned} \tag{6.62}$$

Line l_2

$$\begin{aligned}\frac{\partial}{\partial x_j}(\rho u_j u_i + p'^S \delta_{ij} - \tau''^S_{ij}) = &\frac{\partial}{\partial y}(\rho u_i v) + \overline{\rho}^L u \frac{\partial \widetilde{u}_i^L}{\partial x} + \overline{\rho}^L w \frac{\partial \widetilde{u}_i^L}{\partial z} \\ &+ \widetilde{u}_i^L \big[\frac{\partial}{\partial x}(\overline{\rho}^L \widetilde{u}^L) + \frac{\partial}{\partial z}(\overline{\rho}^L \widetilde{w}^L)\big] \\ &+ m_i''^S \big[\frac{\partial \widetilde{u}^L}{\partial x} + \frac{\partial \widetilde{w}^L}{\partial z}\big] \\ &+ \frac{\partial p'^S}{\partial y}\delta_{i2} - \overline{\mu}^L \big(3\frac{\partial^2 u_i''^S}{\partial y^2} + \frac{1}{3}\frac{\partial^2 v''^S}{\partial y^2}\big).\end{aligned} \tag{6.63}$$

Line l_3

$$\begin{aligned}\frac{\partial}{\partial x_j}(\rho u_j u_i + p'^S\delta_{ij} - \tau''^S_{ij}) = \frac{\partial}{\partial z}(\rho u_i w) + \overline{\rho}^L u\frac{\partial \widetilde{u}_i^L}{\partial x} + \overline{\rho}^L v\frac{\partial \widetilde{u}_i^L}{\partial y} \\ + \widetilde{u}_i^L\big[\frac{\partial}{\partial x}(\overline{\rho}^L\widetilde{u}^L) + \frac{\partial}{\partial y}(\overline{\rho}^L\widetilde{v}^L)\big] \\ + m''^S_i\big[\frac{\partial \widetilde{u}^L}{\partial x} + \frac{\partial \widetilde{v}^L}{\partial y}\big] \\ + \frac{\partial p'^S}{\partial z}\delta_{i3} - \overline{\mu}^L\big(3\frac{\partial^2 u''^S_i}{\partial z^2} + \frac{1}{3}\frac{\partial^2 w''^S}{\partial z^2}\big)\end{aligned} \tag{6.64}$$

- Transport terms in the energy equation:

Line l_1

$$\begin{aligned}\frac{\partial}{\partial x_j}\Big(\rho u_j E + u_j p - \overline{\kappa}^L\frac{\partial T''^S}{\partial x_j} - u_i\tau''^S_{ij} - u''^S_i\widetilde{\tau}^L_{ij}\Big) = \frac{\partial}{\partial x}\Big(\rho uE + up - \overline{\kappa}^L\frac{\partial T''^S}{\partial x}\Big) \\ +\overline{\rho}^L v\frac{\partial \widetilde{E}^L}{\partial y} + \overline{\rho}^L w\frac{\partial \widetilde{E}^L}{\partial z} + \widetilde{E}^L\Big[\frac{\partial}{\partial y}(\overline{\rho}^L\widetilde{v}^L) + \frac{\partial}{\partial z}(\overline{\rho}^L\widetilde{w}^L)\Big] \\ +(\rho E''^S + \rho'^S\widetilde{E}^L)\Big[\frac{\partial \widetilde{v}^L}{\partial y} + \frac{\partial \widetilde{w}^L}{\partial z}\Big] + p\frac{\partial \widetilde{v}^L}{\partial y} + v\frac{\partial \overline{p}^L}{\partial y} + p\frac{\partial \widetilde{w}^L}{\partial z} + w\frac{\partial \overline{p}^L}{\partial z} \\ -\overline{\mu}^L u_i\Big[3\frac{\partial^2 u''^S_i}{\partial x^2} + \frac{1}{3}\frac{\partial^2 u''^S}{\partial x^2}\delta_{i1}\Big] - \overline{\mu}^L\frac{4}{3}\frac{\partial \widetilde{u}^L}{\partial x}\frac{\partial u''^S}{\partial x} \\ -\overline{\mu}^L\Big[\frac{\partial \widetilde{u}^L}{\partial y}\frac{\partial v''^S}{\partial x} + \frac{\partial \widetilde{u}^L}{\partial z}\frac{\partial w''^S}{\partial x}\Big] - \overline{\mu}^L\Big[\frac{\partial \widetilde{v}^L}{\partial x}\frac{\partial v''^S}{\partial x} - \frac{2}{3}\frac{\partial \widetilde{v}^L}{\partial y}\frac{\partial u''^S}{\partial x}\Big] \\ -\overline{\mu}^L\Big[\frac{\partial \widetilde{w}^L}{\partial x}\frac{\partial w''^S}{\partial x} - \frac{2}{3}\frac{\partial \widetilde{w}^L}{\partial z}\frac{\partial u''^S}{\partial x}\Big]\end{aligned} \tag{6.65}$$

Line l_2

$$\begin{aligned}\frac{\partial}{\partial x_j}\Big(\rho u_j E + u_j p - \overline{\kappa}^L\frac{\partial T''^S}{\partial x_j} - u_i\tau''^S_{ij} - u''^S_i\widetilde{\tau}^L_{ij}\Big) = \frac{\partial}{\partial y}\Big(\rho vE + vp - \overline{\kappa}^L\frac{\partial T''^S}{\partial y}\Big) \\ +\overline{\rho}^L u\frac{\partial \widetilde{E}^L}{\partial x} + \overline{\rho}^L w\frac{\partial \widetilde{E}^L}{\partial z} + \widetilde{E}^L\Big[\frac{\partial}{\partial x}(\overline{\rho}^L\widetilde{u}^L) + \frac{\partial}{\partial z}(\overline{\rho}^L\widetilde{w}^L)\Big] \\ +(\rho E''^S + \rho'^S\widetilde{E}^L)\Big[\frac{\partial \widetilde{u}^L}{\partial x} + \frac{\partial \widetilde{w}^L}{\partial z}\Big] + p\frac{\partial \widetilde{u}^L}{\partial x} + u\frac{\partial \overline{p}^L}{\partial x} + p\frac{\partial \widetilde{w}^L}{\partial z} + w\frac{\partial \overline{p}^L}{\partial z} \\ -\overline{\mu}^L u_i\Big[3\frac{\partial^2 u''^S_i}{\partial y^2} + \frac{1}{3}\frac{\partial^2 v''^S}{\partial y^2}\delta_{i2}\Big] - \overline{\mu}^L\Big[\frac{\partial \widetilde{u}^L}{\partial y}\frac{\partial u''^S}{\partial y} - \frac{2}{3}\frac{\partial \widetilde{u}^L}{\partial x}\frac{\partial v''^S}{\partial y}\Big] \\ -\widetilde{\mu}^L\Big[\frac{\partial \widetilde{v}^L}{\partial x}\frac{\partial u''^S}{\partial y} + \frac{\partial \widetilde{v}^L}{\partial z}\frac{\partial w''^S}{\partial y}\Big] - \overline{\mu}^L\frac{4}{3}\frac{\partial \widetilde{v}^L}{\partial y}\frac{\partial v''^S}{\partial y} \\ \widetilde{\mu}^L\Big[\frac{\partial \widetilde{w}^L}{\partial y}\frac{\partial w''^S}{\partial y} - \frac{2}{3}\frac{\partial \widetilde{w}^L}{\partial z}\frac{\partial v''^S}{\partial y}\Big]\end{aligned} \tag{6.66}$$

Line l_3

$$\frac{\partial}{\partial x_j}\Big(\rho u_j E + u_j p - \overline{\kappa}^L \frac{\partial T''^S}{\partial x_j} - u_i \tau''^S_{ij} - u''^S_i \widetilde{\tau}^L_{ij}\Big) = \frac{\partial}{\partial z}\Big(\rho w E + w p - \overline{\kappa}^L \frac{\partial T''^S}{\partial z}\Big)$$
$$+\overline{\rho}^L u \frac{\partial \widetilde{E}^L}{\partial x} + \overline{\rho}^L v \frac{\partial \widetilde{E}^L}{\partial y} + \widetilde{E}^L\Big[\frac{\partial}{\partial x}(\overline{\rho}^L \widetilde{u}^L) + \frac{\partial}{\partial y}(\overline{\rho}^L \widetilde{v}^L)\Big]$$
$$+(\rho E''^S + \rho'^S \widetilde{E}^L)\Big[\frac{\partial \widetilde{u}^L}{\partial x} + \frac{\partial \widetilde{v}^L}{\partial y}\Big] + p\frac{\partial \widetilde{u}^L}{\partial x} + u\frac{\partial \overline{p}^L}{\partial x} + p\frac{\partial \widetilde{v}^L}{\partial y} + v\frac{\partial \overline{p}^L}{\partial y}$$
$$-\overline{\mu}^L u_i\Big[3\frac{\partial^2 u''^S_i}{\partial z^2} + \frac{1}{3}\frac{\partial^2 w''^S}{\partial z^2}\delta_{i3}\Big] - \overline{\mu}^L\Big[\frac{\partial \widetilde{u}^L}{\partial z}\frac{\partial u''^S}{\partial z} - \frac{2}{3}\frac{\partial \widetilde{u}^L}{\partial x}\frac{\partial w''^S}{\partial z}\Big]$$
$$-\overline{\mu}^L\Big[\frac{\partial \widetilde{v}^L}{\partial z}\frac{\partial v''^S}{\partial z} - \frac{2}{3}\frac{\partial \widetilde{v}^L}{\partial y}\frac{\partial w''^S}{\partial z}\Big] - \overline{\mu}^L\frac{4}{3}\frac{\partial \widetilde{w}^L}{\partial z}\frac{\partial w''^S}{\partial z}$$
$$-\overline{\mu}^L\Big[\frac{\partial \widetilde{w}^L}{\partial x}\frac{\partial u''^S}{\partial z} + \frac{\partial \widetilde{w}^L}{\partial y}\frac{\partial v''^S}{\partial z}\Big] \tag{6.67}$$

These, equations were obtained by neglecting, as a first approximation, the following terms μ'^S, κ'^S, $\partial\mu/\partial x_i$, and $\partial\kappa/\partial x_i$ from the small-scale equations only. Once the small-scale field is known, the large-scale unclosed terms can be computed directly.

Momentum:

$$\tau^{TLS}_{ij} = \big[\overline{\rho u_i u_j}^L - \overline{\rho}^L \widetilde{u}^L_i \widetilde{u}^L_j\big]. \tag{6.68}$$

Energy:

$$E^{TLS}_j = \big[\overline{\rho u_j E}^L - \overline{\rho}^L \widetilde{u}^L_j \widetilde{E}^L\big] + \big[\overline{u_j p}^L - \widetilde{u}^L_j \overline{p}^L\big] \tag{6.69}$$

6.2 Numerical Calculations

The validation of the TLS formulation is conducted by simulating the flow over a turbulent boundary layer at $Re = 1400$. The large-scale equations (6.43), (6.45), and (6.47) are resolved using grids with the same dimensions as those described in Section 5.2. However, different resolutions are implemented for TLS, which are summarized on Table 6.1. The small-scale equations (6.56)-(6.58) are resolved over one dimensional lines embedded in the large-scale grid as illustrated in Figure 6.1. These lines are discretized with six grid points per large-scale Δx_i in the streamwise

Table 6.1: Summary of grids implemented in TLS/LES simulations

Grid name	Number of grid points $n_x \times n_y \times n_z$	Large-scale resolution			Small-scale resolution		
		Δx^+	Δy^+	Δz^+	Δx^+	Δy^+	Δz^+
TLS/LES-1400	$101 \times 45 \times 65$	60	$5 - 176$	20	10	0.625	3.33
TLS/LES-3330	$201 \times 91 \times 121$	66	$5 - 189$	22	11	0.625	3.66

and spanwise directions, whereas eight grid points are implemented in the wall-normal direction. The resolution of the small-scale lines is presented also in Table 6.1.

The integration of the large-scale equations uses the same numerical scheme implemented in previous simulations. However, for the small-scale equations (6.56)-(6.58) and following the approach of Kemenov and Menon [49], an explicit two-step component-wise TVD scheme is implemented [110]. The boundary conditions for the small-scale equations are provided in accordance with the physical boundaries, i.e. zero fluctuating condition is imposed at the wall and at the free-stream, at the inflow a fraction (40%) of the turbulent fluctuation is imposed, and at the spanwise direction periodic boundary conditions are enforced. For the initial conditions, the TLS small-scale equations are evolved from a zero initial field.

6.2.1 TLS Validation

To validate the TLS formulation, the turbulent boundary layer is simulated ($Re = 1400$) using the TLS approach in the entire domain. Additionally, the Ma number of the flow is increased to $Ma = 0.9$, to evaluate the compressible formulation. For subsonic flows, compressibility does not affect the turbulence in boundary layers, since the fluctuating Ma number is well below the compressible-effect limit $Ma' < 0.3$ [91]. However, compressibility at this Ma can certainly affect the performance of the TLS-model, which could misbehave if the formulation is incorrect. Additionally, to consistently evaluate TLS results, pure LES simulations at the same Re numbers with $Ma = 0.9$ are also conducted. However, the LES calculations did not differ from

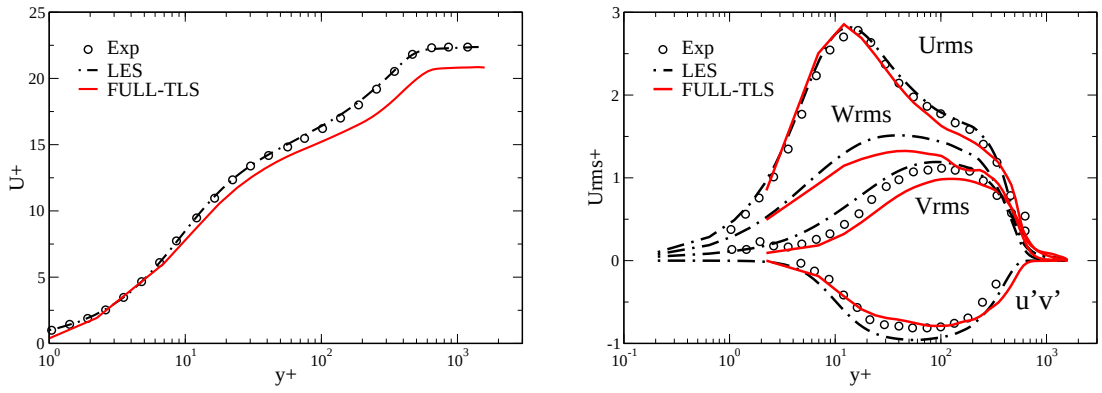

(a) (b)

Figure 6.2: First and second-order statistics for $Re_\theta = 1400$ TLS simulation: (a) mean velocity profile; (b) velocity rms and Reynolds shear stress.

the previous low Ma number simulations ($Ma = 0.3$) as expected.

Figure 6.2 presents the mean velocity profile, using the Van Driest transformation to reproduce the Law-of-the-wall in compressible turbulent boundary layer [20], and the second-order statistics normalized with wall-units. Here, the mean velocity profile computed with TLS slightly overpredicts the friction coefficient, which induces discrepancies with the experimental data and LES results. However, it is important to highlight that the near-wall resolution in the TLS grid is ten times coarser than the LES resolution. On the other hand, the second order-statistics predicted by TLS are found in better agreement with experimental results and LES calculations.

Figure 6.3 presents the large and small scale one-dimensional power-density spectra of the kinetic energy and density, computed with LES and TLS over the homogeneous spanwise direction. The TLS spectra clearly illustrate the differences between the nature of the large and small scales. Here, the large-scales contain the most energetic structures of the flow, hence most of the energy of the turbulence, is at these scales where all the anisotropy and information of the flow is contained. On the other hand, the small-scales do not contain a significant amount of energy at low wave-numbers. Instead, they concentrate most of the energy at wave-numbers located in the inertial and dissipative ranges, which makes them less sensitive to the anisotropy

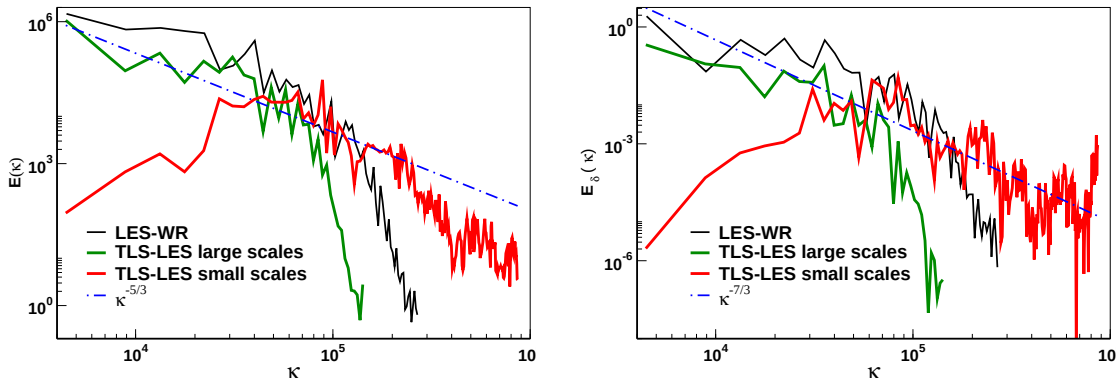

(a) (b)

Figure 6.3: Large and small scale spectra computed at $y^+ \sim 90$ for $Re_\theta = 1400$ TLS and LES simulations: (a) kinetic energy spectrum; (b) density spectrum.

of the flow, thus more universal or "memoryless". Here, the energy cascade from large to small scales through the forcing terms in the small-scale equations, which are generated from the nonlinear terms of the Navier-Stokes equations. Here, it is important to stress that by combining the large and small scale spectra, it is possible to reconstruct a continuous spectrum able to reproduce the LES predictions. In fact, both the reconstructed TLS and LES spectra suggest a region where a scaling of $k^{-5/3}$ for the kinetic energy and $k^{-7/3}$ for the density [7] hold.

Here, it is convenient to discuss the evolution criteria implemented to integrate the small-scale equations. As demonstrated by Figure 6.3, the evolution of the large-scale and small-scale equations is not controlled by the same time and length scales. Using embedded lines in the large-scale grid resolves the problem of resolving different length scales. However, the time integration is more troublesome. A first approach would be to evolve both, large and small scales equations with the time scale imposed by the small-scale equations. However, this is impractical, especially if it is considered that at times-scales that control the small-scale evolution, the changes that the large-scale exhibit are negligible. Therefore, it is possible to adopt a semi-decoupled or frozen approach. Here, the small-scale equations are evolved in time, keeping the large-scale field frozen, this implies that the large-scale variables in the forcing terms

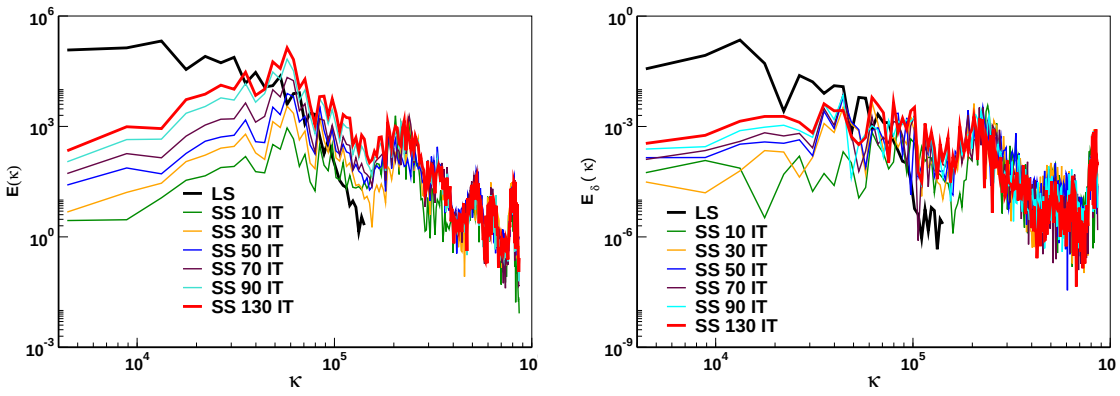

(a) (b)

Figure 6.4: Time evolution of the small-scale field restricted with the TLS evolution criteria, results computed at $y^+ \sim 90$ for $Re_\theta = 1400$, TLS simulation (IT stands for number of time iterations): (a) kinetic energy spectra; (b) density spectra.

in the small-scale equations are fixed. This condition is maintained until the time elapsed during the small-scale integration is large enough to induce variations in the large-scale equations.

The criterion implemented to conduct the small-scale time integration is the one proposed by Kemenov and Menon [48, 49]. This criterion limits the time integration by following the evolution of the small-scale energy spectrum. Here, the integration is stopped when the small-scale energy spectrum levels up its energy at the inertial range with the large-scale spectrum, such that a continuous energy cascade is modeled. This time integration criterion is shown in Figure 6.4, which illustrates the evolution of the small-scale energy and density spectra. Results indicate that during the period of integration the forcing terms in the small-scale equations supply energy from the large-scales, increasing the energy in the inertial range of the small-scale spectrum, while the energy at the dissipative range remains virtually constant. However, if the small-scale time integration is continued, while keeping the large-scale frozen (see Figure 6.5), the energy at all numbers will increase until the energy dissipation rate balances the energy suplied by the forcing terms. At this point the small-scales reached an equilibrium point, that not necessarily matches the large-scale spectrum,

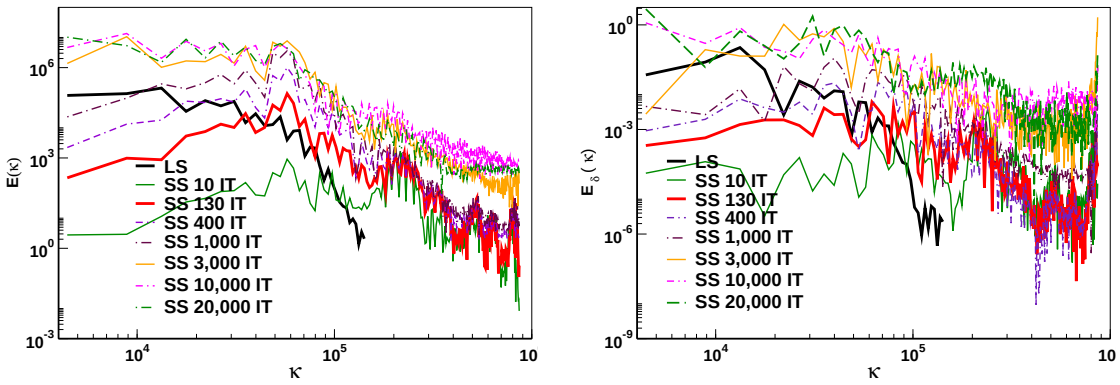

(a) (b)

Figure 6.5: Unbonded time evolution of the small-scale equations, results computed at $y^+ \sim 90$ for $Re_\theta = 1400$, TLS simulation (IT stands for number of time iterations): (a) kinetic energy spectra; (b) density spectra.

and further time integration will not change the small-scale energy spectra. However, at this point the modeled small-scale would be nonphysical, since their spectra do not math the large-scale spectra and their evolution would be in the future with respect of the large-scale field. Therefore, the time integration must be conducted until the small-scale spectra levels up the large-scale spectra.

The time evolution of the velocity and thermodynamic small-scale field, taken over the l_3 line at $y^+ \sim 90$ is shown in Figures 6.6 and 6.7 (in these figures, the axis of the earlier profiles have been switched upward to clearly demonstrate how the small-scales increase during the time evolution, here purple line is the earliest/first and black line is the latest/final time sample). Results show how the small-scale time evolution takes place from zero initial conditions. As mentioned before, the intensity that the small-scale field achieves is dictated by its time evolution and spectral content. If the spectrum matching criterion is not satisfied, especially when the small-scale equations are underevolved, the energy content and intensity of the small-scales would not be enough to model the scales not resolved by the large-scale equations. On the other hand, if the small-scale equations are over evolved the flow would become unphysical and incorrect results will be reproduced.

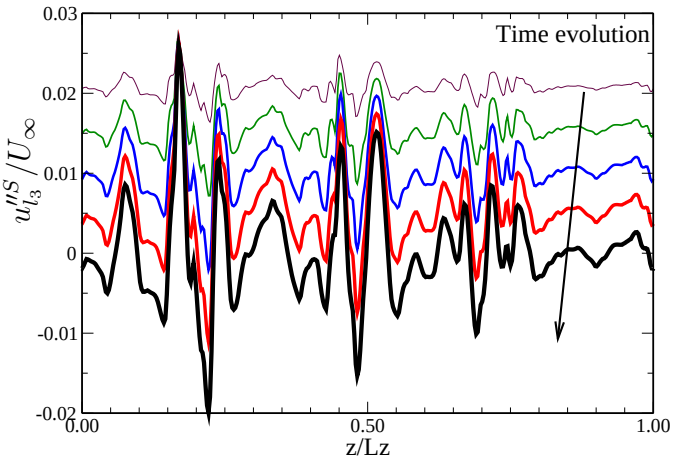

(a)

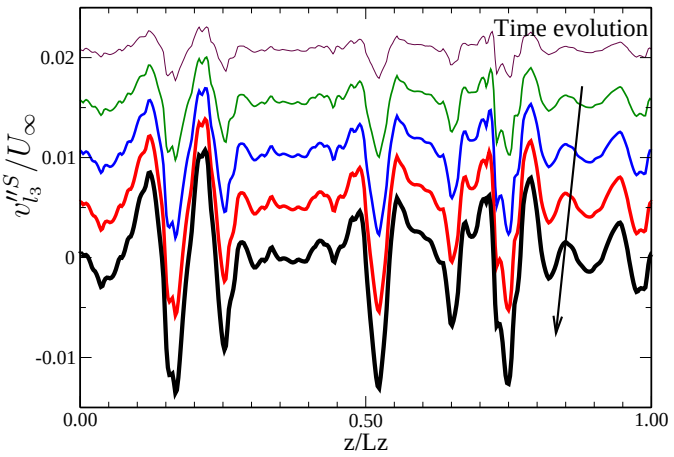

(b)

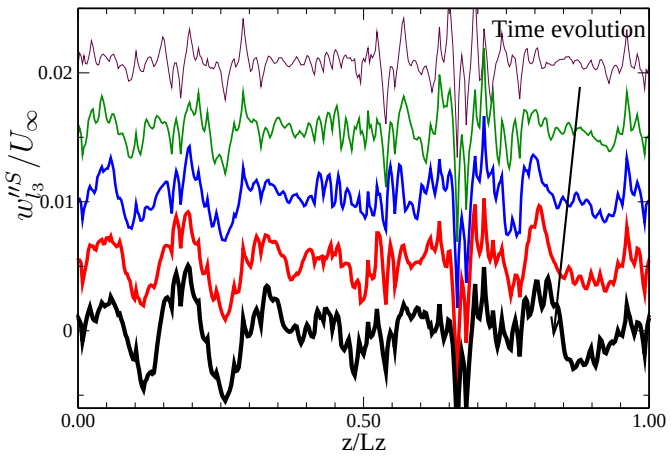

(c)

Figure 6.6: Time evolution of the small-scale velocity field over the l_3 line, at $y^+ = 90$ for $Re_\theta = 1400$ TLS simulation, (the axis of the earlier profiles have been switched upward to clearly demonstrate the time evolution, purple line is the earliest/first and black line is the latest/final time sample): (a) small-scale $u''^S_{l_3}$; (b) small-scale $v''^S_{l_3}$; (c) small-scale $w''^S_{l_3}$.

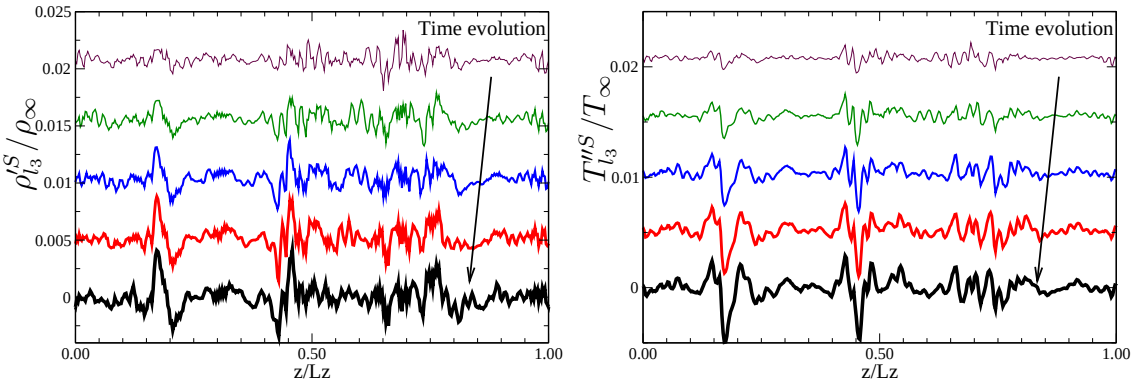

(a) (b)

Figure 6.7: Time evolution of the small-scale density and temperature field over the l_3 line, at $y^+ = 90$ for $Re_\theta = 1400$ TLS simulation, (the axis of the earlier profiles have been switched upward to clearly demonstrate the time evolution, purple line is the earliest/first and black line is the latest/final time sample): (a) small-scale density $\rho'^S_{l_3}$; (b) small-scale temperature $T''^S_{l_3}$.

6.2.2 Hybrid TLS/LES Calculations

Having demonstrated the potential of the full-TLS formulation, the feasibility to blend the TLS formulation with the LES approach as a near-wall model for LES is explored by simulating the turbulent boundary layer at $Re = 1400$ and 3330. In order to blend the TLS and LES formulation the operational nature of the TLS formulation is employed. This implies that the large-scale TLS equations can be obtained also by applying the TLS operator in the Navier-Stokes equations [48]. In fact the TLS operator Eq.(6.1) can be identified as a space filter. Therefore, it is possible to use the generic additive filter formulation derived in Chapter 5 by replacing the RANS operator with the TLS operator in Eqs. (5.16)-(5.18). Since the only thing that has to be changed in the hybrid RANS/LES equations to fit the hybrid TLS/LES approach is the interpretation of one of the operators, there is no need to reproduce the hybrid TLS/LES equations. Instead, Eqs. (5.16)-(5.18) are referred as the hybrid TLS/LES equations, understanding that the RANS operator is replaced with Eq. (6.1).

In order to combine the TLS and LES formulation, a blending function $\mathcal{F}$ has to be defined. Here following the RANS/LES studies, a continuous $\mathcal{F}2$ (Eq. (5.73))

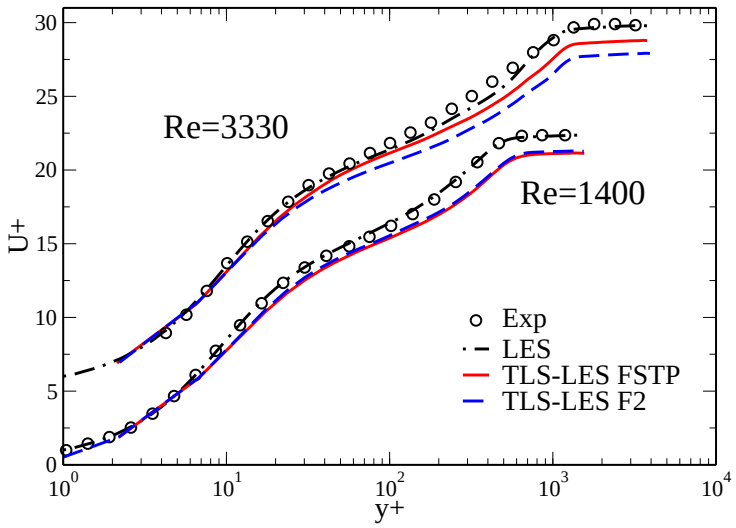

Figure 6.8: Mean velocity profile computed with LES and TLS/LES using $\mathcal{F}^{step}$ and $\mathcal{F}2$ blending functions, simulations for $Re = 1400$ and $Re = 330$ (results switched upward 5 wall-units for presentation clarity).

and discontinuous $\mathcal{F}^{stp}$ located at $y^+ \sim 90$, blending functions are implemented, to evaluate the effect of the blending functions. When the $\mathcal{F}2$ is implemented, the small-scale TLS equations are solved in the entire domain whether or not they are used to close the large-scale equations. On the other hand, when the $\mathcal{F}^{stp}$ function is implemented, the TLS small-scale equations are resolved only in the region where $\mathcal{F} = 1$ (TLS domain).

Figure 6.8 presents the mean velocity profile computed with hybrid TLS/LES approach using the $\mathcal{F}2$ and $\mathcal{F}^{stp}$ functions (the profiles for $Re = 3330$ are switched upward five wall-units for clarity). Results in general slightly overpredict the shear stress at the wall, which induces an under prediction of the law-of-the-wall at the outer layer. These results are consistent with the full-TLS simulations. For the low Re number case, both blending functions predicted the same results. For the higher Re case, the $\mathcal{F}^{stp}$ predicted slightly better the velocity profile at the outer layer. Here once more, the near-wall resolution in TLS/LES calculations is ten times coarser than the LES calculations.

The velocity rms and Reynolds shear stress are presented in Figure 6.9. Here,

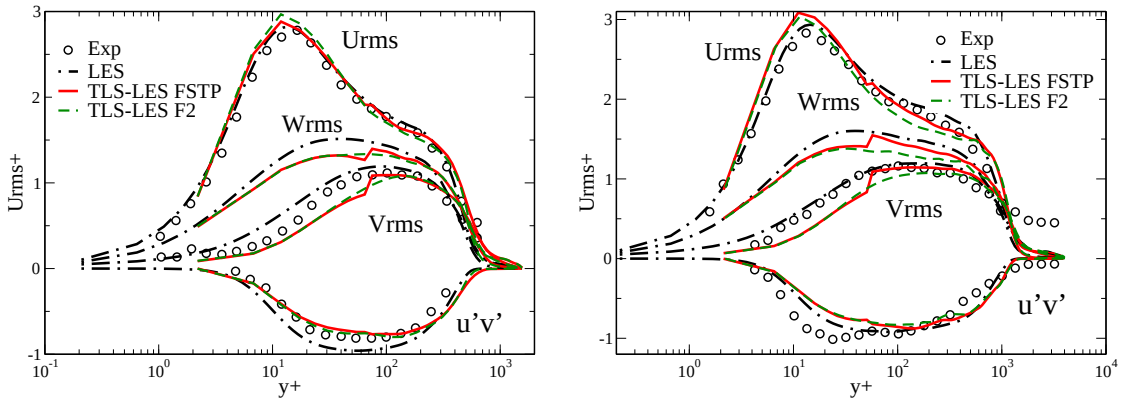

Figure 6.9: Second-order statistics for TLS/LES simulations using the $\mathcal{F}^{stp}$ and $\mathcal{F}2$ blending functions: (a) $Re_\theta = 1400$; (b) $Re_\theta = 3330$.

results are in better agreement with experimental data and LES calculations, as in the full TLS case. Nevertheless, the effect of the blending function is made evident in the second-order statistics. Here, as reproduced with the hybrid RANS/LES approach, the $\mathcal{F}^{stp}$ function induces discontinuities in the statistics for both Re numbers simulated. On the other hand, results that implement the $\mathcal{F}2$ function predict continuous statistics, indicating that, as in the RANS/LES case, smooth transition function should be implemented in the TLS/LES coupling.

Similarly to the hybrid RANS/LES formulation, the hybrid TLS/LES approach include additional hybrid terms (5.22)-(5.27). However, for TLS/LES simulations the effect of these terms is negligible. Here, the hybrid terms were included using the HT-model presented in Chapter 5 for both Re numbers. However, the results were virtually the same than those not including the HT, thus these results are not presented. The fact that the HT terms are not relevant in the TLS/LES formulation can be explained by the difference between the TLS and LES operators. While in the RANS/LES formulation the difference between RANS and LES variables is proportional to the turbulence fluctuation of the flow see Chapter 5, on TLS the difference between LES and TLS large-scale variables is negligible. In fact, it is

possible to identify the TLS large-scale operator with the LES filter [48], explaining why the results were insensitive to whether or not the HT are included. Therefore, the HT can be neglected from the hybrid TLS/LES formulation.

Finally, Figure 6.10 presents coherent structures computed for TLS/LES simulations using the $\mathcal{F}2$ blending function, for $Re = 1400$ and $Re = 3330$. The figures indicate that the vortical structures are not dissipated as in the RANS/LES case (when the HT are neglected). This is explained by the fact that TLS is an unsteady model that reconstructs the modeled scales, whereas RANS is a statistical model where no unsteady turbulence structures are resolved. Consequently, by using TLS as a near-wall model for LES it is possible to maintain the unsteady near-wall dynamics, that is more significantly dissipated when RANS is used as a near-wall model.

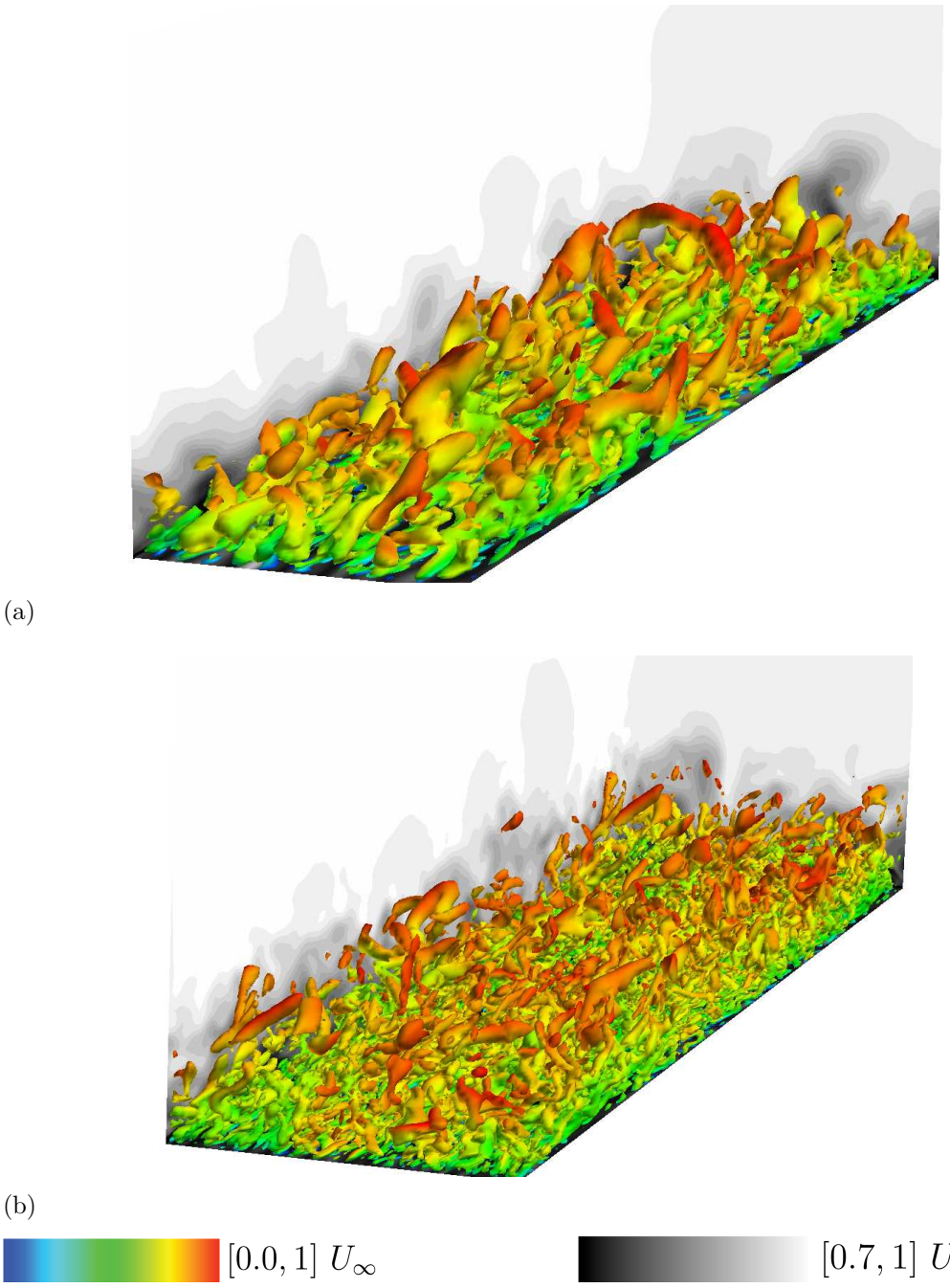

Figure 6.10: Isosurfaces of second invariant of the velocity gradient tensor ($\mathcal{Q}\theta/U_\infty = 1 \times 10^3$) colored with values of streamwise velocity, side contours streamwise velocity, for TLS/LES simulations using the $\mathcal{F}2$ function: (a) $Re_\theta = 1400$; (b) $Re_\theta = 3330$.

CHAPTER VII

CONCLUSION

In this work the potential of RANS and TLS formulations as near-wall models for LES have been studied. The research center its attention to investigate the near-wall approaches from a fundamental standpoint, providing guidance that potentially leads to improvements to hybrid RANS/LES methodologies. Additionally, the TLS approach is introduced as an alternative model, to construct hybrid near-wall models with unsteady capabilities. Simulations focus to calculate the turbulent flow over a flat-plate boundary layer, due to the challenges that this flow posts to the different hybrid RANS/LES methodologies in current use.

7.1 Findings and Contributions

- In Chapter V an additive-filter that combines the RANS and LES operators with a transition function is defined and its properties demonstrated. In particular, it is shown that this hybrid operator in general does not commute with differentiation, independently of the properties of its constitutive operators (in this case independently of the properties of the RANS and LES operators). More importantly, the governing equations derived by applying the additive-filter in the Navier-Stokes equations, predict additional terms that originate due to nonlinearity and due to the non-commutation between the hybrid filter and differentiation. These new terms, named hybrid terms, are proportional to products between the gradient of the blending function and differences between RANS and LES variables. Additionally, the hybrid second-order central moments also predict additional terms proportional to products of differences between RANS and LES variables.

- These hybrid terms represent the interactions between RANS and LES formulations and are only relevant in the RTLT zone. This indicates that the hybridization of RANS with LES, cannot be obtained only through the turbulence model equation, as it is assumed in current hybrid models. By analyzing the exact equations, it is possible to demonstrate that the use of discontinuous blending functions induces discontinuities in the governing equations. This analysis explains, the anomalous discontinuities predicted by zonal approaches and suggests that the implementation of discontinuous functions should be avoided. This simple analysis demonstrates the importance of having a theoretical foundation for the hybrid RANS/LES approach.

  Another important result obtained from the exact hybrid RANS/LES governing equations, is the prediction of ATD in the RTLT zone. As it is mentioned before, ATD occurs when the suppression of RANS modeling is faster than the rate at which those turbulence scales are resolved by LES. The analysis of the hybrid terms indicates, that they represent turbulent scales that are neither resolved by the governing equations nor modeled. Therefore, if the hybrid terms are neglected, ATD is unavoidable incurred independently of the characteristics of the blending function. This prediction is of significant importance, since indicates that every hybrid RANS/LES methodology will suffer ATD, if the hybrid terms are not included. This explains why previous, independent, hybrid RANS/LES simulations of channel flow, on which the hybrid terms were not included, have presented ATD [5,13,14,34,35,47,66,70,97,100]. The prediction of ATD when the hybrid terms are neglected from the exact hybrid RANS/LES equations, is confirmed by the numerical calculations conducted in this work. Calculations show a significant drop of modeled turbulent stresses when the hybrid terms are not included, indicating ATD. This drop in modeled stresses, is responsible for the incorrect prediction of the mean velocity profile and occurs

independently of the blending function implemented. Additionally, when a discontinuous blending function is used, the calculations predict discontinuities in the statistics, in agreement with the prediction of the equations and with previous zonal RANS/LES calculations [34].

Numerical calculations demonstrate, that the hybrid terms are responsible for maintaining in balance the turbulence transport, preventing ATD. Here, the mean velocity profile is predicted in good agreement with experimental data when the hybrid terms are included, in contrast with results obtained when the hybrid terms are neglected. From a practical stand point, the improvement in the mean velocity profile has a direct implication in the prediction of global quantities like, friction coefficients, aerodynamic loads, heat transfer, among others. It is also demonstrated, that by including the hybrid terms the fine unsteady structure of the flow is preserved. However, if the hybrid terms are neglected, the unsteady structure of the flow is dissipated. Additionally, results appear to be less sensitive to the blending function, when the hybrid terms are included. This indicates, that the transition from RANS to LES can be specified arbitrarily as long as the hybrid terms are included. On the other hand, when the hybrid terms are neglected, the calculations are extremely sensitive to the blending function implemented. This explains why different hybrid RANS/LES methodologies, which differ on the way the transition from RANS to LES occurs, are affected differently by ATD [13–15, 34, 66, 70, 97, 100]. In particular, for the attached flat-plate turbulent boundary layer, the weak dependency on the blending function indicates that the transition from RANS to LES could be specified arbitrarily, as long as it is continuous and the RTLT zone in the outer layer, and the hybrid terms are included. However, further efforts have to be conducted to establish this conclusion on more general conditions.

- A new hybrid RANS/LES model equation for the hybrid turbulent kinetic energy ($\mathcal{K}$) is introduced. Here the two-equation RANS-SST $k-\omega$ model is combined with the one-equation LDKM LES model. The model equation is obtained by explicitly combining the RANS k equation with the LES k^{sgs} equations using a blending function. This proposed hybrid equation, unambiguously recovers the LES and RANS models, since the transition is entirely dictated by the blending function. This is the main difference and advantage over more commonly used hybrids approaches, like DES. For instances, in DES the transition from RANS to LES is controlled by the grid characteristics, thus, grid refinements made to improve the description of the geometry can interfere with the model transition [86]. Additionally, the flow has to fulfill specific conditions before DES can recover the LES model. The potential of the new hybrid RANS/LES model equation is demonstrated simulating the flow over a turbulent boundary layer. Additionally, previous studies have successfully implemented this model equation in complex unsteady aerodynamic flows [60, 76].

- Although the importance of the hybrid terms is corroborated by the numerical calculations, a parallel LES simulation is required to compute the hybrid terms. Therefore, to avoid the additional LES simulation and with the only purpose to approximate the hybrid terms, a simple approach to reconstruct the LES field from the hybrid variables is proposed. This model, although could not exactly reproduce the hybrid terms, is able to prevent the ATD predicting mean velocity profiles and second-order statistics in close agreement with the predictions using the exact hybrid terms. The improvements provided by the hybrid terms model, is a great example of the importance of having a theoretical framework to propose a model. The simple model for the hybrid terms could not have been made possible without the exact hybrid RANS/LES governing equations.

Another important result drawn from the exact hybrid RANS/LES equations, is to demonstrate that many of the existing hybrid RANS/LES methodologies in current use, could be derived from the exact equations. The zonal and blended approaches are obtained implementing discontinuous and continuous blending functions, respectively, and neglecting the hybrid terms. DES is found to be a special case of the blended hybrid RANS/LES approach, where the hybrid turbulence viscosity is provided by the modified Spalart-Almaras turbulent model equation. Finally, the approach of Speziale is directly recovered by replacing the LES operator with the identity or DNS operator in the hybrid equations and by neglecting the hybrid terms. Here, the blending function of the additive-filter is found to be directly related with the scaling factor proposed by Speziale [90]. Furthermore, from the analysis of the hybrid terms, it is possible to provide justification to the stochastic forcing approaches, which has been recently proposed to prevent ATD in hybrid RANS/LES simulations [5, 13, 14, 47, 70]. The analysis of the hybrid terms indicates that their nature is unsteady, since they are proportional to differences between RANS and LES variables. This unsteady nature indicates, that the success of the stochastic forcing methods relies on their ability to mimic the effect of the hybrid terms [68]. This provides physical justification to the stochastic forcing approach.

- In the second effort, the Two Level Simulation approach is extended to compressible flows. Here, the small-scale equations are derived and simplified following the assumptions proposed in the original incompressible version of the model [48, 49]. The formulation is validated conducting full-TLS simulations for a turbulent boundary layer in a flat-plate. TLS predicts results in good agreement with experimental data and wall-resolved LES simulations, with wall-normal resolution at the wall ten times coarser than LES. Here, issues related with the evolution of the small-scale equations are addressed. In particular, it

is concluded, as in previous TLS simulations [48, 49], that the evolution of the small-scale equations should be conducted until the small-scale energy in the inertial range of the spectrum matches the inertial-range energy of the large-scale spectrum. Here, the large-scale equations are frozen in time during the integration of the small-scale equations. It is also shown, that if the small-scale integration is continued, the small-scale field would reach a steady state where viscous dissipation balance the large-scale forcing. However, at this point the small-scale field would be unphysical with respect to the large-scale variables. Contrary, if the small-scale equations are under-evolved, the small-scale field lacks enough energy content to accurately model the effect of the unresolved turbulence in the large-scale equations.

- The potential of the TLS to be used as a near-wall model for LES is evaluated by conducting turbulent boundary layer simulations. Here, the generic additive-filter formulation is implemented to blend TLS with LES. Results demonstrate that TLS can be used as a near-wall model, predicting results in reasonable good agreement with experimental data and LES simulations. The issues related with the transition from TLS to LES are similar to those found in the hybrid RANS/LES approach. Here, it is demonstrated that the use of discontinuous functions in the hybrid TLS/LES approach, induces discontinuities in the statistics. However, with smooth blending functions the predicted statistics are continuous. Similar to the RANS/LES approach, the hybrid TLS/LES formulation predicts additional hybrid terms. However, their importance in the TLS/LES formulation is minimum. Results implementing the hybrid term model, predict no significant difference in the statistics. This is explained by the fact that the TLS and LES operators are very much alike. Indeed, the large-scale TLS operator is just another kind of space filter, thus, the differences between TLS and LES variables are negligible, which explains why the

hybrid terms do not make any difference in the calculations. Finally, instantaneous flow visualizations demonstrate that the TLS/LES approach is able to maintain the near-wall unsteady structure of the flow, without drastically dissipating the near-wall structures as in its RANS/LES counterpart. These results demonstrate the potential of TLS as a near-wall model, introducing another option different from RANS.

- During this work, a new finite volume compressible structure-grid CFD code was developed. The space accuracy of this code is extended to 4^{th} order using a central-scheme in divergence form. The scheme is stabilized by implementing an explicit low-pass filter to control the growth of numerical errors. Additionally, a realistic turbulence inflow generation technique, based on boundary layer scaling [59] is successfully implemented and used to conduct accurate space-evolving turbulence simulations. Here, it is important to mention that the boundary layer simulation can be used to provide turbulent inflow boundary conditions to complex flow simulations. Additionally, RANS, LES, TLS, and hybrid RANS(TLS)/LES models are successfully implemented in the solver. These code enhancements completes the new high-accuracy CFD solver developed during this work.

7.2 Proposed Future Work

The importance of resolving the exact hybrid RANS/LES governing equations, is demonstrated in one of the most fundamental problems, the flat-plate turbulent boundary layer. The test case is selected due to its simple nature, which allows an objective evaluation of the new formulation. Here, if the Law-of-the-wall and the second-order statistics are not correctly reproduced, it does not matter how nice the instantaneous flow field looks, the model simply does not work. With this choice, it is intended to focus attention in the fundamental aspects of the model and not

overestimate poor performance just because the model is able to reproduce some good-looking unsteady flow structure present in a more complex flow.

For future work, it is important to evaluate the performance of the exact hybrid RANS/LES equations when adverse-pressure gradients and geometry curvature affect the evolution of attached flows. Additionally, it is also important to evaluate the hybrid RANS/LES equations in unsteady flows, where flow separation and reattachment dominates. Although it is anticipated that the hybrid terms will be of secondary importance in these flows, since the large unsteady structures control the evolution of the flow. However, important aspects like the location of flow separation or reattachment are still controlled by the near-wall dynamics, thus, using the exact hybrid RANS/LES equations could be benefical for the prediction of such flows, specially in aerodynamic applications where the location of flow separation controls the evolution of the large-scale structures.

Further research efforts need to be conducted to establish an automatic way to generate the blending function, especially in complex geometries, where it is not easy to know in advance the characteristics of the flow. It would be interesting to assess the possibility to propose a transport equation for the blending function, which depend on flow and turbulent variables. Additionally, it would be interesting to evaluate the effect of the "unsteady" hybrid terms, which occurs when the blending function is time-dependent. This aspect is of significant relevance, since the blending function in many hybrid RANS/LES methods, is function of the flow and turbulence variables, which induces changes in the location and extent of the RTLT zone in time. The equations already indicate that the hybrid RANS/LES approach cannot adjust immediately RANS variables into LES variables, just because the blending function passed from RANS to LES in one instant of time, does not imply that the local field immediately changed from RANS to LES. In fact, additional "unsteady" hybrid terms need to be provided to help in this transition.

For the TLS/LES approach, the previous points also hold. However, the pure compressible TLS methodology has to be first validated in more complex flows to establish the underlying assumptions of the model. In particular, the effect of curvature and adverse pressure gradients has to be addressed in the pure TLS formulation.

For both RANS(TLS)/LES approaches, the effect of strong compressibility effects has to be assessed. It would be very illustrative to evaluate the performance of the hybrid equations in complex compressible problems like, shock-wave boundary layer interactions, with and without heat transfer at the wall. Additionally, extend the application of both RANS(TLS)/LES approaches to simulate reacting flows would be also very important.

Thus far, the potential of both hybrid methodologies have been presented from a near-wall model standpoint. However, it would be enlightening to demonstrate both hybrid RANS(TLS)/LES methodologies as pure hybrid approaches. In principle, there is no reason why the hybrid methodology must be used only as a near-wall model approach. In fact, the hybrid approach can be used in free shear flows to reduce the number of grid points required in regions of high shear or to implement the RANS or TLS methodologies in zones where the grid is not fine enough to sustain LES calculations.

Other important aspect that need to be addressed in both hybrid RANS(TLS)/LES approaches, is their feasibility to be implemented in an unstructured-grid framework, since the ultimate goal of these methods is to be applied on complex flows of engineering interest. Thus far, both methods have been demonstrated on simple structured grids. However, the potential issues faced on an unstructured-grid framework need to be addressed.

APPENDIX A

THE COMPRESSIBLE HYBRID RANS/LES FORMULATION USING AN ADDITIVE OPERATOR

Mártin Sánchez Rocha and Suresh Menon. *Journal of Computational Physics* (2008), doi:10.1016/j.jcp.2008.11.021

In the present work, the compressible governing equations for the hybrid Reynolds-averaged/large-eddy simulations are formally derived by applying a hybrid filter to the Navier-Stokes equations. This filter is constructed by linearly combining the Reynolds-average (RANS) and large-eddy simulation (LES) operators with a continuous blending function. The derived hybrid equations include additional terms that represent the interactions between RANS and LES formulations. The relevance of these terms is investigated in flat-plate turbulent boundary layer simulations and indicate that these additional terms play a fundamental role in compensating for the turbulence that is neither modeled nor resolved in the transition region between RANS and LES. Results also show that when the additional terms are included, the calculations are not very sensitive to the blending function implemented in the hybrid filter. In the contrary, when these terms are neglected and a step function is implemented in the hybrid filter, nonphysical discontinuities are predicted in the flow statistics.

REFERENCES

[1] Anderson, J. D., *Hypersonic and high temperature gas dynamics*. AIAA, 2000.

[2] Aubertine, C. D. and Eaton, J. K., "Turbulence development in a non-equilibrium turbulent boundary layer with mild adverse pressure gradient," *J. Fluid Mech.*, vol. 532, pp. 345–364, 2005.

[3] Baggett, J. S., "On the feasibility of merging LES with RANS for the near wall region of attached turbulent flows," in *Annual Research Briefs*, pp. 267–277, Center for Turbulence Research, 1998.

[4] Batchelor, G. K., *An Introduction to Fluid Dynamics*. Cambridge University Press, 1967.

[5] Batten, P., Goldberg, U., and Chakravarthy, S., "Interfacing statistical turbulence closures with large-eddy simulation," *AIAA J.*, vol. 42, no. 3, pp. 485–492, 2004.

[6] Baurle, R. A., Tam, C. J., Edwards, J. R., and Hassan, H. A., "Hybrid simulation approach for cavity flows: Blending, algorithm, and boundary treatment issues," *AIAA J.*, vol. 41, no. 8, pp. 1463–1480, 2003.

[7] Bayly, B. J., Levermore, C. D., and Passot, T., "Density variations in weakly compressible flows," *Phys. Fluids A.*, vol. 4, pp. 945–954, 1992.

[8] Befeno, I. and Schiestel, R., "Non-equilibrium mixing of turbulence scales using a continuous hybrid RANS/LES approach: application to the shearless mixing layer," *Flow Turbul. Combust.*, vol. 78, pp. 129–151, 2007.

[9] Bertin, J. J. and Cummings, R. M., "Critical hypersonic aerothermodynamic phenomena," *Annu. Rev. Fluid Mech.*, vol. 38, pp. 129–157, 2006.

[10] Cant, R. S., Dawes, W. N., and Savill, A. M., "Advanced CFD and modeling of accidental explosions," *Annu. Rev. Fluid Mech.*, vol. 36, pp. 97–119, 2004.

[11] Canuto, C., Hussaini, M. Y., Quarteroni, A., and Zang, T. A., *Spectral Methods in Fluid Dynamics*. Springer-Verlag, New York, 1987.

[12] Chapman, D. R., "Computational aerodynamics development and outlook," *AIAA J.*, vol. 17, pp. 1293–1313, 1994.

[13] Davidson, L. and Billson, M., "Hybrid LES-RANS using synthesized turbulent fluctuations for forcing in the interface region," *Int. J. Heat Fluid Flow*, vol. 27, pp. 1028–1042, 2006.

[14] Davidson, L. and Dahlström, S., "Hybrid LES-RANS: an approach to make LES applicable at high Reynolds number," *Int. J. Comput. Fluid Dyn.*, vol. 19, no. 6, pp. 415–427, 2005.

[15] Davidson, L. and Peng, S. H., "Hybrid LES-RANS modelling: a one-equation sgs model combined with a $k - \omega$ model for predicting recirculating flows," *Int. J. Numer. Methods Fluids*, vol. 43, pp. 1003–1018, 2003.

[16] Deardorff, J. W., "A numerical study of three-dimensional turbulent channel flow at large reynolds numbers," *J. Fluid Mech.*, vol. 41, pp. 453–80, 1970.

[17] DeGraaff, D. B. and Eaton, J. K., "Reynolds-number scaling of the flat-plate turbulent boundary layer," *J. Fluid Mech.*, vol. 422, pp. 319–346, 2000.

[18] Delanghe, C., Merci, B., and Dick, E., "Hybrid RANS/LES modelling with an approximate renormalization group. I: Model development," *J. Turbul.*, vol. 6, no. 13, 2005.

[19] Domaradzki, J. A. and Saiki, E. M., "A subgrid-scale model based on the estimation of unresolved scales of turbulence," *Phys. Fluids*, vol. 9, pp. 1–17, 1997.

[20] Driest, E. R. V., "Turbulent boundary layer in compressible fluids," *J. Spacecr. Rockets*, vol. 40, no. 6, pp. 1012–1028, 2003.

[21] Dubief, Y. and Delcayre, F., "On coherent-vortex identification in turbulence," *J. Turbul.*, vol. 1, no. 11, 2000.

[22] Dubois, T. and Jauberteau, F., "A dynamic multilevel model for the simulation of the small structures in homogeneous isotropic turbulence," *J. Sci. Comput.*, vol. 13, pp. 323–367, 1998.

[23] Dubrulle, B., Laval, J. P., , and Nazarenko, S., "A dynamical subfilter-scale model for plane parallel flows," vol. 13, pp. 2045–2064, 2001.

[24] Ducros, F., Laporte, F., Souleres, T., Guinot, V., Moinat, P., and Caruelle, B., "High-order fluxes for conservative skew-symmetric-like schemes in structured meshes: Application to compressible flows," *J. Comput. Phys.*, vol. 161, pp. 114–139, 2000.

[25] Fan, C.-C., Xiao, X., Edwards, J. R., Hassan, H. A., and Baurle, R. A., "Hybrid Large-Eddy/Reynolds-Averaged Navier-Stokes simulations of shock-separated flows," *J. Spacecr. Rockets*, vol. 41, no. 6, pp. 897–906, 2004.

[26] Ferrante, A. and Elghobashi, S., "A robust method for generating inflow conditions for direct simulations of saptially-developing turbulent boundary layers," *J. Comput. Phys.*, vol. 198, pp. 372–387, 2004.

[27] Fureby, C. and Tabor, G., "Mathematical and physical constraints on large-eddy simulations," *Theor. Comput. Fluid Dyn.*, vol. 9, no. 2, pp. 85–102, 1997.

[28] Gaitonde, D. V. and Visbal, M. R., "Pade-type higher-order boundary filters for the Navier-Stokes equations," *AIAA J.*, vol. 38, no. 11, pp. 2103–2112, 2002.

[29] Georgiadis, N. J., Alexander, J. I. D., and Reshotko, E., "Hybrid Reynolds-Averaged Navier-Stokes/large-eddy simulations of supersonic turbulent mixing," *AIAA J.*, vol. 41, no. 2, pp. 218–229, 2003.

[30] Germano, M., "Turbulence: The filtering approach," *J. Fluid Mech.*, vol. 238, pp. 325–336, 1992.

[31] Germano, M., "Properties of the hybrid RANS/LES filter," *Theor. Comput. Fluid Dyn.*, vol. 17, pp. 225–231, 2004.

[32] Ghosal, S., "An analysis of numerical errors in large-eddy simulations of turbulence," *J. Comput. Phys.*, vol. 125, pp. 187–206, 1996.

[33] Girimaji, S. S., "Partially-Averaged Navier-Stokes model for turbulence: A Reynolds-Averaged Navier-Stokes to Direct Numerical Simulation bridging method," *J. Appl. Mech.-Trans. ASME*, vol. 73, pp. 413–421, 2006.

[34] Hamba, F., "A hybrid RANS/LES simulation of turbulent channel flow," *Theor. Comput. Fluid Dyn.*, vol. 16, pp. 387–403, 2003.

[35] Hamba, F., "A hybrid RANS/LES simulation of high-Reynolds-number channel flow using additional filtering at the interface," *Theor. Comput. Fluid Dyn.*, vol. 20, no. 2, pp. 89–101, 2006.

[36] Hanjalic, K., "Will RANS survive LES? a view of perspectives," *J. Fluids Eng.-Trans. ASME*, vol. 127, no. 5, pp. 831–839, 2005.

[37] Heinz, S., "Unified turbulence models for LES and RANS FDF and PDF simulations," *Theor. Comput. Fluid Dyn.*, vol. 21, pp. 99–118, 2007.

[38] Hirsch, C., *Numerical computation of internal and external flows, computational methods for inviscid and viscous flows*. Wiley, 1990.

[39] Hughes, T., Mazzei, L., and Oberai, A., "The multiscale formulation of large-eddy simulation: decay of homogeneous isotropic turbulence," vol. 13, pp. 505–512, 2001.

[40] Hughes, T., Oberai, A., and Mazzei, L., "Large eddy simulation of turbulent channel flows by variational multiscale method," vol. 13, pp. 1784–1799, 2001.

[41] Hutton, A. G. and Ashworth, R. M., "The challenge of turbulence modeling in modern aeronautical design," *Int. J. Numer. Methods Fluids*, vol. 47, pp. 721–737, 2005.

[42] Hylin, E. and McDonough, J., "Chaotic small-scale velocity fields as prospective models for unresolved turbulence in an additive decomposition of the navier-stokes equations," *Int. J. Fluid Mech. Res.*, vol. 26, pp. 539–567, 1999.

[43] Ishihara, T., Gotoh, T., and Kaneda, Y., "Study of high reynolds number isotropic turbulence by direct numerical simulation," *Annu. Rev. Fluid Mech.*, vol. 41, 2009.

[44] Jameson, A., "Time dependent calculations using multigrid, with applications to unsteady flows past airfoils and wings," *AIAA Paper 91-1596*, Jan. 1991.

[45] Jameson, A., Schmidt, W., and Turkel, E., "Numerical solution of the euler equations by finite volume methods using Runge-Kutta time stepping schemes," *AIAA Paper 81-1259*, Jan. 1981.

[46] Kawai, S. and Fujii, K., "Analysis and prediction of thin-airfoil stall phenomena with hybrid turbulence methodology," *AIAA J.*, vol. 43, no. 5, pp. 953–961, 2005.

[47] Keating, A. and Piomelli, U., "A dynamic stochastic forcing method as a wall-layer model for large-eddy simulation," *J. Turbul.*, vol. 7, no. 12, 2006.

[48] Kemenov, K. A. and Menon, S., "Explicit small-scale velocity simulation for high-re turbulent flows," *J. Comput. Phys.*, vol. 220, pp. 290–311, 2006.

[49] Kemenov, K. A. and Menon, S., "Explicit small-scale velocity simulation for high-re turbulent flows. part ii: Non-homogeneous flows," *J. Comput. Phys.*, vol. 222, pp. 673–701, 2007.

[50] Kerstein, A. R., "A linear-eddy model of turbulent scalar transport and mixing," *Combust. Sci. Technol.*, vol. 60, pp. 391–421, 1988.

[51] Kim, W. W. and Menon, S., "An unsteady incompressible navier-stokes solver for large eddy simulation of turbulence flows," *Int. J. Numer. Methods Fluids*, vol. 31, pp. 983–1017, 1999.

[52] Kolmogorov, A. N., "The local structure of turbulence in incompressible viscous fluid for very large Reynolds numbers," *Proceedings of the Royal Society of London Series A*, vol. 434, pp. 9–13, 1991.

[53] Labourasse, E. and Sagaut, P., "Reconstruction of turbulent fluctuations using a hybrid RANS/LES approach," *J. Comput. Phys.*, vol. 182, pp. 301–336, 2002.

[54] Laney, C. B., *Computational Gasdynamics*. Cambridge Univ. Press, 1998.

[55] Laval, J. P., Dubrulle, B., and Nazarenko, S., "Nonlocality of interaction of scales in the dynamics of 2d incompressible fluids," *Phys. Rev. Lett.*, vol. 83, pp. 4061–4064, 1999.

[56] Laval, J. P., Dubrulle, B., and Nazarenko, S., "Nonlocality and intermittency in three-dimensional turbulence," vol. 13, pp. 1995–2012, 2001.

[57] Lesieur, M. and Metais, O., "New trends in large-eddy simulations of turbulence," *Annu. Rev. Fluid Mech.*, vol. 28, pp. 45–82, 1996.

[58] Liu, N. S. and Shih, T. H., "Turbulence modeling for very large-eddy simulation," *AIAA J.*, vol. 44, no. 4, pp. 687–697, 2006.

[59] Lund, T. S., Wu, X., and Squires, K. D., "Generation of turbulent inflow data for spatially-developing boundary layer simulations," *J. Comput. Phys.*, vol. 140, pp. 233–258, 1998.

[60] Lynch, C. E. and Smith, M. J., "Hybrid rans-les turbulence models on unstructured grids," *AIAA paper 08-3854*, 23-26 June, Seattle Washington 2008.

[61] Meneveau, C. and Katz, J., "Scale-invariance and turbulence models for large-eddy simulation," *Annu. Rev. Fluid Mech.*, vol. 32, pp. 1–32, 2000.

[62] Menon, S. and Patel, N., "Subgrid modeling for simulation of spray combustion in large-scale combustors," *AIAA J.*, vol. 44, no. 4, pp. 709–723, 2006.

[63] Menter, F. R., "Two-equation eddy-viscosity turbulence models for engineering applications," *AIAA J.*, vol. 32, no. 8, pp. 1598–1605, 1994.

[64] Moin, P. and Mahesh, K., "Direct numerical simulation: A tool in turbulence research," *Annu. Rev. Fluid Mech.*, vol. 30, pp. 539–78, 1998.

[65] Monin, A. S. and Yaglom, A. M., *Statistical Fluid Mechanics*. MIT Press, 1979.

[66] Nikitin, N., Nicoud, F., Wasistho, B., Squires, K., and Spalart, P., "An approach to wall modeling in large-eddy simulations," *Phys. Fluids*, vol. 12, pp. 1629–1632, 2000.

[67] Paik, H., Escauriaza, C., and Sotiropoulos, F., "On the bimodal dynamics of the turbulent horseshoe vortex system in a wing-body junction," *Phys. Fluids*, vol. 19, pp. 045107–20, 2007.

[68] Piomelli, U., "Wall-layer models for large-eddy simulations," *Prog. Aeosp. Sci.*, vol. 44, pp. 437–446, 2008.

[69] Piomelli, U. and Balaras, E., "Wall-layer models for large-eddy simulations," *Annu. Rev. Fluid Mech.*, vol. 34, pp. 349–74, 2002.

[70] Piomelli, U., Balaras, E., Pasinato, H., Squires, K., and Spalart, P., "The inner-outer layer interface in large-eddy simulations with wall-layer models," *Int. J. Heat Fluid Flow*, vol. 24, pp. 538–550, 2003.

[71] Pitsch, H., "Large-eddy simulation of turbulent combustion," *Annu. Rev. Fluid Mech.*, vol. 38, pp. 453–482, 2006.

[72] Pope, S. B., *Turbulent Flows*. Cambridge University Press, 2000.

[73] Radespiel, R., Rossow, C., and Swanson, R. C., "Efficient cell-vertex multigrid scheme for the three-dimensional Navier-Stokes equations," *AIAA J.*, vol. 28, no. 8, pp. 1464–1472, 1993.

[74] Rogallo, R. and Moin, P., "Numerical-simulation of turbulent flows," *Annu. Rev. Fluid Mech.*, vol. 16, pp. 99–137, 1984.

[75] Sagaut, P., *Large Eddy Simulation for incompressible flows, An introduction*. Springer, third ed., 2005.

[76] Sánchez-Rocha, M., Kirtas, M., and Menon, S., "Zonal hybrid RANS-LES method for static and oscillating airfoils and wings," *AIAA paper 06-1256*, 9-12 January 2006.

[77] Schluter, J. U., Pitsch, H., and Moin, P., "Large eddy simulation inflow conditions for coupling with Reynolds-average flow solvers," *AIAA J.*, vol. 42, no. 3, pp. 478–484, 2004.

[78] Schouten, J. A., *Tensor Analysis for Physicists*. Dover, 1989.

[79] Schumann, U., "Subgrid scale model for finite difference simulations in plane channels and annuli," *J. Comput. Phys.*, vol. 18, p. 376, 1975.

[80] Segel, L. A., *Mathematics applied to continuum mechanics*. Dover, 1965.

[81] Shapiro, A. H., *Dynamics and Thermodynamics of Compressible Fluid Flow*. Jhon Wiley and Sons, 1953.

[82] Smagorinsky, J., "General circulation experiments with the primitive equations: I. the basic equations," *Monthly Weather Rev*, vol. 91, 1963.

[83] Spalart, P. R., "Strategies for turbulence modelling and simulations," *Int. J. Heat Fluid Flow*, vol. 21, pp. 252–263, 2000.

[84] Spalart, P. R., "Young person's guide to detached-eddy simulation grids," *NASA CR-2001 211032*, 2001.

[85] Spalart, P. R., "Detached-eddy simulation," *Annu. Rev. Fluid Mech.*, vol. 41, pp. 181–202, 2009.

[86] Spalart, P. R., Deck, S., Shur, M. L., Squires, K. D., Strelets, M. K., and Travin, A., "A new version of detached-eddy simulation, resistant to ambiguous grid densities," *Theor. Comput. Fluid Dyn.*, vol. 20, pp. 181–195, 2006.

[87] Spalart, P. and Allmaras, S. R., "A one-equation turbulence model for aerodynamic flows," *La Recherche Aerospatiale*, vol. 1, pp. 5–21, 1994.

[88] Spalart, P., Jou, W., Strelets, M., and Allmaras, S. R., "Comments on the feasibility of LES for wings and on a hybrid RANS/LES approach," in *First AFOSR International Conference on DNS/LES*, (Ruston Louisiana), Greyden Press, 4-8 Aug 1997.

[89] Speziale, C. G., "Analytical methods of the development of Reynolds-Stress closures in turbulence," *Annu. Rev. Fluid Mech.*, vol. 23, pp. 107–57, 1991.

[90] Speziale, C. G., "Turbulence modeling for time dependent RANS and VLES: A review," *AIAA J.*, vol. 36, no. 2, pp. 173–184, 1998.

[91] Spina, E. F., Smits, A. J., and Robinson, S. K., "The physics of supersonic turbulent boundary layers," *Annu. Rev. Fluid Mech.*, vol. 26, pp. 287–319, 1994.

[92] Squires, K. D., "Detached-eddy simulation: Current status and perspectives," in *Direct and Large Eddy simulation V* (Friedrich, R., Geurts, B. J., and Metais, O., eds.), pp. 465–480, Kluwer, Dordrecht, 2004.

[93] Strelets, M., "Detached eddy simulation of massively separated flows," *AIAA paper 01-0879*, 8-11 January 2001.

[94] Synge, J. L. and Child, A., *Tensor Calculus*. Dover, 1949.

[95] Tannehill, J. C., Anderson, D. A., and Pletcher, R. H., *Computational Fluid Mechanics and Heat Transfer*. Taylor and Francis, 1997.

[96] Taylor, C. A. and Draney, M. T., "Experimental and computational methods in cardiovascular fluid mechanics," *Annu. Rev. Fluid Mech.*, vol. 36, pp. 197–231, 2004.

[97] Temmerman, L., Hadziabdic, M., Leschziner, M. A., and Hanjalic, K., "A hybrid two-layer URANS-LES approach for large eddy simulation at high Reynolds number," *Int. J. Heat Fluid Flow*, vol. 26, pp. 173–190, 2005.

[98] Tennekes and Lumley, *A First Course in Turbulence*. The MIT Press, 1997.

[99] Thompson, J. F., Soni, B. K., and Weatherill, N. P., *Handbook of Grid Generation*. CRC Press, 1998.

[100] Tucker, P. and Davidson, L., "Zonal $k - l$ based large eddy simulation," *Comput. Fluids*, vol. 33, no. 2, pp. 267–287, 2004.

[101] Vincenti, W. G. and Kruger, C. H., *Introduction to Physical Gas Dynamics*. Krieger Publishing, 1965.

[102] Viswanathan, A. K. and Tafti, D. K., "Detached eddy simulation of flow and heat transfer in fully developed rotating internal cooling channel with normal ribs," *Int. J. Heat Fluid Flow*, vol. 27, pp. 351–370, 2006.

[103] Wang, M. and Moin, P., "Computation of trailing-edge flow and noise using large-eddy simulation," *AIAA J.*, vol. 38, pp. 22201–9, 2000.

[104] White, F. M., *Viscous Fluid Flow*. McGraw Hill, 1991.

[105] Wilcox, D. C., "Reassessment of the scale-determining equation for advanced turbulence models," *AIAA J.*, vol. 26, no. 11, pp. 1299–1310, 1988.

[106] Wilcox, D. C., *Turbulence Modeling for CFD*. CDW Industries 2nd ed., 1998.

[107] Winckelmans, G. S., Jeanmart, H., and Carati, D., "On the comparison of turbulence intensities from large-eddy simulation with those from experiment or direct numerical simulation," *Phys. Fluids*, vol. 14, no. 5, pp. 1809–1811, 2002.

[108] Xiao, X., Edwards, J. R., and Hassan, H. A., "Blending functions in hybrid large-eddy/Reynolds-Averaged Navier-Stokes simulations," *AIAA J.*, vol. 42, no. 12, pp. 2508–2515, 2004.

[109] Xiao, X., Edwards, J. R., Hassan, H. A., and Baurle, R. A., "Inflow boundary conditions for hybrid large eddy/Reynolds Averaged Navier-Stokes simulations," *AIAA J.*, vol. 41, no. 8, pp. 1481–1489, 2003.

[110] Yu, H. and Liu, Y., "A second order accurate, component-wise tvd scheme for nonlinear, hyperbolic conservation laws," *J. Comput. Phys.*, vol. 173, pp. 1–16, 2001.

[111] Zhong, B. and Tucker, P. G., "$k - l$ based hybrid LES/RANS approach and its applications to heat transfer simulation," *Int. J. Numer. Methods Fluids*, vol. 46, pp. 983–1005, 2004.

VITA

Martín Sánchez Rocha was born in Coyoacan México City on July 12 1978. He is the oldest son of Honorio Sánchez Gómez and María Guadalupe Rocha Vilchis. Although at early age he showed potential to outstand in school, he rather spend most of his time playing, which put him in academic problems. It was early in his secondary school education, when his academic life took a shift that would change the rest of his life. In 1991, after almost failing the academic year and being rejected from his school, his parents gave him a second chance to keep studding in the only school that they could find that would accept him, Escuela Tikal (the school closed 5 years after). It was at that school, at the age of 14, where he decided to take school seriously and finish not only secondary school, which at that time looked difficult, but also earning the highest degree possible in Aeronautics. In 1994, he was accepted to study high School at Universidad La Salle, a private school well-known for its strong education. During this time, his parents struggled seriously economically, being unemployed for a while. Fortunately, La Salle provided him the best educational and fun days of his life. In 1997, he was accepted to study Aeronautics at the Instituto Politecnico Nacional, graduating in 2002 with honors as the first of a class of 112. In 2002, he won a national scholarship to study Aerospace Engineering at the Georgia Institute of Technology, where he obtained a M.Sc. and Ph.D. In January 2009, he will start his professional career in Providence Rhode Island, joining SIMULIA as an Associate Development Engineer. Martin combines work with sports and music. He workout regularly, plays soccer, basketball, and plays the drums. He is a hardcore fan of the Mexican national soccer team. He is married to Tzatzilha Torres Guadarrama.